Spring 1-1-2014

Lidar Observations and Numerical Modeling Studies of Thermospheric Metal Layers and Solar Effects on Mesospheric Fe Layers

Zhibin Yu
University of Colorado Boulder, zhibin.yu@colorado.edu

Doctoral Dissertation

Lidar Observations and Numerical Modeling Studies of Thermospheric Metal Layers and Solar Effects on Mesospheric Fe Layers

by

Zhibin Yu
B.S., University of Science and Technology of China, 2009

A thesis submitted to the
Faculty of the Graduate School of the
University of Colorado Boulder in partial fulfilment
of the requirements for the degree of
Doctor of Philosophy
Department of Aerospace Engineering Sciences

December 2014

This thesis entitled:
Lidar Observations and Numerical Modeling Studies of Thermospheric Metal Layers and Solar Effects on Mesospheric Fe Layers
written by Zhibin Yu
has been approved for the Department of Aerospace Engineering Sciences

Prof. Xinzhao Chu

Chair of Dissertation Committee

Dr. Arthur Richmond

Date

The final copy of this thesis has been examined by the signatories, and we find that both the content and the form meet acceptable presentation standards of scholarly work in the above mentioned discipline.

Zhibin Yu (Ph.D., Aerospace Engineering Sciences)

Lidar Observations and Numerical Modeling Studies of Thermospheric Metal Layers and Solar Effects on Mesospheric Fe Layers

Thesis directed by Prof. Xinzhao Chu

By blocking extreme hazards from space and regulating radio wave propagation, the space-atmosphere interaction region (SAIR) – our window to open space – is essential for life on Earth and modern society. However, the physical and chemical processes governing the SAIR are not sufficiently understood due to the woefully incomplete measurements of neutral properties in this region, especially between 100 and 200 km altitude. Thermospheric Fe layers extending from ~70 to 170 km discovered by the Fe Boltzmann lidar at McMurdo, Antarctica have opened a new door to observing the neutral thermosphere and mesosphere. This dissertation is aimed at revealing such new discoveries and advancing our understanding of the thermospheric Fe layer formation, through analyzing the lidar data collected by the author in Antarctic winter and developing the first thermospheric Fe/Fe^+ model.

A one-dimensional high-latitude Fe/Fe^+ model based on physical and chemical first principles has been developed to quantitatively explore the source, formation and evolution of thermospheric Fe layers. We demonstrate that the observed Fe layers are produced by neutralization of converged Fe^+, mainly through the direct electron-Fe^+ recombination. We find that the polar electric field is capable of uplifting Fe^+ ions from the main deposition region into the thermosphere, supplying the source of neutral Fe. Both gravity-wave-induced wind shears and the polar electric field can converge Fe^+ layers. Vertical wind plays a key role in transporting Fe to form the observed wave structures, but horizontal divergence can largely offset the vertical convergence effects. These theoretical studies lay the foundation for exploring the thermosphere by resonance lidars.

The diurnal variations of Fe layers in the mesopause region are characterized with our lidar observations at McMurdo. A new finding is the solar effect on the Fe layer bottomside — daytime downward extension and nighttime upward contraction. We explain qualitatively how both neutral Fe chemistry with H, O and O_3 and photolysis of Fe-containing molecular species may play important roles in such Fe diurnal variations. These are entirely new results that provide

direct, real-time, quantitative evidence for the influence of solar UV radiation on the chemistry and composition of the mesopause region.

Dedicated to my parents and my wife for their endless and unconditional love.

Acknowledgements

First and foremost I would like to express my utmost gratitude to my advisor Professor Xinzhao Chu. Without her aspiring guidance and persistent help this dissertation would not have been possible. I am grateful to Dr. Arthur Richmond not only for his time and effort to advice me, but also for his invaluably constructive criticism. I would also like to thank Dr. Jeffrey Forbes for kindly providing me a numerical framework with which I start to establish the new model, and thank Dr. John Plane for his friendly support and advice to metallic chemistry in the numerical work, and thank Dr. Chester Gardner for the valuable discussions on the work of Fe diurnal variations and solar effects. I would also like to thank Dr. Tim Fuller-Rowell, Dr. Sharon Vadas, Dr. Daniel Weimer, Dr. Rebecca Bishop, Dr. Hanli Liu, Dr. Anne Smith and Ben Foster for their help. I would like to thank all the members of my dissertation committee for their supports and the time spent on my dissertation.

I would like to thank all our group members, Dr. Wentao Huang, Dr. Xian Lu, Dr. Bo Tan, Dr. Zhangjun Wang, John Smith, Weichun Fong, Brendan Roberts, Cao Chen, Jian Zhao, Ian Barry, for their help and support. I would also like to thank USAP personnel, especially the winter-over folks at McMurdo during 2011 winter season for their friendly supports and contributions to McMurdo lidar campaign.

I thank my family for encouraging me in my pursuits over the years. I am especially grateful to my parents, and my wife Dr. Ningyan Guo for their lasting emotionally supports.

Finally, I would like to acknowledge the National Science Foundation (NSF). This dissertation is supported by the NSF grants ANT-0839091 and PLR-1246405.

Contents

List of Tables

List of Figures

Chapter 1

Introduction

This dissertation is motivated by the compelling needs of exploring the Earth's neutral properties of the mesosphere and thermosphere, and their expansion into the geospace. The space-atmosphere interaction region (SAIR) above 50 km altitude is essential to understanding the evolutions of the atmosphere of planets. Mercury and Venus's atmosphere are hazard to sustain life. Water, once upon a time, was substantial on Mars; however it turned to a desert planet through continuously losing its atmosphere containing water vapor [*Moore and Horwitz*, 2007]. Entwined with the strongest planetary magnetic field among the inner planets, the SAIR of Earth, intriguingly, plays an essential role of regulating gaseous escape and sustaining the life on Earth. Furthermore, the SAIR is essential to the prediction of space weather, which is important to the modern society. Partial upper atmosphere is ionized by the extreme solar UV/EUV radiation, forming the ionosphere embedded within the SAIR. Changes in the ionosphere caused by the interaction between the space plasma, magnetosphere and neutral in the SAIR can significantly affect the propagation of radio waves and degrade the performances of radio communication and Global Positioning System (GPS). Some extreme disturbances can even cause communication or GPS blackout. Satellites are orbiting in the environment of SAIR. The drag exerted to spacecrafts by the friction between

the spacecrafts and ambient atmosphere decelerates their orbiting speeds and causes a long-term trajectory altitude decay. The SAIR is also a critical area for monitoring climate change. As predicated by *Roble and Dickinson* [1989], the rising greenhouse gas concentrations could cool down the SAIR, especially the mesosphere and lower thermosphere (MLT) region. However, SAIR is a highly dynamic and complex system, through the interaction between SAIR and solar wind under the presence of the magnetic field, and the mass, momentum and energy deposition from the lower atmosphere. Not only because of the complex system (spatial scales vary from a few kilometers to hundreds of Earth's radius), but also due to the limitations of observations, the neutral and ionic properties, chemical and physical processes in SAIR are not sufficiently described [*OASIS*, 2014]. In particular, measurements of the neutral thermosphere are woefully incomplete and in critical need to advance our understanding of and the ability to predict the SAIR.

To fully explore the SAIR requires measurements of the neutral atmosphere to complement radar observations of the plasma. Lidar measurements of neutral winds, temperatures and species can enable these explorations, an objective of one of the highest priorities for the upper atmosphere science community [*CEDAR: The New Dimension*, 2011; *NRC2013-2022 Decadal Strategy for Solar and Space Physics*, 2013]. To help address these issues, the Chu lidar group from the University of Colorado Boulder (CU-Boulder) deployed an Fe Boltzmann temperature lidar to Arrival Heights at McMurdo, Antarctica. The thermospheric neutral Fe layers up to 170 km [*Chu et al.*, 2011; *Chu et al.*, 2013], discovered by the Fe Boltzmann lidar observations at McMurdo, have opened a new door to observing the neutral polar thermosphere with ground-based instruments.

1.1 Studies of Mesosphere and Thermosphere by Metal Lidar

Lidar is a powerful instrument providing high spatial and temporal resolution data on temperature, winds and constituent densities [*Chu and Papen*, 2005]. Since mesopheric sodium (Na) and iron (Fe) layers were firstly detected by lidars [*Bowman et al.*, 1969; *Granier et al.*, 1985 and 1989], resonance fluorescence lidars, like Na or Fe lidars, were widely used to make measurements of neutral properties in the middle and upper atmosphere. For instance, the thermal structures of middle and upper atmosphere measured by range-resolved lidar at high-latitudes [e.g. *Lübken and von Zahn*, 1991; *Gardner et al.*, 2001; *Chu et al.*, 2002a; *Pan and Gardner*, 2003; *Lübken et al.*, 2014], mid-latitudes [e.g., *She et al.*, 1993, 2000, 2002a; *Senft et al.*, 1994; *States and Gardner*, 2000a,b, *Chu et al.*, 2005], and low-latitudes [e.g. *Fricke-Begemann et al.*, 2002; *Friedman and Chu*, 2007], shed a light on the understanding of dynamics of the middle and upper atmosphere. Metal lidar is also a powerful technology for studying the dynamic processes in the upper mesosphere and lower thermosphere, for instance, the wind and temperature tides observed by full-diurnal-cycle lidar [e.g., *She et al.*, 2003; *She*, 2004; *Yuan et al.*, 2008a,b]; measurements of vertical heat, constituent and momentum fluxes [e.g. *C. S. Gardner et al.*, 1995; *Gardner and Liu*, 2007]; studies of atmospheric instability [e.g. *Gardner et al.*, 2002; *Zhao et al.*, 2003], studies of gravity waves or planetary waves by lidar [e.g. *Chen et al.*, 2013, *Lu et al.*, 2013]. The resonance fluorescence lidar has been used to characterize the mesospheric metallic layers [e.g. *Gardner et al.*, 2011], and polar mesospheric clouds (PMCs) [e.g. *Chu et al.*, 2011a]. However, these studies had been constrained in the region from 80 to 110 km, which is the typical range that resonance fluorescence lidar can provide measurements.

The upper atmosphere in the altitude range of 100–200 km with the largest temperature

gradient is a dynamically complex and important region in the Earth's atmosphere and space environment. However, this region remains one of the least understood regions of the atmosphere. In particular, very little is known about the neutral atmosphere because of limited observations of neutral winds, temperatures and densities [*CEDAR: The New Dimension*, 2011]. Some of the fluorescence lidar studies reported the altitudes of metal layers exceeding 110 km and reaching 130 km. These metal layers diffusively distributed on the top of the main metal layers, hence, have been marked as the 'layer topside' [*Höffner and Friedman*, 2004, 2005], at Kühlungsborn, Germany (54°N, 15°E) in 1997 and 1998. These diffusive metal layers were observed during the period of meteor shower, and *Höffner and Friedman* [2004] suggested the diffusive metal layers to be likely connected to enhanced meteoroids inputs. The observed high-altitude sporadic layers in the literatures are up to 120 km, above and separate from the main layer [*Collins et al.*, 1996; *Gerding et al.*, 2001; *Gong et al.*, 2003; *Ma and Yi*, 2010; *Wang et al.*, 2012]. The limit of 130 km in these observations was consistent with the theory of meteor ablation [*Vondrak et al.*, 2008] and the results of modelling studies [*Feng et al.*, 2013; *Mash et al.*, 2014], and implied that neutral metal atoms hardly exist above about 130 km.

However, the discovery of thermospheric neutral Fe layer reported by *Chu et al.* [2011] has radically changed the view on the extension range of the neutral atoms and hint at their source [*Friedman et al.*, 2013]. In the observations of *Chu et al.* [2011], we reported two events with thermospheric Fe layers extending up to 155 km at McMurdo, Antarctica (77.8°S,166.7°E). Clear thermospheric gravity waves were observed in the neutral Fe layers, and this was the first time that thermospheric gravity waves were observed in the neutral metallic atoms between E-F region in the thermosphere. Since the discovery of thermospheric Fe layer, more observations on thermospheric metal layers have been reported from high to low latitudes. *Chu et al.* [2013] reported the first

thermospheric Fe layers extending over 170 km from McMurdo lidar observations in 2013. In the study of temperature tides in the main Fe layer at Davis, Antarctica (68.56°S, 77.96°E), *Lübken et al.* [2011] reported converged and Fe layer descending from 130–140 km, which is a strong evidence to support the discovery at McMurdo. *Tsuda et al.* [2012] reported the thermospheric Na layer in the altitudes 110–130 km observed at Syowa Station (69.0°S, 39.6°E) in Antarctica at the AGU Fall 2012 conference. Recently, *Friedman et al.* [2013] reported a thermospheric descending layer of neutral potassium with the vertical extent up to $\sim$ 155 km over Arecibo observatory in Puerto Rico (18.35°N, 66.75°W) on 12 March 2005. The descending rate the K layer is consistent with the vertical speed of the semidiurnal tide between 120 and 150 km. Another report from *Xue et al.* [2013] observed two lower thermospheric enhanced Na layers at a low latitude, Lijiang, China (26.7°N, 100.0°E) in 2012. *Gao et al.* [2014] reported the thermospheric Na layers up to 170 km at Lijiang, and *Liu et al.* [2014] reported the thermospheric Na layers up to 170 km at Cerro Pachon [geographic: 30.2°S and 70.7°W; geomagnetic: 41.5°S and 5.5°E]. The observations from the other lidar sites demonstrate that the thermospheric metal layers observed at McMurdo are not unique, and they have global distributions. The thermospheric metal species provide a new look into the thermosphere composition, chemistry, temperatures and dynamics.

The bottoms of metal layers usually locate at the altitude range where the atomic shelf is [*Plane*, 2003] and the sink of metallic layers is. This region is chemically complex, and heavily influenced by the solar radiance and neutral dynamical processes such as tides and gravity waves. As the two most abundant metal species in the mesosphere and lower thermosphere (MLT) [*Plane*, 2003], Iron (Fe) and (Na) layers share many common features, e.g., both come from meteoric ablation and exhibit similar seasonal variations with summer low and autumn/winter high column abundances [*Kane and Gardner*, 1993a; *Gardner et al.*,2005; *Yi et al.*, 2009; *Gerding et al.*, 2000].

We report one of the new lidar observations that reveals a significant extension downward of the Fe layer bottomside when the Sun rises and contraction when the Sun sets. Such behaviour has not been observed in Na [*Clemesha et al.*, 1982; *States and Gardner*, 1999; *Plane*, 2004]. These new data indicate the importance of photochemistry in the metal layers, and the different responses of the Fe and Na layers to solar illumination variations challenge the current understanding of metal chemistry in the upper atmosphere.

Unlike the extensive studies of Na layers by lidars, the reports in the literature on the diurnal variations of or the solar effects on the Fe layer were very rare. Numerous Fe layers observations have been reported in literatures at low latitudes at Arecibo (18° N) [*Raizada and Tepley*, 2003; *Zhou et al.*, 2008], mid-latitudes at Urbana (40°N), Kühlungsborn (54°N) and Wuhan (30°N) [*Kane and Gardner*, 1993a,b; *Gerding et al.*, 2000; *Yi et al.*, 2009; *Ma and Yi*, 2010], and high latitudes at Andøya (69°N), the North Pole (90°N), the South Pole (90°S), Rothera (67.5°S) and McMurdo (77.8°S) [*Alpers et al.*, 1990,1994; *Gardner et al.*, 2001; *Gardner et al.*, 2005, 2011; *Chu et al.*, 2011a, 2011b]. However, these reports mainly focus on the seasonal and latitudinal variations, sporadic layers, meteor trails, thermospheric Fe layers and waves, and polar summer events in connection with polar mesospheric clouds (PMCs) and space shuttle plumes [*Plane et al.*, 2004; *Stevens et al.*, 2005]. The diurnal variations of Fe layer had been ignored for more than two decades, because not only most observations made at mid to low latitudes were nighttime only, and the full diurnal observations at the South Pole and Rothera had little coverage during the transition time of solar illumination in the autumn and spring, but also people would not expect significant solar effects in metal layers since the Na layers were absence of significant extension of the Na layer bottom. *Yu et al.* [2012] reported the new observations covered full diurnal cycles in all four seasons at McMurdo (77.83°S, 166.67°E). In particular, continuous lidar observations were made in the

autumn and spring during the transition of solar illumination between daylight and night darkness, enabling studies of solar effects in the diurnal variations of the Fe layer. Although the report by *Yu et al.* [2012] is the first formal report of significant diurnal variations of the Fe layer to appear in the scientific literature, we are aware that J. Höffner has observed a similar daytime extension of the Fe layer bottomside at Andoya from 2008 to 2009 (J. Höffner, private communication, 2012). In addition, our group also observed this same feature at Boulder, Colorado in August and September 2010 when testing the Fe Boltzmann lidar prior to its McMurdo deployment, as reported in a PhD dissertation by *Wang* [2009].

1.2 Observation of Metallic Ions in the Mesosphere and Thermosphere

Although the thermospheric neutral metal layers have just been observed recently, the observations and studies of metallic ions can be traced back to 1950s. Summarized in this section is a brief description of the ground-based, rocket-borne and satellite-borne measurements of metallic ions in the mesosphere and thermosphere during the past sixty years.

1.2.1 Metallic ion in the mid-/low-latitude mesosphere and thermosphere

The existence of metallic ions was found by ground spectral measurements of atmospheric emissions in 1950s. The emission line 3933.8 Å of Ca II excited by twilight was discovered by *Jones* [1956] at Saskatoon (52.1° N, 106.7°W) during the summer of 1955 with a microphotometer. Later on, the emission of Ca II was also observed by *Dufay* [1958] at geomagnetic latitude 46°N and the geomagnetic South dipole. By utilizing scanning spectrometer and pulse counting techniques, *Broadfoot* [1967] was able to observe Ca II through a wide altitude range from 100 to 280 km at

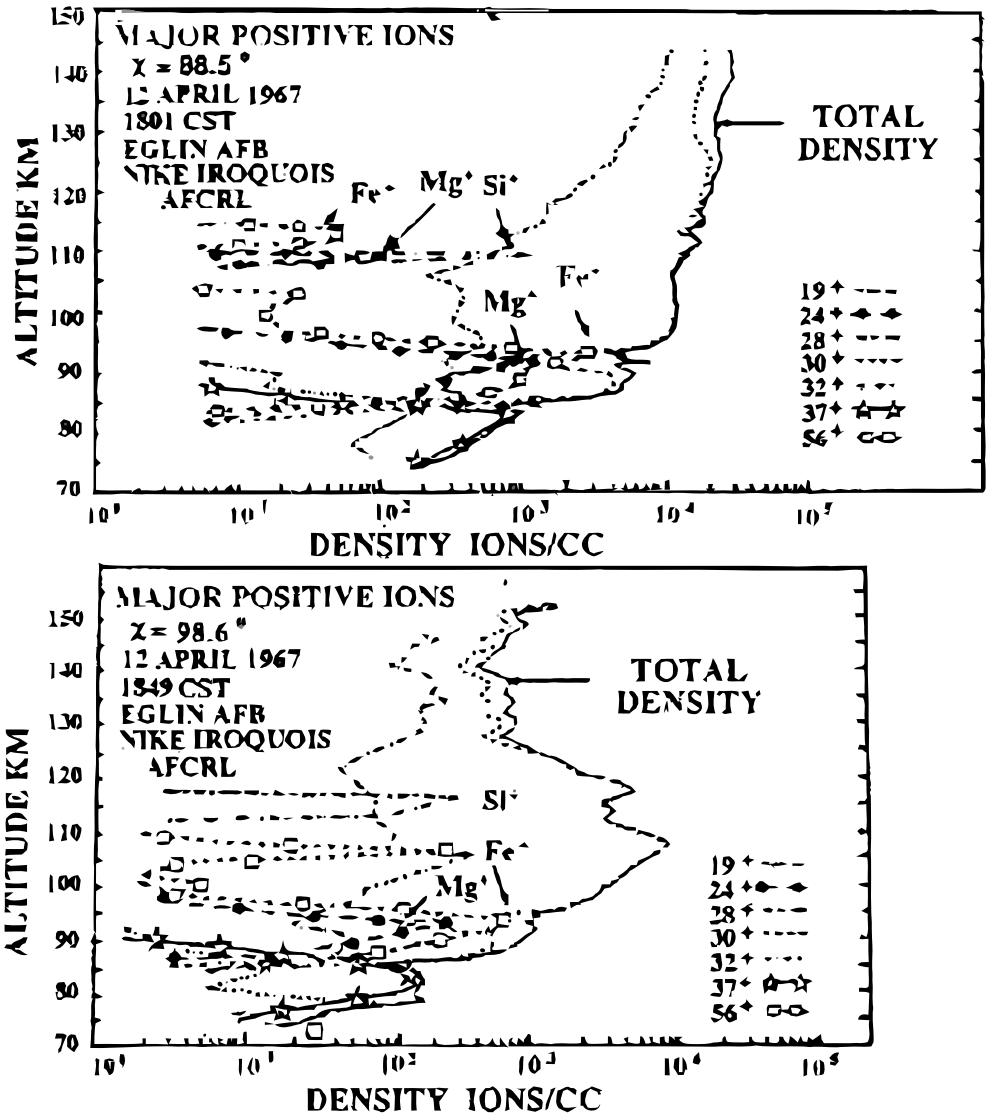

FIGURE 1.1: Two continuous rocket measurements, the time interval between these two rocket flight is less than one hour. The top plot is the measurement before sunset and the bottom is after sunset. From *Narcisi* [1971]

Kitt Peak National Observatory (geographic 31.9°N, 111.6°W; geomagnetic 40°N, 46.0°W), Tucson, Arizona, and the column abundance was estimated at least 2.5×10^7 cm^{-2} above 100 km. The first in-situ measurements were made by rocket-borne mass spectrometer [*Isomin*, 1963] in the middle latitudes of Europe, and it was found that the peak of the layer was largely composed of metallic ions of Fe^+ (1.5×10^4 cm^{-3}), Mg^+ (1.4×10^4 cm^{-3}) and Ca^+ (0.5×10^3 cm^{-3}) near 105 km. *Narcisi and Bailey* [1965] measured the ionospheric compositions by a rocket-borne mass

spectrometer at local noon from Eglin Air Force Base (geographic: 30.5°N, 86.5°W; geomagnetic: 40°N, 16.7°W), Florida. Their measurements offered the first metallic Mg^+ profile between 80 and 115 km with peak densities higher than 10^4 cm^{-3} at $\sim$ 94 km. Since the spectrometer only sampled from 1 to 46 amu, Fe^+ ions were not included in their report [*Narcisi and Bailey*, 1965]. By adopting an advanced mass spectrometer with broader mass coverage, *Narcisi* [1971] reported a complete metal ions layers including Fe^+, Mg^+, Si^+ between the altitude range from 70 to 150 km. The measurements shown in Figure 1.1 from two continuous flights less than one hour apart were reported. The two snapshots of metal-ion layers showed completely different structures, suggesting highly dynamic metal ion layers. The measurements from five rocket flights in the report of *Kopp* [1997] provided that the mean total column abundance of metal ions from 80 km to 125 km was within $4.4 \pm 1.2 \times 10^9$ cm^{-2} without meteor shower activity, and one magnitude higher during Perseid meteor shower. Numerous rocket-borne mass spectrometer measurements [*Aikin and Goldberg*, 1973; *Zbinden et al.*, 1975; *Kopp*, 1997] have demonstrated the presence of metallic ions at E region. A thorough summary of rocket measurements of metal ions in the region between 80 and 120 km at the middle and low latitudes can be found in *Grebowsky and Aikin* [2002]. To sum up, the measurements by rocket are sparse. As a consequence, it is hard to obtain a robust statistic of the distributions of metallic ions in the E-F region. Nevertheless, the existing pool of rocket measurements from 80 to 150 km suggests that the column abundances of metallic ions vary from 10^8 to 10^{10} cm^{-2}, and their peaks are around 95 km, depending on the metal species. For instance, the 17 samples at middle latitudes indicate that the peak of Fe^+ is 95 $\pm$ 2.5 km with densities $\sim 2.3 \times 10^3$ cm^{-3} and $\sim$ 5 km average width of the peaks [*Grebowsky and Aikin*, 2002]. Rocket flight usually has its altitude limitation, for instance, the most of 50 rocket-borne ion mass spectrometers in *Grebowsky and Aikin* [2002] only could reach 130 km. To investigate

intermediate layers, a series of rocket flights with powerful propulsion engines were launched from NASA Wallops Island Flight Facility (geographic: 37.8°N, 75.5°W; geomagnetic: 47.8N, 4.3°W) in 2003 [*Roddy et al.*, 2004]. The altitude range covered by the four rockets in that campaign was from 80 km to ∼200 km, and one of the rockets, Nike-Black Brant, achieved an apogee of ∼225 km. The Rocket Magnetic Sector Ion Mass Spectrometer carried by Nike-Black Brant can sample the Fe^+, Mg^+, O_2^+ and NO^+ ions and measure their concentrations with an altitude resolution of ∼100 m. The column abundance of Fe^+ in the region of high altitude (160–220 km) was 6.01×10^8 cm^{-2} (up) and 1.23×10^9 cm^{-2} (down), intermediate region (116–120 km) was 8.17×10^8 cm^{-2} (up) and 3.81×10^8 cm^{-2} (down), and sporadic-E region (100–106 km) was 1.87×10^{10} cm^{-2} (up) and 5.08×10^9 (down). The column abundance of Mg^+ in high-altitude region was 6.85×10^8 cm^{-2} (up) and 1.77×10^9 cm^{-2} (down), intermediate region was 2.55×10^8 cm^{-2} (up) and 4.53×10^8 cm^{-2} (down), and sporadic-E region was 2.96×10^9 cm^{-2} (up) and 1.36×10^9 cm^{-2} (down) [*Roddy*, 2005]. Here "up" and "down" refer to the up and downlegs of rocket flights.

The first in-situ measurements of metallic ions Fe^+ in the F region were reported by *Hanson and Sanatani* [1970] through analyzing the retarding potential analyser (RPA) on Ogo 6. These measurements were made at 2200 LT in the altitude range from ∼600 to ∼450 km, at approximately 83°W and dip latitudes covering from about −35° to 8°. The Fe^+ densities varied from 10 to 200 cm^{-3} at heights well above F_2 peak, and the peak densities of Fe^+ occurred at dip latitude of −20°. Another measurement by Atmosphere Explorer (AE) E revealed the Fe^+ concentration exceeding 10^4 cm^{-3} near 145 km and at 14° dip latitude on December 21, 1975 [*Kumar and Hanson*, 1980]. The RPA on Ogo 6 also provided latitudinal distributions of Fe^+. The data integrated from 400–1000 km revealed that the distributions of the observed Fe^+ ions highly depended on dip latitude, and mainly concentrated in a dip latitudinal bands from −30°

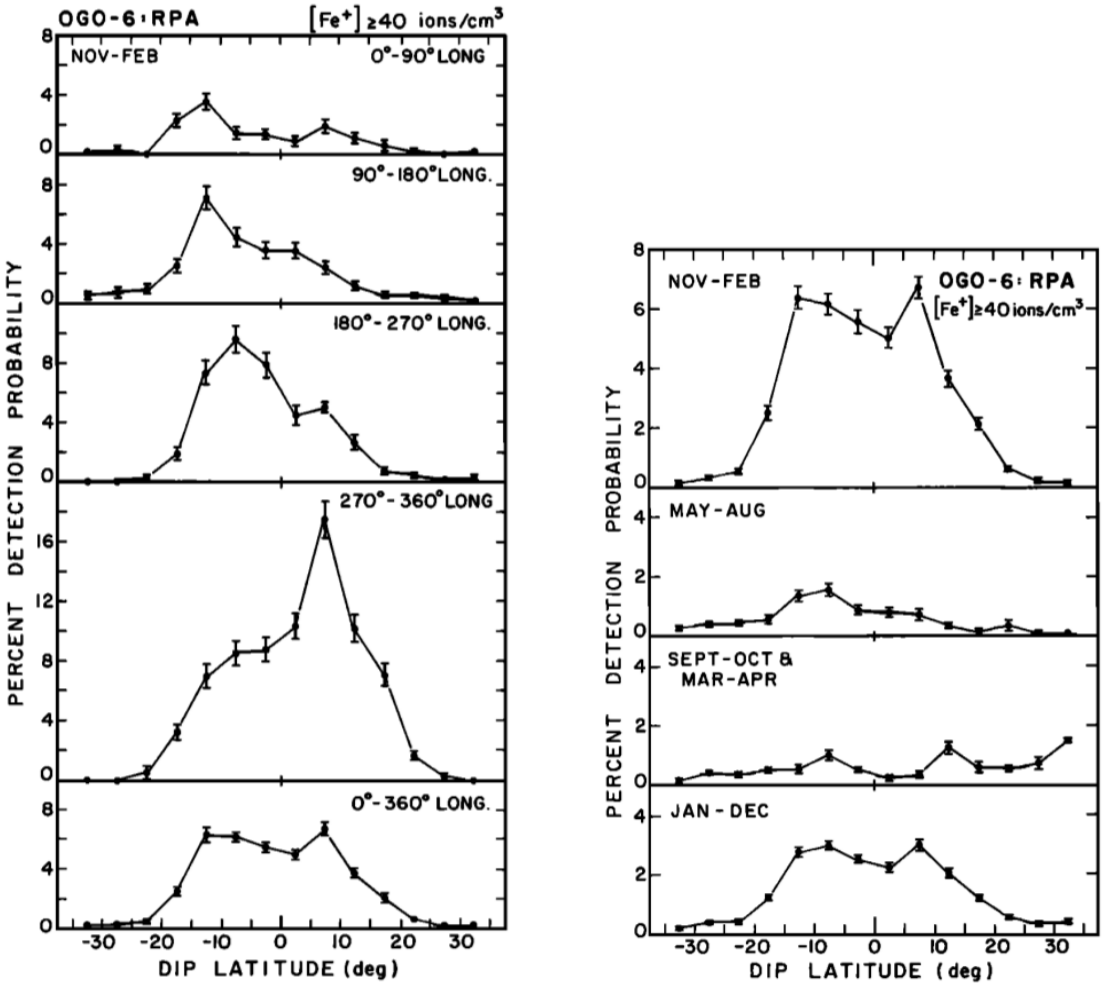

FIGURE 1.2: Detection probability versus dip latitude. Left: the latitudinal distributions of altitude integrated (400–1000 km) Fe^+ at different longitudes were measured by RPA on Ogo 6 at northern winters (November–February); Right: the seasonal variations of altitude integrated Fe^+ from the RPA on Ogo 6. The bar represents one sigma error. The detection probability describes the likelihood of finding Fe^+ whose density is larger than 40 cm^{-3} at different times and places in the upper atmosphere, based on a large data set. From *Kumar and Hanson* [1980].

and 30° with symmetrical structure, as shown in the left plot in Figure 1.2 [*Kumar and Hanson*, 1980]. The distributions of Fe^+ were also highly longitudinal dependent and the dip latitudes of the peaks of Fe^+ vary from $-10°$ to 10° at different longitudes. By utilizing magnetic ion mass spectrometers, satellite AE-C covered full metallic ion mass range with analogue long mode and AE-D covered up to 32 amu with analogue short mode. One example of AE-C measurement is showed in Figure 1.3. Two Fe^+ clusters were found at the dip latitude of $-13°$ and 5° at 234

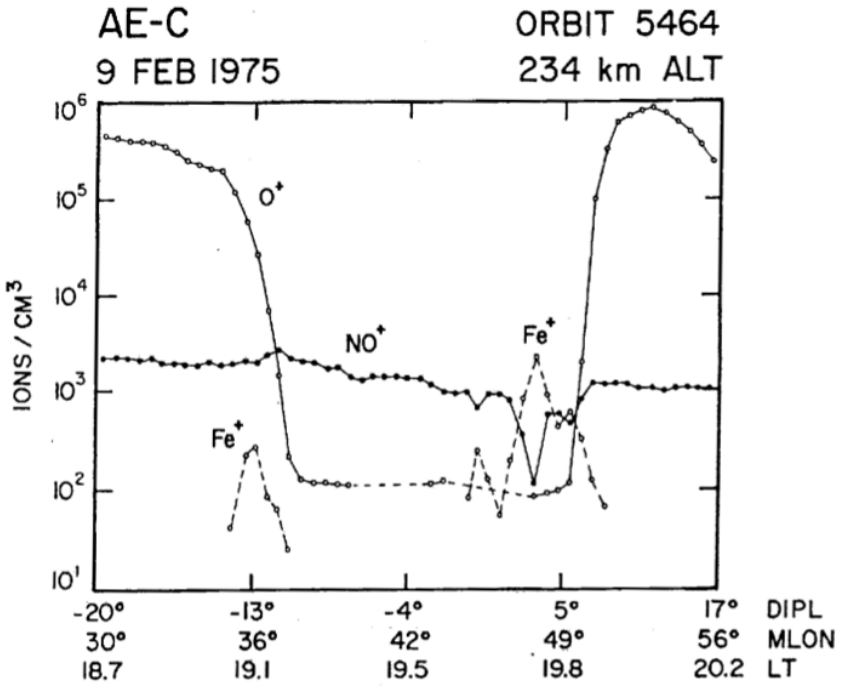

FIGURE 1.3: High altitude measurements of Fe^+ from Atmosphere Explorer C at 234 km by the Bennett Ion Mass Spectrometer. From *Grebowsky and Aikin* [2002]

km [*Grebowsky and Aikin*, 2002]. All these in-situ measurements by satellites shared one common feature that the metallic ions somehow were relatively concentrated in a latitudinal region from dip latitude $-30°$ to $30°$, and the peaks of density concentratios were not above dip equator, but some degrees off the dip equator.

The unique spectral lines of Mg^+ at 2796 Å and 2804 Å are utilized to detect Mg^+ in the mesosphere and thermosphere. Since these are two ultraviolet lines, it had not been observed until *Anderson and Barth* [1971] utilized a rocket-borne ultraviolet spectrometer and observed the Mg II 2800 Å doublet for the first time. The rocket was also launched from Wallops Island. A series of measurements of Mg^+ 2800 Å were also made by spectrophotometers aboard an Esro satellite and AE-E. The measurements by Esro satellite were above 540 km and the airglow of Mg^+ were found within approximately dip latitude 20° [*Gérard and Monfils*, 1974; *Gérard*, 1976]. The visible airglow experiment (VAE) on AE-E satellite provided diurnal variations of range-resolved Mg^+

density measurements through a wide altitude range from 150 km up to 500 km [*Gérard et al.*, 1979], and they found the maxima of Mg^+ densities was around 1400 LT at altitudes from 150 to 200 km. *Fesen and Hays* [1982] reported the latitudinal and longitudinal variations of Mg^+, based on the VAE measurements from AE-E, and they found the importance of zonal winds to the latitudinal and longitudinal variations of the peak concentrations of Mg^+. By taking advantage of imaging technique, *Mende et al.* [1985] reported the distributions of Mg^+ clouds near magnetic equator based on the images of airglow at 2800 Å taken by Spacelab 1 shuttle, and the bright emissions were observed at 12° north dip latitude and 12° south dip latitude with view-column abundance of $0.5 \sim 1.3 \times 10^{10}\ cm^{-2}$. The simultaneous observations of Mg and Mg^+ by the GLO instrument including twelve imagers and nine spectrographs with intensified-CCD focal planes covering spectral lines from 1200 to 11000 Å on the Space Shuttle were reported by *Gardner et al.*, [1995]. The GLO measured neutral Mg at spectral line 2852 Å and Mg^+ at 2796 and 2804 Å. Their measurements were constrained by the orbits of the shuttle, covering geomagnetic latitudes from $-30°$ to 60°. Thermospheric neutral Mg were observed at altitudes between 150 and 230 km with an instrument-view-column abundance of $0.4 \sim 1.4 \times 10^8\ cm^{-2}$, and the simultaneously observed Mg^+ column abundance was $1.4 \sim 5.8 \times 10^9\ cm^{-2}$. The corresponding density of Mg^+ is $\sim$250 cm^{-3} and Mg $\sim$5 cm^{-3}. By measuring the same spectral lines of Mg and Mg^+ as GLO did, *Langowski* [2014] provided monthly mean global vertical and latitudinal and seasonal distributions of Mg and Mg^+ layers between 70 and 150 km based on 4-year measurements from 2008–2012 using SCIAMACHY/Envisat observations. SCIAMACHY is satellite-borne grating spectrometer, carried by Envisat. In the studies of *Longowski* [2014], they found no clear seasonal cycle for Mg, but clear seasonal cycle for Mg^+ with a summer maximum and peak densities at mid-latitudes.

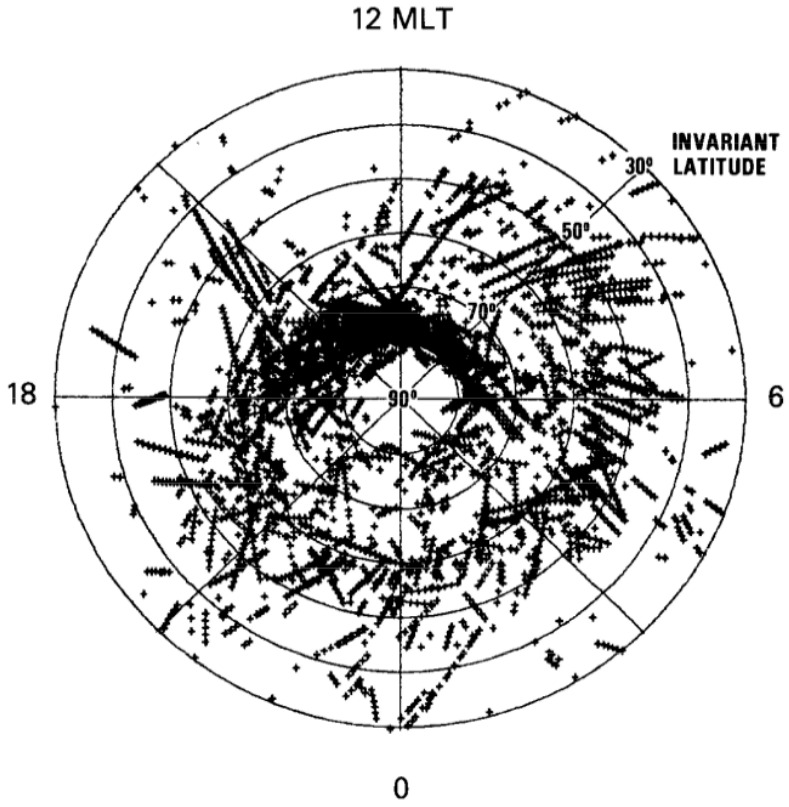

FIGURE 1.4: High-latitude measurements of Fe^+ from AE-C were plotted in terms of invariant magnetic latitude. Each data point represents a sample of Fe^+ measurement with density in excess of 30 cm^{-3}. The total data points were 4-year (1974–1978) accumulated data from AE-C. From *Grebowsky and Pharo* [1985].

1.2.2 Metallic ions in the polar mesosphere and thermosphere

Compared to the observations of metallic ions at mid/low- latitudes, the observations in the polar regions are limited by the geophysical conditions. Firstly, the latitudes are too high for most satellites to cover polar regions well due to the constraints of inclination angles of satellite orbits. Secondly, polar regions are relatively remote, and the southern polar region is particularly remote, thus logistics become a barrier for remote scientific campaign. Nevertheless, the existing data still revealed some characteristics of the distributions of metallic ions in the polar mesosphere and thermosphere.

The rocket-borne mass spectrometer detected meteor ions up to 190 km, and more than $\sim 10^4$ cm^{-3} of Mg^+ in the lower thermosphere in polar ionosphere [*Zhlood'ko et al.*, 1974]. The average peak altitude of Fe^+ in day was 89.9 ± 4.2 km based on 4 samples, and 93.1 ± 3.0 km for nighttime based on 11 samples at polar regions, and the average peak density is about 4.6×10^3 cm^{-3} [*Grebowsky and Aikin*, 2002].

Metallic ions above 200 km have been observed by satellite measurements at polar region [*Gérard et al.*, 1976; *Grebowsky and Brinton*, 1978; *Kumar and Hanson*, 1980; *Grebowsky and Pharo*, 1985, *Viereck et al.*, 1996]. The ultraviolet spectrometer observations from OGO-4 measured Mg^+ in the F region with a column density as high as 5×10^9 cm^{-2}. AE-C covered invariant geomagnetic latitude from $-80°$ to $80°$, and provided good coverage for polar region. Using the data from AE-C, *Grebowsky and Brinton* [1978] observed Fe^+ with densities exceeding 100 cm^{-3} at altitudes ranging from 220 to 320 km. Sometimes, the detected Fe^+ number densities can be as high as 10^3 cm^{-3}. At polar region, higher Fe^+ number densities tended to appear in the vicinity of the cusp magnetic field lines with enhancements of Fe^+ at the dayside auroral zone, as shown in Figure 1.4 [*Grebowsky and Pharo*, 1985].

Despite the numerous observations listed above, we still do not have a clear picture of Fe^+, Mg^+, Ca^+, Na^+ and K^+ in terms of their occurences, altitude distributions, relative column abundances, and global distributions. Partially this is because measurements are not extensive or systematic enough to provide a statistically significant picture; meanwhile, the variability of metallic ions in the thermosphere is so much larger than the neutral species that the snapshot measurements are not able to give a comprehensive picture. Such high variability of metallic ions indicate that the transport and distribution of these ions may be quite different from their neutral counterparts.

1.3 Theoretical Studies of Metallic Ions Transport and Layering

In this section, a brief review is provided on the studies of metallic species in the mesosphere and thermosphere from the aspects of their sources, layering, and numerical modelling studies.

1.3.1 Sources of thermospheric metallic species

The ultimate source of metallic species in the upper atmosphere is extraterrestrial cosmic dust [*Plane*, 2012]. When the meteoroids enter the Earth's atmosphere, colliding with air molecules with relative high speeds between 11 to 72 kms^{-1}, the heat energy generated by frictions melts the metallic species in the meteoroids and deposits metallic species such as Fe, Na, Mg, Ca and K by ablation and sputtering into the region between 80 and 125 km [*Vondrak et al.*, 2008]. This region is referred to the main deposition region of metallic species. As shown in Figure 1.5, the peak production rate of Fe or Mg is more than 0.1 $cm^{-3}s^{-1}$ at altitude ~85 km when the meteor input is about 88 td^{-1}. The shapes of the production rate are similar to Chapman function, generated by the product of air density monotonically decreasing with increasing altitude and the flux of meteoroids increasing with increasing altitude. Above 125 km, it is clear that the injection rates are significantly smaller (about 4 orders of magnitude) than those in the main deposition region below 110 km [*Vondrak et al.*, 2008; *Feng et al.*, 2013].

Then interesting questions intrigued by meteoroid ablation and sputtering theory are why and how metallic ions or neutral atoms get up to the thermosphere above 125 km. Overall, the possible mechanisms of metallic ions or neutral atoms occurring in the thermosphere can be grouped into following categories: (a) direct evaporation from the ablation of meteoroid; (b) sputtering process of high-velocity, low mass meteoroids; (c) vertical and horizontal redistributions driven by neutral winds or electrodynamic forces; (d) in-situ production caused by chemical conversions.

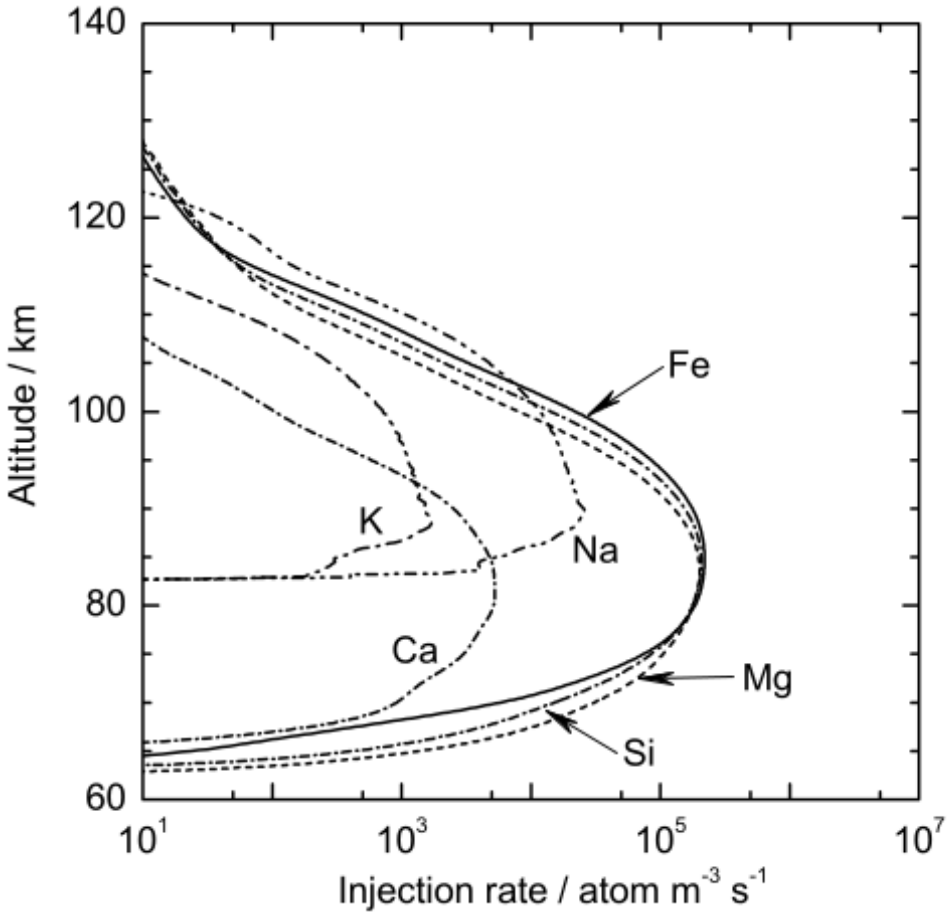

FIGURE 1.5: This is from Figure 11 in *Vondrak et al.* [2008]. Note that the total mass flux is about 88 td^{-1}.

The first two mechanisms are in-situ production, and both occur when meteoroids enter the Earth's atmosphere. *Vondrak et al.* [2008] provided comprehensive studies of the processes of ablation and sputtering. Above 125 km, because of the extremely low air pressure, the frictions and collisions between air gases and meteoroids are not enough so that metallic species, to a great extent, would not be able to release from meteoroid [*Plane*, 2003; *Vondrak et al.*, 2008]. According to the calculation of the Chemical Ablation Model (CAMOD) in *Vondrak et al.* [2008], it would take longer than 10^5 seconds to produce 1 cm^{-3} metallic species. In addition, it is impossible for heavier metallic species floating in the thermosphere forever, because gravity and diffusion gradually move

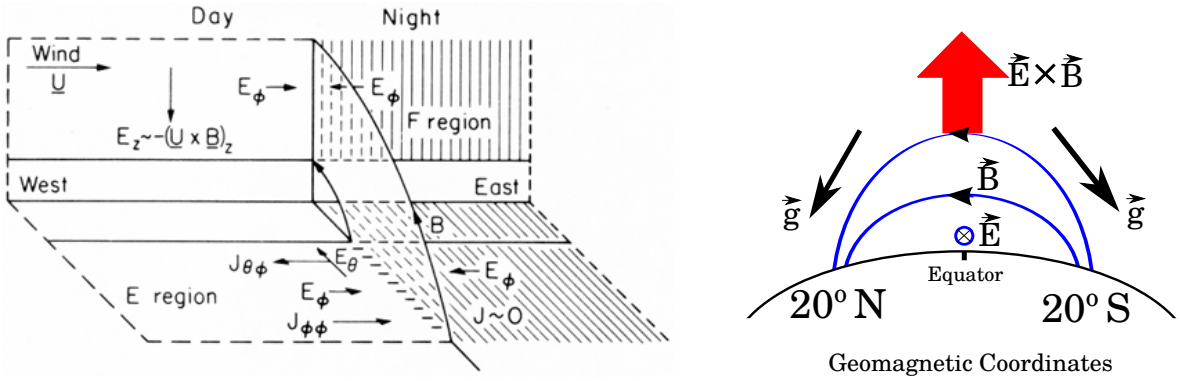

FIGURE 1.6: Left: Oversimplified model of electric field pattern at mid and low latitutdes. From *Farley et al.* [1986]. Right: Fountain effect at equator region.

the heavier metallic species into the MLT region. Even if neglecting the effects of gravity and diffusion, this production rate is too slow to produce appreciable number densities, compared to the observed number densities. Therefore, a consensus of opinions among the previous literatures [*Hanson and Sanatani*, 1970; *Hanson and Sterling*, 1972; *Grebowsky and Brinton*, 1978; *Grebowsky and Pharo*, 1985; *Plane*, 2003] is that the thermospheric metallic species are unlikely produced by in-situ meteor input directly, and the most likely mechanisms are dynamical transport for metallic ions [*Hanson and Sanatani*, 1970; *Grebowsky and Brinton*, 1978] or chemical conversion for metallic neutrals [*J. A. Gardner et al.*, 1995; *Chu et al.*, 2011].

1.3.2 Transport associated with metallic ions

Neutral winds and electric fields have been recognized to be the two fundamental forcing parameters in the process of transporting metallic ions into the thermosphere. Under static and collisionless conditions, metallic ions gyrate about geomagnetic field lines, and the gyrofrequency is about hundreds of Hz and the gyroradius is about 1 meter. When neutral winds or electric fields are present, ions' motion would be heavily modulated by neutrals' motions via ion-neutral collision, producing ion drifts. On one hand, the momentum transferred from neutrals to ions forces ions to

move in the direction of neutral winds; on the other hand, ions cannot freely move with neutrals due to the constrains by the geomagnetic field. The electrostatic force caused by electric field can also generate ion drifts. Upward ion drifts could transport metallic ions from the main deposition region to higher altitudes, if neutral winds and electric fields point to appropriate directions.

At low latitudes, the electric field E_z generated by the F region dynamo $-\vec{V} \times \vec{B}$ mapped to the E region along with the geomagnetic field lines, generates a low latitude Hall current directed to west, and electric field directed to east [*Farley et al.*, 1986], as shown in the left panel of Figure 1.6. The eastward zonal electric field in the equatorial region during the day, drives an upward $\vec{E} \times \vec{B}$ vertical drift velocity. After sunset, the F region dynamo intensifies this easward electric field, and the metallic ions in lower F region are further uplifted to higher altitudes. At some point, the ions fall along with the geomagnectic field lines to higher latitudes due to the gravity and diffusion. The upward transport of metallic ions from the main deposition region up to F region is known as "fountain effect" [*Hanson and Moffett*, 1966; *Hanson et al.*, 1972]. A depiction of the fountain effect is shown in the right panel of Figure 1.6. The fountain effect is mainly driven by the equatorial eastward electric field, and falling motions of ions are controlled by not only gravity, but also the topography of geomagnetic field lines. Therefore, fountain effect is regional effect, usually constrained within dip latitudes from $-30°$ to $30°$. This can explain why the distribution of metallic ion densities in Figure 1.2 and 1.3 were mainly within dip $-30°$ and $30°$, and their peaks were some degree off the dip equator.

The fountain effect does not work at high latitude region. However, ions can be transported upward by the polar electric field. The high-latitude convection electric fields at polar cap regions are originated from the magnetospheric plasma convection, which is the basic ideas developed in 1960s by *Dungey* [1961] and *Axford and Hines* [1961] to explain the polar disturbance (Ds)

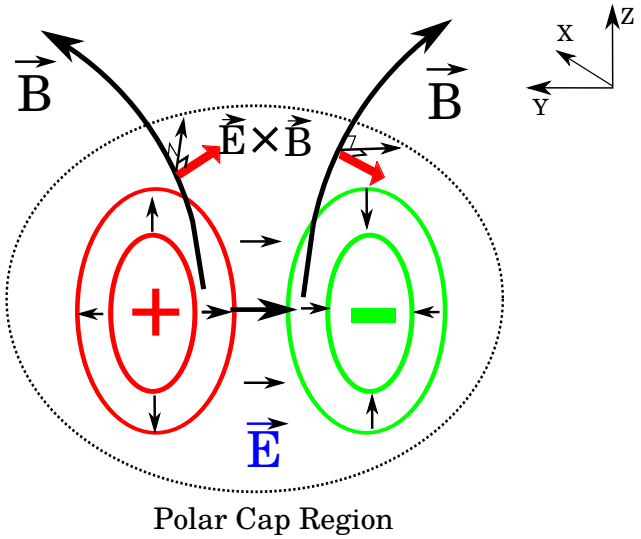

FIGURE 1.7: Convection electric potential and field in the southern hemisphere. The two convection cells are in the paper plane, and the geomagnetic field points out of the paper plane.

current system. An over-simplified model of the convection electric potential and field are shown in Figure 1.7. When magnetospheric potentials project to ionosphere due to the high conductivity of geomagnetic field lines, large-scale and large-amplitude convection electric fields perpendicular to geomagnetic field line are generated. The convection electric field results in high speed of $\vec{E} \times \vec{B}$ ion drifts [*Kumar and Hanson*, 1980; *Grebowsky and Pharo*, 1985], which are essentially similar to the first stage of the fountain effect. The motions of positive ions driven by convection electric field are complex, not only because the collisions with neutrals impede the ion's $\vec{E} \times \vec{B}$ drift, resulting in the direction and magnitude of ion's drift changing with altitude, but also because of the complex pattern of electric field driven by mangetospheric plasma convection. For instance, at higher altitudes where ion-neutral collisions are negligible, the direction of electric field has to be eastward in order to produce upward transport of metallic ions for southern polar cap; at lower altitudes where ion-neutral collisions are important, the electric field has to be poleward directed to produce upward Pedersen drift. It can be seen from Figure 1.7 that convection electric fields change directions and magnitudes in the two convection cells, producing upward transport

at some regions, and downward transport at other regions for the same moment. Furthermore, the convection electric field is intense enough to produce significant upward transport. It is common that the convection electric field exceeding 50 mVm^{-1}, corresponding to approximately 800 ms^{-1} $\vec{E} \times \vec{B}$ drift in the F region [e.g., *Spiro et al.*, 1979; *Shepherd et al.*, 2003]. Despite the high inclination angle of geomagnetic field line, the vertical component of $\vec{E} \times \vec{B}$ drift is still large enough to uplift metallic ions to higher F region.

The last mechanism of transporting metallic ions to F region is the mesospheric and thermospheric neutral winds. *Kumar and Hanson* [1980] showed that the poleward neutral wind in the mid-latitude thermosphere in daytime or equatorward wind at night pushed metallic ions along with geomagnetic field line down from F region to approximately 120 km or from approximately 120 km up to F region, respectively. Approximately, the altitude of 120 km is where gyrofrequency and ion-neutral collision frequency are comparable. Below approximately 120 km, ion's motions are mainly governed by neutral motions via strong ion-neutral collision coupling; therefore, the eastward directed neutral wind can uplift metallic ions from lower altitudes to ~120 km. Figure 1.8 shows the effects of neutral winds on the transport of positive ions in the mesosphere and thermosphere.

Overall, the patterns of electric fields and neutral winds in the upper atmosphere are highly complex and dynamic. As shown in Figure 1.9, the neutral winds in the upper atmosphere are driven by non-uniformed global heat input from short-wavelength solar radiation, and the momentum and energy deposited by planetary waves, tides and gravity waves from lower atmosphere, and the heat caused by ionospheric currents, and the energy particle precipitation coming from magnetosphere. At mid and low latitudes, electric fields are produced self-consistently by neutral winds blowing in the partially ionized atmosphere via dynamo effects. At high-latitude region, the convection

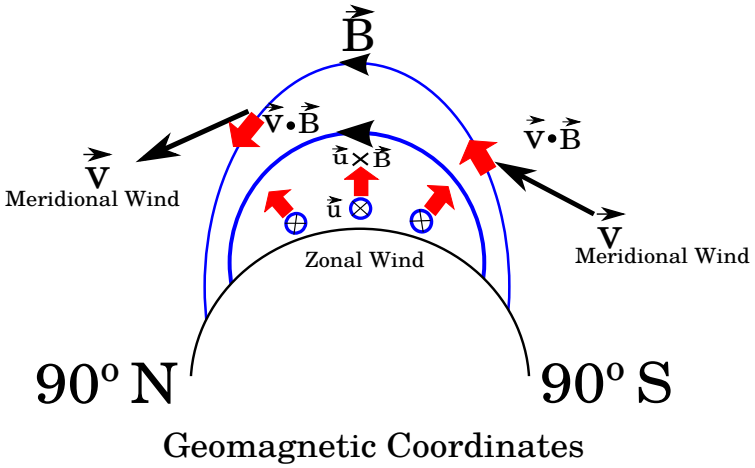

FIGURE 1.8: Ion transport driven by neutral winds.

electric fields are extremely dynamic, depending on the solar activity and the interaction between interplanetary magnetic field (IMF), solar wind and magnetosphere, and interaction between magnetosphere and ionosphere. The neutral winds and electric fields couple into the ion's motions, and the ion's motions couple back to electric field and neutral winds. It leads to complex motions of ions, for instance, ions can be transported upward or downward, converged or diverged.

1.3.3 Mechanisms for ion convergence in the E and F regions

Unlike Fe^+, Fe is free from the electromagnetic forces so that the upward transport of Fe can only rely on the vertical convection of neutral winds. In the earth's gravitational field, neutral vertical transport is constrained by gravitational force, and heavier atoms like Fe tend to sink to the bottom of the atmosphere. Therefore, *Chu et al.* [2011] made a reasonable hypothesis that the production of thermospheric atomic Fe was linked to the neutralization of Fe^+ from layered Fe^+, through direct electron recombination: $Fe^+ + e^- \longrightarrow Fe + h\nu$ above 120 km. However, this direct recombination is very slow, and the reaction rate is on the order of 5×10^{-12} cm^3 s^{-1}. To produce sufficient Fe within a certain time, the hypothesis requires a certain amount

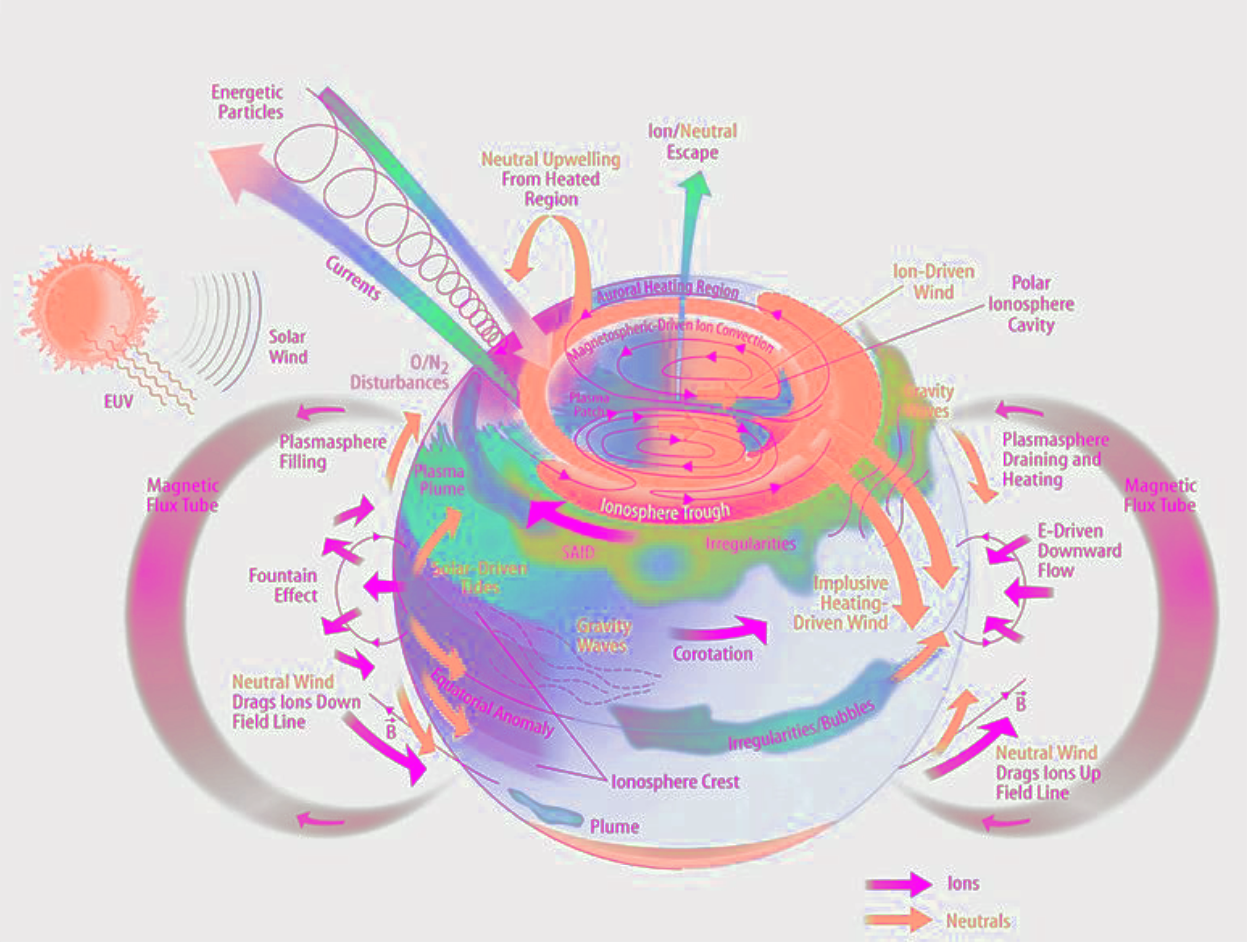

FIGURE 1.9: Magnetosphere, Ionosphere and Thermosphere coupling. Courtesy of Joseph Grebowsky, NASA GSFC.

of Fe^+. The observations introduced in Section 1.2 showed both low and high concentrations of metallic ions above the main deposition region at mid/low- or high-latitudes, but it seemed that low concentrations were more common based on the observations. Then this poses an interesting question how Fe^+ would be concentrated, how converged metallic layers are formed at different geographic and geomagnetic latitudes, and what roles the electric field and neutral winds play in the ion layering.

Under certain circumstance, converged ion layers, which are thin (less than ~5 km vertical thickness) plasma layers with relatively high density on the order of magnitude of 10^5 cm^{-3}, have

been frequently observed [*Mathews*, 1998]. For the past 60 years, these E-F region layers have been observed by ionosondes, radars, and in-situ measurements all over the world. *McNicol and Gipps* [1951] provided one of the early ionosondes observations of converged ion layers. The converged descending layers in the E-F region were frequently observed by incoherent scatter radar (ISR) measurements [*Behnke and Vickery*, 1975; *MacDougall*, 1978; *Tepley and Mathews*, 1985, *Tong et al.*, 1988; *Morton et al.*, 1993; *Mathews et al.*, 1993; *Earle et al.* 2000; *Bishop*, 2000] over Arecibo Observatory (18.35°N, 66.75°W). *Haldoupis* [2011] presented an observations for six consecutive days, showing a regular and repeating pattern of converged descending ion layers over Arecibo. Rocket measurements have demonstrated that the converged layers in the E region were mainly composed of metallic ions. There are only a few observations reporting the composition of converged descending ion layers, which may be comprised of the combination of molecular ions such as NO^+ and O_2^+, metallic ions such as Fe^+ and Mg^+. Above 140 km, the AE-C and AE-E satellites provided measurements of ion composition in converged layers at high altitudes [*Miller et al.*, 1993; *Heelis*, 1993], where the layers were dominated by molecular ions, NO^+ and O_2^+.

One of the basic physical understandings of converged descending layers is the windshear ion convergence mechanism, first proposed and formulated by *Whitehead* [1961] and *Axford* [1963], and it was well developed by many other authors [e.g., see a review by *Whitehead*, 1989]. The core of the windshear mechanism is that thin ionization layers are converged by the vertical drift produced by horizontal wind shears via collisional coupling between neutrals and ions. The windshear mechanism is widely supported either by these ISR observations, or by the in situ probes [i.e., *Smith*, 1970; *Bishop*, 2000]. Besides neutral windshear, electric field is also capable of compressing ions to a thin layer. *Nygrén et al.* [1984] were the first to investigate the details of effect of an electric field on the vertical ion motion in the E-F region, and they proposed a theory of the formation of

thin ionization layer via external electric field. The developments of the ion convergence theory of the electric field were made by several other authors [*Kirkwood and Von Zahn*, 1991; *Bristow and Watkins*, 1991;*Bristow and Watkins*, 1994; *Parkinson et al.*, 1998]. All indicate that the external electric field in an appropriate direction can drive ions to convergence.

1.3.4 Numerical modeling of metallic ions and atoms

Usually a self-consist model is needed to study the ion's motion precisely, which would make the model very complicated. Fortunately, as minor species in the upper atmosphere, the feedback of metallic ions to the background electric field and neutral winds and major compositions can be neglected for most circumstances. Therefore, the following numerical modeling studies of metallic ions are not, and do not have to be, self-consistent models.

By using a numerical solution for the motions of ions, the roles of neutral winds and electric field in localized layering of ionization layers can be carefully examined, for the sake of differences between mid-/low latitudes and high latitudes. Based on measured wind profiles, the early one-dimensional numerical simulations supported the windshear theory that mid-latitude converged ionization layers were caused by neutral-wind-induced compression [*MacLeod et al.*, 1975]. This model was applied to study the observed sporadic layers in the Aladdin 1 experiment at Florida, 1970, taking the chemical reactions of molecular ions and metallic ions and a constant electric field into account. *Mathews and Bekeny* [1979] provided numerical studies of converging mechanism involving tides, the equatorial fountain effect, which might explain the global transport of metallic ions. The global transport and converging metallic ions layers in E-F region were further investigated by a comprehensive numerical model involving physical and chemical processes [*Carter and Forbes*, 1999]. The primary purposes of their studies were to simulate global transport of metallic ions via evaluating the fountain effects, and to simulate the tidal ion layers through

imposing tidal-like winds. *Bishop and Earle* [2003] took a further step. In their simulation, they found that the waves with larger amplitudes and longer wavelengths are more efficient to transport ions, specifically Fe^+, in the direction of the progressing neutral wind field. These studies were aimed to explain the converged metallic ion layers over Arecibo. *Osterman et al.* [1994] simulated the converged ionization layers that can be comprised of ambient ions such as NO^+ and O_2^+ in the nighttime over Arecibo. There are several other studies focusing on modeling of Mg^+ in the upper and thermosphere [e.g., *Fesen et al.*, 1983; *McNeil et al.*, 1996]. At high latitudes, the understanding of converged descending layer is not as clear as that at mid-/low altitudes [*Kirkwood and Nilsson*, 2000]. *Bristow and Watkins* [1991] further investigated the work of *Nygrén et al.* [1984], using a one-dimensional numerical simulation, and predicted that thin ionization layers were formed when electric field directed to northwest and southwest quadrants. To investigated the geographical distribution of thin ionization layers, *Bristow and Watkins* [1994] developed a three-dimensional simulation, and they found the patterns of large areas of thin ionization layers formed by convection electric fields were also related to the configuration of interplanetary magnetic field (IMF). *MacDougall et al.* [2000] found that when sporadic layers occurred, the convection velocity of ions driven by electric field was slow, so they suspected the gravity waves should be the major force of forming sporadic E layers. Their simulation showed that the sporadic E layers formed above the convergent nulls of the gravity waves because of the perturbation induced by gravity wave to the vertical ionization profiles. *Nygrén et al.* [2006] investigated the link between IMF and sporadic E layers within the polar cap. Their model results showed the occurrence of sporadic layer, to a great extent, was in good agreement with the electric field theory of sporadic E. However, the new calculation indicated that the compression of ionization layer happened at altitudes of high vertical convergence rather than a convergent null in the vertical ion velocity. Due

to the lack of neutral observations, the numerical modeling studies listed in this section only focus on simulations of ions.

FIGURE 1.10: A map of Antarctica. McMurdo is marked as a red star. As of 2005, the South Geomagnetic Pole is located at 79.74^{o}S, 108.22^{o}E (geographic), near the Vostok Station.

1.4 McMurdo Lidar Campaign and My Winter-over Work in 2011

McMurdo Station is a United States of America (USA) Antarctic research center, located on the southern tip of Ross Island and has geographic coordinates: 77.8°S, 166.7°E; geomagnetic coordinates: 80.0°S, 33.3°W, as shown in Figure 1.10. McMurdo station is run by the United States Antarctic Program, a branch of the National Science Foundation. McMurdo is the largest research station in Antarctica, supporting around 1000 residents in summer and 150 winter-over residents in winter. McMurdo is located at a geomagnetic latitudes of about 80° close to the Geomagnetic

South Pole, at the poleward edge of aurora oval. It is also close enough to the Geographic South Pole, leading to four-month polar days, four-month polar nights, and four-month day and night transition at McMurdo, Antarctica. There are many days (about 2 months) having total darkness. Therefore, McMurdo station is an excellent site for conducting experiments to examine natural phenomena occurring in the Earth's atmosphere and space. A photo of McMurdo station in March 2011 is shown in Figure 1.11 top left.

To fill a critical data gap in observations of the middle and upper atmosphere between the South Pole and the Antarctic Circle, the University of Colorado lidar group deployed an Fe Boltzmann lidar to McMurdo Station and has been collecting data since the austral summer of 2010-2011 [*Chu et al.*, 2011a, 2011b]. This lidar campaign is a collaboration between the United States Antarctic Program (USAP) and Antarctica New Zealand (AntNZ). The lidar was successfully installed in the AntNZ facility at Arrival Heights near McMurdo, and the first Fe signals were obtained on 16 December 2010. Since then, the University of Colorado lidar researchers have operated the lidar around the clock, weather permitting, through all 12 months of the year to acquire as many Fe observations as possible. Developed at the University of Illinois more than a decade ago [e.g., *Chu et al.*, 2002], the lidar system consists of two independent channels operating at two neutral Fe absorption lines, 372 nm and 374 nm, respectively; and the system diagram is given by Figure 1.12. Thus, the lidar measures the Fe layers in two different wavelengths, and the ratio between these two channels is used to derive temperatures in the MLT region [*Gelbwachs*, 1994; *Chu et al.*, 2002]. Owing to the narrowband interference filters and Fabry-Perot etalons employed in the lidar receivers and the high-power pulsed Alexandria lasers employed in the lidar transmitters, this Fe Boltzmann lidar is capable of full-diurnal measurements of Fe density and temperature, along with Rayleigh temperature in the altitude range of ~30 to 70 km. Principles,

capabilities and error analysis of the lidar can be found in [*Chu et al.*, 2002]. Before its deployment to McMurdo, this Fe Boltzmann lidar was refurbished and upgraded at the University of Colorado to restore its specifications and to further enhance spectral stability, temporal resolution and daytime capability [*Chu et al.*, 2011a; *Wang et al.*, 2012]. These middle left photo in Figure 1.11 shows the transmitter of lidar system in the AntNz laboratory at Arrival Heights, and the middle right photo is the two outgoing laser beams.

Arrival Heights is a small range of low hills near the south-east (SE) end of Hut Point Peninsula, SE Ross Island, 1.5 km north of McMurdo Station and 3 km northwest of Scott Base. Hut Point Peninsula is formed by a line of craters that extend south from the flanks of Mt. Erebus, which is a live volcano. The highest elevation within the Area is the Second Crater at 255 m, one of two inactive volcanoes. The research facility is at approximately 220 m (700 ft) above the mean sea level. Arrival Heights was originally protected area for atmospheric science studies, and it is also a radio quite zone. The close distance of Arrival Heights to McMurdo station and Scott Base allows good access and logistics support year-around. USAP and AntNZ have their own research laboratories at Arrival Heights. A photo of Arrival Heights can be found in Figure 1.11 top right; the left building is AntNz research facility and the right building is the USAP facility.

After passing physical and psychological tests, I was deployed to McMurdo station on 9 December 2010 as the first winter-over lidar scientist and also the first winter-over grantee in the past 25-years at McMurdo. As a second year PhD student, I found the work on the ice was challenging not only because it was remote, but also because we were building a sophisticated system in a remote site. The challenges were not only for me, even for the whole group. During the stage of installing the lidar system, we encountered numerous difficulties. One of the most difficult challenges was the EMI (Electromagnetic Interference) issue, because Arrival Heights requires extreme low

FIGURE 1.11: Photos taken by Z. Yu in the winter of 2011. Top left: McMurdo station in the middle of March 2011, the photo was took at the middle point between McMurdo base and Arrivals Heights, Top right: Arrival Heights (the right building is the AntNZ laboratory and the left building is USAP laboratory); Middle left: the transmitter of Fe Boltzmann lidar in the laboratory at Arrival Heights, Middle right: two outgoing laser beams and AntNZ laboratory, the pink color was the fluorescence from ice crystals and excited by the UV laser; Bottom left: aurora "rain" "falling" from the Milk Way during morning twilight, the white mountain in the middle is Mt. Erebus, the white building is USAP laboratory at Arrival Heights, Bottom right: AntNZ laboratory and southern lights.

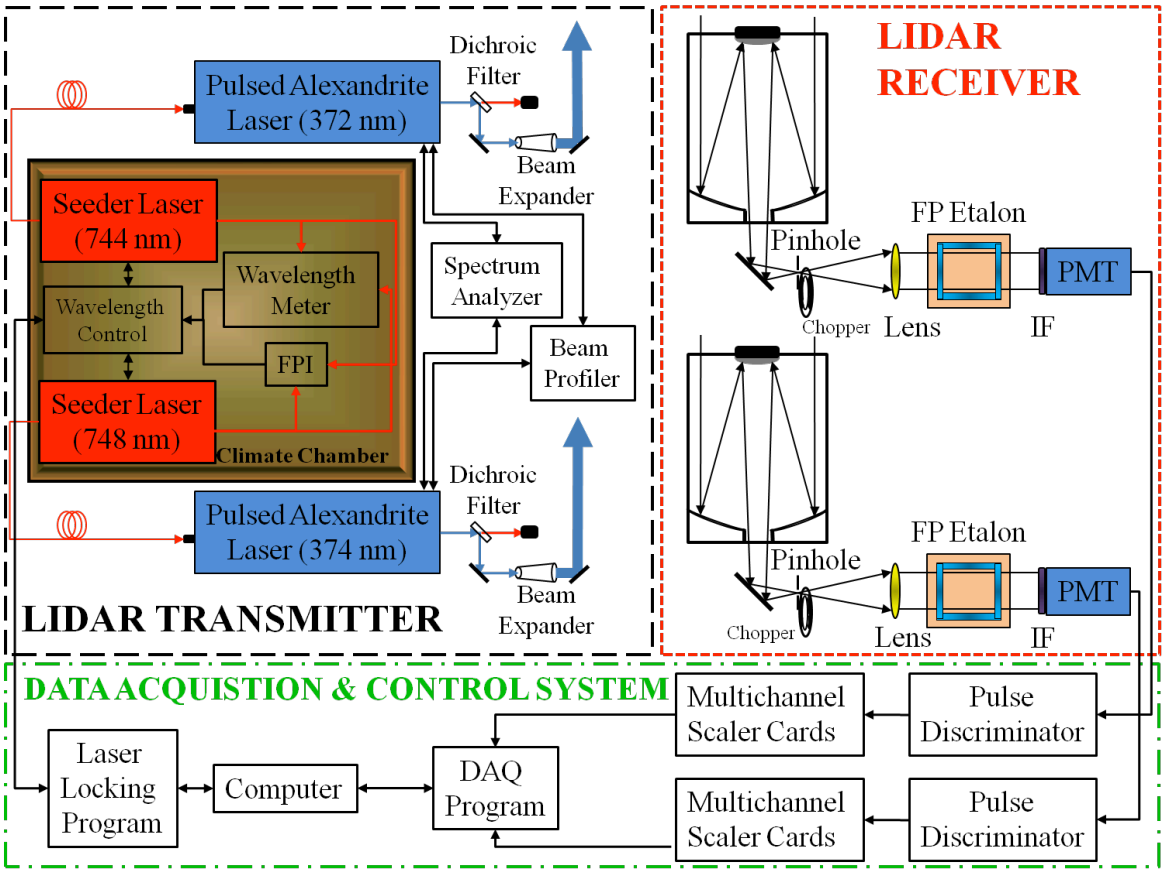

FIGURE 1.12: Diagram of Fe Boltzmann Lidar System, replotted from *Wang et al.* [2012]

electromagnetic interference. After one month's hard work and numerous tests led by Dr. Chu, it was found that the poor isolation of the power grid at Arrival Heights caused the problem, and the electromagnetic noise was eliminated by installing an extra transformer to separate secondary and line filters in the power consoles of Fe lidar system. Even under such challenging circumstance, the first lidar signals were obtained on 13 December 2010, within one month of the arrival of CU lidar team (Prof. Xinzhao Chu, Dr. Wentao Huang, Weichun Fong and John Smith). The excellent work done by the CU lidar team in the summer of 2010-2011 laid a solid basis for the winter operation in 2011. The 2011 winter was successful. Dr. Chu and I discovered a new scientific phenomenon from the data in May 2011. The new discovery greatly extended the studies of metal layer from 110 km

to 160 km, or even higher, and it also opened a new door to study the region between 100 and 200 km with limited observations. Qualitative and quantitative understanding of these thermospheric Fe layers is one of the major topics in this dissertation. Besides the thermospheric Fe layers, several other new scientific topics have been revealed by the first year data from McMurdo lidar campaign. Excellent data analyses work have been done by our group members, for instance, PMC studies by *Chu et al.* [2011a], the first report of diurnal variations of Fe layer and solar effects on the bottomside of Fe layer [*Yu et al.*, 2012], the first coincident observation of inertial gravity wave by radar and lidar [*Chen et al.*, 2013], the first report of planetary waves influences on significant temperature perturbations detected by lidar [*Lu et al.*, 2013], and the first winter temperature tides studies from 30 to 110 km and fast growth of diurnal tidal amplitudes [*Fong et al.*, 2014]. In the work of *Fong et al.* [2014], the data of 2011 and 2012 were included.

1.5 Research Objectives

This dissertation is aimed to explore the new aspects of studying of metallic Fe layer: (a) thermospheric Fe layers, (b) bottomside of Fe layer affected by solar radiance and diurnal variations of Fe main layers. Although we provided qualitative understanding of the thermospheric neutral Fe layers in *Chu et al.* [2011], and quantitative characterizations and qualitative understanding of bottom extension of the bottomside of Fe layer and diurnal variations of Fe main layer in *Yu et al.* [2012], the following topics are still active theoretical issues:

1. Part A: Theoretical issues of thermospheric Fe layers

   (a) Identify the complete set of physical/chemical characteristics of Fe formation and loss in the thermosphere.

   (b) The sources of Fe and Fe^+ in the polar thermosphere.

(c) The transport of neutral Fe atoms, and Fe response to gravity wave in diffusively separated atmosphere.

(d) The extreme contrast of Fe layers. Local relative density perturbations reach 100%.

(e) The role played by aurora in the Fe layer formation.

(f) The dominant mechanisms for converting Fe^+ to Fe.

(g) How many types of thermosphere Fe layer exist in the E-F region and how often do they occur? Do they share the same formation mechanisms?

(h) Metallic ions transported by electric field at high latitudes; the role played by magnetic storms in this drift.

(i) The vertical transport driven by the atmosphere expansion caused by Joule heating.

(j) The windshear mechanism at high latitude; the role played by gravity waves, tides.

(k) Whether, and how electric field plays a role in converging Fe^+ at high latitude.

(l) The effects of diffusion on thin ionization layer especially at high latitude where the vertical drift by windshear may not beat down diffusion at high altitudes.

(m) The influence of the interplanetary magnetic field (IMF) on the formation of Fe^+ layer.

2. Part B: Theoretical issues of diurnal variations of Fe layers and solar effects on the bottomside of Fe layer

(a) Quantitative characterizations of the diurnal variations of Fe layer through four season at McMurdo, Antarctica.

(b) The roles played by atmospheric waves, solar radiation, PMC, minor species like O, O_3, H, H_2O, meteor input in the variations of Fe main layer through four seasons.

(c) Quantitative characterizations of the extension and contraction of the bottomside of Fe layer.

(d) Quantitative explanation of the growth and contraction rate of the bottomside of Fe layer w.r.t. solar elevation angle.

(e) Quantitatively identify the concentrations of bottomside reservoir of Fe and its lifetime through four seasons.

(f) Quantitatively identify the spectrum of solar radiation, which is the fundamental factor of governing the growth and contraction of the bottomside of Fe layer, in the morning or evening sector when solar rays reach the MLT region after passing through the lower atmosphere

(g) Photolysis chemistry of Fe molecules, like FeOH.

In this dissertation, I mainly focus on the theoretical issues arising from the discoveries of thermospheric Fe layers, and resolve these issues via constructing a 1-D model. The modeling efforts will be concentrated on explaining the high-latitude periodic converged ion layers and neutral Fe layers from the aspects of dynamics and chemistry of converged layers and converging mechanisms. Based on the topics above, specific objectives of the modeling studies are aimed to:

1. Establish physical and chemical basis for the observed thermospheric Fe layers;

   (a) Solve the motions of Fe and Fe^+ explicitly;

   (b) Solve Fe chemistry (differetial equations) with backward differential formula method implicitly;

2. Construct 1-D Fe/Fe^+ model for high latitude:

   (a) Numerically solve the advections of Fe/Fe^+ with low numerical diffusion;

(b) Numerically solve Fe chemistry with high accuracy via employing a new chemistry scheme;

(c) Adapt high-latitude electric field, embed the source code of Weimer-2005 into the model;

(d) Adapt high-latitude winds, including tidal winds or gravity-wave winds;

(e) Embed the source code of NRLMSISE00 and IRI2012 into the model;

(f) Embed the source code of the GLOW into the model;

3. Identify the possible sources of thermospheric Fe^+.

4. For the aspects of chemistry, quantitatively explain the observations and measurements made on the thermospheric Fe layer at McMurdo;

(a) Identify thermospheric Fe layer produced through $Fe^+ + e^- \longrightarrow Fe + h\nu$, not through $FeO^+ + e^- \longrightarrow Fe + O$, and elucidate the altitude dependence of these two reactions.

(b) Define the minimum density of Fe^+ needed to generate observed Fe density for different magnitude of windshear.

(c) Define the lifetime of Fe at different altitudes. How long can they exist in the thermosphere under different conditions, such as different magnitudes of the concentration of ambient ions, NO^+ and O_2^+, the ionization of Fe caused energetic electron precipitation and the photoionization of Fe during the daytime?

(d) Define the direct ionization of Fe by the impact of energetic electrons.

5. Define the roles of and relationship among electric field, windshear, gravity and diffusion at high latitude;

(a) Define the roles played by electric field in converging Fe^+ layers. Clarify when the electric field help converge Fe^+, and when it is against windshear by diverging Fe^+. Explain how the electric field produces periodical, downward or upward phase Fe^+ layers.

(b) Elucidate the convergence of Fe^+ by the neutral wind shear produced by gravity waves at McMurdo where the inclination angle of geomagnetic field line is large.

(c) Define the influence of vertical wind on these events like May 28 2011.

(d) Define the influence of diffusion at high altitudes.

6. Investigate occurrence of Fe^+/Fe layers during different geomagnetic activities

(a) Investigate the relationship between geomagnetic storm and the formation of thermospheric Fe layer at McMurdo;

(b) Define the roles of aurora and the influence of energetic electron precipitations on Fe–Fe^+ chemistry.

Some of the theoretical issues of diurnal variation of Fe layer and solar effects on its bottomside are not in the scope of this dissertation, but the quantitative characterizations of the diurnal variations Fe layers through four season at McMurdo, Antarctica, and the quantitative characterizations and qualitative explanations of solar effects on the bottomside of Fe layer are provided in Chapter 6.

Overall the organizations of the dissertation are: Chapter 2 provides some typical observations of thermospheric layer at McMurdo. Chapter 3 details the construction of the numerical model, which was adapted from the framework of *Carter and Forbes* [1999], but the transport and chemistry modules are reconstructed by advanced numerical algorithms. Chapter 6 provides the observation results of diurnal variations of Fe layer and the solar effects on its bottomside,

and qualitative explanations are offered. Chapter 7 summarizes the work in this dissertation and outline potential studies for the future.

Chapter 2

Discovery of Thermospheric Fe Layers in the 100–200 km Altitudes by Lidar Observations

2.1 Preface

The material in this chapter has been published in Geophysical Research Letters [*Chu et al.*, 2011]. The authors of this paper are Xinzhao Chu, Zhibin Yu, Chester S. Gardner, Cao Chen, and Weichun Fong. Z. Yu contributed the data in this work. The original ideas and scientific discoveries were made by Prof. Xinzhao Chu. Besides the cases published in *Chu et al.* [2011], two more cases are added in this chapter, which were observed in Antarctic winter 2012 by Bredndan Roberts.

2.2 Introduction

Currently, there exists a serious observational gap of Earth's neutral atmosphere above 100 km. The measurements of neutral winds, temperatures, and compositions in the most intensive atmosphere-ionosphere interaction region, especially between 100 and 200 km, are sparse. As a consequence, the

knowledge of several key processes including plasma-neutral atmospheric coupling, wave-induced transport and turbulence, wave propagation and dissipation, and cosmic dust influx, to a great extent, has been constrained by the limited observations. By providing high temporal and spatial resolutions, lidar is an excellent technology and can provide better access to the mesosphere and thermosphere with high quality data set that can be used to address many of these topics.

Thermospheric neutral Fe layers up to 180 km, discovered by Fe Boltzmann lidar observations at McMurdo, Antarctica [*Chu et al.*, 2011, 2012, 2013], have opened a new door to observing the neutral polar thermosphere with ground-based instruments. The neutral metal layers provide an excellent tracers for resonance-fluorescence lidars to directly measure the neutral temperatures and winds in the thermosphere. Range-resolved temperature profile up to 170 km has already been demonstrated by the McMurdo Fe lidar [*Chu et al.*, 2013].

In *Chu et al.* [2011], we discovered the neutral Fe layers and observed the thermospheric gravity waves in the neutral Fe layers from 110 to 155 km with the Fe Boltzmann temperature lidar on 2 and 28 May 2011 at McMurdo (77.83°S, 166.66°E), Antarctica. McMurdo is located at high geographic and magnetic latitudes, and is near the poleward edge of the aurora oval. It is extremely remote and clean from light pollution. The extreme darkness creats extremely low background during polar nights, and facilitates the detection of weak metallic layers in the thermosphere. The unique geomagnetic location of McMurdo also provides opportunities to study how the thermosphere is affected by geomagnetic activity. In this chapter, four thermospheric Fe layers events are provided. Quoted in Section 2.4 is the discussion in *Chu et al.* [2011], and we provide our theory of formation of thermospheric Fe layers and qualitative understanding of the processes.

2.3 Observations

The Fe Boltzmann lidar installed at Arrival Heights consists of two independent channels probing respectively the 372 and 374 nm absorption lines of neutral Fe atoms. One of the prominent advantages of two independent channels is to examine the geophysical phenomena via comparing the signals from the two independent channels. Thermospheric Fe layers are frequently observed by the two channels at McMurdo, Antarctica. *Chu et al.* [2011] reported that the occurrence frequency of thermospheric Fe layer events above 120 km is about $\sim$ 18% among the 233 h of lidar observations made on 14 days from May through August 2011. *Chu et al.* [2012, 2013] reported thermospheric Fe layers with different characteristics. In this section, four events of thermospheric Fe layers in 2011 and 2012 are provided. They are classified into three types: 1) The descending multiple Fe layers with fast gravity wave signatures and extra-high contrast; 2) Long duration broad extensive Fe layers with weak gravity wave signature; 3) Gravity wave structured thermospheric Fe layers superimposed on a diffused Fe background.

Here we present the first type of thermospheric Fe layers. Illustrated in Figures 2.1a and 2.1b are the normalized photon counts of neutral Fe layers from 70 to 155 km measured by the 372- and 374-nm lidar channels, respectively, on 28 May 2011. In both plots, the main layers are distributed from $\sim$75 to 110 km with sharp bottom edges but slower decay on the topside, which is consistent with observations of Fe layers elsewhere [e.g., *Plane*, 2003]. However, the distinct Fe layers above 110 km with apparent wave features are unique and have never been reported before. The thermospheric Fe is clear at the beginning of the observation (11.5 UT) with a distinguishable layer up to 133 km. The layer descends with time and merges with the main layer at $\sim$110 km around 13.5 UT. In the meantime, another Fe layer develops at $\sim$145 km and then descends

downward. The third and highest Fe layer occurs around 14.7 UT at 155 km and then descends with time. The wave-like features repeat four more times before the termination of the observations due to clouds, but the starting altitudes of the Fe layers become lower as time progresses. The 6th and 7th layers starting below 120 km are barely visible. Interestingly, when the 4th and 5th layers descend below 115 km, two distinct sporadic Fe layers occur in the range of 105–115 km between 18 and 20.5 UT, standing out clearly in both Fe contours. The striking similarities between these two independent channels and the clear wave signatures make the lidar detection of thermospheric Fe layers unequivocal.

To further quantify the thermospheric Fe layers, we compute Fe temperatures from two channels of normalized photon counts using the Boltzmann technique, and convert the 372-nm counts to Fe densities [*Chu et al.*, 2002]. In the density derivation, the lidar effective cross sections are calculated using the derived Fe temperatures in the MLT region and MSIS-00 temperatures above 110 km. Two representative vertical profiles of Fe densities are plotted in Figures 2.1c and 2.1d. The profiles of the highest Fe layer at 14.8 UT exhibit appreciable Fe densities above 115 km in both 372 and 374 nm channels, when compared to the profiles for 18.8 UT. The noise levels above 130 km in Figure 1d, where the Fe layer disappears, establish detection limits for both channels of 3 cm^{-3}. The number densities in the 372-nm Fe layer vary from ~65 cm^{-3} at 130 km to ~20 cm^{-3} at 150 km, as inferred from Figure 2.1c, which are small when compared to the main layer peak density of ~20,000 cm^{-3}. The 374-nm densities are about 2–4 times lower than the 372-nm densities from 120 to 150 km, but well above the background noise.

A contour of thermospheric Fe density is illustrated in Figure 2.2a. The wave signatures in the Fe layers are very clear. The peak densities vary, with a maximum close to 110 cm^{-3} around 125 km at 13.5 UT. In between two distinct crests the Fe densities vary from 10 cm^{-3} at 130 km

to ∼3 cm^{-3} at 150 km. Consequently, the ratios of the Fe densities between crests and troughs are about 4–15 in this altitude range. Such wave-induced Fe density perturbations are much larger than the concomitant perturbations in the neutral atmosphere and the electron density [e.g., *Djuth et al.*, 2010]. Fe temperatures plotted in Figure 2.2b for the main Fe layers show apparent wave perturbations throughout the observations. The dominant wave has a period of ∼8 h and vertical phase velocity of ∼0.7 m/s. Shorter-period waves of ∼1.5 h are clearly visible below 90 km. The mesopause is located near 100 km with a temperature of ∼190 K. Taking the highest Fe layer that goes to 155 km, we derive the Fe temperatures from 75 to 150 km using the Boltzmann technique. Combining with the Rayleigh integration technique, the Fe lidar is able to measure temperatures from 30 to 150 km as shown in Figure 2c. Also plotted are the MSISE-00 temperatures for McMurdo location on 28 May 2011. The MSIS temperatures are close to the lidar data below 110 km. Above 115 km and below 135 km, the Fe temperatures are much warmer than MSIS, and the difference is up to ∼ 600 K at 132 km.

Both lidar channels show the same wave features in the thermosphere from 110 to 155 km. The wave has a downward phase progression. The vertical phase speed is the largest at the highest altitude but around 125 km the phase speed decreases quickly with decreasing altitude. The vertical wavelength is shortest at 115 km and increases significantly with increasing altitude. Spectral analysis of the Fe layers using wavelet shows that the period T of the wave (∼1.5 h) is nearly constant through the 115–155 km range (Figure 2.3a). By tracking the peak Fe contour, we obtain the phase line (altitude vs time) in the thermosphere, and then the vertical phase speeds c_z are derived by taking the derivative of the phase line altitude with respect to time. The vertical wavelengths λ_z are then calculated as $\lambda_z = c_z \cdot T$. As shown in Figure 2.3b, the downward phase speed increases from ∼2 m/s at 115 km to over 10 m/s above 135 km. The vertical wavelength λ_z

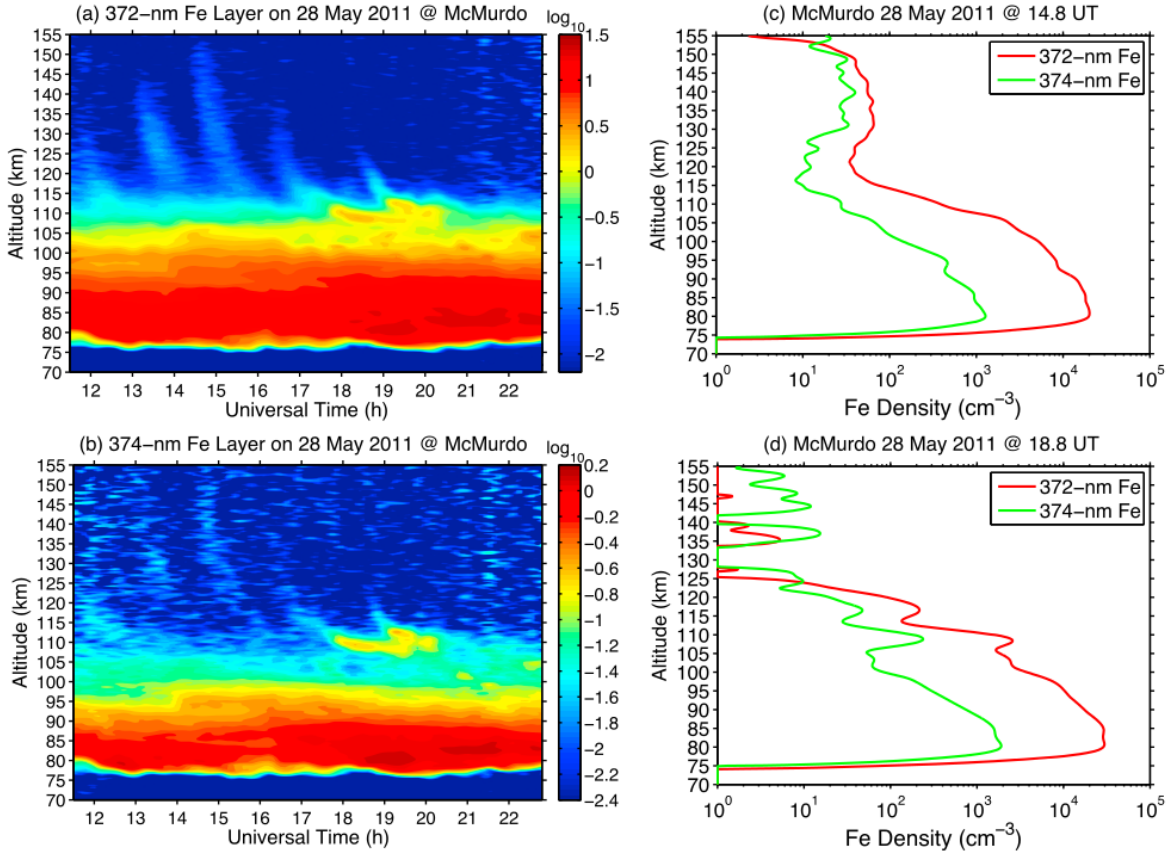

FIGURE 2.1: Observations of neutral Fe layers by 372- and 374-nm lidar channels on 28 May 2011 (UT) at McMurdo, Antarctica. (left) Plotted in log_{10} scale are contours of Fe photon counts normalized to the Rayleigh signals at 45 km for the (a) 372-nm and (b) 374-nm channels. (right) The vertical profiles of Fe densities derived for (c) 14.8 UT and for 0.5 km for Figures 1a and 1b and 0.25 h and 2 km for Figures 1c and 1d (FWHM). The uncertainty of 372-nm Fe density in Figure 2.1 and 2.1 and 0.25 h and 2 km for Figures 2.1c and 2.1d (FWHM). The uncertainty of 372-nm Fe density in 2.1c is 20-30% above 120 km and much less below 110 km [*Chu et al.*, 2011].

varies from ∼13 km at 115 km to ∼70 km around 150 km. These wave characteristics, especially the changes of c_z and λ_z with height, closely resemble the thermospheric gravity waves observed as TIDs in the electron density perturbations by incoherent scatter radar (ISR) [e.g.,*Djuth et al.*, 2010]. The wave period of ∼90 min in the Fe layer is longer than the TIDs observed at Arecibo Observatory by *Djuth et al.* [2010], but TIDs can have periods from 20 min to several hours according to *Thome* [1964]. The downward phase progression indicates the upward propagation of the wave energy. The wave likely originated from the atmosphere below 75 km [*Vadas and Nicolls*,

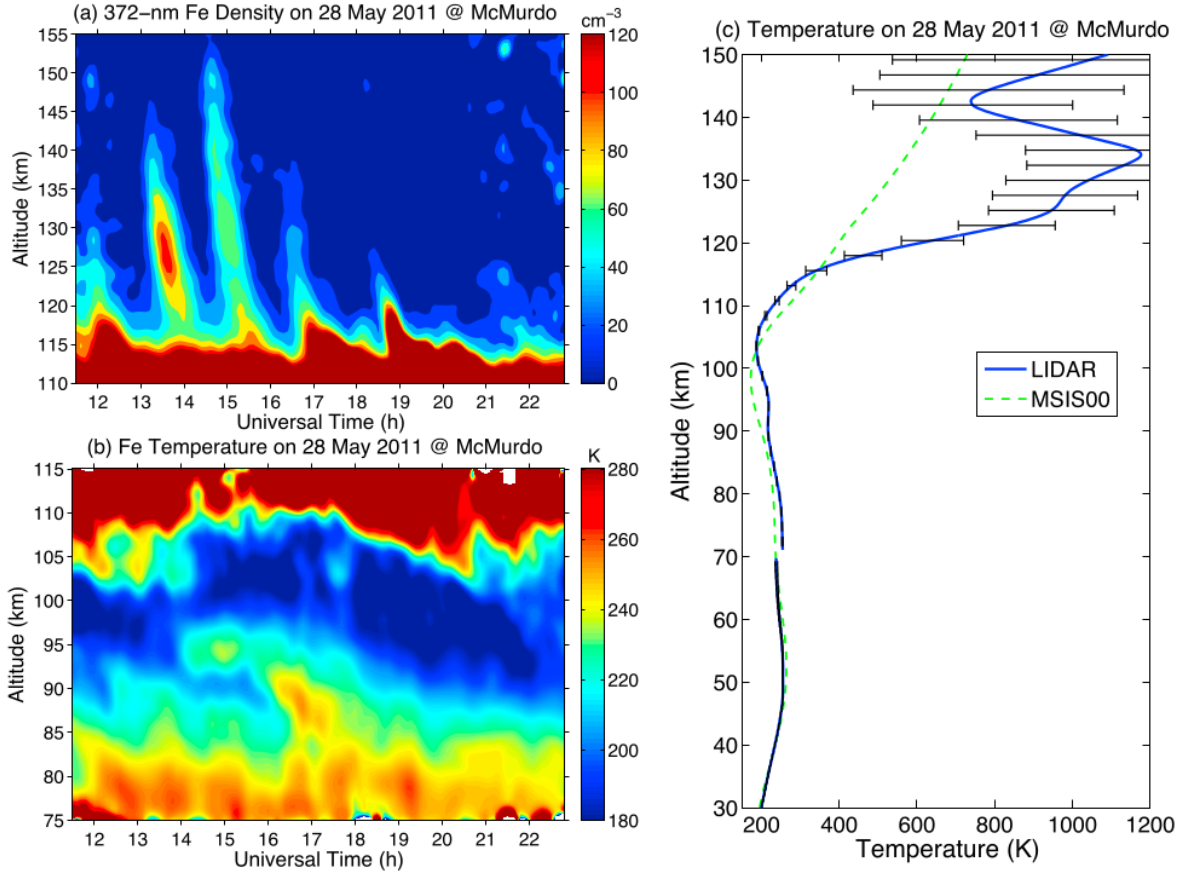

FIGURE 2.2: Event on 28 May 2011 at McMurdo, Antarctica: (a) contour of thermospheric Fe densities from 110 to 155 km, showing fast gravity waves in the thermosphere, (b) contour of Fe temperature from 75 to 115 km, showing waves in the MLT region, and (c) the vertical profile of temperature for 1 h integration around 15 UT. The temperature errors plotted as horizontal bars in Figure 2c are less than 5 K below 110 km. Rayleigh lidar temperatures are plotted below 70 km [*Chu et al.*, 2011].

2009], not from an aurora source above 150 km [*Richmond*, 1978]. In the MLT region, the Fe temperature contour (Figure 2.3b) exhibits short-period waves in addition to the dominant 8-h wave. In order to extract such wave information, we derive the relative temperature perturbations from Figure 2.2b. After subtracting the dominant 8-h wave, a wavelet analysis reveals the wave period around 1.5 h with errors less than 0.3 h from 75 to 115 km, as plotted in Figure 2.3a. The corresponding c_z and λ_z are plotted in Figure 2.3b. Note that the observed wave period can change in time if the background wind changes rapidly [*Eckermann and Marks*, 1996]. The waves

in the MLT region are in general consistent with the thermospheric gravity waves, supporting the hypothesis that the waves originated from the lower atmosphere below 75 km.

A similar thermospheric wave event was also observed on 2 May 2011 at McMurdo. As illustrated in Figure 2.4a, signatures of neutral Fe layers occur in the thermosphere three times around 9.7, 11.8 and 14 UT, with a wave period of slightly over 2 h. The strongest layer occurs around 14 UT, reaching the highest altitude of ∼155 km and with the maximum Fe density of ∼200 cm^{-3} at 120 km. The shape of the layers is similar to the event on 28 May 2011. Figure 2.4b shows the main Fe layers in the MLT. The Fe Boltzmann temperatures within the strongest layer were derived from 75 to 150 km in Figure 4c. Also plotted are the Rayleigh lidar temperatures and the MSIS-00 temperatures at McMurdo for 2 May 2011. The lidar and MSIS-00 temperatures agree well below 105 km. Above 105 km and below 135 km, the Fe temperatures are significantly warmer than the MSIS, similar to the situation on 28 May 2011. The similarities between these two events observed on two different days further confirm the robustness of the lidar detection of neutral Fe layers, elevated temperatures and gravity waves in the thermosphere.

The data on 20–21 March 2012, shown in Figure 2.5 (Top), is the second type of thermospheric Fe layers. Broad Fe layers have been observed in the lower thermosphere between 100 and 130 km. The first broad layer, with width ∼ 9 km, showed up at 14 LT with slower phase progression speed, ending at 18.5 LT. The second layer with wider width, ∼ 18 km, commenced at 20 LT, and began to merge with the main Fe layer at 8 LT on the second day but did not disappear when the lidar observation was terminated. Although the signature is not as obvious as the 2011 cases, 1.5 h short-period waves exhibit in the broad layer, with wave crests located at 21.5 LT, 23 LT, 0.5 LT, 2 LT.

The third type is shown in Figure 2.5 (Bottom). Diffusive neutral Fe layers showed up in the

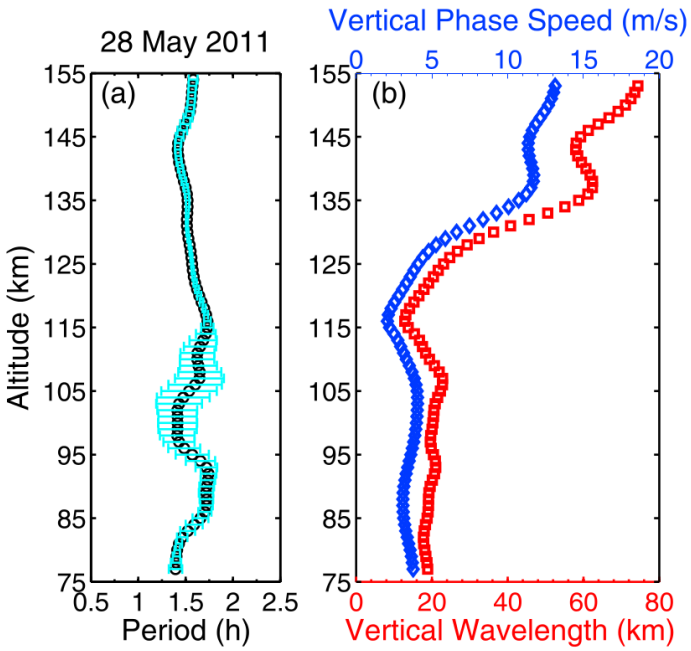

FIGURE 2.3: Ground-based (a) gravity wave period along with (b) vertical phase speed (blue diamonds) and vertical wavelength (red squares) derived for the event on 28 May 2011 at McMurdo. The period errors are plotted as horizontal bars in (a). From *Chu et al.* [2011]

region between the main Fe layer and 150 km during the period of 6 to 19 UT, then thermospheric Fe atoms were gone after 19 UT. The altitude of the topside of the diffusive Fe layer starts at 125 km and gradually increases to 150 km at 18 UT. A striking feature is that three relatively highly concentrated Fe layers with a period of about 3 h showing in the diffusive layer have been observed. Starting from 25 UT, the topside of main Fe layer begins to grow up, and it reaches 130 km at the end of the observation.

2.4 Theory of Thermospheric Fe Layer Formation

The thermospheric Fe layers are different from the conventional concept of sporadic metal layers that also have relatively large density enhancement but occur at altitudes between 90 and 110 km [e.g., *Kirchhoff and Clemesha*, 1983; *Clemesha et al.*, 1978; *Cox and Plane*, 1998; *Collins et al.*, 2002; *Diettrich et al.*, 2006]. Sporadic Na layers have been extensively studied by observations [e.g.,

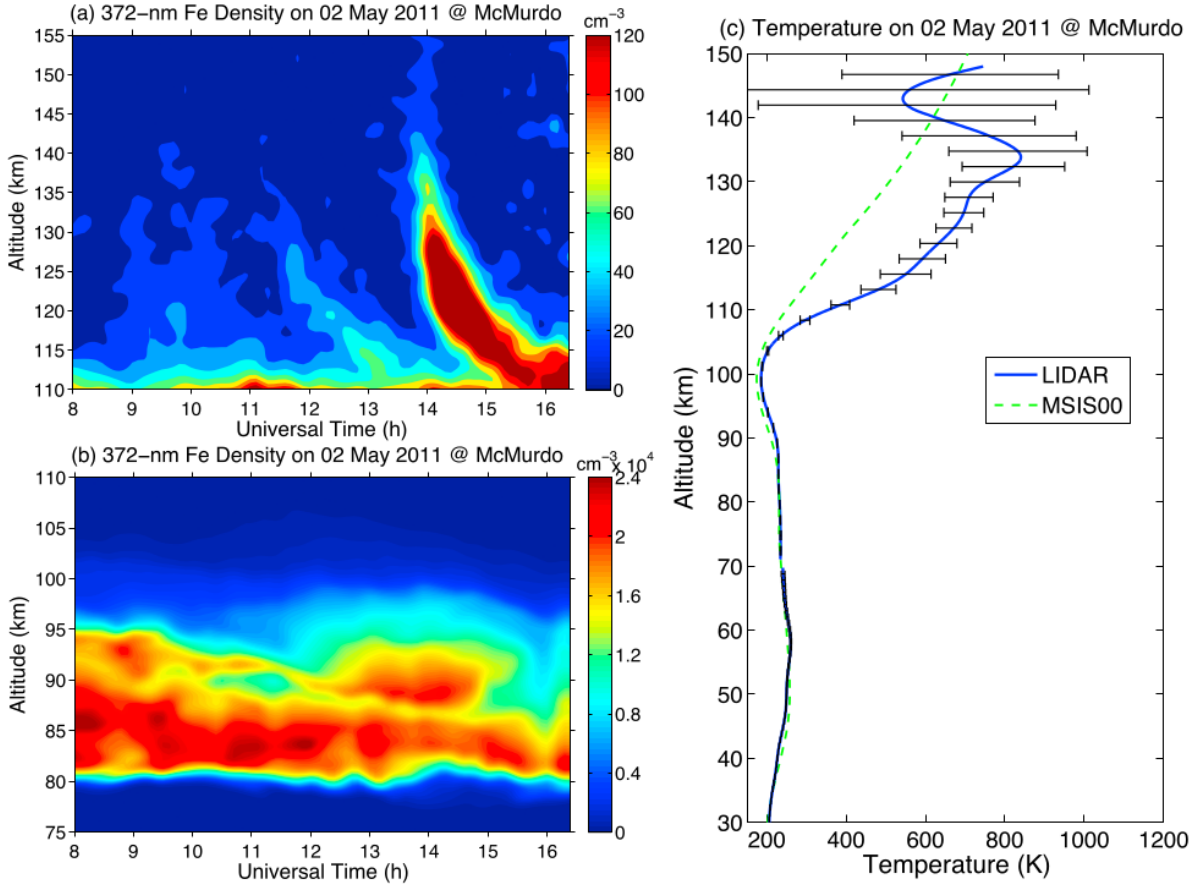

FIGURE 2.4: Event on 2 May 2011 at McMurdo, Antarctica: (a) the 372-nm Fe density contour in the thermosphere, (b) the 372-nm Fe density in the MLT, and (c) the lidar temperature profile for 1-h integration around 14 UT. The temperature errors (horizontal bars) are less than 5 K below 105 km. Rayleigh lidar temperature are plotted blow 70 [*Chu et al.*, 2011].

von Zahn et al., 1987; *Gardner et al.*, 1991; *Gardner et al.*, 1995; *Williams et al.*, 2007; *Dou et al.*, 2009], and experiments and numerical simulations [e.g., *Cox and Plane*, 1998, *Collins et al.*, 2002]. In the studies of sporadic Na layers at lower altitudes, $\sim$ 90 to 110 km, one of the theories for the formation of sporadic Na layers is the ion-molecule chemistry theory that the concentrated Na atoms are converted from converged Na^+ by wind shears interacting with the electrodynamics to form a narrow ion layer [*Collins et al.*, 2002]. Sporadic Fe layers also have been widely studied, for example, *Granier et al.* [1989] reported the first sporadic iron layers. *Alpers et al.* [1993] investigated the correlation between the appearance pattern of sporadic E layers (majorities are metallic ions)

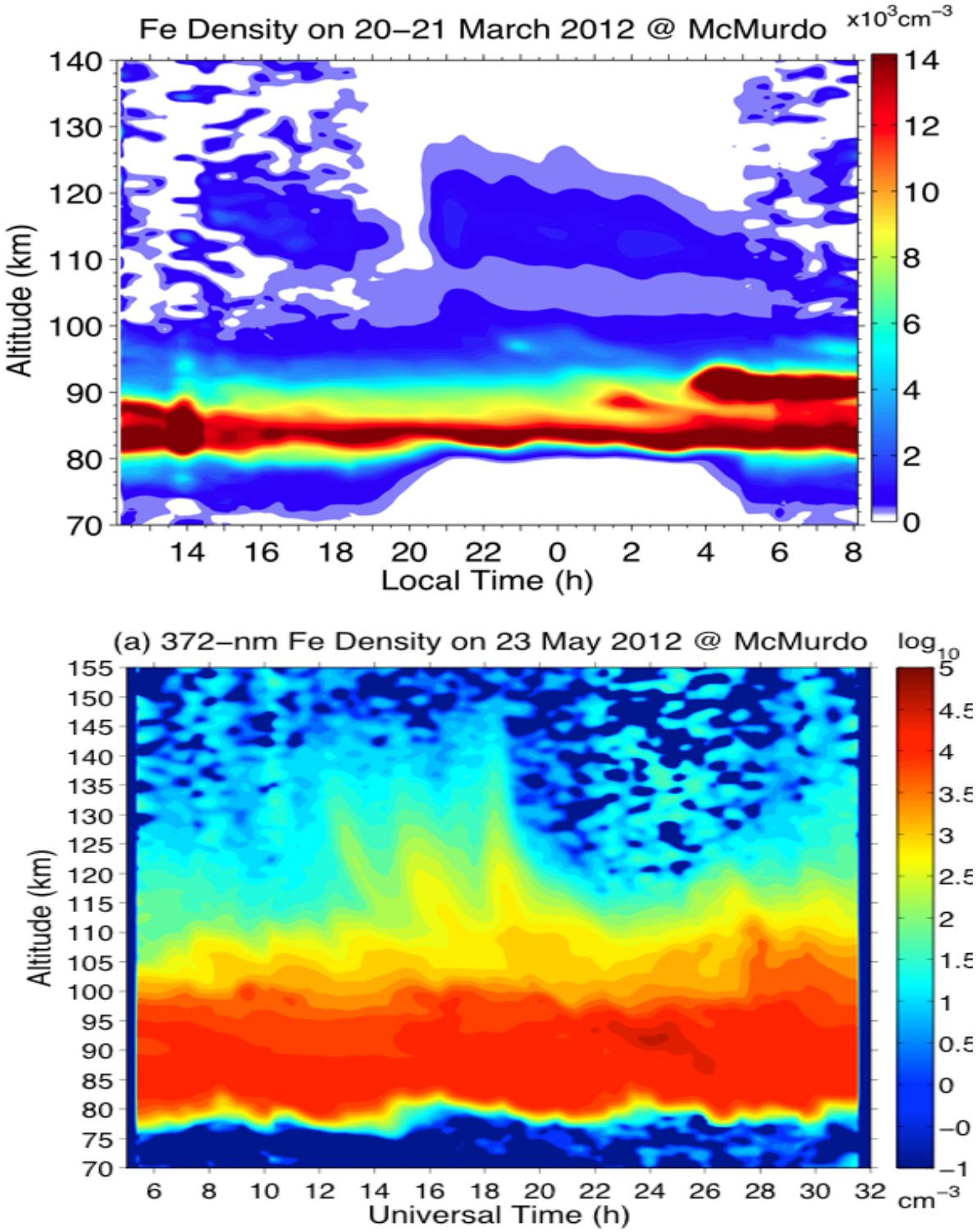

FIGURE 2.5: The top figure is the Fe densities measured by the Fe lidar on 20-21 March 2012; the bottom is the Fe densities on 23 May 2012 [*Chu et al.*, 2012].

and sporadic Fe layers through a multi-instrument observations. *Kane and Gardner* [1993] did further research on the link of sporadic Fe to sporadic E layers, and investigated the influence of chemistry on sporadic Fe formation. *Diettrich et al.* [2006] reported the statistics of sporadic Fe layers from the lidar observations at Rothera Research Station (67.5°S, 68.1°W), Antarctica, and its relation to atmosphere dynamics. Based on the laboratory studies and numerical simulation experiments, *Plane et al.* [2003b] suggested that the sporadic Fe layer were converted from the Fe^+ in descending sporadic E layer through dissociative recombination. In these studies, the sporadic Fe layers were found below 110 km. They are very different from our observed thermospheric Fe layers. Thermospheric Fe layers are also different from the "topside layers" reported by *Höffner and Friedman* [2004, 2005]. These "topside layers" up to 130 km are diffusely exponential decay of the topside of the main metal layer, rarely having wave structures. However, wave structures are a common and prominent feature in the observed thermospheric Fe layers, whose formations are unlikely caused by meteor ablation directly (as argued in Section 1.3).

In the first report of thermospheric Fe layers up to 155 km and also the first observations of gravity waves in neutral metal layers at such high altitudes, *Chu et al.* [2011] propose a new theory of how the neutral Fe layers are formed in the E-F region and how they exhibit such wave signatures. It is unlikely that these neutral atoms are ejected or diffused directly from the main Fe layers in the MLT region, because the expected shape in the time-altitude domain would extend upward from, rather than descend towards, the main layer. The second possible source of neutral Fe is the direct meteor ablation or sputtering off smoke particles. *Plane* [2003] points out that the ablation altitude depends on the entry velocity of meteoroids, and even very fast meteoroids of 40 km/s ablate below 125 km with peak ablation at 101 km, while slow meteoroids peak at 92 km. Furthermore, the differential ablation process releases the volatitle constituents (Na and K) first.

Fe and Mg are released from the molten meteoroid only after the temperature exceeds ~1800 K. As a result, Fe has peak injection rates around 85 km, with Na and K ~8 km higher [*Vondrak et al.*, 2008; *Janches et al.*, 2009]. Such a height profile of ablation cannot explain the observations. If we assume sputtering exists above 110 km or molecular diffusion somehow distributes neutral Fe to 115 km, waves are unlikely to cause sufficient perturbations of the neutral atmosphere to account for the observed "high contrast" of the Fe layers.

Most likely the observed thermospheric Fe layers are linked to the layered Fe^+ ions that are then neutralized to produce neutral Fe atoms. First, the shape of the observed layers in Figures 2.2a and 2.4a indicates descending layers from higher to lower altitude as time progresses, similar to the motions of ion layers observed by the ISR [*Mathews et al.*, 1993]. Secondly, the ratio of the wave crest and trough being far larger than any perturbations in the neutral atmosphere suggests that the Fe layers are related to ions that have been layered by various forces in the thermosphere [*Carter and Forbes*, 1999]. Thirdly, the changes of vertical wavelengths and phase speeds are similar to the TIDs [e.g., *Djuth et al.*, 2010] and are consistent with theoretical expectations for gravity waves [*Vadas*, 2007; *Vadas and Nicolls*, 2009].

The hypothesis of layered Fe^+ being converted to neutral Fe faces several critical issues: the sources of Fe^+, the formation of Fe^+ layer and its shape, neutralization mechanisms to convert Fe^+ to Fe, and transport of Fe and Fe^+. Aurora heating in the polar cap may cause upwelling and thus upward transport of Fe^+ or Fe into the thermosphere [*Burns et al.*, 1991]; however, this mechanism is unproven at these low altitudes. *Carter and Forbes* [1999] point out that the redistribution of meteor deposited Fe^+ in the meridional plane by electric fields is most pronounced at low latitudes in connection with the "fountain effect". Gravity and diffusion redistribute Fe^+ along geomagnetic field lines, and Fe^+ can reach the Fe region. Although the fountain effect may not be effective in

the Polar Regions, Mg^+ ions have been observed by satellites in the thermosphere above 300 km in the polar region [*Viereck et al.*, 1996]. Considering Fe and Mg have similar ablation altitudes [*Vondrak et al.*, 2008] and based on the satellite measurements [*Kumar and Hanson*, 1980], it is reasonable to assume that Fe^+ ions are distributed in the E and F regions over polar regions, most likely by the polar electric field. The formation of Fe^+ layers at McMurdo should share the same mechanisms as the TIDs and sporadic E layers at high latitudes. The observed shape indicates that vertically converged ion layers descend in height with time, following the gravity wave downward phase progression. The wave-induced wind shears in combination with geomagnetic and electric fields provide the needed vertical convergence of ions [e.g., *Hines*, 1963; *Kelley*, 1989; *Bristow and Watkins*, 1991; *Carter and Forbes*, 1999; *Djuth et al.*, 2010]. Layers formed by electrical fields have no systematic vertical motion, unlike the layers produced by gravity-wave wind shears. Wind shears descend with the downward phase velocities of the wave, resulting in the downward transport of the layers. The simultaneous occurrence of two layers at the bottom and top of the profiles in Figures 2.2a and 2.4a, and the repeated layer shapes, supports the wave phase idea. Because the shorter vertical wavelength, slower phase speed waves dominate the power spectral density in the MLT region but dissipate rapidly when propagating upward [Vadas, 2007], the longer wavelength and faster vertical phase speed waves show up more clearly at higher altitudes as we observed. The increase of λ_z with altitude above 115 km is likely due to a decrease of N_2 (buoyancy frequency) and an increase of the neutral wind component in an opposite direction to the wave propagation [*Vadas and Nicolls*, 2009].

Conversion from Fe^+ ions to neutral Fe in the thermosphere is likely through the direct electron recombination: $Fe^+ + e^- \longrightarrow Fe + h\nu$, as Fe^+ is neutralized essentially only by radiative recombination with electrons at altitudes above ~120 km [*Plane et al.*, 2003; *Zhou et al.*, 2008].

Although the value of the reaction rate coefficient is small and given as 4×10^{-12} $cm^3 s^{-1}$ to 1×10^{-11} $cm^3 s^{-1}$ by *Plane* [2003] and *Plane et al.* [2003], it is large enough to produce the Fe densities observed. This is because the Fe density (20–100 cm^{-3}) is a small fraction of the Fe^+ density in sporadic E layers, and the loss rate of neutral Fe in the dark polar night is small. Note that 12.89 UT is the local midnight at McMurdo. The lidar observations reported here span 8–24 UT, corresponding to the local time from 19–11 LT. The solar declination angles on 2–28 May 2011 were 15.6°–21.6°, giving total darkness below 155 km when the thermospheric Fe layers were observed, so photo-ionization of Fe neutrals is absent. The recombination of O_2^+ and NO^+ with electrons proceeds fast with a rate coefficient of $\sim 3 \times 10^{-7}$ $cm^3 s^{-1}$, leading to 30 s to ∼1 h lifetime of O_2^+ and NO^+ depending on electron density. Therefore, these ion densities decay rapidly in the polar night. Assuming their total density is less than 1×10^4 cm^{-3} and the reaction rate coefficient of charge transfer between Fe and O_2^+ and NO^+ is $\sim 1 \times 10^{-9}$ $cm^3 s^{-1}$. This gives an Fe lifetime of ∼27 h during dark night, much longer than the wave period but comparable to the Fe lifetime of 33 h estimated by *Zhou et al.* [2008]. On the other hand, the production rate for converting Fe^+ to Fe is given by $k[Fe^+]N_e$, where N_e is the electron number density. Assuming N_e in the sporadic E layer is 1×10^5 cm^{-3} and $[Fe^+]$ occupies most of the ion density, the Fe production rate ranges from 4×10^{-2} cm^{-3} s^{-1} and 1×10^{-1} $cm^{-3} s^{-1}$. Therefore, neutral Fe densities of 40–100 cm^{-3}, comparable to observations, can be produced within 1000 s, much shorter than the wave period (∼5500 s). Note that these calculation is under the circumstance without auroral ionization. The transport of converted Fe is likely different than that of Fe^+. While the wave transports Fe^+ downward, the wave motion may not affect the neutral Fe atoms that are left in the wake of Fe^+ layers. This leads to slight height difference with the Fe layer located above the Fe^+ layer, as observed in sporadic Na and E layers above 100 km by *Kane et al.* [1993].

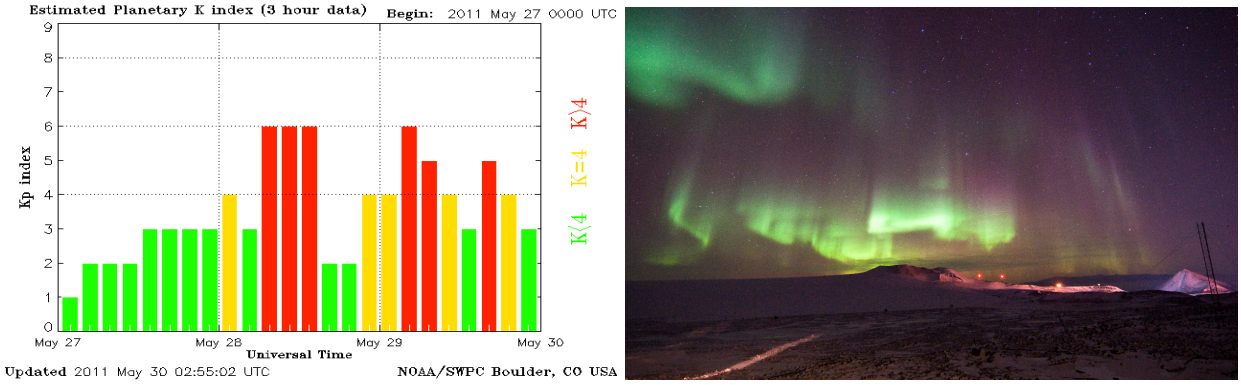

FIGURE 2.6: Geomagnetic storms happened on May 28 2011. The left plot shows the Kp index reached to 6 in the middle of May 28 2011, and the right plot is the photo taken around 12:00 UT at Arrival Heights, shows extensive aurora activities.

Strong aurora was observed at McMurdo on 28 May 2011, corresponding to a geomagnetic storm with the Kp index increased to 6 after 6 UT and lasted until 15 UT, as shown in Figure 2.6. In the case on 2 May 2011, the geomagnetic conditions were relatively quiet but weak aurora was visually seen over McMurdo during the lidar measurements. Auroral particle precipitation may have several effects on the events. They may increase the electron density to facilitate the conversion from Fe^+ to Fe; it may also shorten the lifetime of Fe by direct ionization and by increasing the density of O_2^+ and NO^+ to accelerate charge transfer. The electric fields associated with aurora will increase the Joule heating of neutral atmosphere and frictional heating of ions. Though frictional heating can heat up to over 1000 K [*Maeda et al.*, 2005], what we measured directly is neutral Fe. The freshly converted Fe can have elevated temperatures above the background. Thermalization via collisions with surrounding neutrals only take about 1–2 s even at 150 km where the collision rate is $\sim$20 s^{-1}. However, the above analyses suggest that the neutral Fe atoms have a lifetime on the order of 1000 s; therefore, majority of observed Fe atoms are likely in thermodynamic equilibrium with the surroundings. The mixture of freshly converted and thermalized Fe likely results in Fe temperatures closer to the background neutrals, rather than the ions. Joule heating rates measured by ISR range from 0.1×10^{-6} to 1×10^{-6} W/m^3, and the neutral gas heating

rates are 0.02–0.08 K/s from 110 to 135 km [*Thayer and Semeter*, 2004, and references therein]. If the aurora-enhanced heating has been going on for several hours before the lidar observations started, a significant temperature increase in the lidar observations on May 28 compared to May 2 is consistent with the geomagnetic activities at McMurdo.

2.5 Conclusions and Outlook

Neutral Fe layers with gravity wave signatures were observed for the first time in the thermosphere from 110 to 155 km by both the 372- and 374-nm channels of an Fe Boltzmann temperature lidar at McMurdo, Antarctica on 2 and 28 May 2011. The Fe densities are quite low (20–200 cm^{-3}) in the altitude range of 120–150 km, but sufficient for temperature derivation. Combining the Fe Boltzmann and Rayleigh integration techniques, we are able to derive temperatures from 30 to 150 km using the Fe lidar. While comparable to the MSIS data below 110 km, the lidar temperatures are significantly warmer than MSIS between 115 and 135 km during both 2011 events. These elevated temperatures appear to be related to the Joule heating enhanced by aurora. The observed waves originate from the lower atmosphere and show nearly constant periods of 1.5–2 h through the range of 75–155 km. The downward phase speeds are large at high altitudes, decrease with decreasing altitude and are curved towards increasing time. The vertical wavelengths vary from 13 km at 115 km to ~70 km at 150 km. These wave characteristics closely resemble the TIDs and are consistent with the theoretical expectations for gravity waves. The observed thermospheric Fe layers are most likely linked to the layered Fe^+ ions that are neutralized to produce Fe. Vertically converged Fe^+ ion layers descend in height with time, following the gravity wave downward phase progression, which forms the observed layer shape. It is likely that the direct recombination with electron converts Fe^+ to Fe during the dark polar night. Geomagnetic activities like aurora may have played

roles in the observed events. Quantitative explanations of these events require detailed modeling studies of Fe^+ source and layering, Fe formation and loss, gravity wave source and propagation, and the transport of Fe^+ and Fe at high latitudes, along with simultaneous measurements of Fe, Fe^+ and electrons. Certainly, the observations of neutral Fe layers, elevated neutral temperatures and gravity waves in the thermosphere over McMurdo challenge our understanding of upper atmosphere chemistry, composition, dynamics and thermal structure.

More thermospheric Fe layers with different types are observed in 2012 and 2013. The existence of neutral Fe layers over 170 km poses interesting questions of how neutral Fe atoms are formed in the thermosphere and how gravity waves produce signatures in the Fe layers. These observations raise several key science questions: How are Fe and Fe^+ transported into the polar E-F region? What are the dominant mechanisms for converting Fe^+ to Fe? What roles do gravity waves, tides and aurora play in the Fe layer formation? Quantitative explanations of these events require detailed modeling studies of Fe^+ source and layering, Fe formation and loss, gravity wave source and propagation, and the transport of Fe^+ and Fe at high latitudes, along with simultaneous measurements of Fe, Fe^+ and electrons. Such requirements stimulate the development of a numerical model that will be described in Chapter 3.

Chapter 3

Development of A Thermospheric Fe/Fe^+ Model for Polar Regions

3.1 Introduction

In this chapter, we will introduce the first high-latitude thermospheric Fe/Fe^+ numerical model. The "first" is referring to the first model simulating the thermospheric neutral Fe layers while numerous other models only deal with the Fe^+ ions. The converged Fe^+ layers at high latitudes hypothesized by *Chu et al.* [2011] are expected to share the same mechanisms as the travelling ionospheric disturbances (TIDs), sporadic E layers and intermediate layers at low latitudes. For the sake of studying sporadic E layers or intermediate layers, numerous modelling studies focus on the mechanism of converged ions layers in the E–F region (100–200 km) [*MacLeod et al.*, 1975; *Mathews and Bekeny*, 1979; *Bristow and Watkins*, 1991; *Osterman et al.*, 1994; *Carter and Forbes*, 1999; *MacDougall et al.*, 2000; *Bishop and Earle*, 2003]. These numerical simulations support the early theories of forming thin ionization layers in the E–F region [*Whitehead*,1961; *Axford*, 1963; *Nygrén et al.*, 1984], that is, the converged ion layers are driven by appropriately directed wind

shears in combination with the geomagnetic fields or by strong electric fields with appropriate directions. Although the chemistry of the metallic ions was embedded into some of the models [e.g., *Carter and Forbes*, 1999; *McDougall et al.*, 2000; *Bishop and Earle*, 2003], how the formation of neutral metal atoms are related to layering phenomena in the thermosphere were beyond their scope due to the lack of neutral layer observations. Nevertheless, these previous modelling studies shed a light on the development of a new Fe/Fe^+ model in this study.

Inspired by the mid-/low-latitude model of *Carter and Forbes* [1999], a new high-latitude thermospheric Fe/Fe^+ model has been established for polar region. The primary purpose of the new model Fe/Fe^+ is to understand the formation of thermospheric Fe layers. A description of this thermospheric Fe/Fe^+ model is introduced in Section 3.2. Section 3.3 presents the development of the numerical model that is based on the mathematical model in 3.2. In Section 3.4, simulation of converged ion layers at Arecibo is reproduced and compare to the simulations with published simulations and observations, and the conclusions is given in Section 3.5.

3.2 Mathematical Development of the Model

The thermospheric Fe/Fe^+ numerical model is based on a three-dimensional (3-D) mathematical model that starts with the continuity equations of Fe, Fe^+ and related species. The density changes of Fe and Fe^+ are caused by three mechanisms: Source input (meteor ablation and sputtering), chemical production and loss, and transport of Fe and Fe^+. This understanding forms the basis of the continuity equation 3.1 that describes the time-changing rates of the number densities of Fe and Fe^+ [*Carter and Forbes*, 1999]:

$$\frac{\partial N_M}{\partial t} = S + Q_M - L_M - \nabla \cdot (N_M \vec{V}_M) \tag{3.1}$$

where M stands for ion or neutral species, S is the external source function (meteor ablation and sputtering), N_M is the number density, $\vec{V}_M$ is the transport velocity of species M, and Q_M, L_M are the production and loss terms caused by chemical reactions, and the last term is the divergence flux. E-F region is dominated by molecular ion species NO^+ and O_2^+, and partially O^+. *Osterman et al.* [1994] showed that molecular ions such as NO^+ and O_2^+ having significant lifetimes are the major compositions of converged descending layers. Meanwhile, NO^+ and O_2^+ are important to the neutral Fe chemistry. So it's necessary for us to consider the transport of O^+, NO^+ and O_2^+. In our model, we consider seven major species, Fe, Fe^+, FeO^+, FeO_2^+, FeN_2^+, O_2^+, NO^+ and O^+. The continuity equations of each ion species are calculated separately. These continuity equations can be written as,

$$\frac{\partial N_{Fe^+}}{\partial t} = S_{Fe^+} + Q_{Fe^+} - L_{Fe^+} - \nabla \cdot (N_{Fe^+}\vec{V}_{Fe^+}) \tag{3.2}$$

$$\frac{\partial N_{Fe}}{\partial t} = S_{Fe} + Q_{Fe} - L_{Fe} - \nabla \cdot (N_{Fe}\vec{V}_{Fe}) \tag{3.3}$$

$$\frac{\partial N_{FeO^+}}{\partial t} = Q_{FeO^+} - L_{FeO^+} - \nabla \cdot (N_{FeO^+}\vec{V}_{FeO^+}) \tag{3.4}$$

$$\frac{\partial N_{FeO_2^+}}{\partial t} = Q_{FeO_2^+} - L_{FeO_2^+} - \nabla \cdot (N_{FeO_2^+}\vec{V}_{FeO_2^+}) \tag{3.5}$$

$$\frac{\partial N_{FeN_2^+}}{\partial t} = Q_{FeN_2^+} - L_{FeN_2^+} - \nabla \cdot (N_{FeN_2^+}\vec{V}_{FeN_2^+}) \tag{3.6}$$

$$\frac{\partial N_{NO^+}}{\partial t} = Q_{NO^+} - L_{NO^+} - \nabla \cdot (N_{NO^+}\vec{V}_{NO^+}) \tag{3.7}$$

$$\frac{\partial N_{O_2^+}}{\partial t} = Q_{O_2^+} - L_{O_2^+} - \nabla \cdot (N_{O_2^+}\vec{V}_{O_2^+}) \tag{3.8}$$

$$\frac{\partial N_{O^+}}{\partial t} = Q_{O^+} - L_{O^+} - \nabla \cdot (N_{O^+}\vec{V}_{O^+}) \tag{3.9}$$

In order to solve the continuity equations, in section 3.2.1, we will derive the ion velocities and the velocity of neutral Fe, the section 3.2.5 briefly describes the solution of the chemical reactions used in this model.

3.2.1 Motions of ions

Motions of ions are governed by electric field, $\vec{E}$, and magnetic field, $\vec{B}$, neutral winds through ion-neutral collisions, ion-electron collision, ionic pressure, gravitational force, and Coriolis force. The motion of ions is described by *Gossard and Hooke* [1975],

$$\begin{aligned} m_i N_i \frac{D\vec{V}_i}{Dt} = {} & n_i Ze(\vec{E} + \vec{V}_i \times \vec{B}) - 2m_i N_i \vec{\Omega} \times \vec{V}_i - \nabla P_i + m_i N_i \vec{g} \\ & + m_i n_i \nu_{in}(\vec{V}_n - \vec{V}_i) - N_i m_i \nu_{ie}(\vec{V}_i - \vec{V}_e) + \nabla \cdot \vec{\tau}_i \end{aligned} \tag{3.10}$$

where Z is the number of charges per ions, $\vec{E}$ and $\vec{B}$ are the electric and magnetic fields, respectively, N_i is the number density of ions, m_i is the mass of ions, $\vec{V}_i$ is the velocity of ions, $\vec{V}_n$ is the velocity of neutrals, $\vec{V}_e$ is the velocity of electrons, $\vec{g}_i$ is the gravitational acceleration, $\vec{\Omega}$ is the angular velocity of the Earth, e is the elementary charge, ν_{in} is the ion-neutral collision frequency, ν_{ie} is the ion-electron collision frequency, P_i is the ionic pressure, and τ is the ionic stress tensor.

1. the first item is the Lorentz force;
2. the second item is the Coriolis force;
3. the third item is the pressure gradient force;
4. the forth item is the gravitational force;
5. the fifth item is the momentum transferred between neutrals and ions due to elastic and inelastic collisions;
6. the sixth item is the momentum transferred between ions and electrons due to elastic and inelastic collisions;
7. the seventh item is the stress force.

Under the first-order approximation for ion's motions, we assume the ions are in force balance so no acceleration is considered. The second term, Coriolis force, is negligible based on the first-order approximation, and the momentum transferred between ions and electrons are also negligible due to the light mass of electron, which is only $\frac{1}{1836}$ fractions of the mass of proton. Therefore, the motion of the ions in steady state is governed by Lorentz force, gravitational force, ion-neutral collisions and ionic pressure under force balance, hence equation 3.10 is simplified as the equation 3.11

$$q\vec{E} + q\vec{V_i} \times \vec{B} + m_i\nu_{in}(\vec{V_n} - \vec{V_i}) + m_i\vec{g} - \frac{\nabla P_i}{N_i} = 0 \tag{3.11}$$

In equation 3.11, the first term is the Coulomb force, the second term is the Lorentz force, the third trem represents neutral-ion collision, the forth term is the gravitational force, and the last term is the ionic pressure gradient. We define the sum of the last two terms as $\vec{F} = m_i\vec{g}$ - $\frac{\nabla P_i}{N_i}$ in order to simplify the solution of equation 3.11. The solution of ions' motion is given by equation 3.12 (the derivation is offered in Appendix B)

$$\begin{aligned}\vec{V_i} = {} & \frac{1}{1+\xi^2}\frac{\vec{E}\times\vec{B}}{B^2} + \frac{q\vec{E}\cdot\vec{B}}{m_i\nu_{in}B^2(1+\xi^2)}\vec{B} + \frac{\xi}{1+\xi^2}\frac{\vec{E}}{B} + \frac{\xi}{1+\xi^2}\frac{\vec{V_n}\times\vec{B}}{B} + \frac{1}{1+\xi^2}\frac{(\vec{V_n}\cdot\vec{B})\vec{B}}{B^2} \\ & + \frac{\xi^2}{1+\xi^2}\vec{V_n} + \Big(\frac{\vec{F}\times\vec{B}}{qB^2(1+\xi^2)} + \frac{\vec{F}\cdot\vec{B}}{m_i\nu_{in}B^2(1+\xi^2)}\vec{B} + \frac{\xi}{Bq(1+\xi^2)}\vec{F}\Big)\end{aligned} \tag{3.12}$$

where $\xi = \nu_{in}/\omega_i$, $\omega_i = qB/m_i$, ω_i the ion gyrofrequency. Usually the conductivity along field lines is sufficiently high, leading to a good assumption that the parallel "external" electric field along with the geomagnetic field line is approximated to zero. But an "internal" electric field along with the geomagnetic field line can be established by the diffuse separation between ions and electrons, so the term of $\vec{E}\cdot\vec{B}$ cannot be neglected, or $\vec{E}\cdot\vec{B} \neq 0$. In Appendix B, we provide the derivations of estimating $\vec{E}\cdot\vec{B}$. ξ is the ratio of collision frequency to gyromagnetic frequency, which is highly dependent on altitude, as shown in Figure 3.1. For instance, at low altitudes, $\xi \gg 1$, the ion-neutral

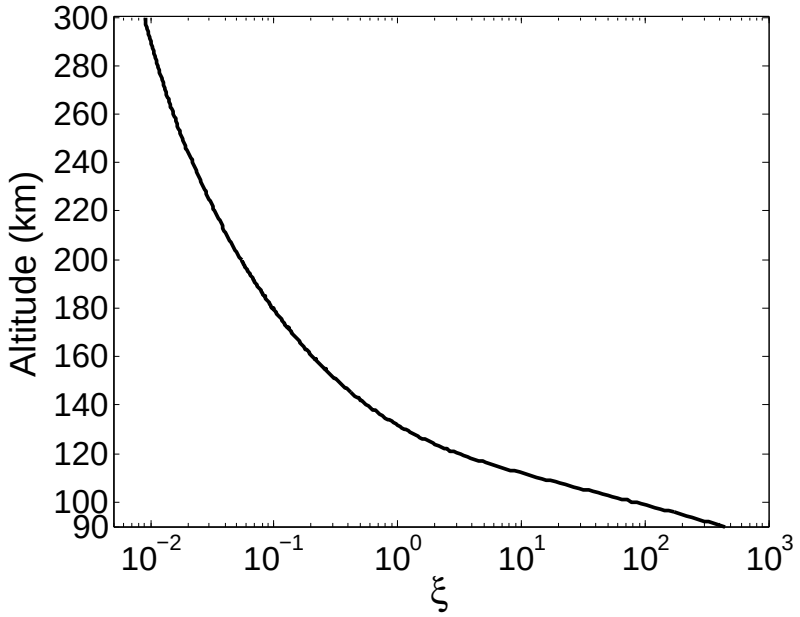

FIGURE 3.1: Altitude dependence of ξ of Fe^{+}.

coupling is so strong that the neutral winds have more profound impact on ion's motions. At very high altitudes, $\xi \ll 1$, where it is nearly collisionless regime, the motion of the ions is dominated by $\vec{E}$ and $\vec{B}$. In the regime where $\xi \cong 1$, the motions of the ions are even more complicated and are governed by all forces in equation 3.11. Inasmuch as the derivation of ion's motion was essentially accurate based on the first-order approximation, and equation 3.12 describe the motion of ions for all altitudes.

By projecting the ion motion's solution equation 3.12 to the vertical direction z, we obtain the vertical drift velocity of ions V_{iz}, which can be decomposed into three groups driven by electric field, neutral winds, and gravity and diffusion. Given the equations (3.13–3.15), V_{ize}, V_{izw}, and V_{izgd} are the vertical drift velocities of ion driven respectively by electric field, neutral wind, and gravity and diffusion, respectively. In Cartesian coordinates, the vertical velocities can be obtained from equation (3.12):

1.

$$V_{ize} = \frac{\cos\Theta_D}{1+\xi^2}\frac{E_x}{B_0} + \frac{\xi}{1+\xi^2}\frac{E_z}{B_0} \tag{3.13}$$

2.

$$V_{izw} = \frac{1}{1+\xi^2}\sin\Theta_D\cos\Theta_D V_{n,y} + \frac{\xi}{1+\xi^2}\cos\Theta_D V_{n,x} + \Big(\frac{\xi^2+\sin^2\Theta_D}{1+\xi^2}\Big)V_{n,z} \tag{3.14}$$

3.

$$V_{izgd} = -\Big(1-\frac{\cos^2\Theta_D}{1+\xi^2}\Big)\frac{g}{\nu_{in}} - \Big(1-\frac{\cos 2\Theta_D}{1+\xi^2}\Big)D_i\Big(\frac{1}{N_i}\frac{\partial N_i}{\partial z} + \frac{1}{T_i}\frac{\partial T_i}{\partial z}\Big) \tag{3.15}$$

The total vertical velocity is

$$V_z = V_{ize} + V_{izw} + V_{izgd} \tag{3.16}$$

where B_0 is the geomagnetic field strength, Θ_D is the inclination angle of geomagnetic field line, and E_x and E_z are the east-west and vertical components of the ionospheric electric, respetively. $V_{n,x}$, $V_{n,y}$, and $V_{n,z}$ are the neutral wind components in the geomagnetic East, North and vertical directions, respectively, D_i is the diffusion coefficient of ion. Here the D_i is defined differently from the normal usage that includes the effects of gravity and ambipolar E in addition to pressure gradients.

3.2.2 Motions of Fe

Motions of neutral Fe are controlled by neutral atmosphere winds, gravitational force, and diffusion. Since the neutral Fe atoms are free of the constraints of electromagnetic forces, we assume that the Fe atoms are immediately balanced by neutral background via thermal collisions and following the motions of the background neutral winds after Fe atoms are formed through neutralization of Fe^+. This is fairly good enough assumption below 200 km, particularly below 150 km, because

of significant collisions in this region. At the altitude of 150 km, it takes less than 1 seconds to force the motion of Fe atoms, whose velocity even opposite to background winds, to be consistent with background neutral wind. Detailed analyses can be found in Section E.2. Additionally, the vertical transport of Fe in the thermosphere is subject to the gravitational force and the molecular diffusion. Therefore, the velocity of neutral Fe motions is determined by the sum of three terms in equation 3.17

$$\vec{V}_{Fe} = \vec{V}_{s,n} + \vec{V}_g + \vec{V}_d \tag{3.17}$$

where $\vec{V}_{Fe}$ is the total Fe velocity, $\vec{V}_{s,n}$ is velocity of Fe that is driven by the neutral background wind through minor-major species collisions, 's' generally represents minor species, $\vec{V}_g$ and $\vec{V}_d$ are the velocities of Fe caused by gravity and diffusion, respectively. The vertical "diffusion velocity" of Fe can be expressed as equation 3.18

$$w_{D,Fe} = -D_{Fe}\Big(\frac{1}{N_{Fe}}\frac{\partial N_{Fe}}{\partial z} + \frac{1}{T_N}\frac{\partial T_N}{\partial z} + \frac{1}{H_{Fe}}\Big) \tag{3.18}$$

where D_{Fe} is the diffusion coefficient, $H_{Fe} = \frac{k_B T}{m_{Fe} g}$ is the scale height of Fe, T_N is the neutral temperature, and N_{Fe} is the neutral density. The effective vertical "eddy diffusion velocity" is expressed as [*Brasseur and Solomon*, 2005]

$$w_{E,Fe} = -K_z\Big(\frac{1}{N_{Fe}}\frac{\partial N_{Fe}}{\partial z} + \frac{1}{T_N}\frac{\partial T_N}{\partial z} + \frac{1}{H_g}\Big) \tag{3.19}$$

where K_z is the vertical eddy diffusion coefficient and $H_g = k_B T/m_{air} g$ is the atmospheric scale height. The velocity caused by gravity is expressed as the scale height term in $w_{D,Fe}$ and $w_{E,Fe}$.

In the Section E.2, we particularly discuss the wave solutions of $\vec{V}_{s,n}$ in diffusely separated atmosphere, when major species have gravity-wave oscillations. The wave solutions of $\vec{V}_{s,n}$ are based

on the assumption that the internal pressure of minor species are negligible, therefore $\nabla P_s \approx 0$. This assumption is equivalent to that the spatial gradients of and number densities n_s and temperature T_s would not impact on the motions of minor species, and only valid for extreme low-density minor species. Therefore minor species are mainly governed by gravitational force and momentum transfer with the major species. As discussed in Appendix E.2, below 200 km, the momentum transfer from collisions are still significant enough to force the minor species follow the motions of major species within a short time (within a few seconds). For example, the simulation in Figure E.4 shows that it only takes 0.5 seconds to force Fe atoms that have opposite velocity with major species to be consistent with the motions of major species at 140 km, and it takes 3.5 seconds at 200 km.

Therefore, it is reasonable to assume that $\vec{V}_{s,n}$ is equal to the motions of major gases below 200 km, namely, $\vec{V}_{s,n} = \vec{V}_n$.

3.2.3 Parametrization of collision frequency

The parametrization of collision is essential for upper atmosphere studies. In the calculation of velocities of Fe^+ and Fe, one of the fundamental parameters is the collision frequency between neutrals and neutrals, neutrals and ions, ions and ions. We adopt the formulas from *Banks and Kockarts* [1973] to calculate these collision frequencies.

Neutral-neutral collision frequency: Binary collision that two particles collide is considered in the major collision process in upper atomphere, and the binary collision frequency is a few tens order higher than the collision frequency of the simultaneous collisions of three or more seperate molecules. The equation 9.18 in *Banks and Kockarts* [1973] provides the definition of the average

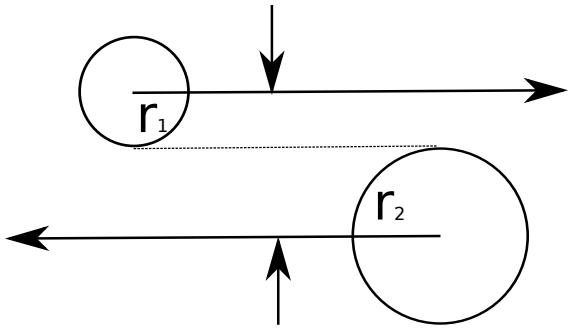

FIGURE 3.2: The model of collision between two rigid spheres.

neutral-neutral binary collision frequency, which is equation 3.20 ,

$$\nu_{12} = n_2 \sigma_0 \bar{v}_{12} \tag{3.20}$$

where '1' and '2' represent the source and target particles, respetively, n_2 is the number density of target particles, and $\bar{v}_{12}$ is the average speed between '1' and '2', and σ_0 is the collision cross section.

Under the assumption of ideal gas, we assume the collisions between two particles are elastic. The ideal gas assumption leads to an ideal model of gas molecule that can be treated as hard spheres. Therefore, as shown in figure 3.2, the collision cross section for ideal gas is given by equation 3.21

$$\sigma_0 = \pi (r_1 + r_2)^2 \tag{3.21}$$

where r is the radius of hard sphere. Note that the radius r is not the radius of the atom or molecular itself. Usually the hard sphere model of an element is larger than the real size of the atom of this element. Equation 3.21 assumes total momentum loss of species 's' whenever hard spheres touch. It neglects relative masses and deflection direction.

The hard-sphere radii are also called van der Waals radii, which mean nonbonded radii.

TABLE 3.1: Van der Waals Radii of Air Gases and Metallic Species.

Atom/Molecular	Radii (Å)
H	1.14
N	1.52
O	1.55
H_2	1.61
O_2	1.77
N_2	1.82
Fe	2.16
Mg	2.31
Na	2.59

The van der Waals radii are hard to accurately measure, and vary with experimental methods. *Batsanov* [2001] provided a comprehensive summary of the available data on van der Waals radii of atoms in molecules and crystals. The van der Waals radii of metals are difficult to determine due to only a small number of structures in which metal atoms can be in contact with another molecule, but some model are developed to calculate the van der Waals radii of metals from the structural data for metals and their molecular compounds. Here some of the molecule useful for thermospheric Fe/Fe^+ model are listed in Table 3.1. Note that the van der Waals radii of the metallic atoms are established from neighbour-neighbour interactions in crystals, and the values may be different values when the metallic atoms are in gaseous phase.

The parametrization of the average relative velocity $\bar{v}_{12}$ is based on the assumption that the gas particles follow the Maxwellian distribution, which is the equation 3.22

$$f(v_m) = n_m\Big(\frac{M_m}{2\pi k_B T_i}\Big)^{3/2} \exp\Big(-\frac{M_m v_m^2}{2k_B T_m}\Big) \tag{3.22}$$

where m identifies the type of particle, n_m is the number density, M_m is the particle mass, T_m is the temperature, and k_B is the Boltzmann's constant. Therefore the average relative speed can be

derived from the equation 3.23

$$\bar{v}_{12} = \int |\vec{v}_1 - \vec{v}_2| f_1(v_1) f_2(v_2)\, \mathrm{d}\vec{v_1} \mathrm{d}\vec{v_2} \tag{3.23}$$

So the average relative speed can be given in equation 3.24

$$\bar{v}_{12} = \Big(\frac{8k_BT}{\pi}\Big)^{1/2} \Big(\frac{T_1}{M_1} + \frac{T_2}{M_2}\Big)^{1/2} \tag{3.24}$$

If the gas particles are in thermal equilibrium, then $T_1 = T_2$, equation 3.24 can be simplified as equation 3.25

$$\bar{v}_{12} = \Big(\frac{8k_BT}{\pi\mu}\Big)^{1/2} \tag{3.25}$$

where μ is the reduced mass, which is given in equation 3.26

$$\mu = \frac{M_1 M_2}{M_1 + M_2} \tag{3.26}$$

Based on the mean collision frequency, equation 3.20, it is easy to obtain the mean collision time and mean free path, as shown in equations 3.27 and 3.28, respectively

$$\bar{\tau}_{12} = \frac{1}{\bar{\nu}_{12}} = (n_2 \sigma_0 \bar{v}_{12})^{-1} \tag{3.27}$$

$$\lambda_{12} = \bar{\tau}_{12} \bar{v}_{12} = (n_2 \sigma_0)^{-1} \tag{3.28}$$

For a rough calculation of atomic Fe, we adopt a set of typical molecular parameters: σ_{Fe} $= 4.9 \times 10^{-15}\ cm^{-2}$, $M_{Fe} = 9.4 \times 10^{-23}\ gm$ at the temperature of 300 K, the collision frequency of atomic Fe is approximated by $\bar{\nu}_{12} = 0.6 \times 10^{-10} n_2\ sec^{-1}$, where n_2 is the number density of N_2.

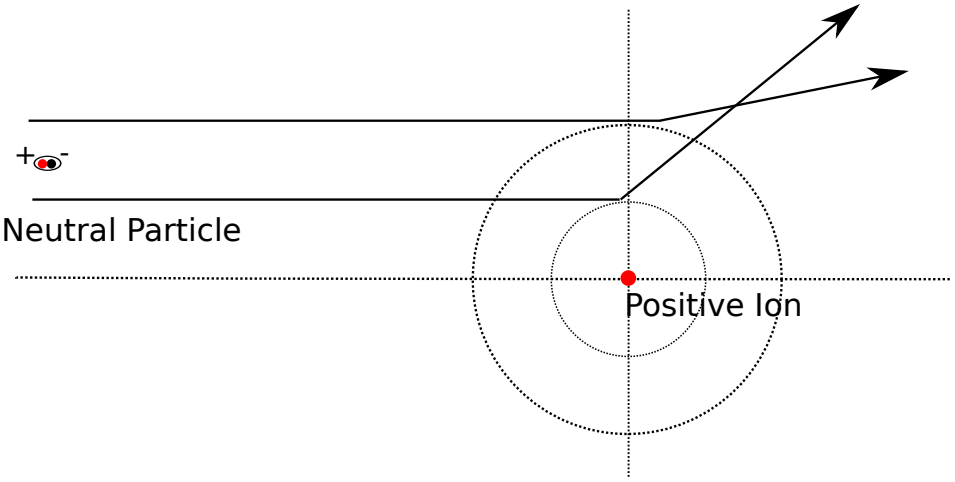

FIGURE 3.3: A simple model of ion-neutral collision. The separation of red and black dots in the neutral particle represent a dipole induced by the positive ion.

Ion-neutral collision frequency: The rigid sphere model does not apply for the ion-neutral collision model, and the electric field caused by ion has to be considered in the ion-neutral collision, as shown in Figure 3.3. At low temperatures, the most important ion-neutral interaction is the attraction between the ion and the induced dipole. The interaction potential, $\phi(r)$, can be described as in equation 3.29 [*McDaniel*, 1964],

$$\phi(r) = \frac{e^2\alpha_0}{2r^4} \tag{3.29}$$

where e is the electric charge, and r is the distance between neutral and ion, and α_0 is the neutral atom polarizability. The polarizability represents a volume related to the size of the outer electronic orbitals. Thus, we can expect that different neutral gas would have different polarizability. In a neutral-neutral system, the polarizability can be taken as a measure of the mutual repulsion, or at least in a range near the equilibrium distance, which is the distance between the nucleus and the center of the electron cloud when the external force is canceled by the force exerted on the nucleus by the electron cloud. The attraction between ions and neutrals depends on the ion-induced multipole interaction. At a large distance r, the ion-induced dipole term is dominant.

Unlike neutral-neutral collision cross section and frequency that are independent of temperature, it is found that the cross section of ion-neutral collision is proportional to $T^{-1/2}$, and the ion-neutral collision frequency is independent of the temperature. Because the Van der Waals radii are independent of temperature, while the interaction between neutral dipole and ion is temperature dependent. When the temperature is lower, the thermal speed of the neutral or ion is slower so that longer time interval of the attraction between neutral dipole and ion are needed, resulting in longer distance when neutral pass by ion so larger cross section would be. On the contrary, higher temperature corresponds to shorter interaction distance and leads to smaller cross section. The average momentum transfer cross section of ion-neutral collision is given by equation [9.71] in *Banks and Kockarts* [1973], which is equation 3.30, and the corresponding numerical expression is equation 3.31

$$\bar{Q}_D = \frac{3\sqrt{2}}{16}\pi^{3/2}\left(\frac{4.88\alpha_0 e^2}{\mu}\right)^{1/2}\left(\frac{k_B T_i}{M_i}+\frac{k_B T_n}{M_n}\right)^{-1/2} \tag{3.30}$$

$$or \quad \bar{Q}_D = 13.3\times 10^{-14}\left(\frac{\alpha_0}{\mu_A}\right)^{1/2}\left(\frac{T_i}{A_i}+\frac{T_n}{A_n}\right)^{-1/2} \tag{3.31}$$

where μ_A is the reduced mass in amu, A_i and A_n are particle masses in amu, α_0 is the atomic polarziability (in units of $10^{-24}\ cm^3$).

The velocity dependent ion-neutral collision frequency is written as equation 3.32

$$\bar{\nu}_{12} = \frac{4}{3} n_2 \bar{v}_{12} \bar{Q}_D \tag{3.32}$$

where $\bar{v}_{12}$ is given by equation 3.33

$$\bar{v}_{12} = \left(\frac{8k_B}{\pi}\right)\left(\frac{T_i}{M_i}+\frac{T_n}{M_n}\right)^{1/2} \tag{3.33}$$

TABLE 3.2: Polarizabilities of neutral gases.

Neutral gas	$\alpha_0(10^{-24}cm^3)$
N_2	1.76
O_2	1.59
H_2	0.82
O	0.79 ± 0.02
H	0.667
He	0.21 ± 0.01
N	1.1 ± 0.1
NO	1.74
CO	1.97
CO_2	2.63
N_2O	3.00
NH_3	2.22
SO_2	3.89

Combine equation 3.30, 3.32 and 3.33, we obtain the ion-neutral collisions, which is given by equation 3.34

$$\nu_{in} = 2.6 \times 10^{-9} n_n \left(\frac{\alpha_0}{\mu_A}\right)^{1/2} \tag{3.34}$$

where α_0 is the polarizabilities of neutral gases in units of 10^{-24} cm^3, which is given in Table 3.2, and $\mu_A = \frac{M_i M_n}{M_i + M_n}$ is the reduced mass in amu. We can see that the ion-neutral collision frequency, equation 3.34, is independent of either neutral or ion temperature.

Ion-ion collision frequency: In the Section 9.7 of *Banks and Korckarts* [1973], the interaction between two charged particles is given by the Coulomb law, which is equation 3.35

$$F_{12} = Z_1 Z_2 e^2 / r^2 \tag{3.35}$$

where Z is the charge state, e is the elementary charge, and r is the distance between two ions. Based on the results of plasma kinetic theory, the basic collision cross sections can be written as

equation 3.36

$$\sigma_D = 2\pi\Big(\frac{Z_1 Z_2 e^2}{\mu v_{12}^2}\Big)^2 \ln\Lambda \tag{3.36}$$

where $\Lambda \equiv (Z_1 Z_2 e^2/\mu g^2 \lambda_D)^{-1}$, and λ_D is the Debye length, equal to $\lambda_D \equiv [4\pi \sum_j (n_j e^2 Z_j/kT_j)]^{-1/2}$.

For the plasma with Maxwellian velocity distribution, the average momentum transfer cross section of two charged particles is given by equation 3.37

$$\bar{Q}_D = \frac{\pi}{2}\Big[\frac{(M_{i1}+M_{i2})Z_1 Z_2 e^2}{M_{i1}M_{i2}}\Big]^2\Big[\frac{k_B T_{i1}}{M_{i1}} + \frac{k_B T_{i2}}{M_{i2}}\Big]^{-2} \ln\Lambda \tag{3.37}$$

The average collision frequency for momentum transfer of charged particles is equation 3.38,

$$\bar{\nu}_{12} = \frac{4n_{i2}}{3}(2\pi)^{1/2}\Big[\frac{(M_{i1}+M_{i2})Z_1 Z_2 e^2}{M_{i1}M_2}\Big]^2\Big[\frac{k_B T_{i1}}{M_{i1}} + \frac{k_B T_{i2}}{M_{i2}}\Big]^{-3/2} \ln\Lambda \tag{3.38}$$

For numerical application, if $T_{i1} = T_{i2}$, then the ion-ion collision frequency is 3.39,

$$\nu_{ii} = 0.0851\mu_A^{-1/2} n_{i2} T_i^{-3/2} \ln[10518 T_i^{3/2} n_{i2}^{-1/2}] \tag{3.39}$$

where $\mu_A = M_{i1}M_{i2}/(M_{i1}+M_{i2})$.

Eddy diffusion The eddy diffusion is obtained from U.S. Standard Atmosphere [1976], (in units of cm^2/sec).

$$D_{eddy} = \begin{cases} 0, & \text{if} \quad Alt > 120km \\ 2\times 10^4, & \text{if} \quad 110 < Alt < 120km \\ 2\times 10^5, & \text{if} \quad 100 < Alt < 110km \\ 1\times 10^6, & \text{if} \quad Alt < 100km \end{cases}$$

3.2.4 Ultimate source of metallic species in mesosphere and thermosphere

The ultimate source of Fe and Fe^+ is extraterrestrial the meteor deposition via meteor ablation and sputtering. When the meteors enter the atmosphere of the earth, they are at high speeds ranging from 11 to 72 km/s. The ablation generated by the high-speed friction produces layers of metal species such as Fe, Mg, Na, and so on in the mesosphere and lower thermosphere [*Plane*, 2012]. *Feng et al.* [2013] provide a meteoric input function (MIF) for injection rates of Fe atom into the atmosphere as a function of height, season, and latitude. The MIF is calculated by the combination of two models, the CABMOD and a meteoroid flux model. The CABMOD [*Vondrak et al.*, 2008] provides the chemical ablation of meteoroids in the upper atmosphere, and computes the ablation profiles of each metallic elements as a function of meteoroid mass ranging from 10^8 to 10^3 μg, velocity ranging from 11 to 72 $km\ s^{-1}$, and the zenith angle of entry trajectories varying from 0 to 90°. The model of meteoroid fluxes [*Fentzke and Janches*, 2008] provides an estimation of global meteoric mass flux into the upper atmosphere. The details of how these two models are combined to generate MIF are introduced by *Marsh et al.* [2013]. Thanks to the MIF data provided by Dr. John Plane and Wuhu Feng, we utilize the MIF data in [*Feng et al.*, 2013] in this study.

The seasonal variation of the meteoric Fe injection rate at McMurdo is shown in the left plot of Figure 3.4, and the annual mean vertical profile of Fe injection rate at McMurdo is shown in the right plot of Figure 3.4. Similar to the vertical profile of the global annual mean in *Feng et al.* [2013], the peak of annual mean vertical profile at McMurdo is at 97.2 km with value of 0.00412 $cm^{-3}s^{-1}$, and a secondary peak is at 108 km with value of 0.00299 $cm^{-3}s^{-1}$. Above 125 km, the injection rate of Fe is less than 10^{-5} $cm^{-3}s^{-1}$. For short period simulations, the contribution of direct injection of Fe above 125 km is negligible.

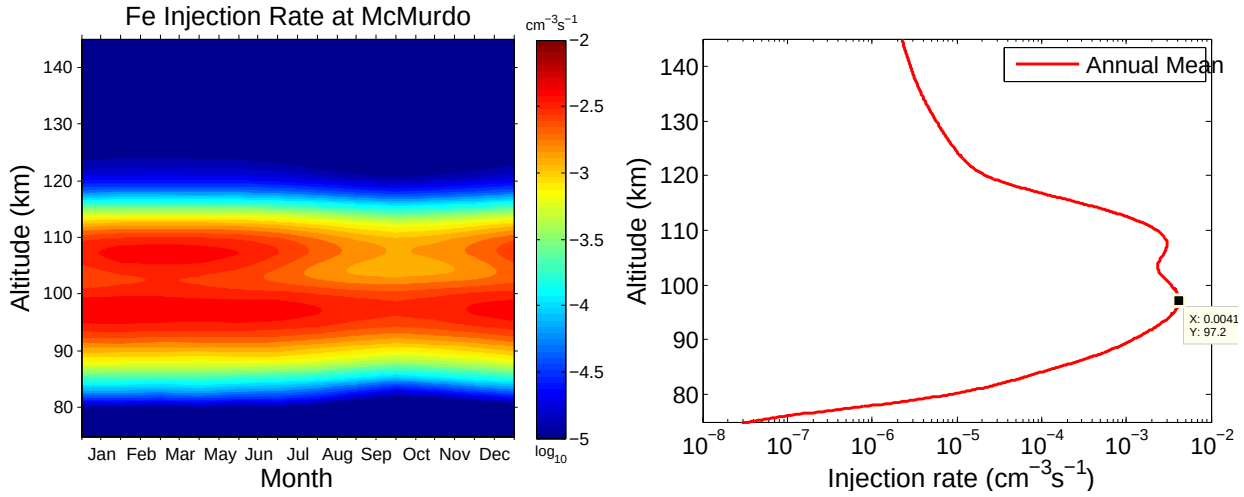

FIGURE 3.4: Left: seasonal varying meteoric Fe injection rate ($cm^{-3}s^{-1}$) at 165^{o}E and 80^{o}S; Right: Annual mean of meteoric injection rate profiles. The data are provided by Dr. John M. C. Plane and Wuhu Feng.

3.2.5 Chemistry of Fe species and related molecular ions

In this section, we focus on the discussion of the chemistry of the Fe species. To understand the metal Fe layer in the mesosphere and thermosphere, we need to understand the characteristics of chemical reactions between Fe species and the ambient atmospheric constituents such as O_3, O_2, O, H, NO^+ and O_2^+. The Fe chemistry reactions are given in Table 3.3, and the relationships between the Fe reactants are given in Figure 3.5.

When the neutral Fe layer is formed in the region between 75 km and 120 km. There are two channels control the losses of neutral Fe atoms. One channel is the conversion of Fe to the neutral compound FeO through oxidation ($Fe \xrightarrow{O_3} FeO$), and the other channel is the ionization of Fe to form Fe^+ ($Fe \xrightarrow{h\nu} Fe^+$ and $Fe \xrightarrow{e^{-*}} Fe^+$), or transfers charge from Fe to NO^+ or O_2^+ ($Fe \xrightarrow{NO^+/O_2^+} Fe^+$). Conversely, FeO can be reduced by atomic O and reverse to atomic Fe ($FeO \xrightarrow{O} Fe$), and Fe^+ can be directly neutralized by electrons and form atomic Fe ($Fe^+ \xrightarrow{e^-} Fe$), or through dissociative electron recombination ($FeO^+ \xrightarrow{e^-} Fe$). At the lower altitude (usually

lower than the peak of the Fe layer), the rapid decrease of the ratio of atomic O to ozone O_3 $[O/O_3]$ and the concentration of atomic H, the loss of the Fe through oxidation overwhelm its production and the Fe quickly goes to relative stable Fe compounds like $FeOH$, $FeOOH$, FeO_3. This explains the sharp transition of Fe profile below its peak we observes from lidar measurements [*Chu et al.*, 2011]. Fe atoms have low ionization potentials (7.9 eV) [*Worden et al.*, 1984], so that Fe^+ can be readily formed through charge transfer reaction with NO^+ and O_2^+, photoionization, or ionization by energetic electrons. The densities of molecular ions like NO^+ and O_2^+ dramatically increase as altitude increasing. At the same time, above 100 km, the rapid decrease of O_3 block the chain reactions from Fe atoms to neutral Fe compounds. Therefore, the region of 80 km to 110 km become a reservoir of Fe^+, and above 110 km, Fe/Fe^+ are produced as a result of mass transport or chemical reactions.

The Fe chemistry in the thermosphere above 120 km is relative simple. Due to the lack of O_3, Fe–Fe^+ chemistry are mainly influenced by the molecular ions, such as NO^+ and O_2^+, and electron density. NO^+ and O_2^+ dominate in the region from 90 km to 140 km, produced by solar radiation or energetic electrons precipitation. Both NO^+ and O_2^+ have fast dissociative recombination reaction rates with electrons. Therefore without continuous ionization, the densities of NO^+ and O_2^+ are readily declined to low level through dissociative recombination. Above 140 km, the dominant ion is O^+ ion, which has relative longer lifetime. The molecular ions reactions and the corresponding reaction rate coefficients are given in Table 3.4.

[a] Rate coefficient unit:

bimolecular, $cm^3\ molecule^{-1}\ s^{-1}$; termolecular, $cm^6\ molecule^{-2}\ s^{-1}$. The data source is given in Table in next page.

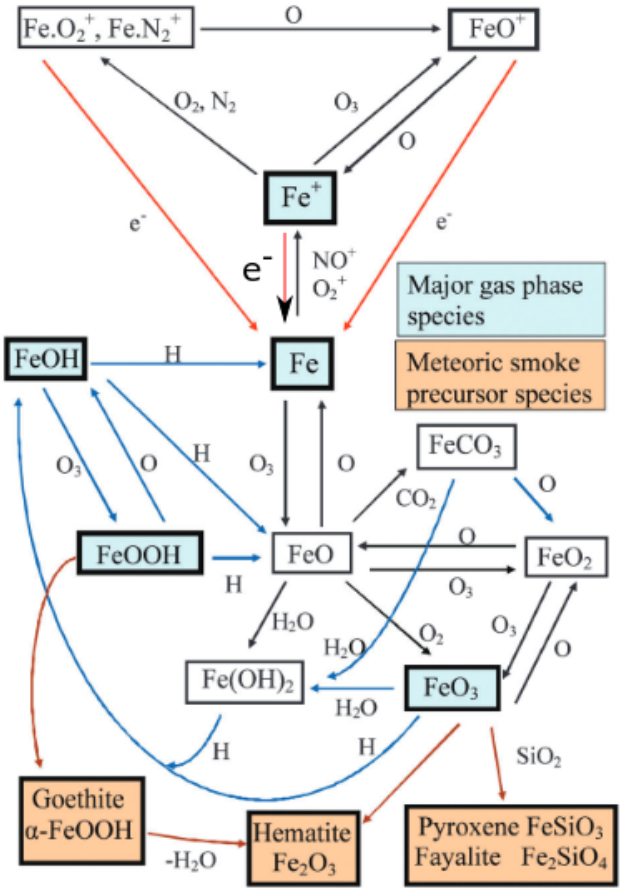

FIGURE 3.5: Fe chemistry in the mesosphere and thermosphere. The black arrows mean the rate coefficients are measured by laboratory, and the others are not. This diagram is slightly modified from the original figure in the paper "Cosmic dust in the earth's atmosphere" by *Plane* [2012].

It can be seen that Fe chemistry Table 3.3 and molecular ion chemistry Table 3.4 are coupled together and form a complex system. Before we establish the full mathematical model of Fe chemistry, let's illustrate how to construct a mathematical model for chemical reactions through starting with two coupled equations 3.40 and 3.41. The reactant A in equation 3.40 is the product of equation 3.41, and the reactant C in equation 3.41 is the product of equation 3.40.

$$A + B \xrightarrow{k_1} C + D \tag{3.40}$$

$$C + E \xrightarrow{k_2} A + F \tag{3.41}$$

TABLE 3.3: Chemical Reactions and Rate Constants of Fe Chemistry

Reaction	Rate Coefficient[a]
$Fe + e^{*-} \longrightarrow e^{*-} + Fe^+ + e^-$	See text
$Fe + h\nu \longrightarrow Fe^+ + e^-$	$k_0 = 5.0 \times 10^{-7}$
$Fe^+ + e^- \longrightarrow Fe + h\nu$	$k_1 = 6.5 \times 10^{-12}(300/T)^{0.51}$
$FeO^+ + e^- \longrightarrow Fe + O$	$k_2 = 4.9 \times 10^{-7}(200/T)^{0.5}$
$Fe + NO^+ \longrightarrow Fe^+ + NO$	$k_3 = 9.2 \times 10^{-10}$
$Fe + O_2^+ \longrightarrow Fe^+ + O_2$	$k_4 = 1.1 \times 10^{-9}$
$FeO_2^+ + O \longrightarrow FeO^+ + O_2$	$k_5 = 5.0 \times 10^{-11}$
$FeO^+ + O \longrightarrow Fe^+ + O_2$	$k_6 = 3.0 \times 10^{-11}$
$FeN_2^+ + O \longrightarrow FeO^+ + N_2$	$k_7 = 5.0 \times 10^{-11}$
$Fe^+ + O_3 \longrightarrow FeO^+ + O_2$	$k_8 = 7.6 \times 10^{-10}e^{-240.5/T}$
$FeO_2^+ + e^- \longrightarrow Fe + O_2$	$k_9 = 3.0 \times 10^{-7}(200/T)^{0.5}$
$FeN_2^+ + e^- \longrightarrow Fe + N_2$	$k_{10} = 3.0 \times 10^{-7}(200/T)^{0.5}$
$Fe^+ + O_2 + M \longrightarrow FeO_2^+ + M$	$k_{11} = 8.3 \times 10^{-30}(T/300)^{-1.86}$
$Fe^+ + N_2 + M \longrightarrow FeN_2^+ + M$	$k_{12} = 4.0 \times 10^{-30}(T/300)^{-1.52}$
$Fe^+ + O + M \longrightarrow FeO^+ + M$	$k_{13} = 2.5 \times 10^{-30}$
$Fe + O_3 \longrightarrow FeO + O_2$	$k_{14} = 2.94 \times 10^{-10}e^{-174/T}$
$FeO + O \longrightarrow Fe + O_2$	$k_{15} = 4.6 \times 10^{-10}e^{-350/T}$
$FeO + O_3 \longrightarrow FeO_2 + O_2$	$k_{16} = 3.0 \times 10^{-10}e^{-177/T}$
$FeO + O_2 + M \longrightarrow FeO_3 + M$	$k_{17} = 4.41 \times 10^{-30}e^{(T/200)^{0.606}}$
$FeO_2 + O \longrightarrow FeO + O_2$	$k_{18} = 1.4 \times 10^{-10}e^{580/T}$
$FeO_2 + O_3 \longrightarrow FeO_3 + O_2$	$k_{19} = 4.4 \times 10^{-10}e^{-170/T}$
$FeO_3 + O \longrightarrow FeO_2 + O_2$	$k_{20} = 2.3 \times 10^{-10}e^{-2310/T}$
$FeO_3 + H_2O \longrightarrow Fe(OH)_2 + O_2$	$k_{21} = 5.0 \times 10^{-12}$
$FeO + H_2O + M \longrightarrow Fe(OH)_2 + M$	$k_{22} = 5.0 \times 10^{-28}e^{(200/T)^{1.13}}$
$Fe(OH)_2 + H \longrightarrow FeOH + H_2$	$k_{23} = 3.3 \times 10^{-10}e^{-302/T}$
$FeO_3 + H \longrightarrow FeOH + H_2O$	$k_{24} = 3.0 \times 10^{-10}e^{-796/T}$
$FeOH + H \longrightarrow Fe + H_2O$	$k_{25} = 3.0 \times 10^{-10}e^{-1264/T}$
$FeOH + FeOH \longrightarrow (FeOH)_2$	$k_{26} = 9.0 \times 10^{-10}$

The changes of the concentrations of reactant A and product C can be described by ordinary differential equations (ODEs):

$$\begin{cases} \frac{dA}{dt} = -k_1 \cdot A \cdot B + k_2 \cdot C \cdot E \\ \frac{dC}{dt} = k_1 \cdot A \cdot B - k_2 \cdot C \cdot E \end{cases}$$

Given the initial values of A, B, C and E, the ODEs provide exact solutions of A and C as the function of time, t. Note that, reaction equations 3.40 and 3.41 are not a closed system. B and E are ambient environmental species decreasing as the reactions going on, and accumulating D, F,

TABLE 3.4: Molecular Chemical Reactions.

Reaction	Rate Coefficient[a]
$NO^+ + e^- \longrightarrow N + O$	$k_{27} = 2.3 \times 10^{-7}(300/T_e)^{0.5}$
$O_2^+ + e^- \longrightarrow O + O$	$k_{28} = 1.9 \times 10^{-7}(300/T_e)^{0.5}$
$N_2^+ + e^- \longrightarrow N + N$	$k_{29} = 3.5 \times 10^{-7}(300/T_e)^{0.5}$
$O^+ + N_2 \longrightarrow NO^+ + N$	$k_{30} = 2.78 \times 10^{-13} e^{2.07(T_f/300)^{-1} - 0.61(T_f/300)^{-2}}$
$O^+ + O_2 \longrightarrow O_2^+ + O$	$k_{31} = 3.33 \times 10^{-12} e^{3.72(T_f/300)^{-1} - 1.87(T_f/300)^{-2}}$
$O_2^+ + NO \longrightarrow NO^+ + O_2$	$k_{32} = 4.4 \times 10^{-10}$
$O_2^+ + N_2 \longrightarrow NO^+ + NO$	$k_{33} = 5.0 \times 10^{-16}$
$N_2^+ + O \longrightarrow NO^+ + N$	$k_{34} = 1.4 \times 10^{-10}(\frac{600}{T_i+T_n})^{0.44}$
$N_2^+ + O \longrightarrow O^+ + N_2$	$k_{35} = 1.0 \times 10^{-11}(\frac{600}{T_i+T_n})^{0.23}$
$N_2^+ + O_2 \longrightarrow N_2 + O_2^+$	$k_{36} = 6.0 \times 10^{-11}$
$O^+ + CO_2 \longrightarrow O_2^+ + CO$	$k_{37} = 9.0 \times 10^{-10}$
$O_2^+ + N \longrightarrow NO^+ + O$	$k_{38} = 1.0 \times 10^{-10}$
$N^+ + O_2 \longrightarrow O_2^+ + N$	$k_{39} = 4.0 \times 10^{-10}$
$N^+ + O_2 \longrightarrow NO^+ + O$	$k_{40} = 2.0 \times 10^{-10}$
$N^+ + O \longrightarrow O^+ + N$	$k_{41} = 1.0 \times 10^{-12}$
$O^+ + NO \longrightarrow NO^+ + O$	$k_{42} = 8.36 \times 10^{-13} - 2.02 \times 10^{-13}\frac{T_f}{300} + 6.95 \times 10^{-14}(\frac{T_f}{300})^2$
$O^+ + e^- \longrightarrow O + h\nu$	$k_{43} = 7.8 \times 10^{-14}(300/T_e)^{0.5}$
$N_2 + h\nu \longrightarrow N_2^+ + e^-$	k_{44} see in text
$O_2 + h\nu \longrightarrow O_2^+ + e^-$	k_{45} see in text
$O + h\nu \longrightarrow O^+ + e^-$	k_{46} see in text

k_1,	*Nahar et al.* [1997];
k_2, k_9, k_{24}, k_{25},	*Plane et al.* [1999];
k_3, k_4,	*Rutherford and Vroom* [1972];
k_5, k_7,	*Rollason and Plane* [1998];
k_6,	*Woodcock et al.* [2006];
k_8, k_{16}, k_{17}, k_{22},	*Rollason and Plane* [2000];
k_{10}, k_{14},	*Helmer et al.* [1998];
k_{11}, k_{12},	*Vondrak et al.* [2006];
k_{13},	*Brown* [1973];
k_{15}, k_{18}, k_{19}, k_{20}, k_{21},	*Self and Plane* [2003];
k_{23},	*Jensen and Jones* [1974];
k_{27}, k_{28}, k_{29},	*Mul and McGowen* [1979];
k_{30}, k_{31},	*Chen et al.* [1978];
k_{32},	*Lindenger and Ferguson* [1983];
k_{34},	*McFarland et al.* [1974];
k_{36},	*McFarland et al.* [1973];
k_{38}	*Fehsenfeld* [1973];
k_{39}, k_{40},	*Langford et al.* [1985],
k_{41},	*Torr* [1985];
k_{42},	*Maurice and Torr* [1978].

which are purely products.

This methodology can also be applied to a complex system. In our model, we solve Fe chemistry, and molecular ions chemistry in the E-F region. For the sake of convenience, we define, $\mathbf{R_{Fe}}$ = (Fe, Fe^+, FeO, FeO^+, FeO_2, FeO_2^+, FeN_2^+, FeO_3, $Fe(OH)_2$, $Fe(OH)$). The changes of ($\mathbf{R_{Fe}}$, NO^+, N_2^+, N^+, N, O_2^+, O^+) are given by the sum of the losses and productions caused by chemical reactions in the Tables 3.3 and 3.4, which can be described by a set of ODEs (equation 3.42 – 3.49). The chemical reactions and corresponding rate coefficients are shown in Table 3.3 and 3.4.

The right-hand side (RHS) of the ODEs, equations 3.42 – 3.49, represents the net rate, which is the sum of production and loss rate of the species. The RHS is the function of reaction rate coefficients and the number density of reactants, leading to a coupled nonlinear system of ODEs. In general, there is no analytical solution for the ODEs, equation 3.42 – 3.49, but numerical method can be applied for approaching the true solution. The numerical solution of equations 3.42 – 3.49 is discussed in the Appendix C.

In our model, chemistry is a partially closed system. The $\mathbf{R_{Fe}}$, and other species NO^+, O_2^+, O^+, N_2^+ are a closed system. It means that the total number density of Fe element, which is the sum of element Fe in each species, is conservative. In other words, $\frac{dFe}{dt} + \frac{dFe^+}{dt} + \frac{dFeO}{dt} + \frac{dFeO^+}{dt} + \frac{dFeO_2}{dt} + \frac{dFeO_2^+}{dt} + \frac{dFeN_2^+}{dt} + \frac{dFeO_3}{dt} + \frac{dFeOH}{dt} + \frac{dFe(OH)_2}{dt} = 0$. Therefore, if we provide the initial conditions of $\mathbf{R_{Fe}}$, NO^+, O_2^+, O^+ and N_2^+, our chemical model is able to compute the density change of $\mathbf{R_{Fe}}$, NO^+, O_2^+, O^+ and N_2^+ without any mass loss or gain. However, there are several other species that are not in this closed system. Therefore, we need to specify the concentrations of these species by other means at each time step. For minor species, like O, O_3, H, OH, H_2O, CO_2 are constrained by the outputs of TIME-GCM, and the major species, like O_2 and N_2 are

constrained by the MSIS model, and N^+ is from the IRI model.

$$\frac{dFe}{dt} = R_1(\mathbf{R_{Fe}}, NO^+, N_2^+, N^+, N, O_2^+, O^+) \qquad \frac{dFe^+}{dt} = R_2(\mathbf{R_{Fe}}, NO^+, N_2^+, N^+, N, O_2^+, O^+) \tag{3.42}$$

$$\frac{dFeO}{dt} = R_3(\mathbf{R_{Fe}}, NO^+, N_2^+, N^+, N, O_2^+, O^+) \qquad \frac{dFeO^+}{dt} = R_4(\mathbf{R_{Fe}}, NO^+, N_2^+, N^+, N, O_2^+, O^+) \tag{3.43}$$

$$\frac{dFeO_2}{dt} = R_5(\mathbf{R_{Fe}}, NO^+, N_2^+, N^+, N, O_2^+, O^+) \qquad \frac{dFeO_2^+}{dt} = R_6(\mathbf{R_{Fe}}, NO^+, N_2^+, N^+, N, O_2^+, O^+) \tag{3.44}$$

$$\frac{dFeN_2^+}{dt} = R_7(\mathbf{R_{Fe}}, NO^+, N_2^+, N^+, N, O_2^+, O^+) \qquad \frac{dFeO_3}{dt} = R_8(\mathbf{R_{Fe}}, NO^+, N_2^+, N^+, N, O_2^+, O^+) \tag{3.45}$$

$$\frac{dFe(OH)_2}{dt} = R_9(\mathbf{R_{Fe}}, NO^+, N_2^+, N^+, N, O_2^+, O^+) \qquad \frac{dFeOH}{dt} = R_{10}(\mathbf{R_{Fe}}, NO^+, N_2^+, N^+, N, O_2^+, O^+) \tag{3.46}$$

$$\frac{dNO^+}{dt} = R_{11}(\mathbf{R_{Fe}}, NO^+, N_2^+, N^+, N, O_2^+, O^+) \qquad \frac{dN_2^+}{dt} = R_{12}(\mathbf{R_{Fe}}, NO^+, N_2^+, N^+, N, O_2^+, O^+) \tag{3.47}$$

$$\frac{dN^+}{dt} = R_{13}(\mathbf{R_{Fe}}, NO^+, N_2^+, N^+, N, O_2^+, O^+) \qquad \frac{dN}{dt} = R_{14}(\mathbf{R_{Fe}}, NO^+, N_2^+, N^+, N, O_2^+, O^+) \tag{3.48}$$

$$\frac{dO_2^+}{dt} = R_{15}(\mathbf{R_{Fe}}, NO^+, N_2^+, N^+, N, O_2^+, O^+) \qquad \frac{dO^+}{dt} = R_{16}(\mathbf{R_{Fe}}, NO^+, N_2^+, N^+, N, O_2^+, O^+) \tag{3.49}$$

For instance, $R_1(\mathbf{R_{Fe}},, NO^+, N_2^+, N^+, N, O_2^+, O^+)$ is given by equation 3.50,

$$\begin{aligned} R_1(\mathbf{R_{Fe}}, NO^+, N_2^+, N^+, N, O_2^+, O^+) = {} & k_1[Fe^+][e^-] + k_2[FeO^+][e^-] + k_9[FeO_2^+][e^-] \\ & + k_{10}[FeN_2^+] + k_{15}[FeO][O] + k_{25}[FeOH][H] \\ & - k_3[Fe][NO^+] - k_4[Fe][O_2^+] - k_{14}[Fe][O_3] \end{aligned} \tag{3.50}$$

where k_i is the reaction rate coefficients, and $[M]$ are the number density of the species 'M'.

3.2.6 Mass transport by the divergence of $N_M\vec{V}_M$

The divergence term $\nabla \cdot (N_M\vec{V}_M)$ in equation 3.1 represent the density change rate associated with the number density transport $N_M\vec{V}_M$. It describes the number density flowing in and out of a grid cell, and can be decomposed into vertical and horizontal in-out. Therefore $\nabla \cdot (N_M\vec{V}_M)$ is written

as equation 3.51:

$$\begin{aligned}\nabla \cdot (N_m \vec{V}_M) &= \vec{V}_M \cdot \nabla N_m + N_m \nabla \cdot \vec{V}_M \\ &= V_h \nabla_h N_m + N_m \nabla_h \cdot \vec{V}_h + V_z \frac{\partial N_m}{\partial z} + N_m \frac{\partial V_z}{\partial z}\end{aligned} \tag{3.51}$$

A 3-D model is required to fully calculate the mass flux. However, for the primary interests of this thesis, a 3-D model is non-essential. The equation 3.51 can be numerically resolved by taking one assumption: If the horizontal gradient of N_m is negligible, then $\nabla_h N_m \approx 0$, and equation 3.51 becomes,

$$\nabla \cdot (N_m \vec{V}) \approx \frac{\partial (N_m V_z)}{\partial z} + N_m \nabla_h \cdot \vec{V}_h \tag{3.52}$$

In sections 3.2.1 and 3.2.2, we have provided the solutions of the vertical velocities of ions and neutral Fe, respectively. For neutral Fe, $\nabla_h \cdot \vec{V}_{Fe,h}$ is equal to the divergence of horizontal winds of background atmosphere ($\nabla_h \cdot \vec{V}_{n,h}$); for ions like Fe^+, $\nabla_h \cdot \vec{V}_{i,h}$ is approximated by $\frac{\xi^2}{1+\xi^2} \nabla \cdot \vec{V}_{n,h}$. Details of derivations are provided in Appendix E. Under the most of circumstances, there is no explicit solution for $\nabla_h \cdot \vec{V}_{n,h}$. However $\nabla_h \cdot \vec{V}_{n,h}$ can be parametrized by the vertical winds or other known parameters of gravity waves, therefore this 1-D model can numerically resolve the equation 3.52.

3.3 Numerical Modeling Developments

The numerical modeling of thermospheric neutral Fe layer is based on the mathematical model described in section 3.2. The establishment of the numerical framework is inspired by the comprehensive model developed by *Carter and Forbes* [1999]. The model includes the key processes, such as meteoric source, ion transport, and chemical reactions. One of our primary focuses is the

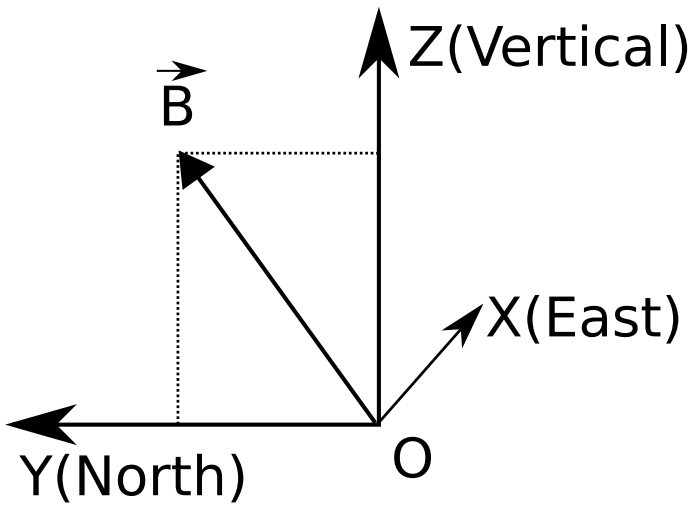

FIGURE 3.6: Coordinates system used in our model. North indicates geomagnetic north, and east is geomagnetic east, vertical is perpendicular to sea level.

metallic Fe^+ ions and neutral Fe atoms. Our purpose of the numerical modeling is to investigate the mechanism of forming neutral thermospheric Fe layers at polar region. The development of our model will carefully address both neutral atomic Fe and atomic ions Fe^+ model, at the same time, adapt the mid-/low-latitude electrodynamics in *Carter and Forbes* [1999] to high-latitude region.

The numerical model framework is built upon a right-handed Cartesian coordinate system with geomagnetic east, geomagnetic north and vertical up (Figure 3.6), which is common practice when dealing with geomagnetic field [e.g., *Mathews*, 1998; *Carter and Forbes*, 1999]. Taking the configuration of vertical lidar beam, the numerical model is built along the one-dimensional vertical direction consisting of a stack of grids with different spacing extending vertically from 90 to 600 km. As illustrated in Figure 3.7, the cell grid is set to the highest resolution of 0.5 km in the E–F region (90–200 km) covered by lidar measurements, and then to 1 km between 200 and 300 km, and finally to 5 km above 300 km. Above 600 km, we set up a stack of ghost cells with 20 km grid size from 600 km to 900 km.

The core of the numerical model consists of three main modules: Ultimate source of Fe^+

and Fe, vertical transport, and chemical reactions (see Figure 3.7b). The density change in each grid is caused by chemical reactions (Q and L terms in equation 3.1) and mass exchange between two adjacent grids in the vertical direction (the transport term in equation 3.1). An ideal sink is applied at the lower boundary, by which the Fe/Fe^+ are permanently removed from the modelled regions if the mass flux is downward at the bottom boundary. A similar treatment is applied to the top boundary when the mass flux is upward. Since the real top boundary is 900 km, in most the simulations the ions would not be able to reach 900 km so that the number density of ions are greatly conserved due to the transport. The source term S in equation 3.1 coming from direct meteor deposition, which is based on the model results developed by Plane and his co-workers [*Vondrak et al.*, 2008; *Feng et al.*, 2013]. We take the outputs from other models to set up the atmospheric and ionospheric parameters.

The chemical processes for the 1-D runs included 26 chemical reactions involving Fe species, 16 reactions about the ambient ions. Section 3.2 provides mathematical description of the model, solving for ion motion explicitly and building up mathematical model for chemistry. Section 3.3.1 introduces the numerical methodology used to solve the mass transport and the chemical reactions in the model. Section 3.3.2 briefly describes the external models providing the ambient neutral and ionospheric environment parameters, empirical electric field, neutral wind, and ionization rate. In section 3.3.3, we introduced the set-up for running the simulation and computational flow of the model.

3.3.1 Numerical methodology

Mathematically, our model also can be written as another form, advection-diffusion-reaction(ADR) model whose system governing equation is [*Fazio and Jannelli*, 2009],

$$\frac{\partial \mathbf{c}}{\partial t} = A(\mathbf{c}) + D(\mathbf{c}) + R(\mathbf{c}) \tag{3.53}$$

where $\mathbf{c} = \mathbf{c}(\mathbf{x}, t)$, $\mathbf{x}$ are the space variables and t denote the time. $A(\mathbf{c})$ is the advection term, $D(\mathbf{c})$ is diffusion term, and $R(\mathbf{c})$ is reaction term. We use the Strang splitting [*Strang*, 1968] approach: if $\mathbf{c^n}$ is the approximate solution at time t^n, we obtain the solution $\mathbf{c^{n+1}}$ at next time $t^{n+1} = t^n + \Delta t$ by the following sequence of steps:

$$\mathbf{c^{n+1}} = \mathbb{T}(\Delta t/2)\mathbb{R}(\Delta t/2)\mathbb{T}(\Delta t/2)\mathbf{c^n} \tag{3.54}$$

where $\mathbb{T}(\cdot)$ representing the product of $\mathbb{A}(\cdot)\mathbb{D}(\cdot)$ is discretized transport operator, $\mathbb{R}(\cdot)$ represents reaction operator, respectively. The advantages of the fractional step method is that a different time integration method can be chosen [*Fazio and Jannelli*, 2009]. The reaction part is sometimes very stiff and it requires the use of implicit methods. By using the splitting technique we can achieve higher order accuracy if each sub problem is solved by higher order accurate method.

Finite volume methods (FVM) is applied for the discretization of the continuity equation 3.1; for a detailed description see e.g. *Eymard et al.* [2001]. Finite volume methods are based on the integral formulation, i.e., the mass conservation law is integrated over a disjunct set of control volumes covering the domain. For 1-D model, the cellar geometry is a single stack of cells forming a cylindrical volume in height, with the bottom cell's midpoint at 90 km, and top cell at 600 km,

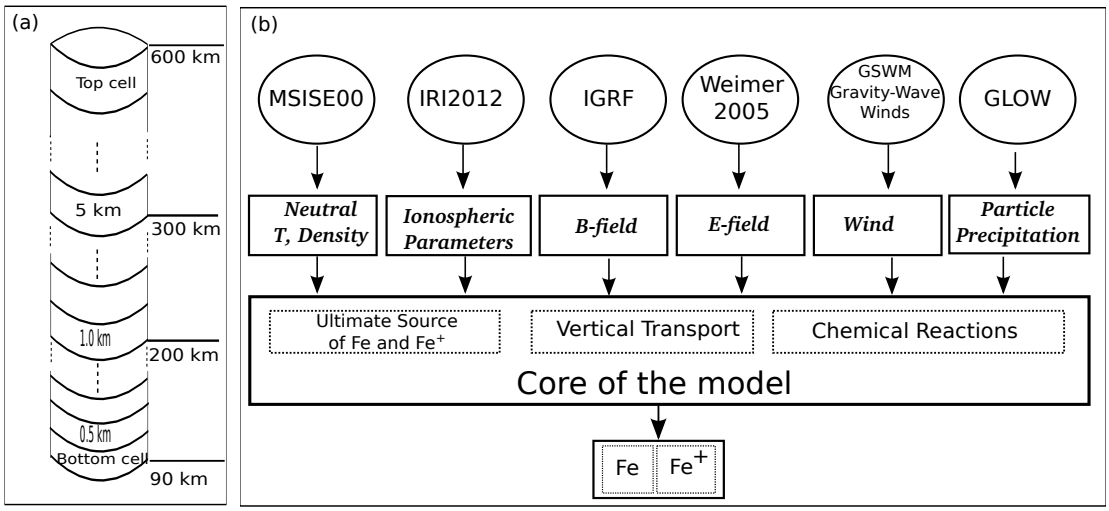

FIGURE 3.7: Finite volume cell geometry of schematic of 1-D cell configuration (single vertical stack).

as shown in Figure 3.7. Currently, we are interested in the geographic location of the cellular stack at McMurdo.

For 1-D model, the discretization of the equation 3.1 is

$$\frac{\Delta n}{\Delta t} = \frac{1}{2}\Delta n_{Transport} + \Delta n_{chemistry} + \frac{1}{2}\Delta n_{Transport} \tag{3.55}$$

where $\Delta n_{chemistry}$ is the density change caused by the chemical reactions, and $\Delta n_{Transport}$ is the density change caused by vertical mass flux. Chemical and transport processes are calculated separately, following the sequence of steps in equation 3.54. For each cell, the chemical production and loss are calculated independently, and transport mass flux happens between cells.

Numerical solution of transport For the first term $\frac{\partial(N_m V_z)}{\partial z}$ in equation 3.52, *Carter* [1995] provided the numerical solution of the transport term in equation 3.55, which is calculated by the

mass flux across the cell in z directions ,

$$\Delta N_m = \frac{\Delta \Phi_z}{\Delta z} \Delta t \tag{3.56}$$

$$= (\Phi_{z1} - \Phi_{z2}) \frac{\Delta t}{\Delta z} \tag{3.57}$$

$$= (\Phi_{z1} - \Phi_{z2}) \frac{A \Delta t}{\Delta V} \tag{3.58}$$

where $\Phi_z = N_m V_z$, z_1 and z_2 are the low and upper boundaries, respectively. A and V are the boundary area and volume parameters. The velocity vector is given by equation 3.12. In Cartesian coordinates, the vertical velocities is provided by equations (3.13) – 3.15.

However this low-order algorithm experiences strong numerical diffusion [*Durran*, 2010], which would lead to unrealistic conditions of wind or electric fields in order to form these converged layers. In order for the model to deal with converged layers that can evolve to sporadic layers of high Fe^+ concentration within one or two kilometers, we need to resolve the issue caused by numerical diffusion. We employ the flux corrected transport (FCT) technique [*Zalesak*, 1979] in the transport module to resolve the numerical diffusion issue so that the flow of ions can be modelled accurately. FCT is an algorithm originally designed for mass transportation to handle steep gradients of mass densities, as well as shock formation [*Boris and Book*, 1973]. It combines a high-order solution to cancel out the diffusive errors and a low-order solution limiting the anti-diffusive fluxes to maintain positivity through the use of flux limiter. We use a non-clipping flux limiters proposed by [*Zalesak*, 1979] in our model. The details of the FCT algorithm are provided in Appendix D.

The second term $N_m \nabla_h \cdot \vec{V}_h$ is associated with the horizontal divergence of horizontal winds. For irregular horizontal winds, our 1-D Fe/Fe^+ model doesn't have the capability to numerically resolve this term because $N_m \nabla_h \cdot \vec{V}_h$ describes the mass exchange in horizontal direction. But for the wave-induced horizontal winds, we can parametrize the term $\nabla_h \cdot \vec{V}_h$ to offset the density changes

caused by the divergence of horizontal winds. The parametrization highly varies from case to case. For example, for simulating the case with tidal winds, $\nabla_h \cdot \vec{V}_h$ can be set to zero because horizontal tidal winds are relatively homogeneous for a single location. For simulating much smaller scale waves, for instance gravity waves, the term of $\nabla_h \cdot \vec{V}_h$ caused by gravity waves cannot be neglected. In Chapter 5, the parametrization of $\nabla_h \cdot \vec{V}_h$ is provided.

To conclude, the procedure of computing mass transport is:

1. First, compute the mass transport in vertical direction with FCT method:

$$N_*^{t+\Delta t} = \mathbb{T}(N_i^t) \tag{3.59}$$

2. Second,correct the mass change with the divergence of horizontal winds:

$$N_i^{t+\Delta t} = \frac{N_*^{t+\Delta t}}{1 + \Delta t \cdot \nabla_h u_h} \tag{3.60}$$

Numerical solution of chemistry reactions In this new model, we propose a new chemical scheme. Given the initial condition ($\mathbf{R_{fe}}$, NO^+, N_2^+, N^+, N, O_2^+, O^+)$_t$ at time t, the new chemical scheme will solve the ODEs 3.42 $\sim$ 3.49 via backward differentiation formulas for time-stepping, which provides the solution at $t + \Delta t$, ($\mathbf{R_{fe}}$, NO^+, N_2^+, N^+, N, O_2^+, O^+)$_{t+\Delta t}$.

To illustrate backward differentiation formula (BFD) method, a general procedure of BFD is introduced here. Letting $\boldsymbol{C} = (\mathbf{R_{fe}}, NO^+, N_2^+, N^+, N, O_2^+, O^+)$, then equation 3.42 $\sim$ 3.49 can be written as a simplified format,

$$\frac{\boldsymbol{dC}}{\boldsymbol{dt}} = \boldsymbol{f(C, t)} \tag{3.61}$$

where $\boldsymbol{C}$ and $\boldsymbol{f}$ are column vectors. $\boldsymbol{f}$ is a nonlinear function of the unknown variable $\boldsymbol{C}$. Suitable solvers for stiff problems are all implicit time-difference approximations, which can also be applied to nonlinear differential equations that generate nonlinear algebraic equations. For example, we can discretize equations 3.61 using Backward-Euler method, letting $\boldsymbol{\phi_n}$ be the numerical approximation to $\mathbf{C}(n\Delta t)$, we obtain

$$\boldsymbol{\phi_{n+1}} = \boldsymbol{\phi_n} + \boldsymbol{\Delta t f}(\boldsymbol{\phi_{n+1}}) \tag{3.62}$$

Non-linear equations (3.62) can be solved by iterative method. For example, given the initial conditions, $\boldsymbol{\phi_t}$, using Newton's iterative method, we can solve the preceding equation for $\boldsymbol{\phi_{t+\Delta t}}$ at time step, $t + \Delta t$. By using iterative method, we can achieve the desired accuracy, but it also takes more time to do iteration to find a set of solution within the desired accuracy. It also brings in more difficulties in code implementation. Fortunately, we have numerous standard solvers providing reasonable solutions for the nonlinear system like equation 3.42 – 3.49. MATLAB solver ODE15s and FORTRAN solver DDASPK [*Brown et al.*, 1994] are specifically designed for large-scale differential-algebraic systems.

To solve the ODEs 3.42 $\sim$ 3.49, we adopt an algorithm for large systems of differential algebraic equations (DAEs) – the DASPK solver [*Brown et al.*, 1994]. Due to the complexity of Fe/Fe^+ and related molecule and ion chemistry with many orders magnitude differences in reaction rates, the numerical solutions of Fe/Fe^+ chemistry equations could be very stiff. DASPK solves the stiff DAEs via backward differentiation formula with the Krylov method [*Brown et al.*, 1994]. It solves the nonlinear systems at each time step via Newton iteration. If the solutions do not converge, the DASPK solver will automatically reduce the time step until the solutions of chemistry equations can converge to desired accuracy. An advantage of using such chemical reaction solver is that the solutions are independent of the sequence order of chemical reactions listed in the module.

More detailed discussion of numerical solution of chemistry reaction is provided in the Appendix C

3.3.2 The external models

The model is focusing on the transport and chemistry of ions and molecules related to Fe/Fe^+, and is not a self-consistent model that is of the capability to resolve all the atmospheric, ionospheric and electrodynamical parameters. We choose to input the background parameters from external sources instead of self-consistently modeling of all parameters. Furthermore, Fe species are minor constituents in the upper atmosphere. For example, the peak number density of main Fe layers distributed between 70 and 100 km is usually 8th order less than atmosphere density or even lower [*Chu et al.*, 2011]. Density of Fe^+ usually is less than 10% of electron density above 100 km [*Kopp et al.*, 1997]. Therefore, the feedback of Fe and Fe^+ to the background neutral and ionized atmosphere is negligible. Only under a few circumstances like sporadic E layers, Fe^+ could be dominant in a thin layer because in such cases most NO^+ and O_2^+ have neutralized by converged electrons. Therefore, the use of stand-alone models for external inputs would be necessary to produce environmental data: neutral temperature, plasma temperature, neutral an ionic composition and densities, electric field, geomagnetic field, and neutral winds.

The neutral atmosphere: MSISE-00 The MSISE model is the empirical atmospheric model, describing the neutral temperature and densities in Earth's atmosphere from ground to thermosphere. Below 72.5 km, for MSIS-86, the measurements from pitot tube, falling sphere, pressure gauge, grenade sounde, rocket from 1947 to 1972 were taken into consideration. MSISE-90 [*Hedin*, 1991] revised MSIS-86 model by taking into account data derived from space shuttle flights, newer incoherent scatter radar, and satellite-borne data. In this study, we are using the latest generation of MSISE model, NRLMSISE-00. The new NRLMSISE-00 mainly upgraded the MSISE-90 in

thermosphere [*Picone et al.*, 2002]. The new model took advantages of the new database, including the following data: (1) total mass density measurements from satellite accelerometers, (2) newer temperature measurements from 1981–1997 by incoherent scatter radar, (3) new measurements of $[O_2]$ number density from SMM mission. The MSIS model is sensitive to the level of geomagnetic activity. F10.7 and A_p index can be set to the values for desired geomagnetic activity levels, from quiet to magnetic storm case.

The ionosphere: IRI-2012 The International Reference Ionosphere (IRI) is an international project sponsored by the Committee on Space Research (COSPAR) and the International Union of Radio Science (URSI). The database used by IRI is from the measurements of worldwide network of ionosondes, incoherent scatter radars, the ISIS and Alouette topside sounders, and in situ instruments on several satellites and rockets. IRI provides monthly averages of the electron density, electron temperature, ion temperature, and ion composition in the altitude from 50 km to 2000 km. IRI is updated yearly with newer data and better modeling techniques, leading to a series of key editions of the model version such as the IRI-78 [*Rawer et al.*, 1978], IRI-85 [*Bilitza*, 1986], IRI-1990 [*Bilitza*, 1990], IRI-2000 [*Bilitza*, 2001], and IRI-2007 [*Bilitza and Reinisch*, 2008]. The newest version of the IRI model, IRI-2012, which is the newer version of IRI-2011. There have not been any literature's introducing the upgrades of IRI-2012. For IRI-2011, it includes significant improvements of representations of electron density, electron temperature and ion composition (O^+, H^+, He^+, NO^+, O_2^+) [*Biliza et al.*, 2011]. IRI-2012 is used in our simulation.

The electric field: Weimer 2005 Polar regions have relatively complex geomagnetic environments, which are directly impacted by the activities of magnetosphere. The electric fields play fundamental roles in the ionospheric dynamics. The electric fields in the ionosphere over polar caps

are originated from solar-wind-induced convections in the magnetosphere and the dynamo effect in the lower thermosphere, showing large spatial and temporal variations [*Richmond*, 1995]. We utilize the empirical electric potential model of *Weimer* [2005] to set up the convection electric field, which is taken as external electric field in our model.

Weimer 2005 is a statistical electric potential model for the high-latitude ionosphere, developed by Daniel Weimer [*Weimer*, 2005]. This improved empirical model is based on satellite measurements of ionospheric electric fields, and simultaneous measurements of solar wind and interplanetary field (IMF) conditions. The model is constructed using spherical harmonic functions within a small area at the pole, and multiple Fourier series functions of longitude at lower latitudes based on the electric and magnetic field measurements obtained from the Dynamics Explorer 2 satellite, which operated between August 1981 and March 1983 in a polar orbit 300–1000 km [*Hoffman and Schmerling*, 1981]. The performance of the new electric potential estimated by the improved model showed good agreement with the satellite measurements by the instruments on the DMSP spacecraft [*Weimer*, 2005] by taking advantage of more accurate field values, more accurate boundary locations, and better reproduction of nonlinear saturation effects in the solar wind-magnetosphere coupling. However, because of the temporal resolution, the model cannot provide good predictions at different MLT locations when there are sudden IMF changes, and also cannot show the changes in the ionosphere when there are sudden changes in the solar wind. For the sake of our numerical simulations, this model is suitable for providing realistic electric fields under the circumstance of different levels of geomagnetic activity.

Weimer 2005 provides high-latitude electric potentials and magnetic field-aligned currents (FAC) as a function of the solar wind parameters, but does not give the electric field directly, which can be calculated by equation $\vec{E} = -\nabla_s \Phi$, where ∇_s is the "surface gradient" in geomagnetic

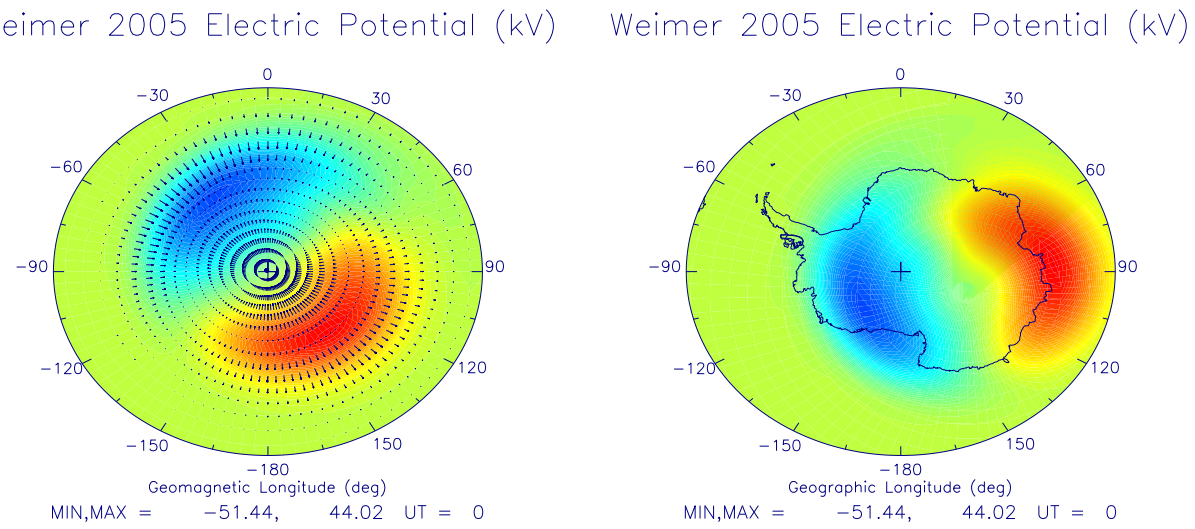

FIGURE 3.8: The contour are electric potentials output from Weimer 2005. The blue color means negative potentials, and red color are positive potentials. The IMF has a fixed magnitude of b_z = -5 nT, b_y = 0 nT, the solar wind velocity is 450 km s^{-1}, the solar wind the density is 4 cm^{-3}, and the dipole tilt angle is 0 degree. The left plot is under geomagnetic coordinates, the vectors represent the electric field. The right plot is under geographic coordinates.

coordinate frame, and Φ is the electric potentials. Two examples are illustrated in Figure 3.8. The components of electric potential are driven either by magnetosphere or dynamo in the lower thermosphere, which are uncorrelated to solar wind and IMF, are not included. The irregularly dynamo-generated electric fields on the order of 3 mV/m or and lower are one magnitude smaller than that of the convection electric fields, thus are neglected in the Weimer-2005 model. The perturbations of electric field associated with plasma irregularities are neglected as well.

One of the input parameters of Weimer-2005 model is magnetic local time (MLT), which can be calculated by equation 3.63

$$MLT = \frac{24}{2\pi}(\phi_m - \phi_0) \pm 24n \tag{3.63}$$

where MLT in *hours*, the magnetic longitude ϕ in *radians*, and ϕ_0 is defined by the night-side dipole

longitude of Sun-Earth line, where MLT is 0 hr. ϕ_m is the magnetic longitude of the location. n is an arbitrary integer.

Within ± 20 *mins* approximation, the MLT can simplified as equation 3.64

$$MLT = UT + \frac{\phi_m^\circ - 70^\circ}{15^\circ} \pm 24n \tag{3.64}$$

Aurora: GLOW The global airglow model (GLOW) model is an energetic electron transport and energy deposition model providing ionization and excitation rates, energetic electron production and transport, excited species densities, and air-glow emission rates for the terrestrial thermosphere [*Solomon et al.*, 1988; *Bailey et al.*, 2002]. The GLOW model was developed to analyse and explain O^1D airglow emission in the Earth's thermosphere [*Solomn and Abreu*, 1989]. Using two-stream algorithm [*Banks and Nagy*, 1970; *Nagy and Banks*, 1970; *Banks et al.*, 1974], the GLOW simulates the energetic electrons (photoelectrons, secondary electrons, and precipitated electrons) flux, and this approach was validated by the comparison with measurements [*Solomon et al.*, 2001]. For the problem at hand we consider the production rates of NO^+ and O_2^+ after auroral energetic electrons deposition. The GLOW model can handle both photoelectrons and auroral electrons simultaneously. The computer code is available online (*http://download.hao.ucar.edu/pub/stans/glow/*).

The input electron spectra of the GLOW is generated by the equations 3.65 [*Meier et al.*, 1989], distribution $\Phi(E)$, including the low-energy tail, is:

$$\Phi(E) = \Phi_M(E) + 0.4\Phi_{max}\frac{E_0}{E}e^{-E/b} \tag{3.65}$$

where E_0 is the characteristics energy. Let us designate $\Phi_M(E)$ by the Maxwellian distribution, so $\Phi_M(E)$ is given by equation 3.66,

$$\Phi_M(E) = \frac{Q}{2\pi E_0^3} E e^{-E/E_0} \tag{3.66}$$

where Q is the incident energy flux in unit $ergs\ cm^{-2}\ s^{-1}$. Φ_{max} in equation 3.65 is the maximum value of $\Phi_M(E)$ and b depends on E_0, given by equation 3.67

$$b = \begin{cases} (0.8E_0)^{-1} & E_0 < 0.5 \quad keV \\ (0.1E_0 + 0.35)^{-1} & E_0 \geq 0.5 \quad keV \end{cases} \tag{3.67}$$

Neutral Winds: gravity-wave or tidal winds For tidal winds input: wind fields are used tidal model incorporating solar diurnal and semi-diurnal forcing functions [*Forbes*, 1982a, 1982b; *Carter*, 1995; *Cater and Forbes*, 1999]. The gravity-wave winds are set up by forward modeling.

3.3.3 Computational flow of the model:

The framework of the model is the finite volume method. The differential equation was discretized in space and time domain. Each process was updated according to the set-up time intervals, and each process was synchronized in time with all other processes in the model. The spatial aspect of the problem was addressed by dividing the volume of interest into a network of cells. The cell must be small enough so that both chemical and transport processes can be treated as uniformas possible in the cell. Overall, as shown in Figure 3.9, the computation process can be summarized by 6 steps:

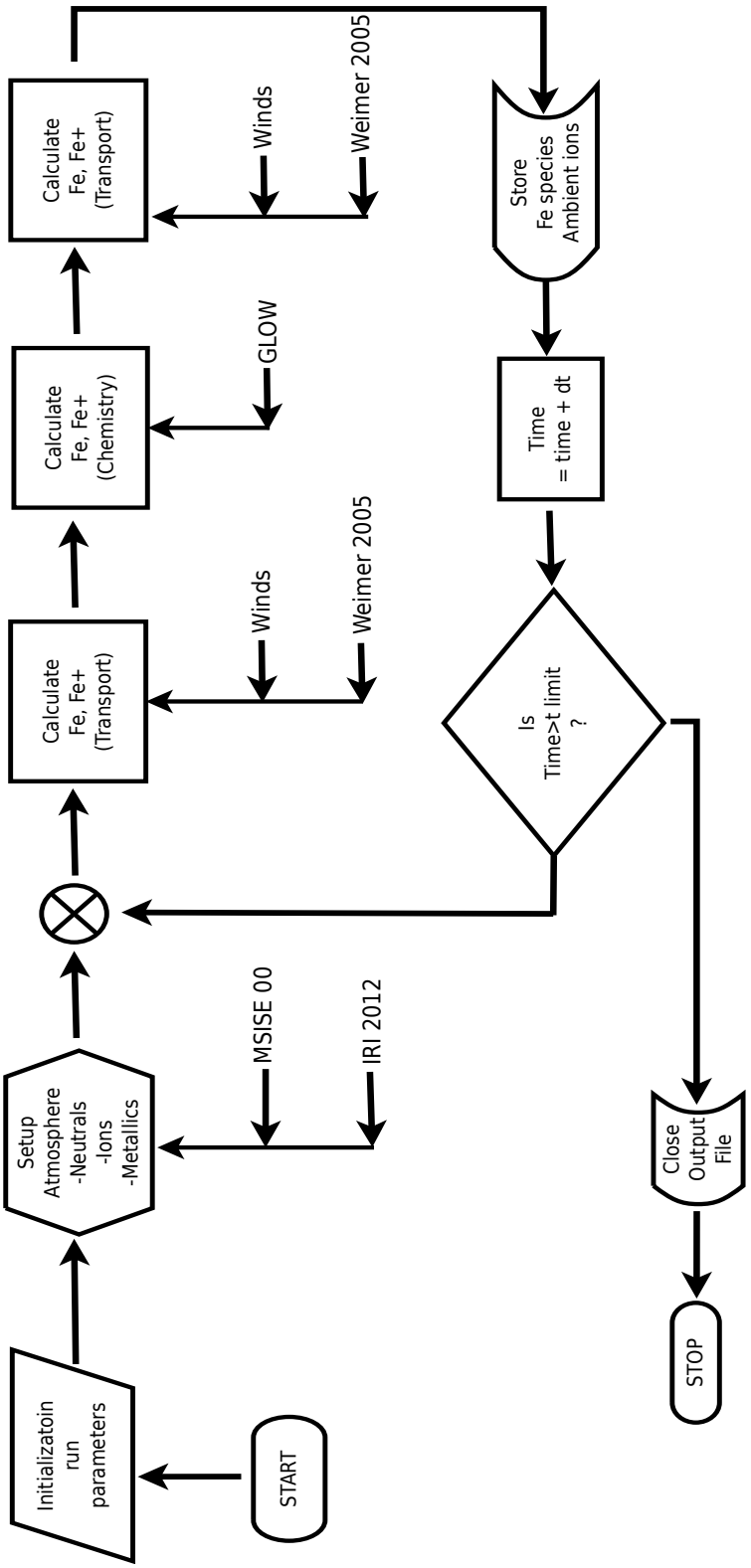

FIGURE 3.9: Simplified block diagram of computational flow.

1. Initialization: Read in specific run conditions, physical constants, cellular grid geometry, magnetic field parameters, winds, $\vec{E} \times \vec{B}$ scaling coefficients, etc.

   In 1-D mode, magnetic field is specified by IGR-11 model. The electric field model is adopted from *Richmond et al* [1980] for Arecibo, and *Weimer* [2005] for McMurdo station. The neutral winds are from the output of a tidal model, TIDE18V, which is a modified version of the *Forbes* [1982a, b] for the specific location, Arecibo. The tidal winds at McMurdo is specified by GSWM, and gravity-wave winds are set up by a forward model.

2. Initial set up of atmosphere: The background neutral and ionospheric parameters are called from external routines (MSIS00 and IRI2012), initialize metallic deposition sequence, call wind and electric field routines, set up associated velocity component arrays for later access by transport routine.

3. Transport: Call transport routine to calculate total velocities for ions and neutrals and use resultant flux values for the first half of time interval $\frac{\Delta t}{2}$. Update ion densities to time t + $\frac{\Delta t}{2}$.

4. Chemical reactions: given the initial densities of all species at t + $\frac{\Delta t}{2}$ from the last step, solve equation 3.42 – 3.49 by new chemical scheme, update ($\mathbf{R_{fe}}$, NO^+, N_2^+, N^+, N, O_2^+, O^+) densities to time t + Δt.

5. Transport: start from the last step, call transport routine again, calculate total velocities for ions and neutrals and compute the mass fluxes for second half of time interval $\frac{\Delta t}{2}$. Update ion densities to time = t + Δt. At this point the calculation from t to t + Δt is finished.

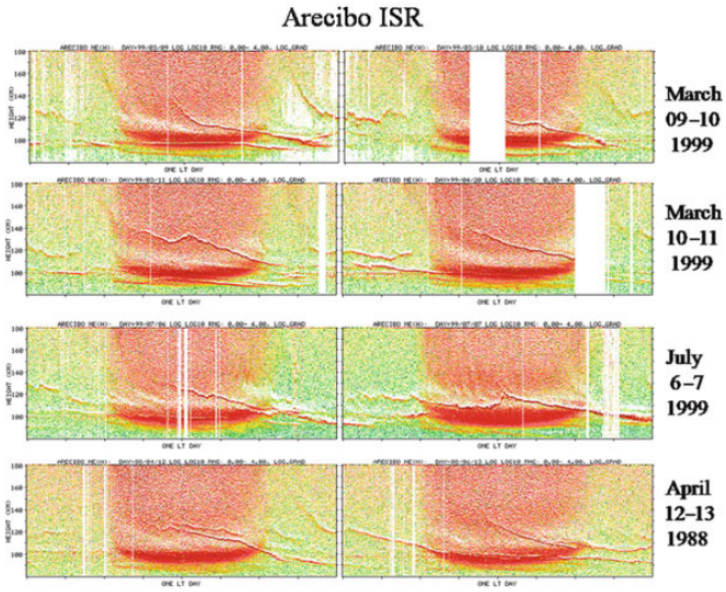

FIGURE 3.10: TIL observed ISR at Arecibo, showing a repeating pattern of diurnal and semidiurnal tidal phase descending layers. The vertical height-axis in each plot ranges from 80 km to 180 km. From *Haldoupis* [2011].

6. Update: the current wind and E-field data are updated after certain time (usually 10 minutes), and go back to step 2 and setup the updated data. When reaching at output time points, store results in the output array.

7. When $t = t_{limit}$: produce output file and stop execution.

3.4 Simulating Converged Layers at Arecibo

Sporadic E layers have been regularly observed by incoherent scatter radar (ISR) at Arecibo (Magnetic dip $\sim 50°$). Due to these converged layers descending with tidal phases speed, *Mathews* [1998] proposed "tidal ion layers" [TIL] as a more appropriate name. One example of TIL is shown in Figure 3.10, which revealed a typical patterns of TIL whose formations were controlled by diurnal and semidiurnal tides [*Mathews*, 1998; *Haldoupis*, 2011]. The tidal phases of TIL can be fairly explained by wind shear theory, however, atmospheric dynamics and electrodynamics in the E-F region can

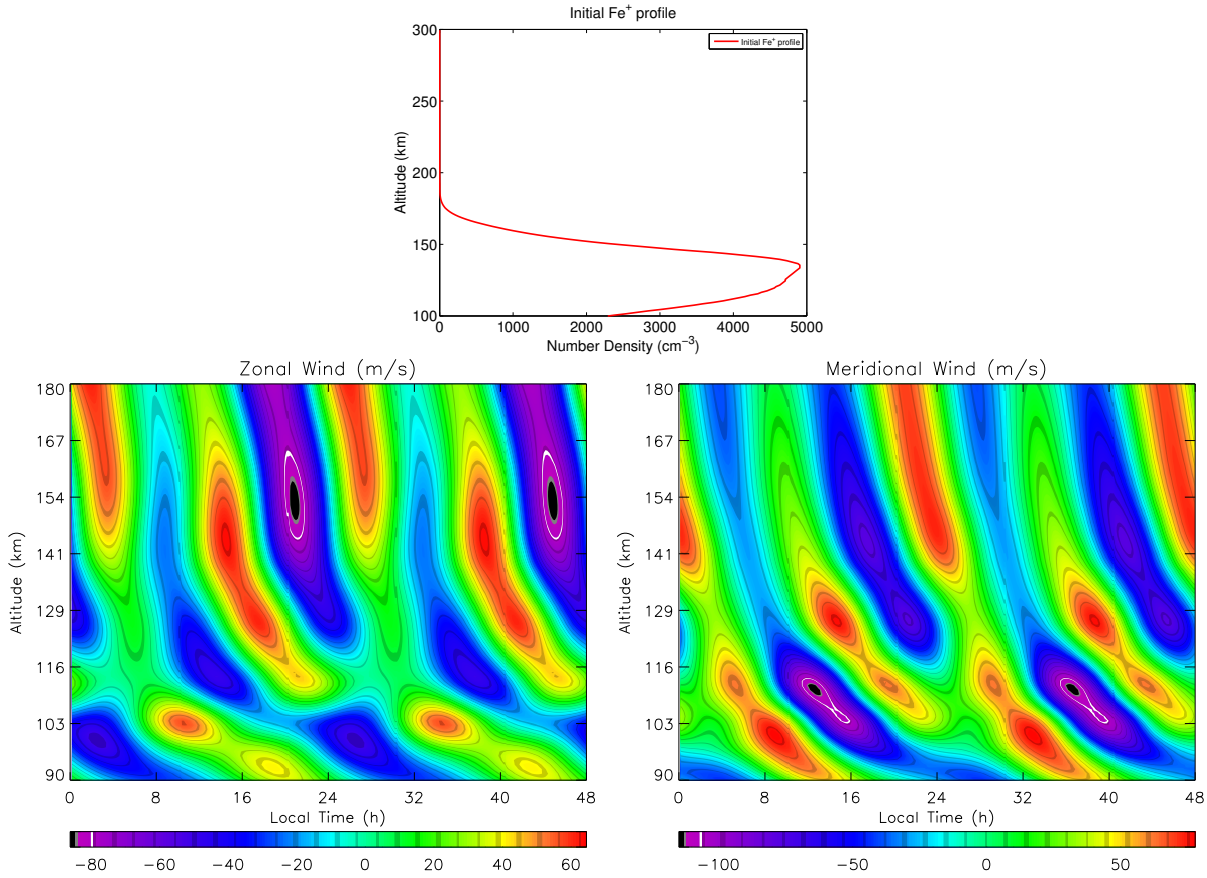

FIGURE 3.11: The top plot is the intial profile of Fe^{+}, the bottom panel is the wind fields are used in the simulations for Arecibo. Bottom left: zonal wind; bottom right: meridional wind (m/s).

be complex due to lower-upper atmosphere, and thermosphere-ionosphere coupling. *Carter and Forbes* [1999] established a numerical model to quantitatively investigate of roles the tidal zonal and meridional winds in addition to electric field, their simulations in the left panel of Figure 3.12, to a great degree, agreed with the measurements.

The purpose of this numerical test is to reproduce the converged layer simulations at Arecibo (geographic: 18°N, 67°W; geomagnetic 28°N, 2°E) reported by *Carter and Forbes* [1999]. The ambient atmospheric parameters and ionospheric parameters are set up by MSIS00 and IRI2012, respectively, and the tidal winds is set up by the tidal model incorporating solar diurnal and semi-diurnal forcing functions [*Forbes*, 1982a, 1982b; *Carter*, 1995; *Cater and Forbes*,

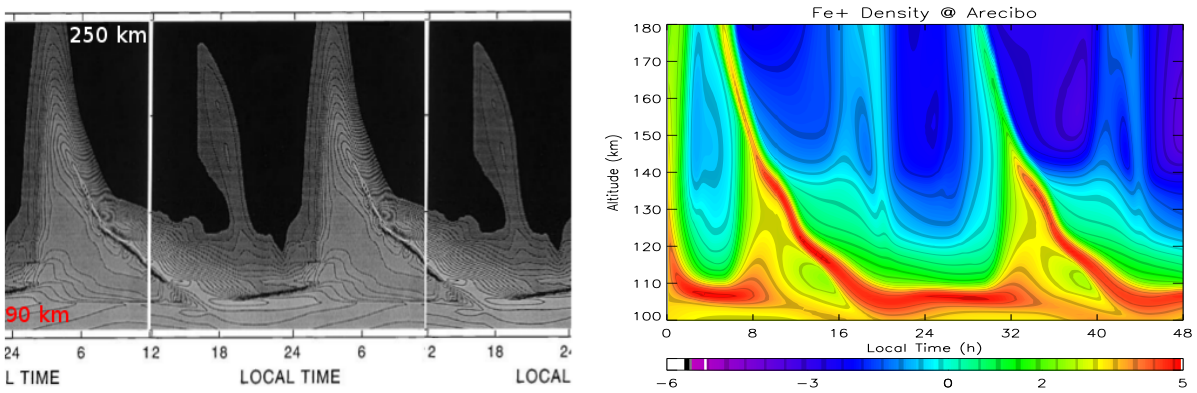

FIGURE 3.12: Height versus local time contours of $log_{10}[Fe^+]$ at Arecibo from 1-D simulation, and the ions are driven by zonal and meridional winds in addition to electric fields. The left panel is from *Carter and Forbes* [1999]; the right panel is the simulation obtained by Fe/Fe^+ model. Please note the altitude scale of left and right panels are different, and the right panel is used the scale in Figure 3.10.

1999], and Figure 3.11 shows the zonal and meridional winds used in this simulation. The electric field model for Arecibo is utilized the empirical model developed by *Richmond et al.* [1980]. Eddy diffusion is set up with the same way as *Carter and Forbes* [1999], that is, 10^6 $cm^{-2}s^{-1}$ below 100 km, and decreased to 2×10^5 at 110 km, 2×10^4 at 120 km and 0 above 120 km (US Standard Atmosphere, 1976). The intial Fe^+ is given by the left plot of Figure 3.12, and the initial Fe is set to zero.

The simulation result is given by the right plot of Figure 3.12, which is the case corresponding to "Meridional and zonal winds, with electric field" in *Carter and Forbes* [1999]. First and foremost, the pattern of TIL in the right panel agree most part with the left panel in Figure 3.12, suggesting that the simulation with the new Fe/Fe^+ model is right. The slight difference may be introduced by the initial Fe^+ profile and other parameters like Fe chemistry and Fe deposition. Secondly, with the full winds plus the electric field, Figure 3.12 demonstrates that winds are the dominant mechanism to form the converged descending layers. When the first major layer formed, the vertical drift introduced by wind shear greatly deplete the ions above 150 km. Thirdly,

the uplifting driven by electric field in the morning transport ions into higher altitudes, therefore the second minor layer with smaller density can be formed after depletion of ions caused by the formation of the first major layer.

3.5 Conclusions

We have developed a high-latitude thermosphere Fe and Fe^+ model to explore the source, formation and evolution mechanisms of thermospheric neutral Fe layers recently discovered by lidar in the altitude range of 100–200 km in Antarctica. This 1-D numerical model is developed from a 3-D mathematical model based on the continuity equation, force balance equation, and Fe and Fe^+ chemistry. By modeling the z-component of the 3-D motion field while assuming horizontal homogeneity of density, the thermospheric Fe/Fe^+ model is built along the vertical direction as the lidar configuration.

Chapter 4

Source, Formation and Evolution of Thermospheric Fe Layers: 1. Exploration with A Thermospheric Fe/Fe^+ Model for Polar Regions

4.1 Introduction

Chu et al. [2011] reported for the first time the lidar observations of neutral Fe layers reaching over 155 km at McMurdo, Antarctica. The theory proposed by *Chu et al.* [2011] hypothesizes that the thermospheric Fe layers are formed through the neutralization of vertically converged Fe^+ layers that descend in height following the gravity wave downward phase progression. They further propose that the direct recombination of Fe^+ with electron ($Fe^+ + e^- \rightarrow Fe + h\nu$) is the main mechanism that converts Fe^+ to Fe during the dark polar night, and geomagnetic activity like aurora may have played roles in the observed events at McMurdo [*Chu et al.*, 2011]. This theory of layered metal ions neutralized to form neutral atomic layers has been adapted to plausibly explain the thermospheric K layer observed at Arecibo by radiative electron recombination with

K^+ within a tidal ion layer, which descends with the downward phase progression of the semidiurnal tide [*Friedman et al.*, 2013]. A main reason of invoking the layered metal ions is the extremely high contrast of the observed neutral layers at both McMurdo and Arecibo, where the ratios of Fe density between the wave crest and trough are far larger than any perturbations in the neutral atmosphere [*Chu et al.*, 2011]. Such features distinguish these thermospheric metal layers from the weak diffusive metal layers extended up to 130 km [*Höffner and Friedman*, 2005]. We are particular interested in the thermospheric Fe layer event observed on 28 May 2011 at McMurdo [*Chu et al.*, 2011] because of its intriguing features. The May 28th event exhibits apparent gravity wave features, with a wave period of ∼1.5 h. The vertical wavelength increases from ∼14 km at 100 km to ∼70 km at 150 km. The thermospheric Fe densities are ∼20 cm^{-3} at 150 km but exhibit a maximum of ∼110 cm^{-3} around 125 km. From ∼12 to ∼20 UT the Fe layers repeatedly occur at least 5 times, and the maximum layer height of each occurrence changes from ∼130 km at 12 UT to the highest ∼155 km near 15 UT, and then decreases to ∼125 km at 18.5 UT.

The questions raised by *Chu et al.* [2011] include:

1. Source of Fe layers – where are Fe and Fe^+ from, how are Fe^+ ions transported to the E–F regions, and how are Fe^+ layered in the polar cap?

2. Formation of Fe layers – What are the conversion mechanisms from Fe^+ to Fe and what roles does aurora particle precipitation play in such conversion?

3. Transport and shape of Fe layers – What determines the Fe transport and Fe layer shape, and why do the observed Fe layers follow the gravity wave phases so faithfully?

4. Energetics of the thermosphere – What processes cause the elevated temperatures and what role does geomagnetic activity play?

In this study we aim to investigate the questions 1 – 3 by utilizing the thermospheric Fe/Fe^+ model for polar cap to simulate the event on 28 May 2011.

A description of the set up of the numerical simulation of thermospheric Fe/Fe^+ is provided in Section 4.2. Numerical simulations in Section 4.3 reveal the important role of polar electric field in transporting Fe^+ ions from their main deposition region to the E and F regions, which supplies the source of the thermosphere Fe layers. Section 4.3 also shows the importance of wave-induced vertical wind in transporting Fe^+ and Fe layers. Neutralization chemistry to form Fe from Fe^+ is studied in Section 4.4. Sixteen nonlinear differential equations of chemical reactions of Fe, Fe^+ and ambient ions and neutrals are solved by backward differentiation formula. The direct electron-Fe^+ recombination, dissociative recombination and the role of aurora in the conversion are quantified with the model. In Section 4.5, the thermospheric Fe layer event on 28 May 2011 at McMurdo is reproduced with this new model using realistic or measured parameters. A new finding is that wave-induced vertical wind plays a key role in transporting Fe layers to form the observed shapes of repeated layers with downward phase progression. The study also sheds a light on the causes of varying Fe layer heights observed over time. This chapter is concluded in Section 4.6.

4.2 Model Setup

The ultimate source input of Fe and Fe^+ is treated as two initial density profiles of Fe and Fe^+ in our model, instead of continuous input. This is reasonable as the model simulations are for relatively short time periods thus the meteor input is very minor compared to the mean background profiles of Fe and Fe^+ densities as argued below. The ultimate source of Fe and Fe^+ is believed to be extraterrestrial–the meteor deposition via meteor ablation and sputtering. The resulted altitude profiles of injection rate of Fe species have been calculated from the physics and chemistry of meteor

ablation and sputtering by *Vondrak et al.* [2008], considering the distributions of meteoroid mass, velocity and direction, relative abundance of Fe species in meteoroids and ablated vapor, etc. The mean density distributions of Fe and Fe^+ are determined, to the first-order approximation, by the product of the mean injection rates and the mean lifetimes of Fe species in the MLT regions. Such mean densities should match observations of Fe and Fe^+ densities regardless a very large uncertainty (ranging from 2 to 300 t/d) currently associated with the total meteor input flux [*Plane*, 2013; *Feng et al.*, 2013; *Gardner et al.*, 2014]. It is clear that the injection rates above 120 km are significantly smaller (about 4 orders of magnitude) than those in the main deposition region below 110 km [*Vondrak et al.*, 2008; *Feng et al.*, 2013]. If taking the relatively high estimate of injection rates by *Vondrak et al.* [2008] for $\sim$ 88 t/d meteor influx, the injection rates above 120 km are about or less than 10 $m^{-3}s^{-1}$ or 10^{-5} $cm^{-3}s^{-1}$. Then it takes at least 10^5 $s = 27.8h$ for the entire Fe species to accumulate to 1 cm^{-3} density above 120 km, even without considering the downward transport loss caused by gravity and various atmospheric waves. The total meteor influx smaller than 88 t/d will take even longer time. Therefore, the meteor injection above 120 km is negligible compared to the required Fe^+ ($\sim 10^5 cm^{-3}$) to produce the observed Fe density ($\sim$ 10–100 cm^{-3}) above 120 km. The Fe and Fe^+ initial profiles used in our simulations of 28 May 2011 event are shown in Figure 4.1. The Fe densities below 100 km are the mean of the first half-hour lidar observations on 28 May 2011 with the peak density of $\sim 1.6 \times 10^4$ cm^{-3} [*Chu et al.*, 2011]. Above 100 km the Fe densities are set to linearly decrease to 0 at and above 110 km in order to remove the thermospheric Fe layers that have already begun to form when the lidar observations started. Our purpose is to start the numerical simulations with zero Fe background above 110 km so that it can be shown how the thermospheric Fe atoms are produced from Fe^+ ions that are transported into the E–F regions. The initial Fe^+ profiles is set to the combination

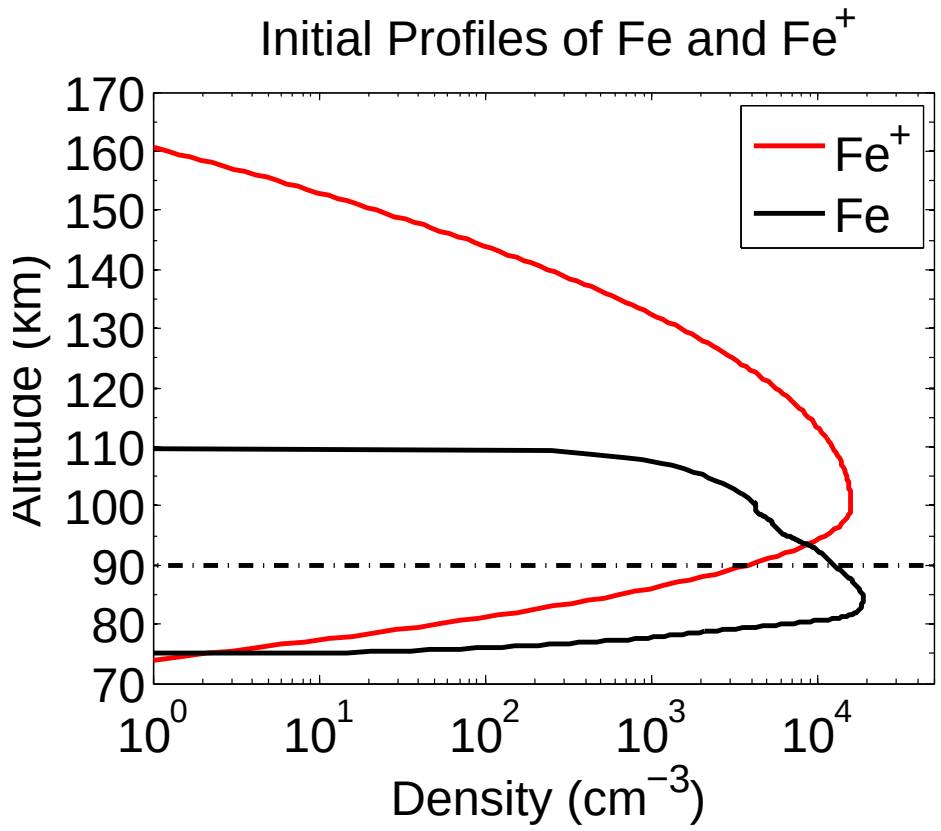

FIGURE 4.1: Initial profiles of Fe (black line) and Fe^+ (red lines) used in the simulations of the thermospheric Fe layer event on 28 May 2011 at McMurdo.

of two Gaussian profiles with the peak density of $\sim 1.4 \times 10^4\ cm^{-3}$ at 100 km. The combined Gaussians have a full width at half maximum (FWHM) of ~20 km above 100 km and 9 km below it, corresponding to a column abundance of $3.6 \times 10^{10}\ cm^{-2}$. This Fe^+ initial profile is similar to the Fe^+ shown in Figure 5 of *Feng et al.* [2013] for WACCM-Fe over Urbana (40° N) where their peak density is $\sim 9000\ cm^{-3}$ at $\sim$ 96 km.

The neutral environmental data are taken from NRLMSISE-00 [*Picone et al.*, 2002] while the International Reference Ionosphere (IRI-2012) is used to specify ionic parameters, such as the densities of O^+, O_2^+ and NO^+, and temperatures of ions and electrons T_i and T_e. The International Geomagnetic Reference Field (IGRF-11) is used to specify the geomagnetic field (B-field) whose

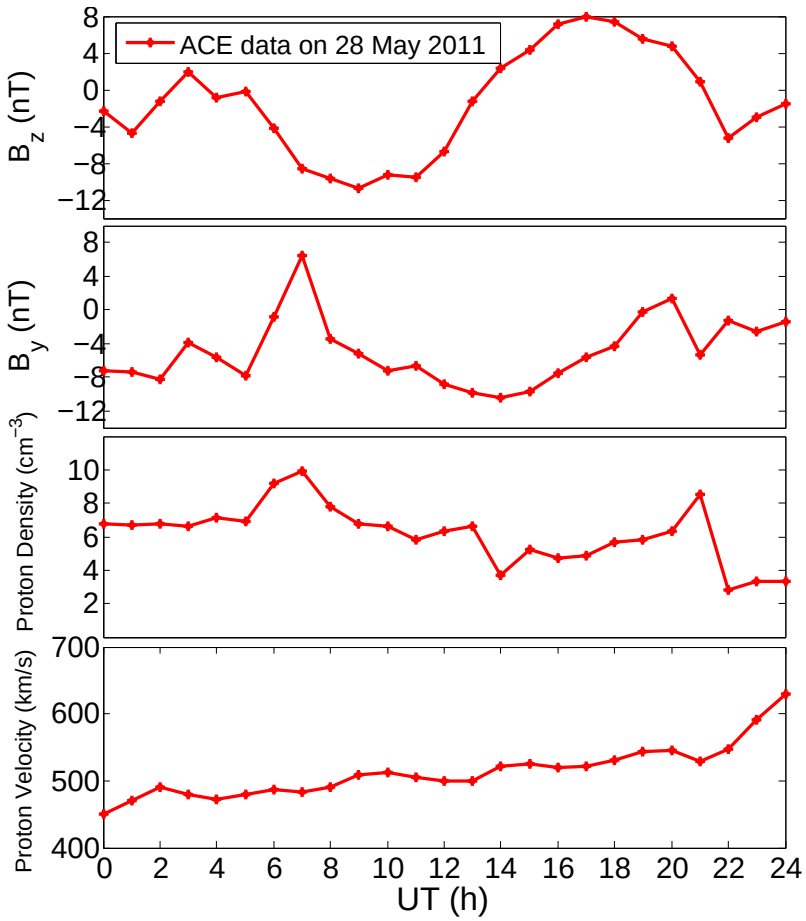

FIGURE 4.2: The hourly averaged IMF and solar wind data measured by ACE on 28 May 2011. These data are used as input to the Weimer-2005 model for computing the polar electric field.

main field is quite stable. In contrast, the polar electric field (E-field), particle precipitation, and the neutral wind fields are complex and highly variable due to the strong influences from the magnetosphere, solar activity, and wave dynamics. The GLOW model developed by *Solomon et al.* [1988] is utilized to characterize the ionization by the impact of auroral electron precipitation.

Polar region has relatively complex geomagnetic environment, which is directly impacted by the activities of magnetosphere. The electric fields play fundamental roles in ionospheric dynamics. The electric fields in the ionosphere over polar cap are originated from solar-wind-induced convections in the magnetosphere and the dynamo effects in the lower thermosphere, showing large spatial and temporal variations [*Richmond*, 1995]. We utilize the empirical electric potential model

of Weimer [2005] to set up the convection electric field, which is taken as external electric field in our model. The Weimer-2005 model provides empirical high-latitude electric potentials and magnetic field-aligned currents (FAC) as a function of solar wind and interplanetary magnetic field (IMF) and dipole tilt angle with higher accuracy [*Weimer*, 2005]. The components of electric potential driven by either magnetosphere or dynamo in the lower thermosphere, which are uncorrelated to solar wind and IMF, are not included. The irregularly dynamo generated electric fields are neglected in the Weimer-2005 model. The perturbations of electric field associated with plasma irregularities are neglected as well. For geomagnetic conditions on 28 May 2011, we utilize the hourly-averaged solar wind and IMF data from *http://omniweb.gsfc.nasa.gov/* (Figure 4.2), and compute the electric field using the Weimer-2005 model. The results for McMurdo location are shown in Figure 4.3a.

The observed gravity waves on 28 May 2011 show period of 1.5–2 h between 100 km to 150 km, and vertical wavelength changes from ∼15 km at 100 km to ∼65 km at 150 km [*Chu et al.*, 2011]. In our modeling, the gravity wave is simulated by a forward model. We simply assume a monochromatic gravity wave whose period is 1.57 h and the vertical wavelength is set up by the lidar observations (Figure 2.3b) below 155 km and approximated by the vertical wavelength profiles in *Vadas* [2007] above it. The amplitude of vertical wind velocity at 150 km is assumed to be 12 m/s, which is comparable with the amplitudes of vertical wind reported by *Larsen and Meriwether* [2012]. The amplitude of gravity-wave-driven vertical wind velocity below 200 km is calculated by $w(z) = w_{z0}\sqrt{\frac{\rho_{z0}}{\rho_z}}$, where $z0$ is 150 km, w_{z0} is the vertical velocity at 150 km, and ρ is air density. The amplitude of horizontal wind velocity is approximated by a simplified polarization relationship

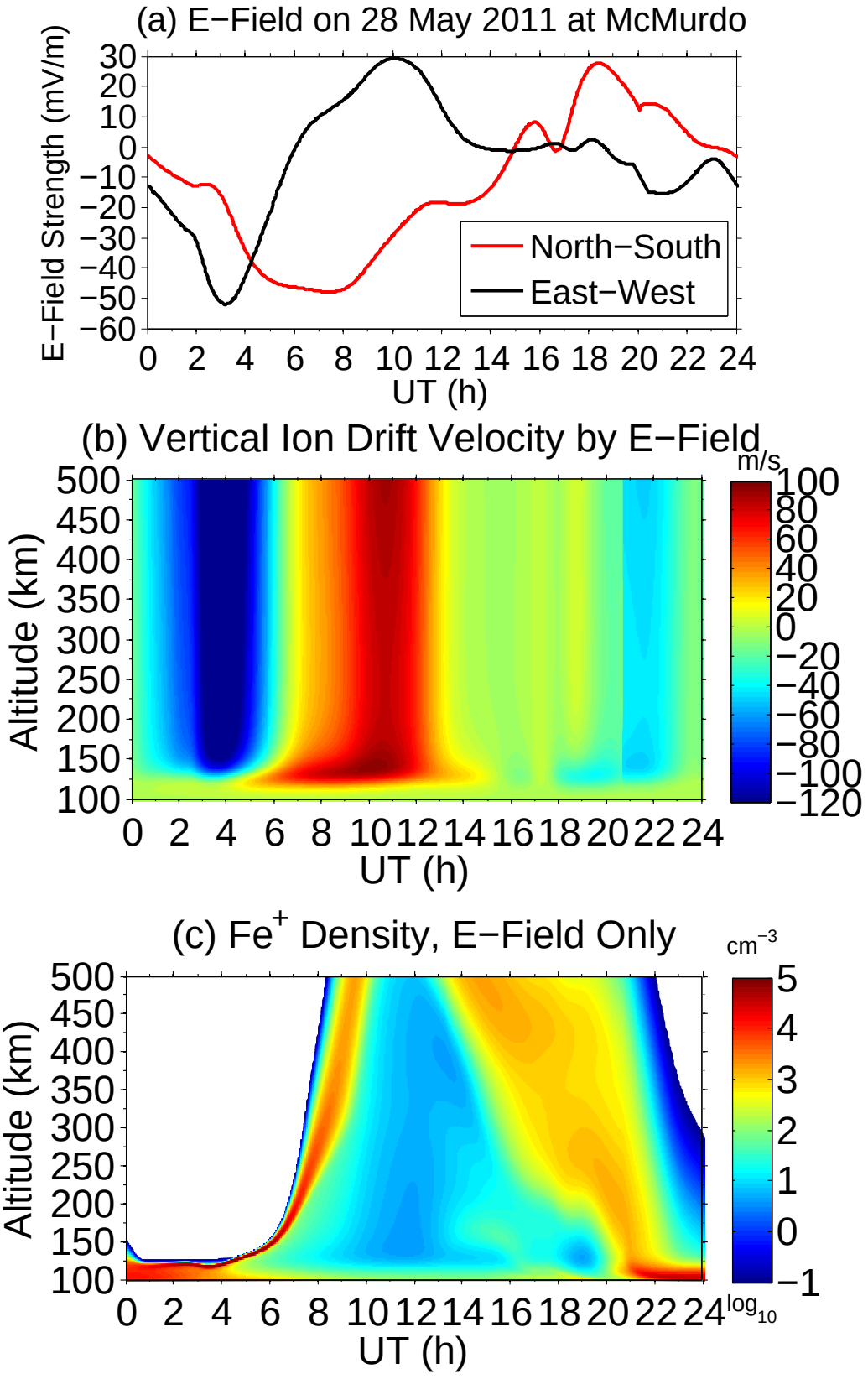

FIGURE 4.3: (a) Calculated electric field by Weimer-2005 model on 28 May 2011 at McMurdo, (b) the corresponding vertical ion drift velocity, and (c) variations of Fe^{+} density (see text).

of gravity wave,

$$u_h = -\frac{m}{k_h} w \tag{4.1}$$

$$u_x k_y = u_y k_x \tag{4.2}$$

where k_h is the horizontal wave number and $k_h = \sqrt{k_x^2 + k_y^2}$, and m is the vertical wave number; when the phase propagation is downward, $m < 0$. The horizontal wavelength is estimated through comparing the measured vertical wavelength with the calculated vertical wavelength in *Vadas* [2007] and *Djuth et al.* [2010], giving rise to the best estimation of 800 km horizontal wavelength. Due to the fact that horizontal wavelength remains constant with altitude if the background winds and temperatures change only with altitude [*Vadas and Nicolls*, 2009], in our simulation, the 800 km horizontal wavelength is set to constant through the whole altitude range. k_x is set to be positive and equal to k_y. Therefore, the wave propagates in north-east direction. An example of horizontal and vertical wind profiles is shown in Figure 4.6a.

The divergence of horizontal winds is appreciable if the vertical wind shear is significant. In order to compute the wave-induced density perturbations, the effect caused by the divergence of gravity-wave horizontal winds has to be taken into account. As discussed in Chapter 3, the correction can be done by equation 4.3, which is written in an implicit way

$$N_i^{t+\Delta t} = \frac{N_i^t}{1 + \Delta t \cdot \nabla_h \cdot \vec{u}_h} \tag{4.3}$$

where N_i^t is the number density at grid i and time t, Δt is the time step. Here, we utilize equation 5.16 in Chapter 5 to estimate $\nabla_h \cdot \vec{u}_h$ for Fe, and equation 5.24 to estimate $\nabla_h \cdot \vec{u}_{i,h}$ for ions. The effects of horizontal divergence will be detailed in Chapter 5 when simulations are aimed to

TABLE 4.1: Conditions for simulations

Conditions[a]		Numerical Experiments [b]					
		Figure 4.3	Figure 4.8	Figure 4.10	Figure 4.11	Figure 4.17	Figure 4.18
Zonal wind		Off	On	On/Off	On	Off	On
Meridional wind		Off	On	On/Off	On	Off	On
Vertical wind		Off	On	On/Off	On	Off	On
Electric field		On	Off	On	On	On	On
Horizontal divergence		Off	Off	On	Off	Off	Off
GLOW Model:		On	Off	On	On/Off	On/Off	On
	Energy	1.0		1.0	1.0	1.0	1.0
	Energy flux	1.5		1.5	1.5	1.5	1.5
Gravity wave parameters:							
Measured vertical wavelength (Figure 2.3b): T = 1.5 h; w_{150} = 12 m/s; k_h = 800 km; $k_x = k_y$; North-east direction							

[a]'Energy' represents the characteristic energy in unit [keV] of the input Maxwellian electron spectrum; 'Energy flux' represents the integrated energy in unit [erg/($cm^2 s^1$)] of the input electron spectrum.

[b]'On' and 'Off' mean that the corresponding parameters or modules are turned on or off. 'On/Off' means that the parameters or modules are switched on or off.

reproduce the event on 28 May 2011.

Table 5.1 summarizes the conditions for the simulations conducted in the following sections.

4.3 Source of Fe Layers in the Thermosphere – Fe^+ Transport and Layering

As mentioned in Introduction 4.1, a main question raised by *Chu et al.* [2011] is the Fe and Fe^+ sources in the polar thermosphere and Fe^+ layering in the E and F regions. Although the ultimate source of Fe and Fe^+ is the meteor input, the main meteor deposition region of Fe and Fe^+ is below 120 km [*Vondrak et al.*, 2008]. Consequently, the background Fe^+ density in the E–F region is usually low (see Figure 4.1), thus insufficient to generate appreciable Fe atoms. To form neutral Fe from Fe^+, two conditions are needed at least. First, a large amount of Fe^+ ions must be transported from the main deposition region upward to the E–F region. Second, the Fe^+ ions in the E–F region must be converged to form Fe^+ layers that are dense enough to produce

appreciable Fe atoms. Such ideas are illustrated in Figure 4.4a. The main goal of this section is to investigate such transporting and layering mechanisms, which concern the Fe^+ and Fe motions. The mechanisms of the conversion from Fe^+ to Fe will be investigated in Section 4.4.

4.3.1 Fe^+ transport by electric field

As indicated in the introduction, metallic ions were frequently observed in the F region. However, The source of F metallic ions is still not well resolved. Figure 4.4 schematically summarizes the dominant vertical transport mechanisms for metallic ions. Gravitational transport, ion diffusion are not displayed in the figure. At high latitude, intense electric fields perpendicular to the magnetic field lines, as shown in Figure 4.4, are a common feature. One of the possible dominant upward transport mechanism of metallic ions from low altitude source is the Pedersen drift associated with the convection E-field [*Grebowsky and Pharo*, 1985]. The poleward directed electric field drives metallic ions drift upward along with the magnetic field lines. Once the electric field is intense enough, the upward motion would beat down gravity drag and ion diffusion so metallic ions would accumulate in the F region. At the auroral region, large electric fields exceeding 100 $mV \cdot m^{-1}$ have been observed [*Spiro et al.*, 1979]. Another possible candidate for inducing upward transport of metallic ions is atmospheric expansion caused by Joule heating. Joule heating easily produce vertical neutral winds speeds of several tens of $m \cdot s^{-1}$ in the thermosphere, $\sim$ 300–500 km altitude range [*Bates*, 1974]. If metallic ions are transported from their main deposition region below 125 km up to higher altitudes by Joule heating, the Joule heating must happen below 125 km thus upward transport of Fe^+ or Fe into the thermsosphere [Burns et al., 1991]; however, this mechanism is unproven at these low altitudes.

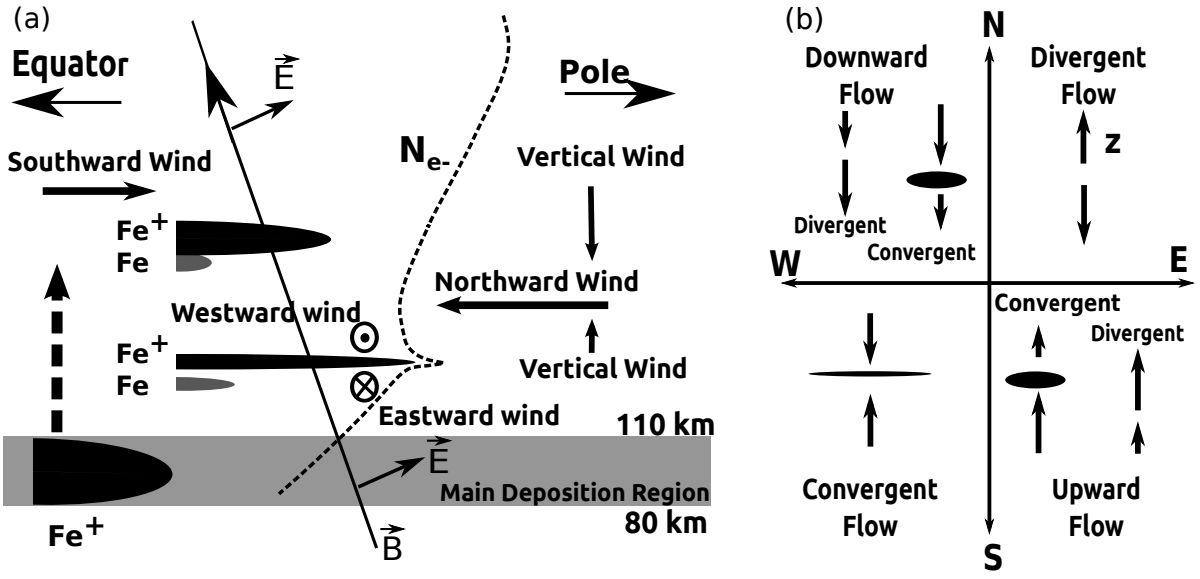

FIGURE 4.4: It schematically indicates the dominant vertical transport mechanisms in southern hemisphere. This figure is adpated from *Grebowsky and Pharo* [1985].

At high latitudes, the ionospheric electric field becomes a substantial driving force of transporting ions in the vertical direction [*Nygrén et al.*, 1984; *Bristow and Watkins*, 1991]. The electric-field-driven vertical drift velocity of ion V_{ize} expressed in equation 3.13 can be decomposed into two vertical components of $\vec{E} \times \vec{B}$ and $\vec{E}$ drifts, corresponding to Hall drift and Pedersen drift, respectively.

$$V_{ize} = \frac{\cos\Theta_D}{1+\xi^2}\frac{E_x}{B_0} + \frac{\xi}{1+\xi^2}\frac{E_z}{B_0}$$

We define:

$$f_H = \frac{\cos\Theta_D}{1+\xi^2} \tag{4.4}$$

$$f_P = \frac{\xi}{1+\xi^2} \tag{4.5}$$

where f_H and f_p are Hall and Perdson mobility coefficients, respectively. The Hall and Pedersen

mobility coefficients are plotted as functions of altitude in Figure 4.7a. At high altitudes, larger Hall mobility coefficient leads to stronger $\vec{E} \times \vec{B}$ drift, while at low altitudes the ions move in the direction of the electric field. The directions of Hall and Pedersen drifts are determined by the direction of the electric field relative to the geomagnetic field line (see Figure 4.4b). For instance, if the electric field points to the south-east direction, both Hall and Pedersen drifts would produce upward ion flow, which suggests a potential mechanism for transporting metallic ions into the thermosphere. The orientations of E_x and E_z are another candidate for forming thin ionization layers. When the electric field points to the south-west direction, thin converged ionization layers can be formed at the null where Hall drift moves ions downward from above and Pedersen drift moves ions upward from below. Let $\tan\alpha = \vec{E}_z/\vec{E}_x$, equation (3.13) can also be written as

$$V_{ize} = \frac{E_x/B}{1+\xi^2}(\cos\Theta_D + \xi\tan\alpha) \tag{4.6}$$

when the configuration of $\vec{E}_x$ and $\vec{E}_z$ satisfies $\tan\alpha = -\cos\Theta_D/\xi$, V_{z2} will be equal to zero. If V_{ize} is positive below and negative above the null altitude where $V_{z2} = 0$, ions are driven towards the null altitude, forming a thin ionization layer.

Shown in Figure 4.2 is the IMF measured by satellite ACE on 28 May 2011 that turned its direction from southward to northward at around 12 UT. The solar wind density varied from 4 to 10 cm^{-3}, and the solar wind velocity changed from 500 to 600 km/s. With these observational data, the electric field on 28 May 2011 calculated by the Weimer-2005 empirical model is shown in Figure 4.3a, while the vertical drift velocity of Fe^+ calculated using equation 3.13 is plotted in Figure 4.3b. The variations of Fe^+ density versus time and altitude are illustrated in Figure 4.3c. In this simulation the Fe^+ profile shown in Figure 4.1 is used as the initial profile with the majorities of Fe^+ ions distributing below 120 km. Neutral winds are turned off but the electric field,

gravity and diffusion are in action. From 0 to 6 UT when the electric field points to the south-west direction (Figure 4.3a), the Hall drift pushes ions downward from above and the Pedersen drift pushes ions upward from below (Figure 4.3b). Consequently, the Fe^+ ions are converged to form a thin layer around 130–140 km in Figure 4.3c. Starting from ∼6 UT until ∼13 UT, the electric field points to the south-east direction (Figure 4.3b). Consequently, a strong upward ion flow is seen in Figure 4.3c and the Fe^+ ions in the main deposition region are transported into the F regions around 400–500 km by the strong south-east electric field. From ∼13 to ∼16 UT, the east-west electric field is close to zero while the north-south electric field is reversing its direction from the south to the north. During this period, the vertical ion drift is relatively slow, and the ions float at high altitudes first and then slowly drift downward because of the gravity and small component of north-west electric field. Since ∼16 UT the electric field starts to gain larger magnitudes in north-west direction. Consequently, the Fe^+ ions are moved downward in Figure 4.3c. A strong downward ion flow is seen around 20–24 UT in Figure 4.3b and the Fe^+ ions are even converged above 100 km in Figure 4.3c when the Fe^+ ions at higher altitudes catch up the Fe^+ at lower altitudes. The simulation results in Figure 4.3 clearly show that Fe^+ ions in the main deposition region are uplifted into the Fe region by the strong south-east electric field, demonstrating that the polar electric field is sufficient in transporting metallic ions into the thermosphere, thus providing the source of Fe^+.

4.3.2 Fe^+ transport by neutral winds

The first windshear theory aimed to explain the physics of sporadic E layers in mid and low latitudes was proposed and formulated by *Whitehead* [1961] and *Axford* [1963], and then further developed by e.g. *Whitehead* [1989]. The ionization layers can be transported or converged by the vertical ion drift driven by neutral winds blowing across the geomagnetic field via Lorentz force. The picture of

windshear ion convergence mechanisms are illustrated in Figure 4.5. That is, below about 125 km where $\xi \gg 1$, ions are sufficiently coupled, via collisions, to the neutral atmosphere. The westward wind carrying ions above yields downward ion drift, and eastward wind below drives upward ion drift, Figure 4.5 (left). Therefore, the ions are accumulated by downward and upward ion drifts at the wind shear null, and a thin ionization layer forms. At the higher altitudes where collision frequency is lower than gyrofrequency ($\xi < 1$), the influence of zonal winds on the vertical ion drifts is greatly reduced by the decrease of neutral-ion collision frequency. At this moment, the neutrals can only partially govern the motions of ions, and the ions' motion is also partially contrained by geomagnetic field line due to Lorentz force. Meridional winds become important to transport ions vertically, although the meridional winds would not produce any vertical ion drifts via $\vec{V}_{merid} \times \vec{B}$ force because $\vec{V}_{merid} \times \vec{B}$ lies in the horizontal plane. The ions' momentum obtained from meridional winds of neutrals has a component in the direction of geomagnetic field. Since it is much easier for ions to move along with the geomagnetic field lines, comparing with the ions' motion perpendicular to the geomagnetic field lines, the component of momentum along with the geomagnetic field lines can induce significant vertical motions of ions, as shown in the middle panel of Figure 4.5 (for the southern hemisphere). Northward wind below and southward wind above also can converge the ions into a thin layer at windshear null where V = 0. For northern hemisphere, an opposite meridional windshear, northward wind above and southward wind below, can drive the formation of a thin ionization layer. Vertical winds have the similar effect on the ions' motion as the meridional winds, as shown in the right panel of Figure 4.5. When the inclination angle of the geomagnetic field line becomes larger, vertical winds are more important in transporting ions vertically. Equation 3.14 gives the vertical drift velocity V_{izw} driven by geomagnetic zonal, meridional and vertical neutral

winds as follows:

$$V_{izw} = \frac{\sin(2\Theta_D)}{1+\xi^2} V_{n,y} + \frac{\xi}{1+\xi^2} \cos\Theta_D V_{n,x} + \left(\frac{\xi^2 + \sin^2\Theta_D}{1+\xi^2}\right) V_{n,z}$$

We define the dimensionless wind factors:

$$f_y = -\frac{\sin(2\Theta_D)}{2(1+\xi^2)} \tag{4.7}$$

$$f_x = \frac{\xi\cos\Theta_D}{1+\xi^2} \tag{4.8}$$

$$f_z = 1 - \frac{\cos^2\Theta_D}{1+\xi^2} \tag{4.9}$$

where $f_{i=x,y,z}$ denote the wind factors associated with the zonal, meridional and vertical components of the neutral winds, respectively. The horizontal wind-shear mechanisms dominate over the vertical wind shear at the mid and low latitudes [*Carter and Forbes*, 1999; *Bishop et al.*, 2003]. However, in the polar regions the horizontal wind shears are no longer dominant because the horizontal wind factors f_x and f_y drop fast as the geomagnetic inclination angle Θ_D approaching 90°. At the same time, the vertical wind factor f_z becomes significantly larger. This gives rise to much more efficient converging force by the vertical wind than by the horizontal winds. Three wind factors are compared in Figure 4.7b for McMurdo where the geomagnetic inclination angle is 80.1°. Comparing f_x and f_y, zonal wind is more efficient in drifting ions vertically below 120 km because of the strong ion-neutral coupling, but above 130 km the meridional wind factor exceeds the zonal wind factor because the less ion-neutral coupling allows ions to drift along the geomagnetic field lines. When the inclination angle of geomagnetic field line is close to 90°, the horizontal wind factors f_x and f_y become significantly small but the vertical wind factor f_z approaches one. Therefore, the neutral vertical wind can induce vertical ion drift velocities with magnitudes similar as or even larger than

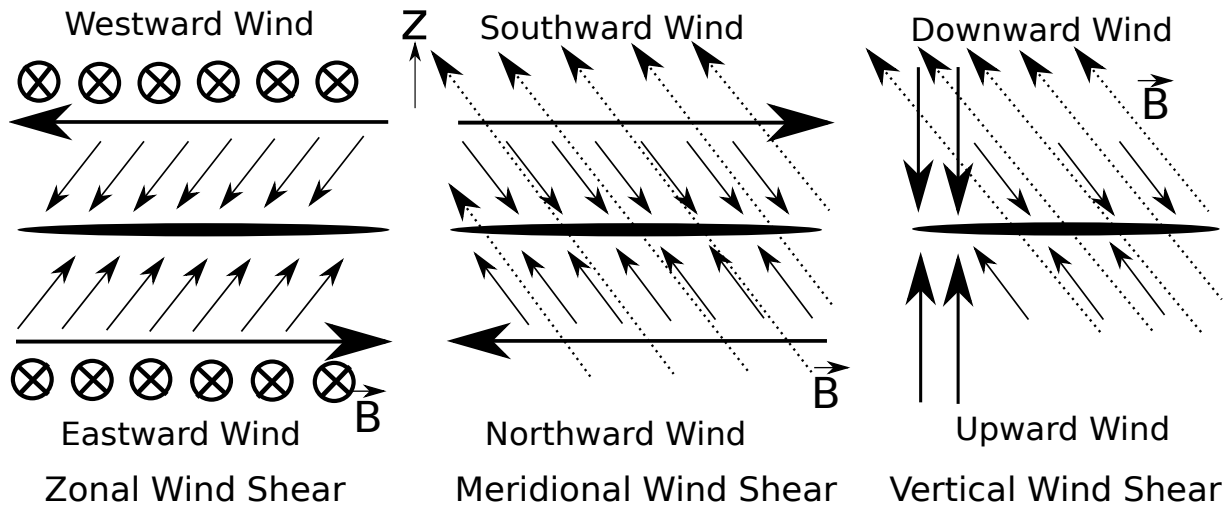

FIGURE 4.5: Sketches of the zonal (left), meridional (middle), vertical (right) wind shear mechanism for the Southern Hemisphere.

those by the neutral horizontal winds, despite the vertical wind is much smaller than the horizontal winds as demonstrated in Figure 4.6.

Using the forward-modeled gravity wave parameters described in Section 4.2, Figure 4.6a shows the gravity-wave-induced wind profiles at time t=0, in which the zonal wind is set to equal the meridional wind. The simplified polarization relation equation $u_h = -\frac{m}{k_h} w$ indicates that null of zonal, meridional and vertical winds locate at the same altitude. Figure 4.6b gives the vertical drift velocity of Fe^+ caused by each wind component as given in Figure 4.6a. Below 120 km, the vertical drifts caused by horizontal winds are close to zero, and the Fe^+ ions follow the neutral vertical wind and converge at the null of vertical wind. Above 120 km, the vertical drift caused by meridional wind increases fast with the increasing altitude, since f_y and meridional wind amplitude increase at the same time. The vertical drift caused by zonal wind increases slowly first and then decreases with the increasing altitude, because the increase of zonal wind amplitude is cancelled out by the decrease of zonal wind factor f_x. The altitudes of the nulls of vertical ion drifts by three winds are identical as the nulls of the winds as illustrated in Figure 4.6. At the same time, the local

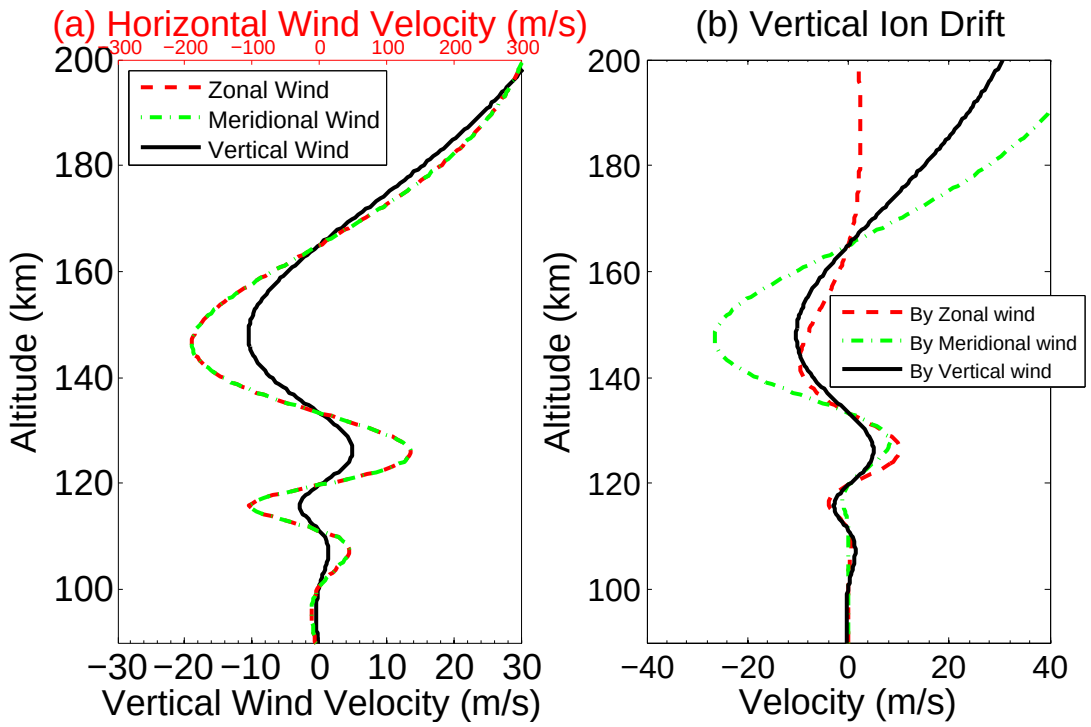

FIGURE 4.6: (a) Forward-modeled wind profiles induced by gravity wave. The vertical wind values are represented by the bottom x-axis, while the zonal and meridional winds are set to be equal to each other and shown by the top x-axis. (b) The vertical drift velocities of Fe^+ driven by the wind shears shown in (a).

maximum of the vertical drift is determined by the product of wind factor and wind amplitude; therefore, the altitudes of the local maxima of the three vertical ion drifts can be different from each other depending on the overall effects of wind factors and wind magnitudes.

To investigate the impacts of neutral wind-shear mechanisms on the transport and convergence of polar Fe^+ ions, we design an experiment in Figure 4.8, in which the electric field is turned off but one of the three neutral winds (shown in Figure 4.6a) is switched on each time at time t = 0 with initial phase $\phi_0 = 0$. The initial profile of Fe^+ is given by the blue dotted line in Figure 4.8, whose Fe^+ densities at higher altitudes are substantially higher than those of the initial profile shown in Figure 4.1. We compare the evolutions of the Fe^+ profile with three different wind inputs: zonal wind only, meridional wind only, and vertical wind only. The rest initial conditions for McMurdo are identical for these three simulations. Because the initial meridional

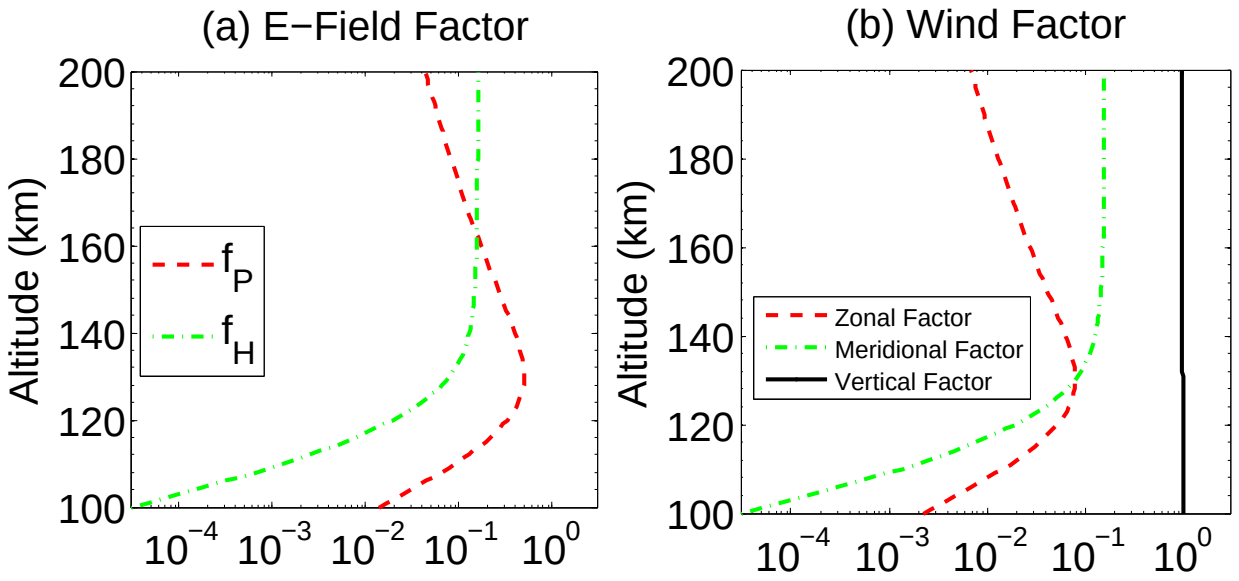

FIGURE 4.7: Comparison of dimensionless electric field factors and wind factors in producing vertical drift velocities of ions at McMurdo, Antarctica. (a) Electric field factors by Pedersen and Hall drift, and (b) three wind factors by zonal, meridional and vertical winds.

wind is strongly northward above 160 km, Fe^+ ions are transported upward initially around t = 0.21, resulting in the green solid line exceeding the initial Fe^+ at high altitudes. Figure 4.6 shows that all three winds can transport Fe^+ both upward and downward but in general the simulations give downward transport of Fe^+. Zonal wind plays a minor role while the meridional and vertical winds are more efficient in converging ions at higher altitudes. Below 115 km, the zonal and meridional winds can hardly move the Fe^+ ions and the vertical wind dominates this region. The altitudes of the peaks of the Fe^+ layers are away from the present wind nulls, because the formation of Fe^+ layer peak is related to the previous convergent nulls. When the convergent nulls move downward as the gravity wave propagating upward, the converged Fe^+ layers are not able to move as fast as the wind nulls, so the present wind null is always below the peak of Fe^+ layer. When the divergent nulls catch up the converged Fe^+ layers, the Fe^+ layers would be broadened by the divergent wind. This experiment demonstrates that the neutral wind-shear mechanisms

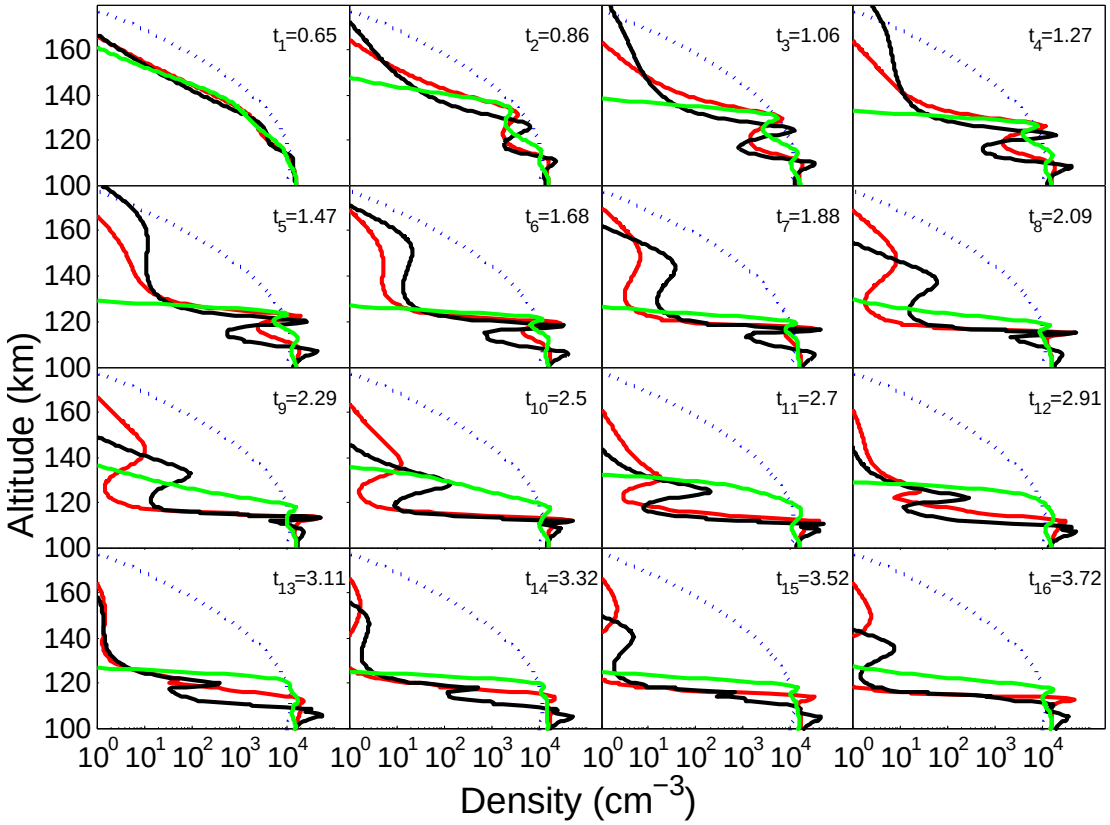

FIGURE 4.8: The Fe^+ density profiles starts at 0.21 h, and the interval between two successive profiles is 0.205 h. The blue dashed line is the initial Fe^+ profile, and the solid lines are Fe^+ transport driven by different winds: Red, green and black lines represent the zonal, meridional and vertical wind only, respectively.

can still transport and converge ion layers in the polar region of high inclination as long as the wind shears are sufficient. The wind amplitudes used in the simulations (Figure 4.6a) are in the reasonable range of observed neutral winds in the thermosphere. Furthermore, the horizontal and vertical wind shears can have comparable effects on the ion transport and convergence, depending on altitude and relative wind magnitude. It is worth to point out that Figure 4.8 over-estimates the vertical wind effects because the horizontal divergence is neglected. The horizontal divergence largely offsets the vertical convergence, and details will be discussed in Chapter 5.

4.3.3 Fe^+ transport in the simultaneous presence of winds and electric field

The motions of Fe^+ are governed by the electric field and the Lorentz force at the same time. At high latitudes, the convection electric field has more profound impact on the vertical redistribution of Fe^+. Taking McMurdo as an example, Figure 4.9 shows the ion drift velocities driven by 150 m/s zonal and meridional wind, 1 m/s vertical wind, and 1 mV/m E_z and E_x. Below 107 km, the vertical wind induced the highest Fe^+ drift velocity. Between 107 and 125 km, the 1 mV/m E_z and 150 m/s zonal wind drive the highest Fe^+ velocities. Above 130 km, the 150 m/s meridional wind drives higher Fe^+ vertical drift than the 1 mV/m E_x. However, the polar electric field has a diurnal convection pattern and its peak magnitude is about tens mV/m, so it can easily overwhelm the horizontal neutral winds in transporting Fe^+. When the electric field is weak, the driving forces caused by electric field and neutral winds can be comparable.

In Figure 4.10 we investigate how the wind mechanisms work in the presence of the polar electric field. The simulation conditions for Figure 4.10 are identical to those for Figure 4.3c except now the neutral winds given by Figure 4.6a are turned on since the beginning and the horizontal divergence is considered. Horizontal and vertical winds are applied in Figures 4.10a and 4.10c, respectively. Despite some small differences, similar patterns of Fe^+ motion are shown in Figure 4.10a and 4.10c. That is, the motion of Fe^+ is dominated by the strong electric field at the beginning, and a readily upward transport of Fe^+ is found. Then at the second stage of electric field, when it reverses its direction, the Fe^+ convergence by the wind shears becomes more apparent. Finally strong thin Fe^+ layers are formed by downward transport of electric field and wind shears. Figure 4.10 indicates that neutral winds can still converge Fe^+ layers in the presence of the electric field. While they have similar effects on converging Fe^+ ions, the horizontal and vertical winds have very different effects on transporting the neutral Fe atoms as demonstrated in Figures 4.10b

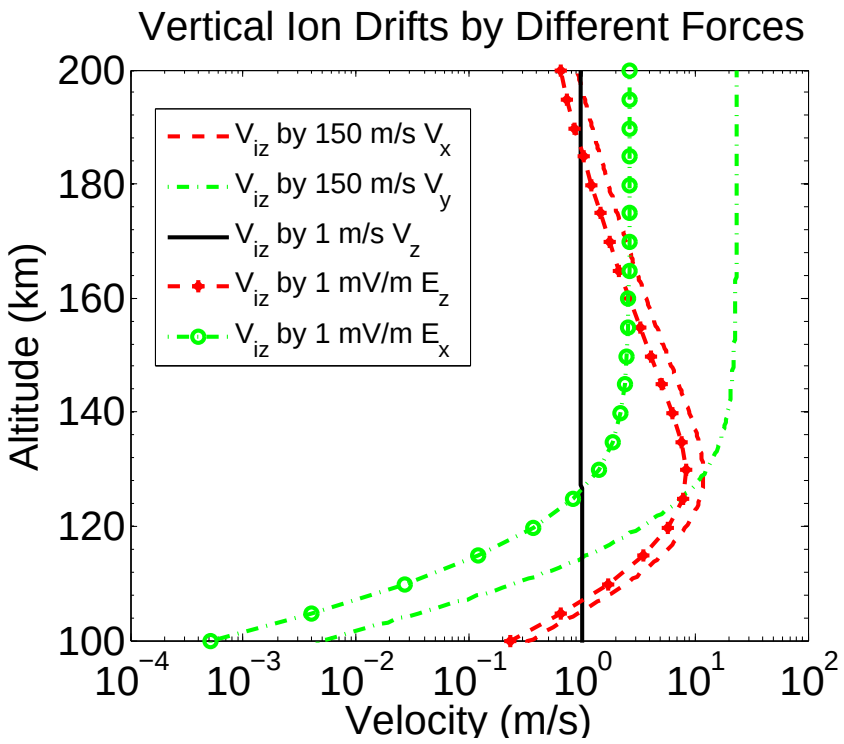

FIGURE 4.9: The vertical ion drift velocities driven by 150 m/s zonal wind (red dashed line), 150 m/s meridional wind (green dash-dotted line), 1 m/s vertical wind (black solid line), 1 mV/m vertical electric field (red dash-starred line), and 1 mV/m east-west electric field (green dash-circled line).

and 4.10d. Broad thermospheric Fe layers are found in Figure 4.10b when there is no vertical wind. Under this circumstance, the Fe atoms are localized and lost only through charge transfer and ionization. Since the lifetime of Fe atoms is much longer than the wave period, the second Fe layer emerges when the first Fe layer has not been depleted. In contrast, when the vertical wind is present in Figure 4.10d, the produced Fe layers become much thinner in time than those in Figure 4.10b. In this case, the neutral Fe atoms are transported downward by the vertical wind following the phase of gravity wave. Because the Fe layer shape in Figure 4.10 is much more comparable to the lidar observations than that in Figure 4.10b, it demonstrates the importance of vertical wind in shaping the observed Fe layers. It is worth to point out that the horizontal divergence has been considered in Figure 4.10 simulations.

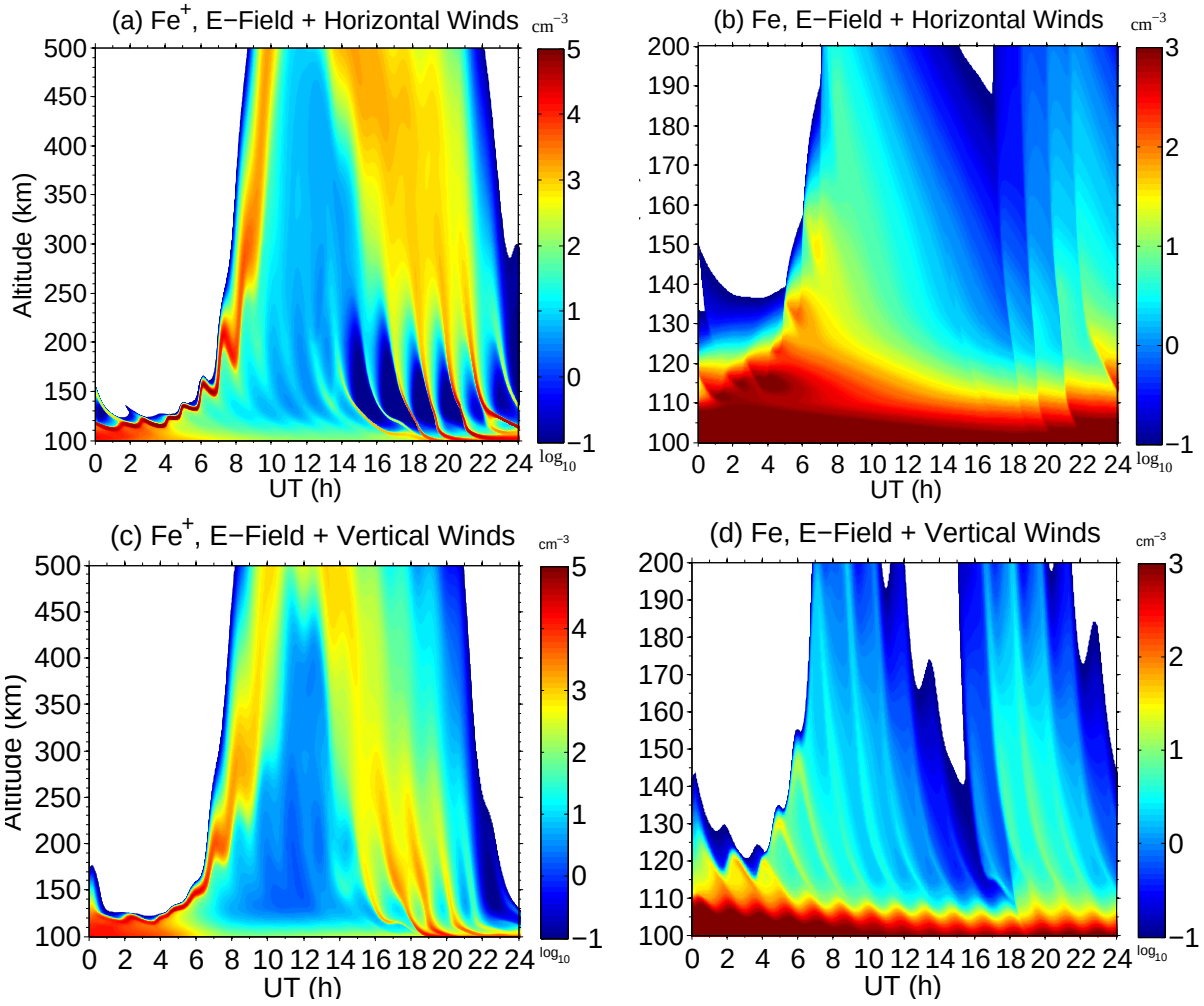

FIGURE 4.10: Experiments of Fe^+ transport by the combination of electric field and winds. Figure 4.3a shows the electric field used, and the aurora electron input is turned on using GLOW model for McMurdo on 28 May 2011. The spectrum of the aurora electron is set up by Maxwellian distribution with 1.0 keV characteristics energy and 1.5 $erg/(cm^{-2}s^{-1})$ energy flux input. Fe^+ and Fe densities in (a) and (b) are for horizontal wind only, in (c) and (d) for vertical wind only, which includes the effects of horizontal divergence of horizontal winds for both Fe^+ and Fe.

4.4 Formation of Fe Layers – Fe^+ Neutralization via Fe and Fe^+ Chemistry

What the major mechanisms are for conversion from Fe^+ to Fe is another major question raised by *Chu et al.* [2011]. Basically there are two known channels of neutralizing Fe^+ to form Fe atoms. The first channel is the direct electron-Fe^+ recombination. That is, Fe^+ directly combines

with electron to produce Fe via radiative recombination (RR) and dielectronic recombination (DR) [*Nahar et al.*, 1997]. Both RR and DR lead to emission of a photon with energy $h\nu \geq 7.9eV$ (R1):

$$R1: \qquad Fe^+ + e^- \longrightarrow Fe + h\nu$$

Such direct recombination reactions are slow, and the total recombination rate coefficients are around 6.5×10^{-12} and 5.2×10^{-12} cm^3s^{-1} at temperature of 300 and 500 K, respectively [*Nahar et al.*, 1997]. The second channel is the dissociative electron recombination. That is, once Fe^+ is oxidized by O_3 to produce more active FeO^+ (R2), an electron will react with FeO^+ to dissociate the molecular and form a neutral Fe atom in the meantime (R3).

$$R2: \qquad Fe^+ + O_3 \longrightarrow FeO^+ + O_2$$

$$R3: \qquad FeO^+ + e^- \longrightarrow Fe + O$$

$$R4: \qquad FeO^+ + O \longrightarrow Fe^+ + O_2$$

However, FeO^+ is also quite reactive with atomic O that converts FeO^+ back to Fe^+ (R4). The competition between R3 and R4 leads to the lifetime of Fe^+ highly dependent on the density ratio of atomic O and O_3 in the upper mesosphere and lower thermosphere [*Plane*, 2003]. Because its reaction rate coefficient is on the order of 10^{-7} cm^3s^{-1} [*Plane et al.*, 1999], the reaction rate coefficient of dissociative recombination reaction (R3) is significantly larger than that of R1. However, above 115 km, O_3 is significantly reduced because the extremely low pressure prevents the formation of O_3 from the recombination of O and O_2 [*Allen et al.*, 1984; *Plane*, 2003], and photolysis consumes O_3 efficiently. Consequently, it is expected that FeO^+ concentration above 115 km is insufficient for producing the observed Fe density via R3 and R4 competition, so the neutralization

of Fe^+ above 115 km is mainly through the direct recombination R1 as hypothesized by *Chu et al.* [2011].

Such a hypothesis must be tested with quantitative simulations. Furthermore, whether the direct electron-Fe^+ recombination R1 is sufficient to produce the lidar-observed Fe density requires detailed quantitative modeling investigations.This is because the slow production reaction must compete with various loss reactions that convert Fe back to Fe^+ or to compound molecules. Once neutral Fe is formed, it can be lost through photoionization (R5), ionization caused by energetic electrons (R6), charge transfer reactions with O_2^+ and NO^+ (R7 and R8), and oxidization by O_3 (R9):

$$R5: \quad Fe + h\nu \longrightarrow Fe^+ + e^-$$

$$R6: \quad Fe + e^{-*} \longrightarrow Fe^+ + e^- + e^{-*}$$

$$R7: \quad Fe + O_2^+ \longrightarrow Fe^+ + O_2$$

$$R8: \quad Fe + NO^+ \longrightarrow Fe^+ + NO$$

$$R9: \quad Fe + O_3 \longrightarrow FeO + O_2$$

$$R10: \quad FeO + O \longrightarrow Fe + O_2$$

The loss of Fe is mainly through charge transfer and photoionization if there is sunlit condition above 115 km where O_3 is lacking. Under dark polar night conditions, photoionization is absent but aurora particle precipitation may have significant impacts on the production and loss of Fe. The major goal of this section is to investigate the chemical production and loss mechanisms of Fe, test the hypothesis given in *Chu et al.*, [2011], and inspect the roles of aurora activity.

4.4.1 Tests of two known channels of Fe^+ neutralization

To test the hypothesis of direct recombination being the major channel to convert Fe^+ to Fe in the thermosphere proposed by *Chu et al.* [2011], the following two model runs are performed. In the first run, we shut down the direct electron recombination R1 by setting the reaction rate coefficient $k_1 = 0$ while keeping all other coefficients in Tables 3.3 and 3.4. In the second run, we shut down the dissociative electron recombination R3 by setting $k_3 = 0$ while keeping all other coefficients including k_1 in Tables 3.3 and 3.4. The model conditions of source and transport are kept the same for both runs, in which the electric field, horizontal and vertical winds are given by Figures 4.3 and 4.6, and the initial Fe and Fe^+ profiles are taken from Figure 4.1. All initial parameters of major and minor species of neutrals and ions are kept the same for both runs and simulations start at 11 UT. The simulation results of these two runs are compared in Figure 4.11, and the differences are stunning. Above ~120 km, the dissociative recombination is ineffective to produce Fe atoms because of the low O_3 concentration (Figure 4.11a). Although the direct recombination is slow, it is sufficient to produce appreciable Fe densities above 120 km as shown in Figure 4.11b. Below 120 km, the situation is reversed, i.e., the first run with R3 generates significantly more Fe densities than those by the second run with R1. Certainly, to what altitudes R3 can be effective depends on the O_3 concentration profiles as well as on how effective the competing reaction R4 is. Nevertheless, Figure 4.11 demonstrates clearly that the major neutralization mechanism above ~120 km in the thermosphere is the direct electron-Fe^+ recombination, supporting the hypothesis made by *Chu et al.* [2011].

Why is the slow direct recombination able to produce appreciable Fe densities? We further investigate it by comparing the production and loss rates of Fe. The production rate of Fe by the direct electron recombinations function of Fe^+ and electron density is shown in Figure 4.12a, while

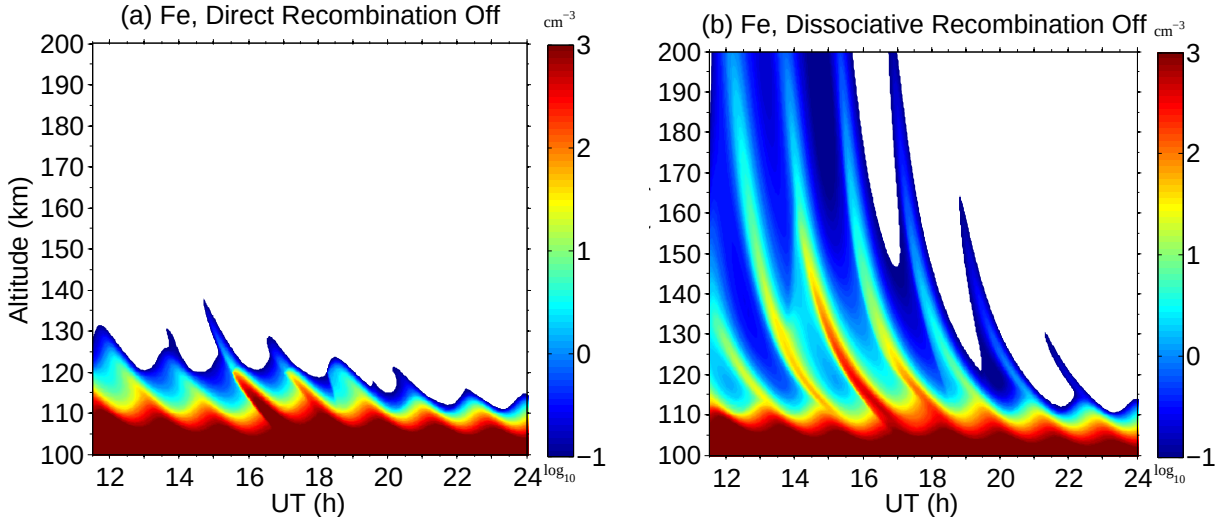

FIGURE 4.11: Numerical experiments of two known channels for Fe^+ neutralization to form neutral Fe in the thermosphere. The contours of Fe density formed from Fe^+ neutralization when (a) shutting off the direct electron-Fe^+ recombination channel, and (b) shutting off the dissociative electron recombination channel. See text for simulation conditions.

the loss of rate of Fe by charge transfer as function of NO^+ and O_2^+ densities is given in Figure 4.12b. The production rate is on the order to 0.2 $cm^{-3}s^{-1}$ for Fe^+ and e^- densities of about 10^5 cm^{-3}, while the charge transfer loss rate is on the order of 0.02 $cm^{-3}s^{-1}$ for NO^+ and O_2^+ densities around 5×10^4 cm^{-3} and Fe density of 400 cm^{-3}. Because the thermospheric Fe layers were observed during dark polar nights, photoionization of Fe is absent. The low concentration of O_3 also makes the loss of Fe and Fe^+ through oxidization negligible. As will be discussed in Section 4.4.2, the Fe ionization by aurora energetic particles is also small. Consequently, the production and loss rates shown in Figure 4.12 are major ones for Fe, while the production of Fe via R1 is the major loss mechanism of Fe^+. Using these rates, we estimate that the Fe^+ lifetime is on the order of several days, and Fe lifetime varies from several hours to about a day that relies on the concentrations of NO^+ and O_2^+. It is clear from these simulations that a very small portion of Fe^+ is converted to Fe via R1, but because the converged Fe^+ layers posses high density (on the order of 10^5 cm^{-3}) and the loss rate of Fe in dark polar night is low, it is sufficient to produce the

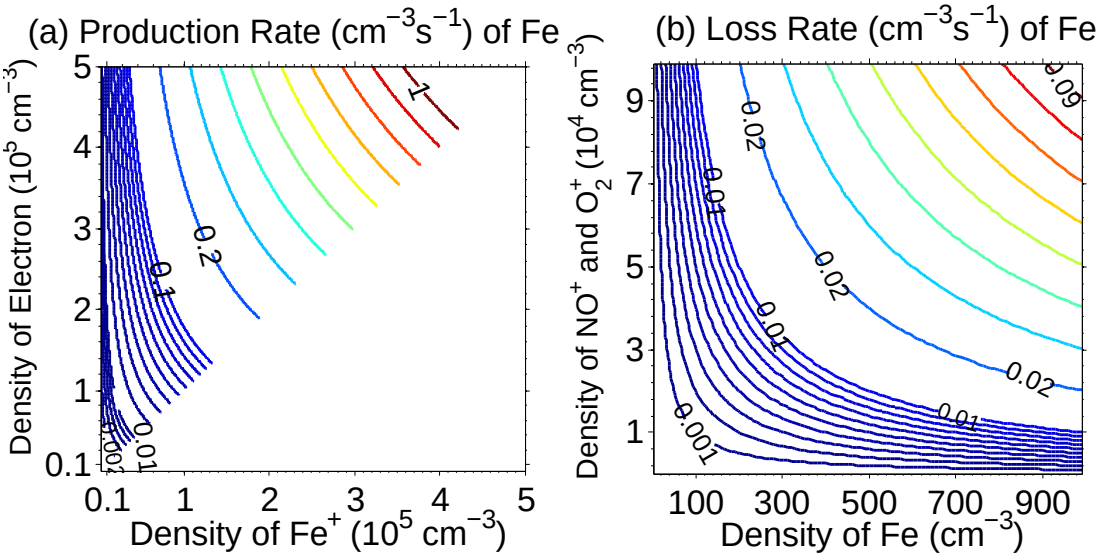

FIGURE 4.12: The loss rate in unit of $cm^{-3}s^{-1}$ of Fe^+ through direct recombination reaction, and the loss rate in unit of $cm^{-3}s^{-1}$ of Fe through charge transfer reactions. The temperature for direct recombination reaction is set to 400 K.

observed Fe densities via R1.

4.4.2 Impacts of aurora activity

Aurora electron precipitation has substantial effects on the partitioning chemistry between Fe and Fe^+, since the energetic electron precipitation penetrating into the thermosphere and mesosphere can cause significant changes of chemical constituents [*Aikin and Smith*, 1999; *Sinnhuber et al.*, 2012] and ionization of neutral atmosphere [*Frahm et al.*, 1997]. The thermospheric Fe layer events reported in *Chu et al.*, [2011] were observed during diffusive aurora activity (occasionally with discrete aurora), so it is worthwhile to investigate how aurora impacts the formation of Fe layers. In contrast to the discrete aurora that has sharply peaked spectrum, diffusive aurora has continuous temporal and large extent spatial signature [*Lui et al.*, 1973]. Diffusive aurora typically comprises

the major energy of aurora input into the polar upper atmosphere [*Sandford*, 1968], and has uniformly impact on the E-F region over scale lengths of thousands of kilometers and for time on the order of hours [*Whalen*, 1983; *Robinson and Vondrak*, 1985]. Aurora electrons can increase plasma density via enhancing the ionization of neutrals, which has been parametrized by different methods [*Roble and Ridley*, 1987; *Solomon et al.*, 1988; *Solomon*, 2001; *Fang et al.*, 2008]. The increase of electron density helps speed up the neutralization of Fe^+ to form Fe, while increasing NO^+ and O_2^+ densities can increase the loss of Fe through enhanced charge transfer. Aurora can also reduce the concentration of O_3 in the upper mesosphere and thermosphere by increasing readily oxidizable substances like NO_x and OH *Sinnhuber et al.* [2012]. Furthermore, the energetic electrons generated by aurora can cause the loss of Fe atoms through direct ionization. In our model, the ionization of Fe in the MLT region by energetic electron impact is quantified.

Given the energetic electron fluxes and ionization cross-section of Fe, the ionization rate of Fe atoms by energetic electrons can be obtained by equation 4.10

$$I_M(z) = \int_{E_T}^{\infty} \phi(E, z) \cdot \sigma(E) \cdot n_M(z)\, \mathrm{d}E \tag{4.10}$$

where M represents the atmosphere species (Fe in this case), $I_M(z)$ is the ionization rate of M at altitude z, $\phi(E, z)$ is the total electron flux, $\sigma_M(E)$ is the ionization cross section of M, $n_M(z)$ is the number density of M, and E_T is the threshold of ionization energy of M. In our model, we adopt GLOW model to compute the energetic electron flux introduced by aurora electron precipitations. The GLOW model provides the ionization rates of the major species like N_2, O_2, and O, but not for Fe. To compute the electron impact on ionization of Fe atoms, we utilize the ionization cross sections of Fe by electron impact, based on the laboratory measurements [*Shah et al.*, 1993]. *Shah et al.* [1993] measured the ionization cross section of R6 for the electron energy spectrum from the

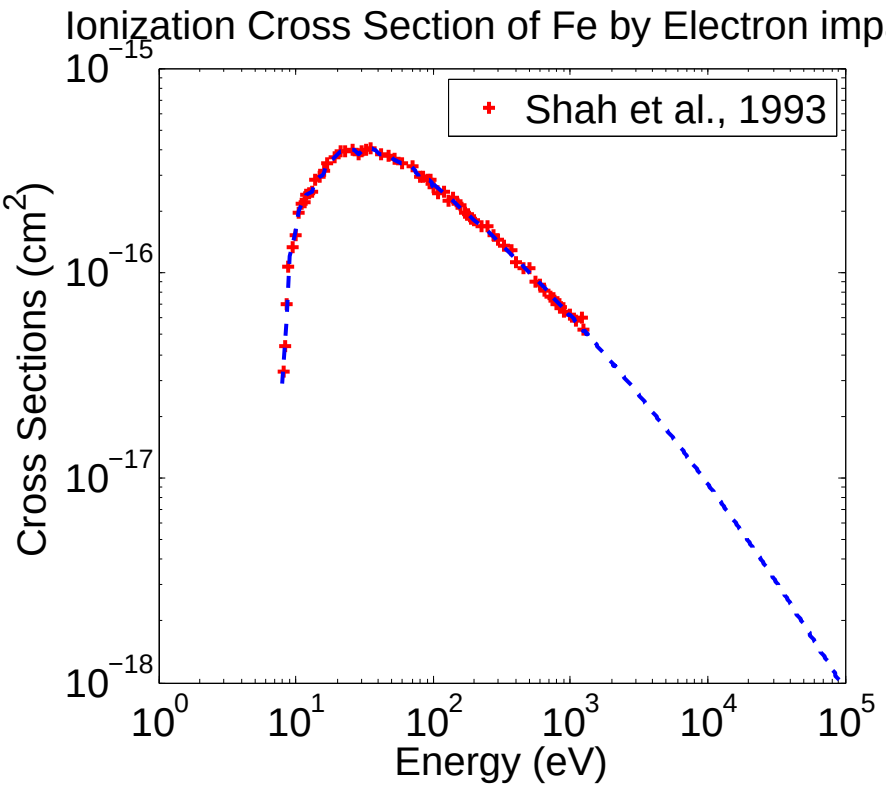

FIGURE 4.13: Ionization cross section of Fe by electron impact. The red cross is the data from *Shah et al.* [1993], and the blue dashed line is the interpolated (between 8 eV and 100 eV) and fitting data (above 100 eV).

ionization threshold 8 eV to 1.25 keV. To obtain the cross section higher than 1.25 keV, we utilize an exponential function, as shown in equation 4.11, to fit the measured cross sections between 100 and 1250 eV,

$$\underset{E>100eV}{\sigma_{Fe}} = e^{aE^2+bE+c} \tag{4.11}$$

By minimizing the fitting error, we obtain that a = -0.0398, b = -0.181, c = -34.169. Below 100 eV, the cross section at any electron energy is interpolated from the measured values. The ionization cross section of Fe used in our model is shown as blue line in Figure 4.13.

The energetic electron flux is computed with the GLOW model. The GLOW model is an energetic electron transport and energy deposition model, providing ionization and excitation

rate of major species, energetic electron production and transport, excited species densities, and air-glow emission rates for the thermosphere [*Solomon et al.*, 1988; *Bailey et al.*, 2002]. Typically, the energy spectrum of diffusive auroral electron is from 0.1 eV $\sim$ 50 keV with Maxwellian energy distribution. The energies of major auroral electrons are well above the thresholds of ionization energy of atmosphere gases (on the order of tens eV), creating energetic secondary electrons during the process of auroral electrons ionizing neutral gases. The roles of primary and secondary electrons in all radiation and ionization phenomena have been recognized for decades [*Green and Sawada*, 1972, *Solomon et al.*, 1988]. The GLOW model utilizes two-stream formalism [*Nagy and Banks*, 1970] to calculate the primary and secondary electron fluxes, as well as the photoelectrons flux generated by solar radiation. As shown in Figure 4.16, the solid lines are the average electron and molecular densities over the 12-h modeling with auroral electron precipitation and the dashed lines are the plasmas densities taken from the output of IRI model for the nighttime conditions. The comparision shows that the electron densities are enhanced by two orders of magnitude, and so are the NO^+, O_2^+ and O^+ densities. The aurora conditions on 28 May 2011 are used in the modeling. Given the total input energy flux and input electron energy spectrum, the energetic electron fluxes at each altitude in the atmosphere are computed by the GLOW, as shown in Figure 4.14. In general, the more total input energy flux, the more energetic electrons generated and the higher ionization rate would be. The higher energy of the electrons, the lower altitude of the peak energetic electron flux is located, leading to less ionization in the upper altitudes but more ionization in the lower altitude region [*Fang et al.*, 2008]. For 100 keV auroral electrons input, the energetic electron flux at lower energy span is 2 $\sim$ 3 magnitudes smaller than that with 1 keV electrons input. At higher energy span, the energetic electron flux does not decay from altitude 126 to 109 km, compared to the input electron flux. By integrating the ionization cross section and energetic electron flux with

unit Fe density using equation 4.10, the ionization rates (in unit of s^{-1}) of Fe are computed and plotted in Figure 4.15 for four conditions of auroral electron input. The rate dramatically decreases when the altitude is lower than 110 km for 1 keV electrons input. At higher altitude above 115 km, the rate with 1 keV electrons input is several magnitudes larger than that with 100 keV electrons input. When the characteristic energy of input electrons is 1 keV, the 10 $erg\ cm^{-2}s^{-1}$ total energy flux input would produce one magnitude higher ionization rate than that by 1 $erg\ cm^{-2}s^{-1}$, and the difference of ionization rate is also about one order of magnitude between 10 and 1 $erg\ cm^{-2}s^{-1}$ energy flux inputs when the characteristic energy of input electrons is 100 keV.

As argued above, auroral electron precipitation plays the role of a double-edged sword in the formation of thermospheric Fe layers. On one hand, the energetic electron fluxes created by auroral electrons dramatically enhance the electron densities in the E-F region, which can speed up the production of Fe atoms via neutralization of Fe^+. On the other hand, aurora also speeds up the loss of Fe atoms via enhanced charge transfer by increased densities of NO^+, O_2^+ and O^+ and via direction ionization. The competition of production and loss of neutral Fe is determined by plasma densities for a given Fe^+ abundance. To investigate the impacts of aurora on the thermospheric Fe layers, we designed an experiment below (Figure 4.17). In the test, square shape initial profiles of Fe^+ and Fe are used, in which Fe^+ ions of $10^4\ cm^{-3}$ distribute from 150 to 160 km and Fe atoms of 200 cm^{-3} distribute from 120 to 130 km. The electric field is set to 1 mV/m, pointing to the east. Uplifted by the electric field, the Fe^+ layer shows an upward motion (Figures 4.17a and 4.17c). The neutral winds are set to zero, so only gravity and diffusion impact the motion of neutral Fe. When GLOW is on, the Fe layer in Figure 4.17b is depleted via charge transfer with NO^+ and O_2^+, and the Fe layer exhibits a slow downward motion caused by gravity. In the region with initial Fe^+ but zero Fe, say 160 km, there is no neutral Fe in the beginning but then the Fe

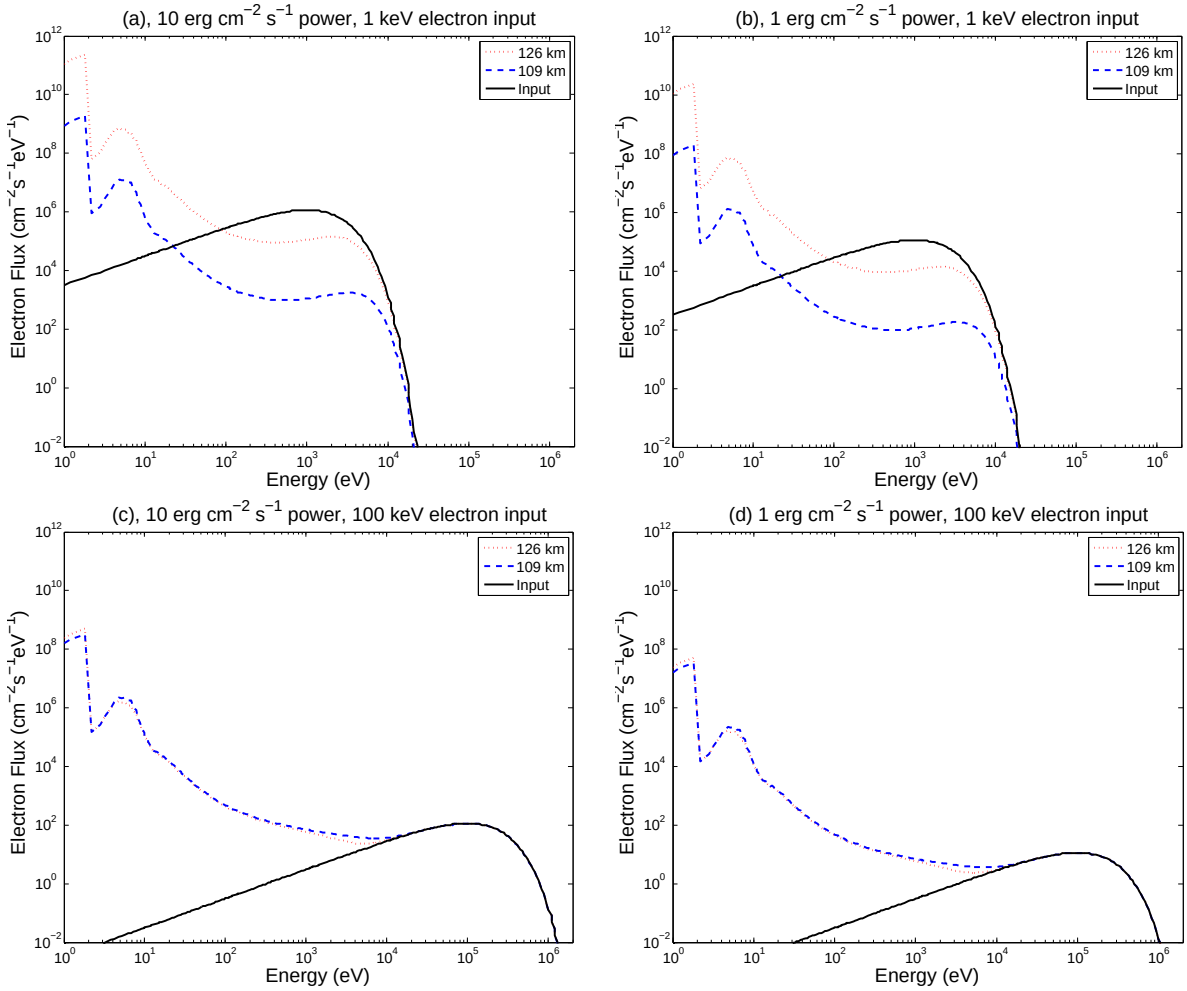

FIGURE 4.14: Downward energetic electron fluxes at 126 km (red dotted line), and 109 km (blue dashed line) by auroral electrons (the solid black line) from the calculation of the GLOW model. The characteristic energy of the auroral electron spectrum is given by Maxwellian: (a) 1 keV characteristic energy and 10 $erg\ cm^{-2}s^{-1}$ integrated energy flux; (b), 1 keV mode energy and 1 $erg\ cm^{-2}s^{-1}$ integrated energy flux; (c), 100 keV mode energy and 10 $erg\ cm^{-2}s^{-1}$ integrated energy flux; (d) 100 keV mode energy and 1 $erg\ cm^{-2}s^{-1}$ integrated energy flux.

atoms are produced through neutralization of Fe^+. Since the Fe^+ density is high in the beginning, the net gain of Fe atoms is seen at first. However, after 15.5 UT the major Fe^+ ions are moved away from 160 km by electric field, so Fe^+ and Fe layers are decoupled and a net loss from Fe layer is seen at 160 km. At higher altitudes, the Fe densities are increased by the increasing densities of Fe^+. When GLOW is off, slightly loss of the initial Fe layer is caused by the lower NO^+ and O_2^+ density, and the initial Fe layer is dragged down by the gravity. Above 140 km, it is hard to see

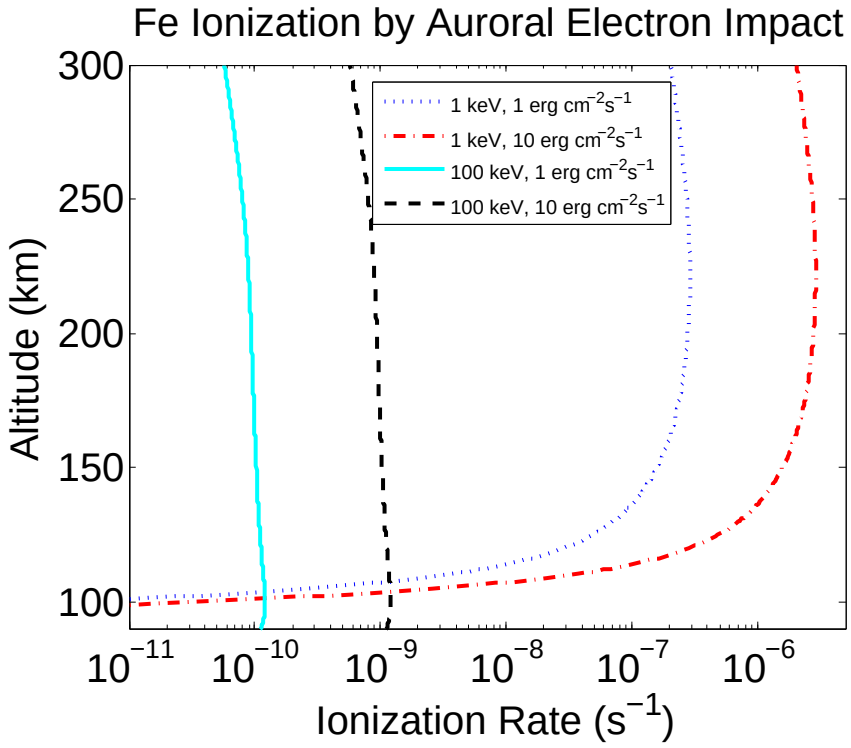

FIGURE 4.15: Rate of ionization of Fe by electron impact under the four types of input of auroral electrons: blue line with 1 keV and 10 $erg\ cm^{-2}s^{-1}$ integrated energy flux input; red line 1 keV and 1 $erg\ cm^{-2}s^{-1}$ integrated energy flux input; black line with 100 keV and 10 $erg\ cm^{-2}s^{-1}$ integrated energy flux input; cyan line with 100 keV and 1 $erg\ cm^{-2}s^{-1}$ integrated energy flux.

net production from Fe^+ neutralization because of the lower electron density. A diffusive Fe layer originated from the initial Fe layer is observed, and it is caused by the diffusion. Because of the shape of initial Fe layer, its large density gradient on the top edge of Fe layer gives rise to very big diffusion velocity. This test demonstrates that the energetic electron precipitation caused by the diffusive aurora enhances the neutralization of Fe^+ in the converged Fe^+ layer by increasing the electron densities. When the Fe and Fe^+ layers are decoupled, the lack of Fe production leads to net loss of Fe via charge transfer with NO^+ and O_2^+. Such net loss of Fe can be enhanced by the increased NO^+ and O_2^+ densities due to aurora particle precipitation.

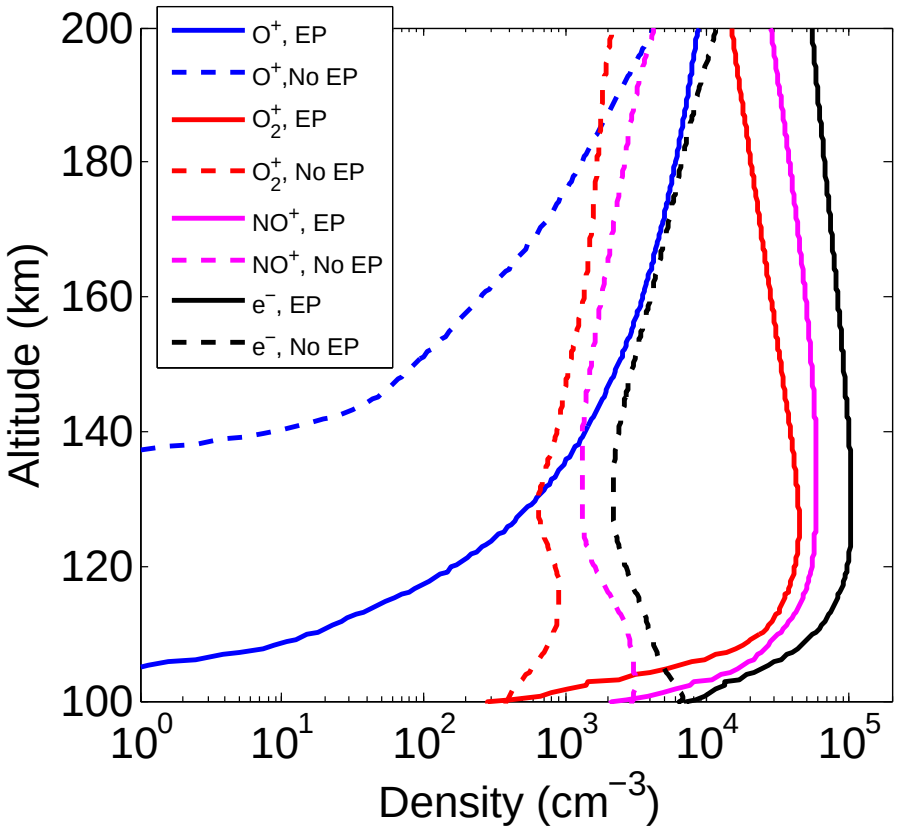

FIGURE 4.16: The average densities of NO^+, O_2^+, O^+ and e^- over 12 hours. The solid lines represent the molecular ion density with auroral electrons precipitation, and the dashed lines without electron precipitation.

4.5 Simulations of Gravity-Wave-Dominated Thermospheric Fe Layer

As pointed out in *Chu et al.* [2011], there was a geomagnetic storm on 28 May 2011 with Kp index of 6. The empirical electric potential model [*Weimer*, 2005] is used to compute the high-latitude electric potential and magnetic field-aligned current. The electric field strength calculated from the electric potential, $\vec{E} = -\nabla\Phi$, is illustrated in Figure 4.3a. For the particle precipitation on 28 May 2011, the average hemisphere power input between 11 UT and 23 UT is about 37.1 GW, which is obtained from the measurements of NOAA POES satellites. The location of McMurdo is close to

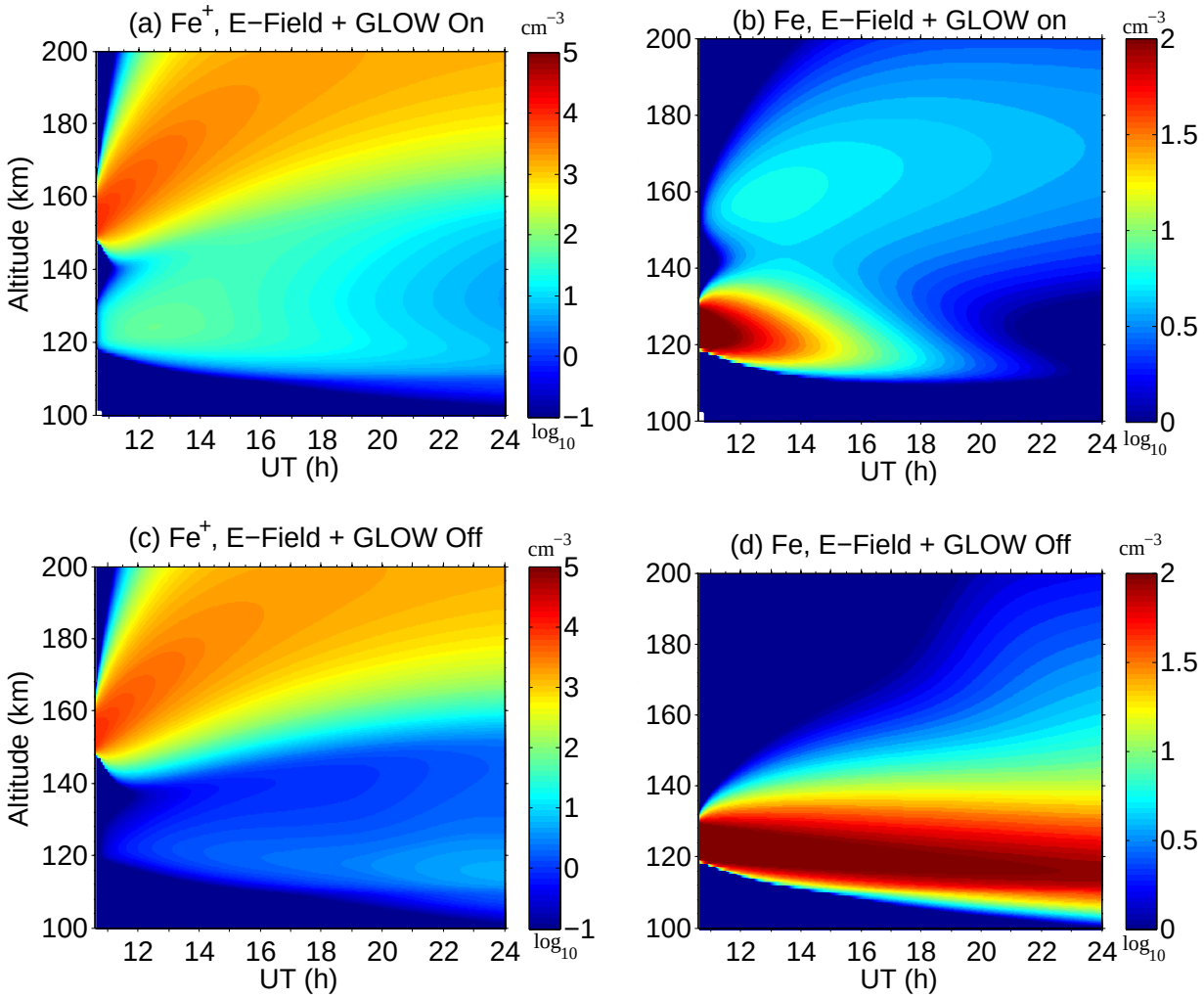

FIGURE 4.17: Tests of aurora effects on the thermospheric Fe and Fe^{+} layers. Wind is turned off, and electric field is set to 1 mV/m directing to east. GLOW is in for (a) and (b), and GLOW is off for (c) and (d).

the poleward edge of aurora oval, and we take 1.5 $erg/(cm^2 s^1)$ as input energy flux for the GLOW model. The auroral electron spectrum input is set to Maxwellian distribution with characteristic energy of 1 keV. The initial environmental neutral and ionic parameters are provided by MSIS and IRI models for the specific date and geomagnetic conditions. The time step is set to one second, and the data are saved every two minutes. The simulation starts at 11 UT and runs for 12 hours, the same as the lidar observation period. In this simulation, the horizontal divergence of horizontal

wind is turned off, and the density variations of Fe/Fe^+ only can be changed by vertical transport or chemical reactions.

Combining all the factors together, the pattern of Fe^+ layers on 28 May 2011 is simulated and shown in Figure 4.18a. The produced thermospheric Fe layers in Figure 4.18b are a quite close replicate of the observed Fe layer shapes on 28 May 2011 [*Chu et al.*, 2011]. The initial Fe^+ density profile used in the model for reproducing the Fe observations is given in Figure 4.1, whose peak density altitude stay around 100 km at the start time of 11 UT. The simulations show that in the phase of upward transport by electric field, the Fe^+ ions are sufficiently transported upward and reach over 300 km. The first Fe^+ layer with weak convergence is found around 150–160 km. The density of Fe^+ in the converged layer is high enough to produce net accumulation of Fe through direct recombination with electrons. The produced Fe atoms follow the neutral vertical wind and move downward, forming the first Fe layer around 12 UT. The second Fe^+ layer emerges from higher altitudes with stronger convergence when the upward transport by electric field becomes weaker. When the Fe^+ layer reaches the altitude of 130–140 km, the upward transport by electric field push the layer back to 170 km, and the layer is broadened by electric field. The second Fe layer is formed around 13–14 UT with the formation of the second Fe^+ layer. When the Fe^+ layer is pushed to higher altitudes, the Fe layer continuously moves downward by the neutral vertical wind, following the phase of the gravity wave. Due to the separation from the Fe^+ layer, less production of Fe leads to net loss of Fe below 125 km. Therefore, we see the second Fe layer shows lower density below 125 km. The third Fe^+ layer emerges at the phase of electric field reversing its direction, and a thin Fe^+ layer with strongest convergence is found when the electric field points to northward, corresponding to the downward transport of Fe^+. The third Fe layer is formed around 15 UT through the direct recombination of Fe^+ with electrons. In Figure 4.18b, the third Fe layer

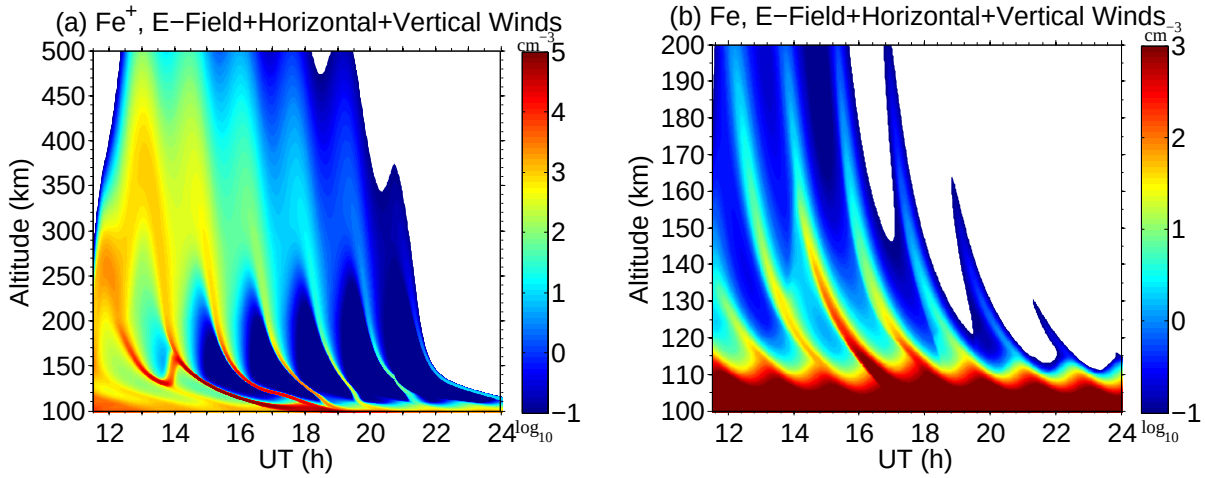

FIGURE 4.18: Simulation of the thermospheric Fe layer event on 28 May 2011 at McMurdo with the combination of all winds (both horizontal and vertical winds), electric field and auroral electron precipitation input. (a) and (b) are the simulations without horizontal divergence.

is connected to the second Fe layer by a Fe layer with low density. This connecting Fe layer is produced by the upward moving Fe^+ layer driven by electric field between the second and third Fe^+ layers. According to the simulation, if the gravity wave activity continues, the Fe^+ layers are converged for another 4 times before the end of the observations around 23 UT. Correspondingly, the neutral Fe layers are formed several more times but with lower peak heights and less Fe density above 130 km because of the lower height and density of Fe^+ layers.

The early observations presented the metallic ions (Fe^+/Mg^+) existing to at least 400 km in the F region [*Mende et al.*, 1985; *Grebowsky and Reese*, 1989; *Gardner et al.*, 1998; *McNeil et al.*, 1998]. Previous observations by satellite or rocket found the metallic ions (Mg^+ or Fe^+) exiting in a wide range from 100 to 500 km and high Mg^+ or Fe^+ density of $\sim 10^4\ cm^{-3}$ at 200 km [*Taylor*, 1973; *Zhlood'ko et al.*, 1974; *Gérard*, 1976, *Grebowsky and Brinton*, 1978]. The simulated Fe^+ altitudes and densities in Figure 4.18a match these observations quite well. To compare the simulated Fe densities with observations, two sets of comparisions for the time series of Fe density variations at 130 and 140 km are provided in Figure 4.19. Figures 4.18 and 4.19 demonstrate

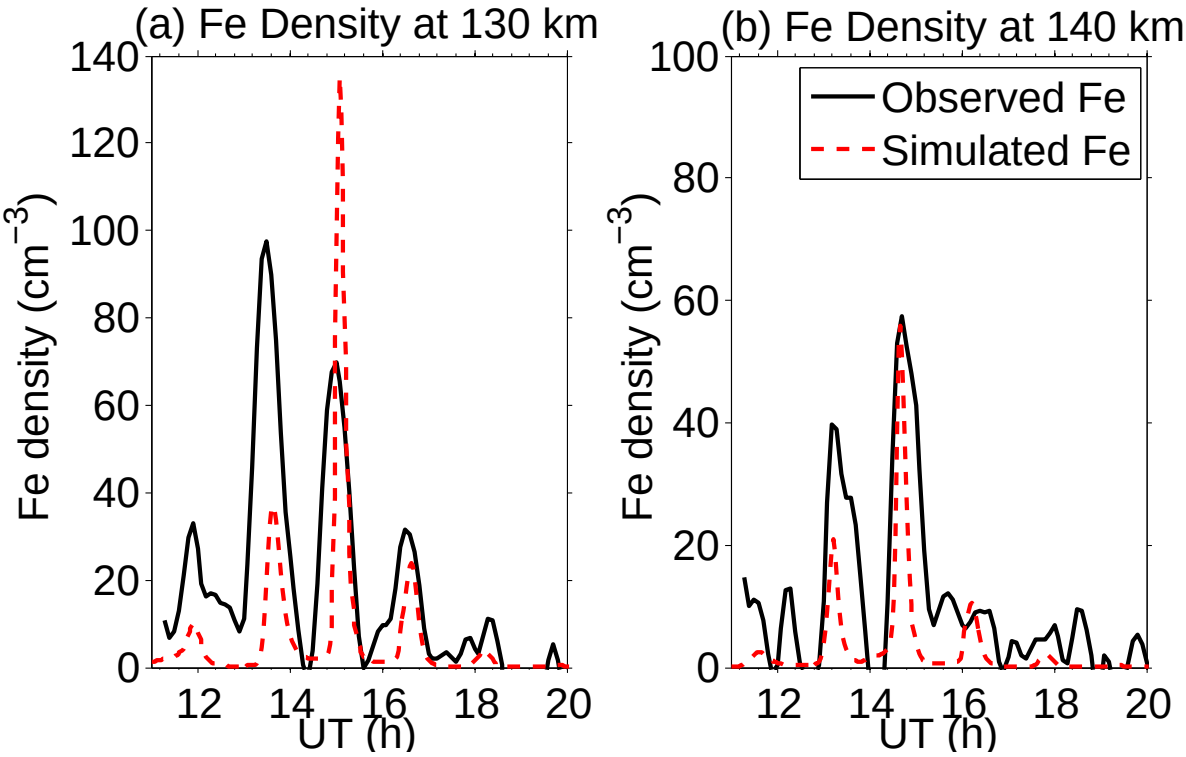

FIGURE 4.19: Comparison of the simulated Fe densities (red dashed line) with the lidar-observed Fe densities (black solid line) at (a) 130 km and (b) 140 km through the observation period.

that the model is able to reproduce the lidar observations satisfactorily in general after putting all considerations together, when the transport caused by horizontal divergence of horizontal wind is neglected.

4.6 Conclusions

With a newly developed 1-D thermospheric Fe/Fe^+ model, we explore the source, formation and evolution mechanisms of thermospheric neutral Fe layers recently discovered by lidar in the altitude range of 100–200 km in Antarctica. Overall numerical simulations confirm the hypothesis proposed by *Chu et al.* [2011] that the thermospheric Fe layers are produced through the neutralization of vertically converged Fe^+ layers. By incorporating the latest reaction rate coefficients and accurate solvers for chemical reactions, the model quantitatively demonstrates that the conversion from

Fe^+ to Fe above 120 km is mainly through the direct electron-Fe^+ recombination via radiative and dielectronic recombinations. If shutting down the direct recombination channel, the dissociative recombination fails to produce sufficient Fe density above 120 km because of the lack of O_3. The energetic electron precipitation by diffusive aurora enhances the neutralization of converged Fe^+ layers by increased electron density, thus increasing the neutral Fe density. Once decoupled from Fe^+, Fe layers experience net loss due to the charge transfer with NO^+ and O_2^+. During aurora periods, such net loss of Fe can be enhanced due to the increased NO^+ and O_2^+ densities.

While the meteor injection rate of iron species is negligible above 120 km as shown in various studies like *Vondrak et al.*, [2008], our model demonstrates that the polar electric field is sufficient in transporting Fe^+ ions from their main deposition region (∼80–110 km) to the E–F regions, therefore, supplying the source for thermospheric Fe layers. The transport of Fe^+ by the electric field depends on its direction and magnitude. In the Southern Hemisphere, the south-east electric field (relative to the geomagnetic field) produces upward ion flow, while the north-west direction produces downward ion flow. The south-west and north-east electric fields lead to convergent flow and divergent flow, respectively. Another new finding from the modeling study is that the wave-induced vertical wind plays a key role in transporting neutral Fe atoms to form the repeated Fe layers with downward phase progression. Because of the high inclination angle of the geomagnetic field line at McMurdo, the vertical wind has a large wind factor and therefore can induce vertical ion drift velocities with magnitudes similar as or even larger than those by the neutral horizontal winds, despite the vertical wind is much smaller than the horizontal winds. Wave-induced vertical shears of both vertical and horizontal winds can converge Fe^+. Certain directions of electric field can also converge Fe^+ layers as illustrated in Figure 4.4. Once Fe is formed from Fe^+ neutralization, Fe is no long subject to the constraint of electromagnetic force but is quickly balanced by the

neutral background wind via collisions and also influenced by gravity and diffusion. Consequently, in the altitude of 100–200 km where the collision is still sufficient, neutral Fe atoms move with the backgroud medium that is perturbed by the gravity-wave-induced winds, forming the repeated layers as observed by lidar.

The gravity-wave-dominated thermospheric Fe layer event on 28 May 2011 is reproduced with estimated geomagnetic conditions, neutral winds and initial Fe^+ and Fe density profiles when the horizontal divergence is neglected. At high latitudes, the convection electric field powered by the plasma convection in the magnetosphere is essential for uplifting Fe^+ ions from the main deposition region (below ∼110 km) into higher altitudes. The thermospheric Fe layers are then produced through the neutralization of converged Fe^+ layers mainly via the direct electron-Fe^+ recombination. Convergence of Fe^+ layers is driven by the vertical shears of gravity-wave-induced winds under the presence of electric field. Furthermore, the convection electric field exhibits diurnal variations, leading to the ion flow going through a diurnal cycle of upward, downward, convergent and divergent flow. As a result, the converged Fe^+ layer heights vary with time as the simulations show, therefore, leading to the varied maximum heights of observed Fe layer in *Chu et al.* [2011]. The fact that horizontal transport is not included in such successful event simulations strongly indicates that the vertical transport is the primary driver of the observed Fe layer shapes in the polar cap while the horizontal transport is secondary or plays a minor role.

Chapter 5

Source, Formation and Evolution of Thermospheric Fe Layers: 2. Simulations of 28 May 2011 Event

5.1 Introduction

The thermospheric Fe layers observed on 28 May 2011 feature gravity-wave structures with multiple distinguished layers, whose relatively density perturbations are over 100%, and great altitude extension up to 155 km. The question to ask in this chapter is the evolution of the observed neutral Fe layers on 28 May 2011. Once Fe atoms are formed from converged Fe^+ layers, the neutral Fe atoms are no longer subject to Coulomb and Lorenz forces. Without considering the horizontal transport, the Fe motion is determined by equation 3.18. That is, the Fe atoms are balanced by the neutral background winds via collisions, and also influenced by gravity and diffusion. Contrarily, Fe^+ ions are strongly influenced by electromagnetic forces in addition to the neutral winds, gravity and diffusion, so Fe^+ motions can deviate from the neutral-wind-constrained Fe motion.

Consequently, Fe and Fe^+ can separate from each other, depending on the electric field strength and direction. Once the Fe layer is decoupled from the Fe^+ layer, the Fe production stops and then net loss of Fe results from charge transfer with NO^+ and O_2^+. However, because the Fe^+ loss due to the Fe production is very minor, the remaining Fe^+ layer still contains sufficiently high density so that it continues producing Fe. Therefore, neutral Fe atoms will be generated at multiple times and locations. If the Fe^+ layer stays with the Fe layer, the Fe production can exceed the Fe loss due to charge transfer, leading to increasing Fe density. All these factors affect the neutral Fe layer shape and contribute to the variations in Fe density and layer height. We have investigated the interplay of these various factors via simulating the event on 28 May 2011 in Section 4.5. The simulation results showed in Figure 4.18 in Chapter 4, to a great extent, reproduced many features of the lidar observations after neglecting one critical process — terms of horizontal transport driven by horizontal winds.

In the studies of polar caps sporadic-E layers, the importance of vertical winds in transporting ions at high latitudes has been recognized by *MacDougall et al.* [2000a, b]. During their sporadic-E observations, *MacDougall et al.* [2000a] noted that the convection velocity driven by the electric field was slow, so the ion convergence caused by the electric field was excluded and they attributed their observed sporadic-E layers to theb vertical convergence motions of ions induced by gravity waves. In the numerical modeling study by *MacDougall et al.* [2000b], they simulated the sporadic-E layer through modeling the vertical motions of ions caused by gravity waves, but the motions due to the convective electric field and horizontal winds had been neglected.

The neglect of horizontal winds could be troublesome for simulations of both Fe and Fe^+ layers. Under the reasonable assumption that atmosphere is relatively incompressible, the vertical convergence motions induced by the vertical wind shear of gravity-wave-induced vertical wind are

always accompanied by the horizontal divergence of horizontal winds. When vertical wind shears converge ions to thin layers, the horizontal divergence of horizontal winds can largely offsets the convergence especially when the gravity-wave vertical wind shears are large. In this chapter, we will investigate the impact of horizontal divergence on the formation of thermospheric Fe/Fe^+ layers. Section 5.2 offers the analytical expression of horizontal divergence of horizontal winds caused by gravity waves for neutrals and ions. Section 5.3 will explore how to reproduce the thermospheric Fe event on 28 May 2011, through itegrating all the necessary physical and chemical processes.

In this chapter, we take the same model setup in Chapter 4 for simulations of Fe/Fe^+ layers. Without particular explanations, the intial profiles of Fe/Fe^+, the calculation of electric field, auroral electron parameters and gravity wave setup in Chapter 4 are continued to be used in this chapter. The starting time of simulations are set to 11 UT, the same as the setup in Figure 4.18.

5.2 Horizontal Divergence of Horizontal Gravity-Wave Winds

As discussed in Chapter 3, the divergence of number density flux $\nabla \cdot (N_m \vec{V}_m)$ can be decomposed into horizontal divergence of number density flux and vertical transport: $\nabla \cdot (N_m \vec{V}_m) \approx \frac{\partial N_m V_{m,z}}{\partial z}$ $+ N_m \nabla_h \cdot \vec{V}_{m,h}$ by assuming relatively horizontal homogeneous N_m. In the simulation of Figure 4.18, the contribution of the term $N_m \nabla_h \cdot \vec{V}_{m,h}$ to the Fe density variations has been neglected, leading over-estimated wave-induced density perturbations in Figure 4.19. To reasonably simulate the Fe/Fe^+ layers perturbed by gravity waves, the horizontal divergence of horizontal winds ($\nabla_h \cdot \vec{V}_{m,h}$), associated with the gravity-wave vertical wind shears, needs to be taken into account. By adopting gravity wave theory [*Hines*, 1974], $\nabla_h \cdot \vec{V}_{m,h}$ is linked to the vertical wind via gravity wave polarization relation. The purpose of this section is to assemble the mathematical relations on the

$\nabla_h \cdot \vec{V}_{m,h}$ for both neutrals and ions, and evaluate the influence of horizontal divergence on the Fe/Fe^+ layer formation.

5.2.1 Horizontal divergence of gravity-wave horizontal winds

By assuming a relative idealized model in which the atmosphere is stationary and uniform in both temperature and composition, *Hines* [1974] provided a set of simplified equations 5.1 – 5.3, governing the atmospheric oscillations under static conditions ($\bar{u}_h = 0$),

$$\rho_0 \frac{\partial \vec{u'}}{\partial t} = \rho' \vec{g} - \nabla p' \tag{5.1}$$

$$\frac{\partial p'}{\partial t} + \vec{u'} \cdot \nabla p_0 = C_s^2 (\frac{\partial \rho'}{\partial t} + \vec{u'} \cdot \nabla \rho_0) \tag{5.2}$$

$$\frac{\partial \rho'}{\partial t} + \vec{u'} \cdot \nabla \rho_0 + \rho_0 \nabla \cdot \vec{u'} = 0 \tag{5.3}$$

where the variables with prime represent the perturbed physical parameters, and the variables with subscript 0 mean the unperturbed background. $\vec{u}$ is wind velocity, ρ is density, p is pressure, $\vec{g}$ is the gravitational acceleration, and the speed of sound C_s, which is equal to $C_s^2 = \gamma \frac{p_0}{\rho_0}$. Equations 5.1, 5.2 and 5.3 are the linearized equations of momentum, adiabatic state, and mass conservation.

The hydrostatic condition gives equation 5.4

$$\rho_0 \vec{g} - \nabla p_0 = 0 \tag{5.4}$$

and the unperturbed background p_0 and ρ_0 decrease exponentially with respect to altitude, and can be described as equation 5.5

$$p_0, \rho_0 \propto e^{-z/H} \tag{5.5}$$

where $H \equiv C_s^2/\gamma g$ is the scale height and z is a Cartesian coordinate in vertical direction.

Assume the solutions of the gravity wave have complex Fourier forms:

$$(u'_h, u'_z, p', \rho') = (\tilde{u_h}, \tilde{u_z}, \tilde{p}, \tilde{\rho}) e^{i(\omega t - k_h x - k_z z)} \tag{5.6}$$

where $(u'_h \vec{e_h},\ u'_z \vec{e_z}) = \vec{u'}$, $\vec{e}$ is the unit vector. Substituting equation 5.6 into equations 5.1 to 5.3, we have a set of algebraic equation

$$i\omega\rho_0 \tilde{u_h} - ik_h \tilde{p} = 0 \tag{5.7}$$

$$i\omega\rho_0 \tilde{u_z} + \tilde{\rho} g - ik_z \tilde{p} = 0 \tag{5.8}$$

$$i\omega\tilde{p} - \rho_0 g \tilde{u_z} + C_s^2(-i\omega\tilde{\rho} + \frac{\rho_0}{H}\tilde{u_z}) = 0 \tag{5.9}$$

$$i\omega\tilde{\rho} - \frac{\rho_0}{H}\tilde{u_z} - \rho_0(ik_h\tilde{u_h} + ik_z\tilde{u_z}) = 0 \tag{5.10}$$

Here we used equations 5.5 and $\nabla\rho_0 = -\rho_0/H$.

Substitute equation 5.7 into equation 5.9, we have

$$\frac{i\omega^2\rho_0}{k_h}\tilde{u_h} - \rho_0 g\tilde{u_z} + C_s^2(-i\omega\tilde{\rho} + \frac{\rho_0}{H}\tilde{u_z}) = 0$$

or

$$\frac{i\omega^2}{k_h}\tilde{u_h} - g\tilde{u_z} + C_s^2(-i\omega\frac{\tilde{\rho}}{\rho_0} + \frac{1}{H}\tilde{u_z}) = 0 \tag{5.11}$$

From equation 5.10, we have

$$i\omega\frac{\tilde{\rho}}{\rho_0} = \frac{1}{H}\tilde{u_z} + i(k_h\tilde{u_h} + k_z\tilde{u_z}) = 0 \tag{5.12}$$

Substitute equation 5.12 into equation 5.11, we have

$$\frac{i\omega^2}{k_h}\tilde{u_h} - g\tilde{u_z} + C_s^2(-\frac{1}{H}\tilde{u_z} - ik_h\tilde{u_h} - ik_z\tilde{u_z} + \frac{1}{H}\tilde{u_z}) = 0 \tag{5.13}$$

So,

$$\frac{i\omega^2 - iC_s^2k_h^2}{k_h}\tilde{u_h} - g\tilde{u_z} - iC_s^2k_z\tilde{u_z} = 0 \tag{5.14}$$

Utilizing equation 5.6, we rewrite equation 5.14 to a differential equation 5.15

$$\frac{\omega^2 - C_s^2k_h^2}{k_h^2}\nabla_h \cdot \vec{u}_h = -gu_z + C_s^2\frac{\partial u_z}{\partial z} \tag{5.15}$$

So the horizontal divergence of horizontal wind is given by equation 5.16

$$\nabla_h \cdot \vec{u}_h = \frac{gu_z - C_s^2\frac{\partial u_z}{\partial z}}{C_s^2 - \frac{\omega^2}{k_h^2}} \tag{5.16}$$

If the background wind is not zero, the frequency ω should be intrinsic frequency $\omega_i = \omega - k_h\bar{u}$.

For the purpose of numerical calculation, the speed of sound also can be written as [*Bass et al.*, 2007]

$$C_s^2 = \frac{\gamma RT}{M} \tag{5.17}$$

where γ is the ratio of the specific heat at constant pressure C_p to the specific heat at constant volume, C_v, ranging from 1.4 to 1.67; R is the universal gas constant at 8314.48 J/kmol K; T is the temperature at Kelvin; and M is the mean molecular mass in unit of kg/kmol.

5.2.2 The impact of horizontal divergence on Fe^+ layers

The effects of horizontal gravity-wave wind divergence on Fe^+ are evaluated by taking the divergence of equation 3.12. Here we only consider the horizontal gradients associated with the gravity-wave wind, neglecting the horizontal gradients caused by the electric field, ionic pressure and gravity. Therefore, we have,

$$\nabla \cdot \vec{V_i} \approx \frac{\xi}{1+\xi^2}\frac{\nabla \cdot (\vec{V_n} \times \vec{B})}{B} + \frac{1}{1+\xi^2}\frac{\nabla \cdot ((\vec{V_n} \cdot \vec{B})\vec{B})}{B^2} + \frac{\xi^2}{1+\xi^2}\nabla \cdot \vec{V_n} \tag{5.18}$$

where $\vec{V_n}$ is neutral winds, $\vec{V_i}$ is ion drift velocity.

The first term of equation 5.18 is

$$\nabla \cdot (\vec{V_n} \times \vec{B}) = \vec{B} \cdot (\nabla \times \vec{V_n}) - \vec{V_n} \cdot (\nabla \times \vec{B}) \tag{5.19}$$

By neglecting $\nabla \times \vec{B}$, we can approximate equation 5.19 by only considering the curl of gravity wave winds, meanwhile, the equation 5.7 leads to $\tilde{u_x}k_y = \tilde{u_y}k_x$, which gives rise to the zero curl of $\vec{V_h}$, $\left(\nabla \times \vec{V_h} = \frac{\partial V_{n,y}}{\partial x} - \frac{\partial V_{n,x}}{\partial y} = 0 \right)$

$$\begin{aligned} \nabla \cdot (\vec{V_n} \times \vec{B}) &= -\Big(\frac{\partial V_{n,z}}{\partial x} - \frac{\partial V_{n,x}}{\partial z}\Big)B_y + \Big(\frac{\partial V_{n,y}}{\partial x} - \frac{\partial V_{n,x}}{\partial y}\Big)B_z \\ &= -(\frac{\partial V_{n,z}}{\partial x} - \frac{\partial V_{n,x}}{\partial z})B_y \end{aligned} \tag{5.20}$$

The second term of equation 5.18, by neglecting $\nabla \cdot \vec{B}$

$$\begin{aligned} \nabla \cdot ((\vec{V_n} \cdot \vec{B})\vec{B}) &\approx \nabla(\vec{V_n} \cdot \vec{B})\vec{B} \\ &\approx \frac{\partial V_{n,y}}{\partial y}B_y^2 + \frac{\partial V_{n,z}}{\partial y}B_zB_y + \frac{\partial V_{n,y}}{\partial z}B_yB_z + \frac{\partial V_{n,z}}{\partial z}B_z^2 \end{aligned} \tag{5.21}$$

The third therm of equation 5.18

$$\nabla \cdot \vec{V_n} = \nabla_h \cdot \vec{V_h} + \frac{\partial V_z}{\partial z} \tag{5.22}$$

To sum up, the horizontal divergence associated with gravity-wave winds is given by equation 5.23

$$\nabla_h \cdot \vec{V_i} \approx -\frac{\xi}{1+\xi^2}\frac{\partial V_{n,z}}{\partial x}\cos\Theta_D + \frac{1}{1+\xi^2}\Big(\frac{\partial V_{n,z}}{\partial y}\cos\Theta_D \sin\Theta_D + \frac{\partial V_{n,y}}{\partial y}\cos^2\Theta_D\Big) + \frac{\xi^2}{1+\xi^2}\nabla_h \cdot \vec{V_h} \tag{5.23}$$

Specifically, we neglect the term of $\partial V_{n,y}/\partial y$ because $\cos^2\Theta_D$ is small when the Θ_D is large, for instance, $\cos^2 80^\circ \approx 0.03$ for McMurdo. We also neglect the horizontal gradient of vertical wind because of the small magnitude of vertical wind and large horizontal wavelength. Therefore, the effects of horizontal divergence on ions by the gravity wave can be approximated by equation 5.24

$$\nabla_h \cdot \vec{V_i} \approx \frac{\xi^2}{1+\xi^2}\nabla_h \cdot \vec{V_h} \tag{5.24}$$

5.2.3 The Impact of Horizontal Divergence on Fe/Fe^+ Layers

The impact of horizontal divergence of horizontal winds on Fe/Fe^+ layer formation driven by vertical wind is investigated in this section. The divergence term in the continuity equation 3.1 can be rewritten as $\nabla \cdot (N_m\vec{V}) = \nabla_h \cdot (N_m\vec{V}_{m,h}) + \frac{\partial N_m V_{m,z}}{\partial z}$. If the horizontal gradient of N_m is negligible, then $\nabla_h N_m \approx 0$. The divergence term for neutral Fe becomes,

$$\nabla \cdot (N_{Fe}\vec{V}_{Fe}) \approx \frac{\partial N_{Fe}V_{Fe,z}}{\partial z} + N_{Fe}\nabla_h \cdot \vec{V_h} \tag{5.25}$$

TABLE 5.1: Conditions for simulations

Conditions[a]	Numerical Experiments [b]				
	Figure 5.1	Figure 5.2	Figure 5.6	Figure 5.8	Figure 5.11
Zonal wind	Off	On	On	On	On
Meridional wind	Off	On	On	On	On
Vertical wind	ON	On	On	On	On
Electric field	Off	On	On	On	On
Horizontal divergence	On/Off	On/Off	On	On	On
Chemistry	Off	On	On	On	On
GLOW Model:	Off	On	On	On	On
Energy		1.0	1.0	1.0	1.0
Energy flux		1.5	1.5	1.5	30.
Gravity wave parameters:					
Measured vertical wavelength (Figure 2.3b); T = 1.5 h; w_{150} = 12 m/s; k_h = 800 km; $k_x = k_y$; North-east direction					

[a]'Energy' represents the characteristic energy in unit [keV] of the input Maxwellian electron spectrum; 'Energy flux' represents the integrated energy in unit [erg/($cm^2 s^1$)] of the input electron spectrum

[b]'On' and 'Off' mean that the corresponding parameters or modules are turned on or off. 'On/Off' means that the parameters or modules are switched on or off.

and for Fe^+, the divergence term becomes:

$$\nabla \cdot (N_{Fe^+} \vec{V}_{Fe^+}) \approx \frac{\partial (N_{Fe^+} V_{Fe^+,z})}{\partial z} + \frac{\xi^2}{1+\xi^2} N_{Fe^+} \nabla_h \cdot \vec{V}_h \tag{5.26}$$

$\nabla \cdot \vec{V}_h$ is given by equation 5.16.

The offset of horizontal divergence of horizontal winds is computed by equation 5.16. The effects of horizontal divergence can be switched off or on by setting the divergence term $\nabla \cdot \vec{V}_h$ to zero or the results from equation 5.16. To isolate the effects of horizontal divergence of horizontal winds, we set the zonal/meridional winds to zero and turn off electric field and chemistry module, therefore, the change of Fe or Fe^+ densities are only caused by vertical winds, gravity diffusion, and horizontal divergence. We utilize the same set of gravity wave parameters, which are 1.57-h period, 12 m/s vertical wind amplitude at 150 km, 800 km horizontal wavelength and measured vertical wavelength, in Chapter 4 to compute $\nabla \cdot \vec{V}_h$. To compare the effects of horizontal divergence on neutrals and ions, we set the same initial profiles for Fe and Fe^+ with the Fe^+ profile in Figure 4.1.

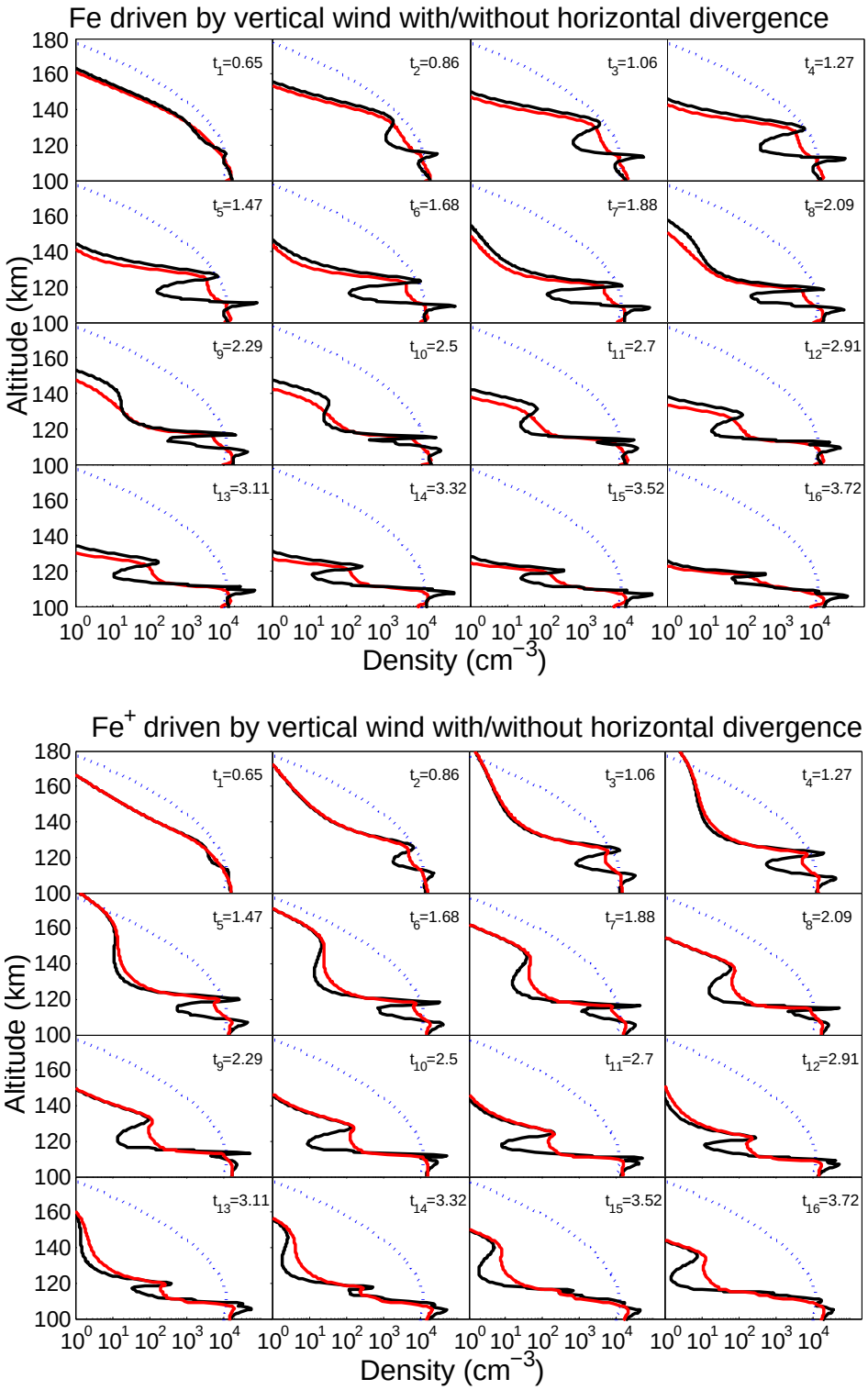

FIGURE 5.1: Fe (top) and Fe^+ (bottom) profiles driven by vertical wind only with (red solid lines) and without (black solid lines) the correction of horizontal divergence of horizontal winds. The blue dotted lines are the initial profiles, and time label in unit of hour. The initial profile of Fe is modified, and set up with the same profile as Fe^+. The initial profile of Fe^+ is from Figure 4.1.

The black solid lines in Figure 5.1 are the Fe/Fe^+ density perturbations driven by vertical wind only without including the horizontal divergence of horizontal winds. Firstly, the solid lines deviate from the blue dotted lines moving downward in the beginning, and the deviations become larger as time goes. The gravity force makes heavier elements like Fe moving downward, so that the whole Fe/Fe^+ layers gradually move away from the thermosphere. Then the black lines begin to converge and divergence due to the vertical wind shears of vertical winds. The converged Fe/Fe^+ layers move downward as the downward phase progression of gravity wave, at the same time, the peak densities of the converged Fe layers are greatly enhanced by the vertical transport induced by vertical wind shear of vertical wind. Fe^+ motions are not governed by vertical wind directly, and it is via neutral-ion coupling. The convergence efficiency of Fe^+ ions by vertical wind can be characterized by the vertical wind factor, equation 4.9. Due to the constrain of inclined geomagnetic field line, the vertical wind factor is less than one, for instance, it is about 0.98 at McMurdo. The less convergence efficiency, the smaller densities enhancement of Fe^+ black line has, comparing to the Fe black line in Figure 5.1. Therefore, only with vertical wind, the layer of Fe^+ is not converged as much as Fe layer, but it still generates converged Fe^+ with high peak densities. Without considering the horizontal divergence of horizontal winds, both converged Fe and Fe^+ layers are greatly overestimated. This is because that the assumption of neglecting horizontal divergence leads to totally compressible atmosphere.

By implementing the horizontal divergence of horizontal winds, we recompute the Fe/Fe^+ density variations using equations 5.25 and 5.26. The results are shown as red solid lines in Figure 5.1. The overestimated density perturbations (black lines) driven by vertical winds only are greatly offset by horizontal divergence of horizontal winds. The converged layers in the Fe black solid lines are smoothed out, and the red solid lines show wave perturbations but with much smaller relative

density perturbations. The impact of horizontal divergence on Fe^+ layers depends on altitude. At higher altitude region above 125 km, the less neutral-ion collision leads to less influence of horizontal divergence on Fe^+ layer, and stronger convergence. Although the peak densities are decreased from the Fe^+ black solid line to red line above 125 km, the converged Fe^+ layer has much larger densities enhancement, compared to the Fe layer at the same altitude. At the altitude region below 125 km, the strong neutral-ion coupling gives rise to significant impact of horizontal divergence of horizontal wind on Fe^+. The convergence of vertical wind is associated with the divergence of horizontal winds. Therefore, no significant convergence is found in the Fe^+ line below 125 km.

5.3 Attempts to Reproduce Thermospheric Fe Layer Event on 28 May 2011

We have discussed the transport of Fe/Fe^+ driven by electric field, neutral winds, and the chemistry of Fe/Fe^+ with and without auroral electron precipitation condition, and also discussed effects of horizontal divergence of horizontal wind on the Fe/Fe^+ layer formation. In this section, we combine all the factors together to simulate the thermospheric Fe layer on 28 May 2011, and investigate the roles played by the electric field, neutral winds, auroral electron precipitation and horizontal divergence of horizontal winds.

5.3.1 Simulations of thermospheric Fe layer event on 28 May 2011 with the best estimated parameters

With the best estimated parameters provided in Chapter 4 including the horizontal divergence of horizontal winds, the pattern of Fe^+ layers on 28 May 2011 is simulated and shown in Figure 5.2a.

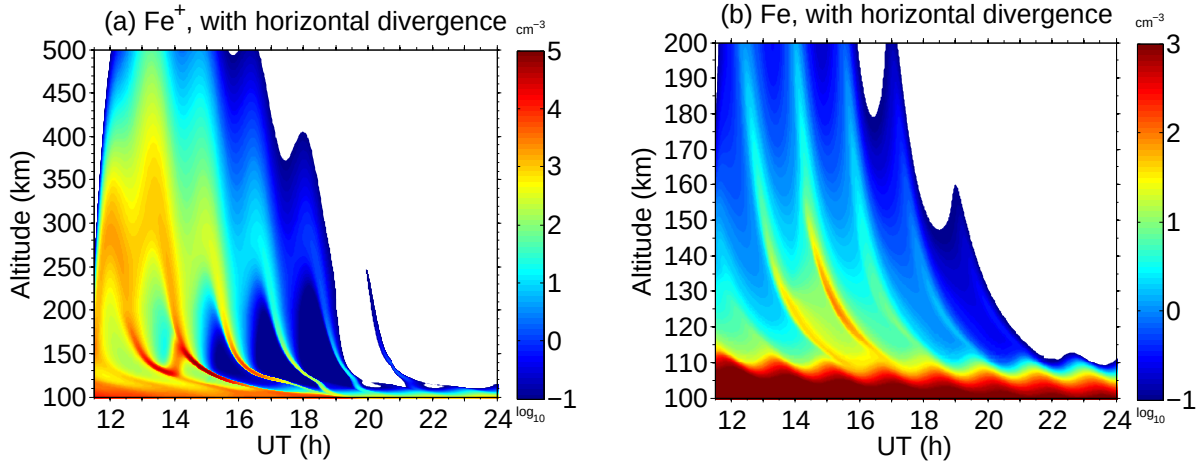

FIGURE 5.2: Simulation of the thermospheric Fe layer event with correction of horizontal divergence on 28 May 2011 at McMurdo.

The simulated thermospheric Fe layers in Figure 5.2b , to a great extent, replicate the observed Fe layer shapes on 28 May 2011 [*Chu et al.*, 2011], but the contrast of Fe layer in Figure 5.2b is not comparable with the observed thermospheric Fe layers. The initial Fe^+ density profile used in the model for reproducing the Fe observations is given in Figure 4.1, whose peak density altitude stays around 100 km at the start time of 11 UT.

The Fe layer shape is determined by multiple factors. Although the convergence of Fe^+ layers is mainly determined by the neutral wind shears, the Fe^+ layer shape may not follow the neutral winds all the time as it can be modified by the electric field depending on the electric field strength and direction. For example, despite the downward phase progression of the gravity waves, the Fe^+ layers in Figures 5.2a sometimes show upward phase progression due to the upward drift by the electric field. Even for the downward phase, the Fe^+ layers may not follow the gravity wave precisely but deviate to certain degrees. Net production of Fe atoms occurs in the thermosphere wherever the Fe^+ layer density is sufficiently high so that the Fe production exceeds the Fe loss. Consequently, the altitude and shape of converged Fe^+ layers strongly affect where and when Fe atoms are produced in the thermosphere but cannot solely determine the Fe layer shape. This is

because once they are formed, neutral Fe atoms are no longer subject to electromagnetic forces but driven by the neutral winds. When the neutral winds are dominated by gravity waves, the produced Fe atoms will follow the gravity-wave-induced neutral winds quite well in the region below 200 km where collision is still frequent enough that gravity and diffusion have minor influences on Fe motions. Be ware that the remaining Fe^+ layer will continue producing Fe atoms as long as Fe^+ density is still sufficiently high. Both the earlier-produced and later-produced Fe atoms from the Fe^+ layer contribute to the observed shape of neutral Fe layers. Therefore, depending on whether the later-produced Fe atoms are in the same phase as the earlier-produced Fe atoms, the Fe layer could stay thin or be broadened or stretched. This is actually shown in Figure 5.2b.

If the electric field is in the transition from up/downward to down/upward, the weaker electric field wind have much less influence on Fe^+ motions. As a result, Fe^+ layers will basically stay with the Fe layers following the neutral winds. In this case, the later-produced Fe atoms are in phase with the earlier-produced Fe atoms, leading to relatively thin Fe layers. Contrarily, if the electric field is in strong upward or downward phase, it can push the Fe^+ layers up or down, deviating from the motion of the earlier-produced Fe atoms. The the later-produced Fe atoms from the shifted Fe^+ layers will not overlap the transported locations of earlier-produced Fe atoms exactly, thus the observed Fe layers will be broadened. This explains why the very thin 2nd, 3rd, and 4th Fe^+ layers below 150 km in Figure 5.2a generate much broader Fe layers in Figure 5.2b.

Compared with Figure 4.18, Figure 5.2 remains the similiar gravity-wave structured Fe/Fe^+ layers after implementing the horizontal divergence of horizontal wind. The similarity between Figures 4.18 and 5.2 suggests that gravity-wave-induced vertical wind are essential to shape the Fe/Fe^+ layers. The difference between Figures 4.18 and 5.2 lies in the layer peak densities and the contrast of Fe/Fe^+ layers. For Fe^+ patterns, Figure 5.2a presents the same structure as the Fe^+

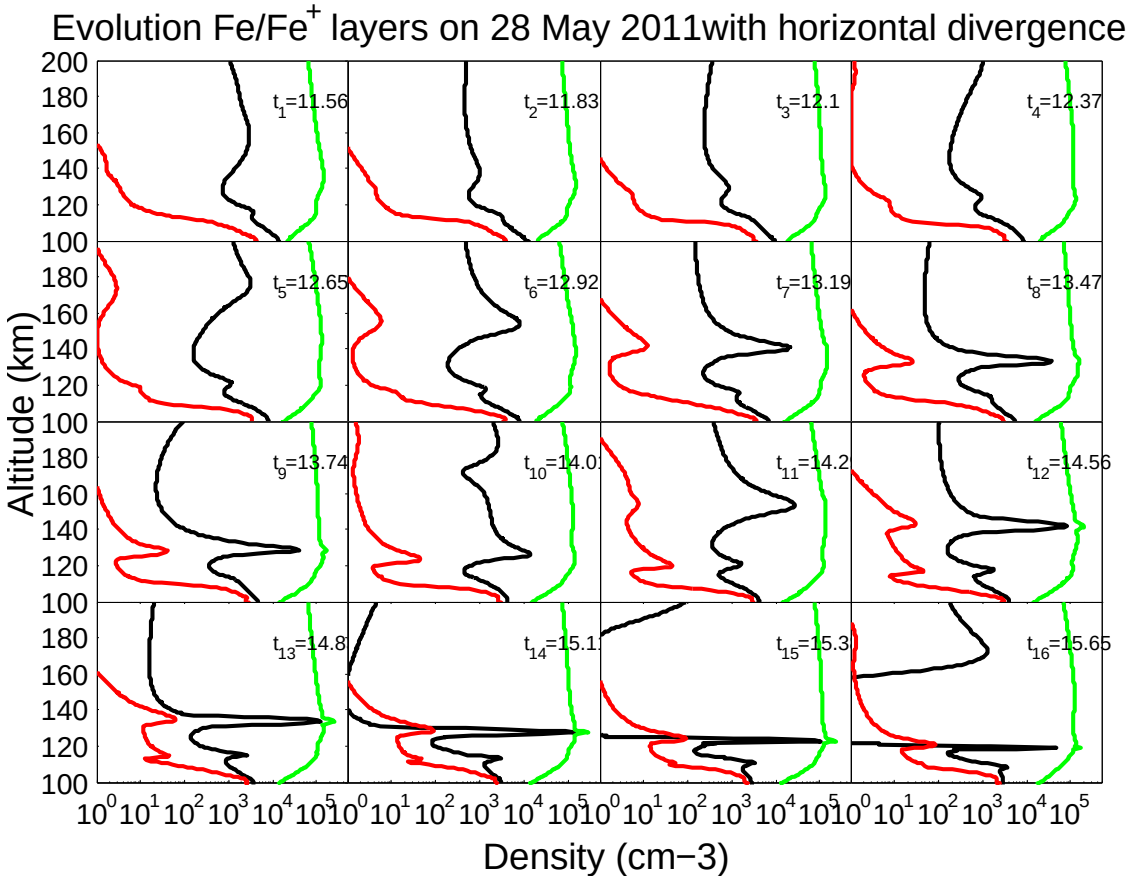

FIGURE 5.3: Time sequence of evolution of simulated thermospheric Fe^+ and Fe layers with horizontal divergence on 28 May 2011. The green lines are electron profiles, the black lines are Fe^+ profiles and the red lines are Fe profiles.

layers in Figure 4.18a above 125 km, but shows much weaker Fe^+ layers, gradually diminishing after 15 UT below 125 km. It is because that the growths of converged Fe^+ layers driven by vertical winds are greatly offset by the divergence of horizontal winds. As a consequence, the lower densities of Fe^+ layers, the less Fe atoms are produced in Figure 5.2b. As the Fe atoms formed by the neutralization of Fe^+ layers, Fe atoms are perturbed by gravity waves, moving up and down with the vertical winds. However, the relative density perturbations of Fe layers are greatly reduced by horizontal divergence, therefore the horizontal divergence leads to much worse contrast of Fe layers in Figure 5.2b, compared to extra high contrast of Fe layers in Figure 4.18b.

In Figure 5.3, we provide the evolution of Fe and Fe^+ with respect to time. In the upper altitude region, the Fe layer emerges at the altitudes where Fe^+ ions are converged. The first Fe^+ layer is rapidly diverged by the upward transport driven by electric field. The second Fe layer emerges around the altitude of 172 km with density of 2.8 cm^{-3} after the formation of the second Fe^+ layer with a peak density of about 0.3×10^4 cm^{-3} around 12.65 UT. The Fe layer follows the Fe^+ layer moving downward with the same speed while growing in density. At ~13.47 UT, the peak of Fe layer grows up to 26 cm^{-3} at altitude of 132 km. At this moment, the peak density of Fe^+ layer is 3.8×10^4 cm^{-3} at altitude of 133 km. The motions of Fe and Fe^+ layers are decoupled by the electric field, and the Fe^+ moves back to higher altitude region, then the third Fe layer is formed. At ~15.1 UT, the peak density of Fe^+ layer reaches to 1.4×10^5 cm^{-3} at 128 km. A spike is found on the electron density profile, suggesting the formation of sporadic E layer. It is quite clear from Figure 5.2 that the peak heights of Fe layers are mainly determined by the altitudes of the converged Fe^+ layer peaks. As Fe^+ layer peaks are driven by both the electric field and the neutral wind shears, the relative phase between the electric field and the gravity waves along with the time history will determine how high the Fe^+ layers are pushed to each time, leading to varied peak heights of produced Fe layers as lidar observed.

To compare the simulated Fe densities with observations, two sets of comparisions for the time series of Fe density variations at 130 and 140 km are provided in Figure 4.19 without horizontal divergence, and in Figure 5.4 with horizontal divergence. Without horizontal divergence, the simulated Fe layers in Figure 4.19 at 130 and 140 km shows the contrast as good as obervations expect for the second peak at 130 km is lower than the observation. However, the good contrast in Figure 4.19 is greatly offset by the horizontal divergence in Figure 5.4. Compared to Figure 4.19, the crests of simulated Fe layers in 5.4 decrease and the troughs increase so that the crest-trough

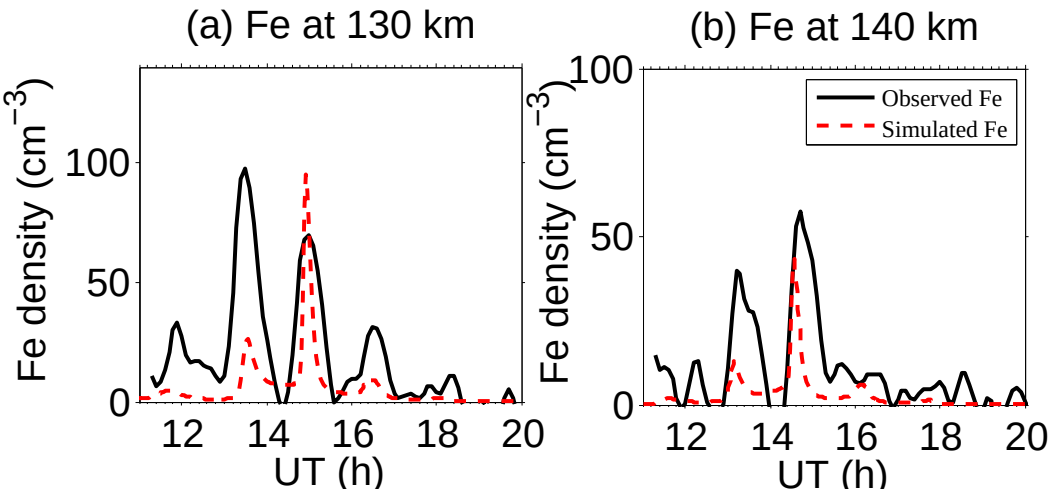

FIGURE 5.4: Comparison of the simulated Fe densities with lidar-observed Fe densities at 130 km and 140 km for the simulations with horizontal divergence correction (a) and (b).

ratio is much smaller than that the simulated Fe layers in Figure 4.19.

Combine all the best estimated factors, the simulations in Figure 5.2 can reproduce the structure and shape of thermospheric Fe layers on May 28, 2011, only except that the extra high contrast of observed Fe layers cannot be reproduced. The relatively incompressible upper atmosphere gives rise to the horizontal divergence of horizontal wind consistent with the vertical wind shear of vertical wind. The convergence driven by vertical winds is associated with a divergence by horizontal winds. When neutral Fe atoms are formed in the thermosphere, the gravity-wave winds move these Fe atoms up and down with the background medium so that 100% relative Fe density perturbations cannot be achieved by perturbing the Fe layers with gravity wave only. This suggests that the extra high contrast of observed Fe layers are likely caused by the chemistry of Fe through $Fe - Fe^+$ layers coupling. In Section 5.3.2, we will investigate the formation of extra high contrast of Fe layers from the aspects of $Fe - Fe^+$ layer coupling and chemistry.

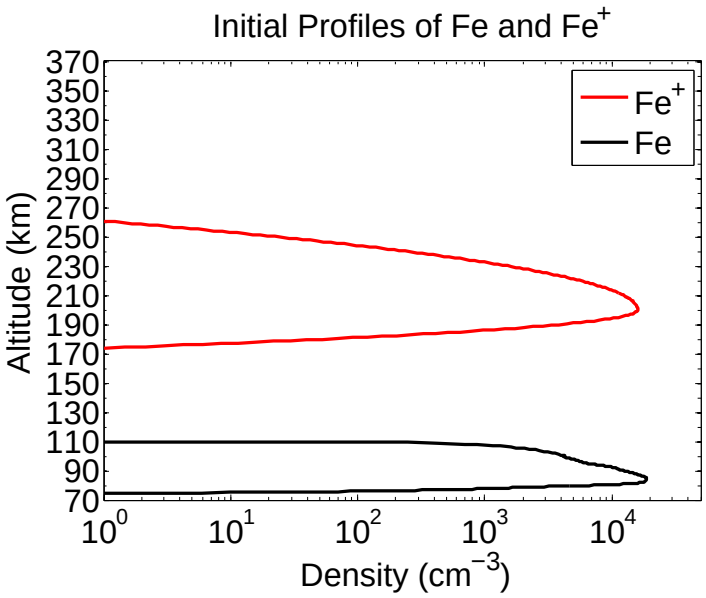

FIGURE 5.5: Initial Fe^+ changed

5.3.2 Simulations of thermospheric Fe layer event on 28 May 2011 by conditions

Experiment I, change initial Fe^+ profile The low peak altitude of initial Fe^+ profile in Figure 4.1 used in above event simulations makes the first Fe layer occurring at relatively low altitude as observed. In this first experiment, only initial Fe^+ profile is changed, but the other simulation parameters keep the same as those used in Section 5.3.1. The new initial Fe^+ profile is given in Figure 5.5, which is same shape as the Fe^+ layers in Figure 4.1 with the same peak densities and FWHMs but the peak altitude is 200 km.

The simulation results are shwon in Figure 5.6. Starting with Fe^+ profile at much higher altitude, the Fe^+ layers would make the starting Fe layer profiles in Figure 5.6b around 11 UT to be much higher than observed, and by moving the intial Fe^+ profile upward, it does not help to enhance the contrast of Fe layers.

These results also imply that under the strong convection electric field as given by Figure 4.3a, the Fe^+ profile has to somehow stay in relatively lower altitudes when the lidar observations

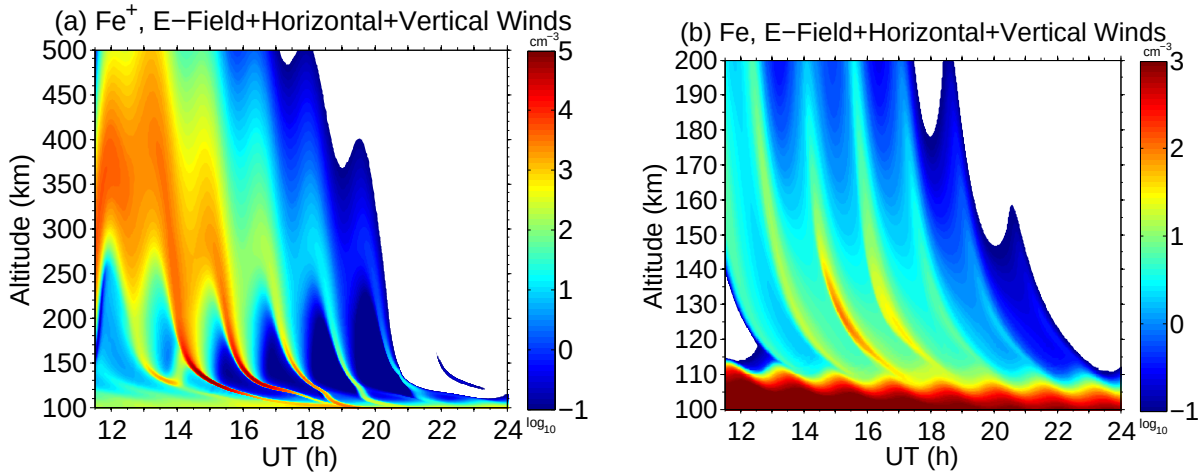

FIGURE 5.6: Simulation of the thermospheric Fe layer event on 28 May 2011 at McMurdo with new initial profile. (a) and (b) are the simulation with horizontal divergence.

started in order for the model to reproduce the observed Fe layer shapes. There could be several possibilities. On one hand, we do not have the information on atmospheric waves and corresponding neutral winds before the lidar observations started. Inertial gravity waves as a distinct strong feature at McMurdo [*Chen et al.*, 2013; *Chu et al.*, 2011] are not included in the model, and neither are various tidal components [*Fong et al.*, 2014] or planetary waves. Strong downward vertical winds or certain direction zonal or meridional winds can push down the Fe^+ layers when the electric field generates upward flow. Some inconsistencies between the simulated and observed Fe densities, e.g., the maximum Fe density and its occurrence time as well as the Fe layer duration (i.e., width in time), are likely due to the gravity wave used in the model being too ideal when compared to the reality of atmospheric waves and background neutral winds above the polar cap near McMurdo. Wave dissipation is not considered in the forward-modeled gravity wave because we have no information on the wave dissipation. Including realistic wave dissipation will not change the overall simulated Fe layer shapes, but may make the simulated Fe density matching the observation better. On the other hand, horizontal transport may play a role in bringing the needed initial Fe^+ profiles over the lidar station. One of the prominent features of the polar electric field is characterized by

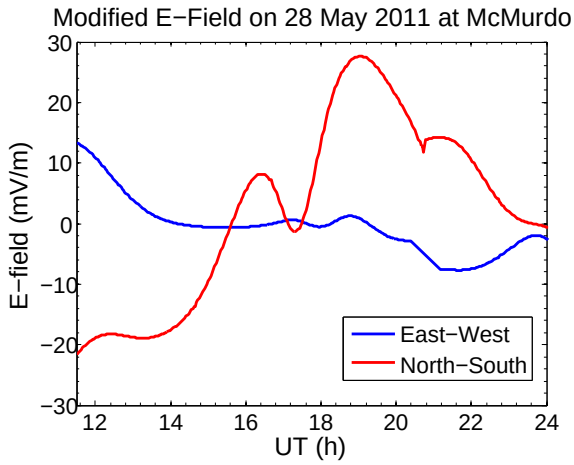

FIGURE 5.7: Modified E-field based on the electric field calculated by Weimer-2005 model. East-west is decreased by 50%, and north-south component does not change.

diurnal variations of the convection patter of electric field [*Weimer*, 2005]. For a single location, the magnitude and direction of electric field has diurnal variations as shown in the Figure 4.3b. For a single time, some regions correspond to upward motion while some other regions correspond to downward motion. When using the IMF and solar wind conditions on 28 May 2011 to calculate the electric field and the resulted vertical ion drift over the entire polar cap in the Antarctic, it is obvious that there are regions of strong downward flow and other regions of strong upward flow. Fe^+ can be pushed down and accumulated at relatively lower altitude in the downward flow regions. Once horizontally advected to McMurdo, such regions can provide the needed initial profiles similar to Figure 4.1.

Experiment 2: changing E-field In this experiment, the electric field and gravity wave amplitude are changed, and the other parameters remain the same as those used in Section 5.3.1. On way to increase the contrast of simulated Fe layers is to increase the chemical production ($Fe^+ + e^- \longrightarrow Fe + h\nu$). Higher densities of Fe^+ layers would give higher production of Fe. Therefore, the purpose of changing electric field and wave amplitude is to alter the formation of Fe^+ layer.

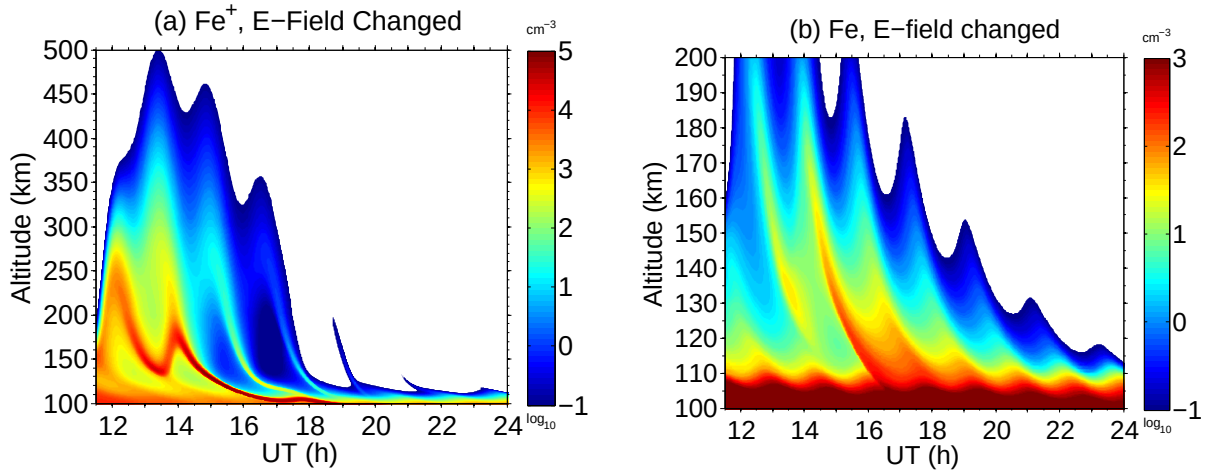

FIGURE 5.8: Simulation of the thermospheric Fe layer event on 28 May 2011 at McMurdo with 50% east-west electric field with horizontal divergence.

To achieve higher Fe^+ concentrations in the lower altitudes, the east-west electric field is decreased by 50% (Figure 5.7), leading to weaker upward transport of Fe^+ by electric field. The wider of Fe^+ layers also help increase the production of Fe, so the wave amplitude is decreased from 12 m/s to 10 m/s at 150 km, and the wave amplitudes at other altitudes are changed according to $w_z = w_{150}\sqrt{\frac{\rho_{150}}{\rho}}$. The other wave parameters are not changed.

The simulation results are shown in 5.8. Compared with Figure 5.2a, the Fe^+ layers in Figure 5.8b are concentrated in the lower altitudes due to the smaller electric field, and the smaller wave amplitudes make the converged Fe^+ become wider. The increase of Fe^+ densities in the lower altitudes substantially enhances the production of Fe. The crest Fe densities at 130 and 140 km in Figure 5.9 are even slightly higher than the observations. However, the increase of Fe^+ densities also increases the trough Fe densities, therefore, the contrast of simulated Fe layer are still far away from the observed Fe layer contrast.

Increasing Fe^+ densities in the lower altitudes by changing electric field and wave amplitude can enhance the production of neutral Fe, but it does not affect the lifetime of neutral Fe in the thermosphere so that it cannot profoundly enhance the contrast of simulated Fe layers. Note that

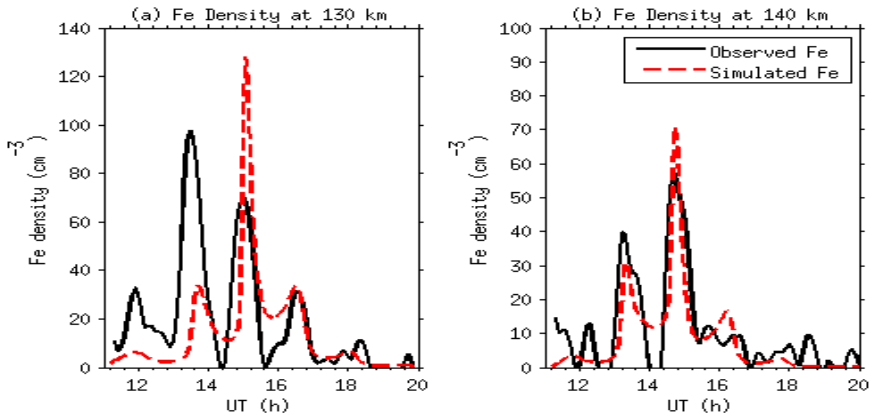

FIGURE 5.9: Comparison of observed and simulated Fe densities at 130 and 140 km when the east-west electric field is decreased by 50%.

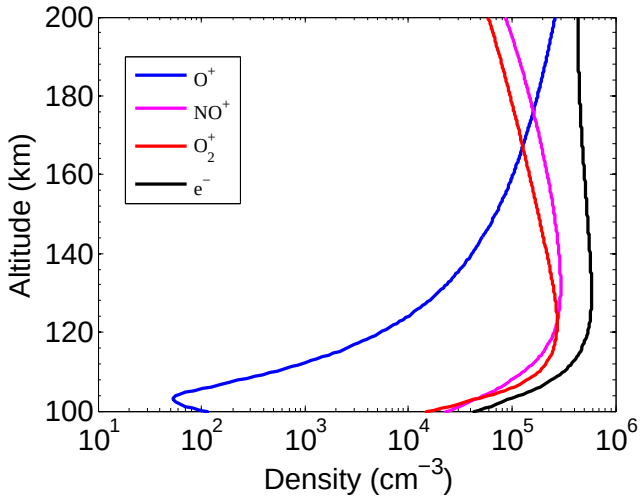

FIGURE 5.10: The average densities of O^+, NO^+, O_2^+ and e^- over 12 hours when auroral electrons is increased to 30 $erg/(cm^2 s^1)$.

the simulated Fe layer widths in Figure 5.9 are comparable with the observed layer widths.

Experiment 3: changing auroral electron input As discussed in Section 4.4, the role of auroral electron precipitation in the formation of thermospheric Fe is a double-edged sword. On one hand, the enhancement of electron concentrations by auroral electron precipitation can accelerate the neutralization of Fe^+ through direct electron recombination; on the other hand, the enhancement of NO^+ and O_2^+ and direction ionization of Fe by auroral electrons can accelerate the loss of

neutral Fe. This mechanism may help increase the crest and decrease the trough densities of thermospheric Fe layers, so to achieve extra high contrast. Therefore, in the experiment, the auroral electron input is changed, and input energy flux increases from 1.5 $erg/(cm^2s^1)$ to 30 $erg/(cm^2s^1)$, but the electron characteristic energy is still 1 keV. The other parameters remain the same as those used in Section 5.3.1. The 30 $erg/(cm^2s^1)$ auroral electron fulx at 1 keV is extremely high, and much greater than the energy input expected under normal circumstances.

Figure 5.10 shows the ions and electron densities with 30 $erg/(cm^2s^1)$ auroral electron input. Compared to the ions and electron densities in Figure 4.16, the ions and electron densities increase about 8 times than those with 1.5 $erg/(cm^2s^1)$ input. The simulation results are presented in Figure 5.11, and the comparison between simulated and observed Fe layers is given in Figure 5.12. Higher electron densities produce more Fe atoms when $Fe - Fe^+$ layers are coupled together, so it produces the crests of Fe layers with higher densities, comparable with the observations. After $Fe - Fe^+$ are decoupled, the higher densities of NO^+ and O_2^+ substantially increase the loss the neutral Fe and create much lower trough densities of simulated Fe layers, as shown in Figure 5.11. Overall, both enhancements of electron and NO^+/O_2^+ densities can help create the extra high contrast of simulated Fe layers, which is comparable with the contrast of observed Fe layers.

5.4 Conclusions

In this chapter, the horizontal divergence of horizontal winds on the Fe/Fe^+ layer formations is particularly discussed. Although vertical winds are important in shaping Fe/Fe^+ layers, but the convergence caused by vertical shear of vertical winds is profoundly offset by horizontal divergence of horizontal winds. Vertical winds are still important to converge Fe^+ above 125 km, because of weaker neutral-ion coupling, horizontal winds have less influence on Fe^+ at higher altitudes.

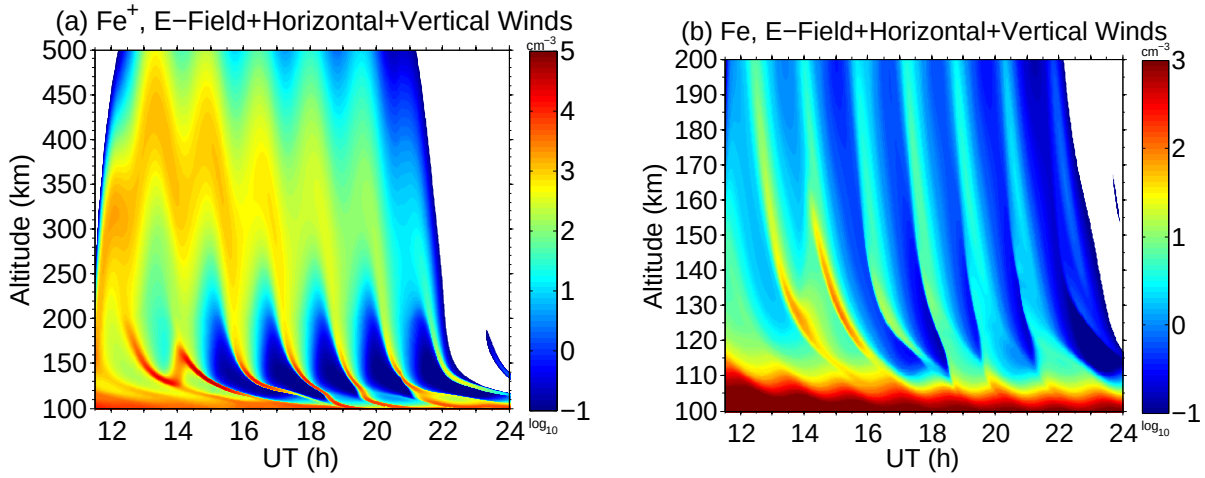

FIGURE 5.11: Simulation of the thermospheric Fe layer event on 28 May 2011 at McMurdo with 30 $erg/(cm^2 s^1)$ auroral electron energy input. (a) and (b) are the simulation with horizontal divergence.

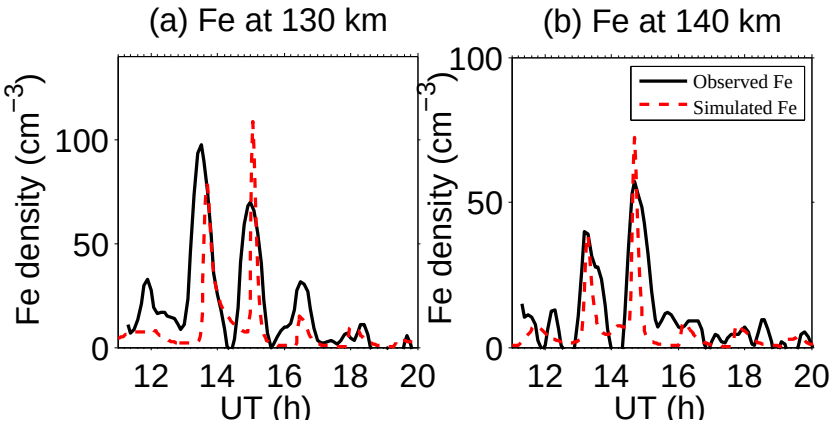

FIGURE 5.12: Comparison of observed and simulated Fe densities at 130 and 140 km when the energy flux of auroral electrons is increased to 30 $erg/(cm^2 s^1)$.

With the best estimated parameters, the structure and shape of thermospheric Fe layers on 28 May 2011 can be fairly reproduced, but the model fails to reproduce the extra high contrast of observed Fe layers. By increasing the energy input of auroral electron density, the model is able to reproduce the lidar observations satisfactorily in general after putting all considerations together.

The large horizontal winds caused by atmospheric waves as shown in Figure 4.6 introduce the horizontal motion oscillations, instead of a unique direction advection. The background wind can be large as 100–300 m/s above 125 km in polar regions and the thermospheric Fe layers had

been detected by lidar for many hours, suggesting that the thermospheric Fe patches may have a great horizontal extension. On a further consideration, different polar locations may have different phases of ion transport produced by the convection electric field. That is, upward flow/convergent flow may appear at different times at different locations. Therefore, at what time/location ions are uplifted by the south-east electric field to the higher altitudes will vary with location. Whether the ions have been transported upward by the electric field at the phase of ion convergence driven by atmospheric wave-induced winds will mainly determine how high the converged ion layers can reach at that location. Because different locations experience different atmospheric waves, e.g., very strong gravity wave activities are observed at McMurdo [*Chu et al.*, 2011; *Chen et al.*, 2013] while tides are a more dominant feature at Davis [*Lübken et al.*, 2011], the convergence of ion layers introduced by atmospheric waves can also have different phases at different locations. The convergent and divergent ion flows induced by the electric field in different directions can either help or destruct the wave-induced convergence, respectively, depending on the relative phase and strength between the waves and electric field. Therefore, such phase and magnitude relationship can determine if metal ion layers can be formed at certain local time and how high they can be, which can determine the occurrence of thermospheric neutral metal layers produced from the converged ion layers. This idea may explain lidar observations of tidal-period occurrence of thermospheric Fe layers from Davis and McMurdo, which will be a topic for future studies using this new thermospheric Fe/Fe^+ model.

Chapter 6

Diurnal Variations of the Fe Layer in the Mesosphere and Lower Thermosphere: Four Season Variability and Solar effects on the Layer Bottomside at McMurdo, Antarctica

6.1 Preface

The material in this chapter has been published in Journal of Geophysical Research [*Yu et al.*, 2012]. The authors of this paper are Zhibin Yu, Xinzhao Chu, Wentao Huang, Weichun Fong and Brendan R. Roberts. This is a team work by all authors. The major contributions of Z. Yu include major data collection and data analyses. The contents in this thesis are enhanced by adding a case of solar effects on the bottomside of Fe layer in September 19–20 2012 collected by Mr. Brendan Roberts to have symmetric observations: two cases in fall and 2 cases in spring.

6.2 Introduction

Knowledge of Fe layer characteristics in the MLT has been dramatically improved in the last two decades, owing to lidar observations by numerous groups as mentioned in the Introduction of Chapter 1, and the modeling and laboratory work by Plane and co-workers [e.g.,*Helmer et al.*, 1998; *Self and Plane*, 2003; *Plane et al.*, 2003]. A coupled chemical and dynamical system determines the characteristics and variations of neutral Fe layers and Fe-containing species in the MLT. The source of Fe and Fe species in the MLT is meteoric ablation. Sporadic meteoroids are the major sources, although meteor showers also contribute [*Plane*, 2004; Ceplecha et al., 1998; Baggaley, 2002]. Several tens of tons of micrometers are believed to enter the Earth's atmosphere every day [Plane, 2004]. The meteor influx is balanced by the downward transport to chemical sinks below 85 km. The residence time for a typical Fe atom in the layer is several days before it is removed to a stable reservoir. FeOH is believed to be the major reservoir species for Fe [*Plane et al.*, 2003]. FeOH and other Fe-containing molecules are then permanently removed from the MLT region by forming or condensing onto meteor smoke particles that eventually settle into the stratosphere under the influence of gravity [*Saunders and Plane*, 2006]. Therefore, the Fe system is not a closed system cycling among neutral Fe atoms, Fe^+ ions and Fe-containing species, but an open system with meteor input at high altitudes as the sources, and permanent removal on meteor smoke particles below the mesopause as the sinks. Such Fe-rich meteor smoke particles are transported downward through the stratosphere and troposphere and eventually settle onto the Earth's surface.

The partitioning among Fe, Fe^+ and Fe-containing species is altitude dependent. On the topside of the Fe layer, ion chemistry predominates, while neutral chemistry dominates the underside [*Self and Plane*, 2002; *Plane*, 2003]. Most of the important chemical reactions have

been studied in the laboratory, and their reaction rate coefficients and temperature dependence have been measured [e.g., *Plane et al.*, 2003; *Vondrak et al.*, 2006; *Woodcock et al.*, 2006]. In ion-molecule chemistry, neutral Fe atoms are converted to Fe^+ mainly via charge transfer with NO^+ and O^+, but photoionization of Fe also contributes. The conversion back to neutral Fe is mainly through dissociative electron recombination after various ion compounds are formed, as the direct recombination of Fe^+ with electrons is a slow process. The neutral Fe chemistry at the underside of the Fe layer is mainly controlled by odd oxygen (O and O_3) and hydrogen (H) chemistry, although reactions with H_2O, CO_2 and O_2 are also important. Consequently, the underside of the Fe layer is highly sensitive to O, H and O_3 concentrations. Fe chemistry is quite temperature dependent, as the reaction of FeOH with H has a significant activation energy, causing the partitioning of iron between Fe and FeOH to shift to the former at higher temperatures [*Plane*, 2003;*Gardner et al.*, 2011]. Besides the above factors (ablation, transport, removal, partitioning with ion-molecule and neutral chemistry, O, H and O_3 concentrations, and temperatures), two more factors should be added to the study of the diurnal variations of Fe layers: One is the influence of atmospheric tides and another is Fe photochemistry, analogous to the study of Na diurnal variations [*Plane*, 2004]. For high polar latitudes, geomagnetic activity and particle precipitation influence the ion and electron densities in the ionosphere, potentially affecting ion-molecule chemistry. In addition, Fe depletion via heterogeneous removal by mesospheric ice particles is a big effect in summer at high polar latitudes [*Plane et al.*, 2004; *Gardner et al.*, 2011].

Many uncertainties and unknowns remain in these factors and their effects on the Fe layer and its diurnal variations. In particular, none of the photochemical reactions of Fe-containing molecular species has been included in the currently published Fe chemistry models. Therefore, the diurnal variations of the Fe layer are a new region to explore, with the solar effects on the

Fe layer far from being understood. This chapter provides one of the first observational reports of Fe diurnal variations and solar effects on the Fe layer bottomside using Fe Boltzmann lidar measurements made at McMurdo, Antarctica from December 2010 through the end of 2011, along with one individual case in March 2012, and another one in September 2012. The nearly 1000 h of data allow the characterization of Fe diurnal variations in four seasons throughout the year as well as more in-depth case studies. Quantitative information is derived from the lidar data for comparison with future Fe modeling. A most significant feature of the reported measurements is the distinct bottomside extension of the Fe layer during local sunrise and contraction during sunset. We argue that daytime Fe production below 80 km is related to photochemistry involving the Fe-containing species and neutral Fe chemistry with H, O and O_3. These entirely new results provide direct, real-time quantitative evidence for the influence of solar UV radiation on the chemistry and composition of the mesopause region.

6.3 Observations

The upgraded Fe Boltzmann lidar was enhanced its spectral stability, temporal resolution and daytime capability [*Chu et al.*, 2011a; *Wang et al.*, 2012]. The full-diurnal capabilities enable our investigation of the diurnal variations of the MLT Fe layer in the current study. Table 6.1 summarizes the distribution of lidar observations from 16 December 2010 through the end of 2011, which are used in the current study. The 20 h of data taken on 20–21 March 2012 and 26 h of data on September 19–20 2012 were also used in the case study but not included in the table. More data were collected during the four summer months (November through February) than in the other three seasons because of greater availability of lidar personnel and better weather conditions. From March through August weather conditions limited the data collection, although

a single operator each year (Z. Yu in 2011 and B. Roberts in 2012) would try his best to establish more than 24-h continuous observations. In September and October 2011, the campaign suffered temporary instrument difficulties, resulting in low data coverage. As a consequence, the current data set is adequate for seasonal studies of diurnal variations, but not for monthly studies. The diurnal distributions of data hours plotted in Figure 6.1 demonstrate the availability of sufficient data samples for all four seasons. Here the definition of season is based on the solar illumination conditions in the MLT region. Polar summer experiences 24-h sunlight and polar winter is under 24-h darkness, while the polar autumn and spring have alternation of day and night. The seasonal divisions and the observation hours in each season are given in Table 6.2. We defined the seasons this way to assess the diurnal impacts of solar illumination on the Fe layers, which is greatest in autumn and spring.

TABLE 6.1: Lidar Observations of Fe layers at McMurdo From December 2010 Through 2011.

Month	Jan	Feb	Mar	Apr	May	Jun	Jul	Aug	Sep	Oct	Nov	Dec	Total [a]
Days	8	7	8	4	6	4	3	5	1	3	9	8	66
Hours	173	108	47	54	59	70	48	72	9	55	122	146	963

[a]December data were taken in both 2010 and 2011, while the other months were in 2011 only. The 20-h of data on 20–21 March 2012, and 24-h data on 19–20 September 2012 used for case studies were not included in this table.

The first step in analyzing the data is to form a composite day of Fe density profiles for each season by adding together all the data taken during the same season at a particular time and altitude. Outliers caused by sporadic Fe layers were removed with a box plot method [*Tukey*, 1977] before taking arithmetic means for each seasonal composite. The algorithm of box plot method is given in the Appendix G. The data resolutions are set to fixed 100 m $\times$ 0.5 h grid in order to quantify the Fe layer consistently through the year. The data in every half hour starting with 0 or 0.5 h are grouped to represent the half hour grid. The final composite contours are smoothed by

TABLE 6.2: Southern Polar Season Division and Total Observational Hours

Season	Start Date to End Date	Total Observational Hours
Polar Autumn	1 Mar 2011 to 6 May 2011	112 h
Polar Winter	7 May 2011 to 6 Aug 2011	175 h
Polar Spring	7 Aug 2011 to 31 Aug 2011	127 h
Polar Summer	1 Nov 2011 to 28 Feb 2011	549 h

a 2-D Hanning window with 1-km spatial and 2-h temporal full-width-at-half-maximum (FWHM). By taking composite means, the effects of non-coherent waves are reduced, helping reveal the true diurnal variations.

6.4 Diurnal Variations of the Fe layer Through Four Seasons

Four seasonal composites of diurnal variations of Fe densities are plotted versus local time and altitude in Figure 6.2a–d for autumn, winter, spring and summer. Summer Fe layers show lower density, higher altitude, and narrower width than those of the other three seasons. The winter topside extends to over 105 km, much higher than the other seasons. The peak of Fe density occurs around 86–87, 85–86, ∼84 and 90 km for autumn, winter, spring, and summer. Around the peak, Fe density undergoes substantial variations through a diurnal cycle in each season with a tendency of higher peak density around local noon and lower density near local midnight. A striking feature in the seasonal composites is the downward extension of the Fe layer on the bottomside during the day in autumn and spring. In Figures 6.2a and 6.2c, the layer bottom changes from ∼80 km in the night to ∼72 km around noon. Interestingly, the downward extension in the morning has a steeper slope than the upward contraction in the afternoon.

The density perturbations are plotted in Figure 6.2e–h, which are derived by taking the differences between the half-hourly mean Fe profiles and the diurnal-mean Fe density profile at each

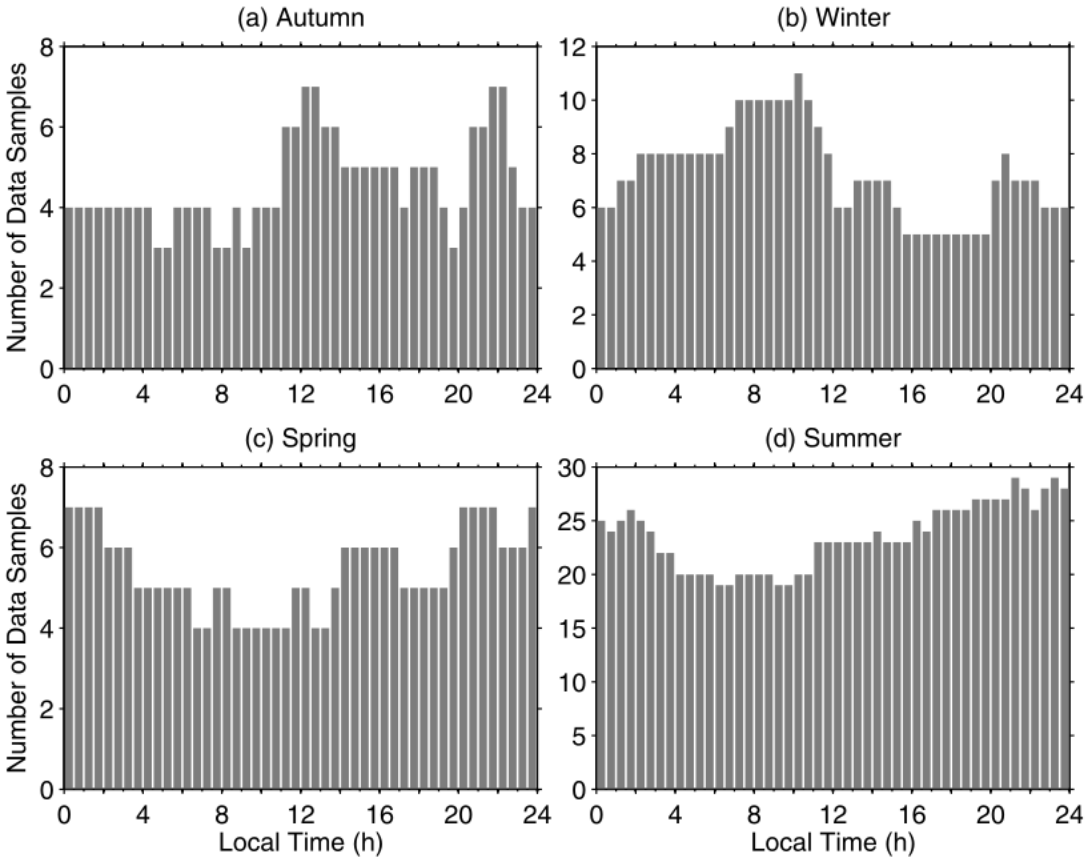

FIGURE 6.1: Diurnal distribution of half-hourly lidar data samples in the season of (a) autumn, (b) winter, (c) spring, and (d) summer.

altitude in the corresponding season. Around the below 80 km in the autumn and spring (Figure 6.2e and 6.2g), Fe density enhancement during the day and reduction in the night result from the layer bottom extension observed in Figures 6.2a and 6.2c. However, the winter density perturbations at the bottom in Figure 6.2f appear to be random with local time when sunlight is absent from the MLT. These phenomena indicate that the daytime downward extension on the bottomside is a solar effect, which is strongly influenced by the diurnal variation of solar illumination. In Figure 6.2h, the summer density perturbations show a weak enhancement near 84 km around noon. This is likely related to the tides observed in the main layer, and the Fe layer around this altitude is also strongly influenced by PMC ice particles in the polar summer.

In the summer main layer between 84 and 98 km, the Fe density perturbations (Figure 6.2h) clearly show a downward phase progression with the vertical phase speed of about -1.25 km/h. The 24- and 12-h oscillations have comparable amplitudes. Such clear phase progressions likely represent tidal perturbations in the summer. This is because averaging over 20–25 data samples (Figure 6.1) in each time bin largely reduces the perturbations caused by gravity waves, helping reveal the tidal perturbations. Strong wave perturbations with amplitudes as large as 20–30 K have been found in the lidar temperatures at McMurdo [*Chen et al.*,2012; *Chu et al.*, 2011a, 2011b, 2012], but the tidal amplitudes are only ∼2–4 K in the winter according to our preliminary results. The complex structures in autumn, winter and spring main layers are most likely due to residual gravity wave effects because the data samples in these seasons number only 4–5 for most hours of the day. We notice that the tidal perturbations in the summer Fe layer at McMurdo are comparable to the tidal features observed by a lidar at Davis (69°S, 78°E), Antarctica in the summer season of 2010–2011 [*Lübken et al.*, 2011].

To further characterize the diurnal variations of Fe layers in the four seasons, the Fe column abundances, centroid altitudes, RMS widths, and bottom altitudes are derived from the seasonal composites of Fe densities, and the results are plotted in Figure 3. The integration range for the first three parameters is from 70 to 105 km, and the bottom altitude is defined as the altitude of the 300 cm^{-3} Fe density contour on the bottomside. The summer layers are quite distinct from the other three seasons with lower abundance and smaller width but higher centroid and bottom altitudes. This is consistent with the current understanding that both the low MLT temperature in the polar summer and the heterogeneous removal of Fe atoms by visible and sub-visible ice particles significantly reduce the Fe density, especially below ∼90 km thus making the surviving layers weaker, narrower and weighted to higher altitude [*Plane et al.*, 2004; *Gardner et al.*, 2005,

2011]. In addition, the upwelling over the summer pole associated with the summer-to-winter-pole meridional circulation also contributes to the higher layer altitudes via advection transport[*Gardner et al.*, 2005]. To characterize the dominant harmonic components, a harmonic fit consisting of mean plus diurnal, semidiurnal and terdiurnal oscillations, as shown in Equation 6.1, is applied to the Fe parameters for all four seasons:

$$y = A_0 + A_{24}\cos\left[\frac{2\pi}{24}(t - P_{24})\right] + A_{12}\cos\left[\frac{2\pi}{12}(t - P_{12})\right] + A_8\cos\left[\frac{2\pi}{8}(t - P_8)\right]. \quad (6.1)$$

The fitting results are shown as the solid curves in Figure 6.3, and fitted parameters are summarized in Table 6.3. The large correlation coefficients in most of the fits indicate good correlations between the fitting equation and the data.

Both the centroid and bottom altitudes in autumn and spring show strong dependence on local time with noon altitudes lower than those in the night. The amplitudes of the fitted diurnal oscillations are much larger than those of the semidiurnal and terdiurnal oscillations. For the column abundance, the summer and winter seasons have comparable amplitudes of 24-h and 12-h oscillations, which are about 5% of the mean abundance of the corresponding seasons. The 24-h and 12-h oscillations in autumn are also comparable and about 7.3% of the mean abundance. The amplitude of 24-h oscillation in spring is $\sim$ 13% of the mean abundance, double the amplitude of the 12-h oscillation. Springtime noon hours have higher column abundance and larger RMS width than those at night. The autumn column abundance and RMS width have weaker dependence on local time but in general larger noon values.

Due to the largest difference of solar radiation between noon and midnight, the comparison of Fe profiles at these two local times can shed light on the roles of solar radiation in the diurnal variations. In Figure 6.4 we compare Fe density profiles at midnight and noon for the four seasons

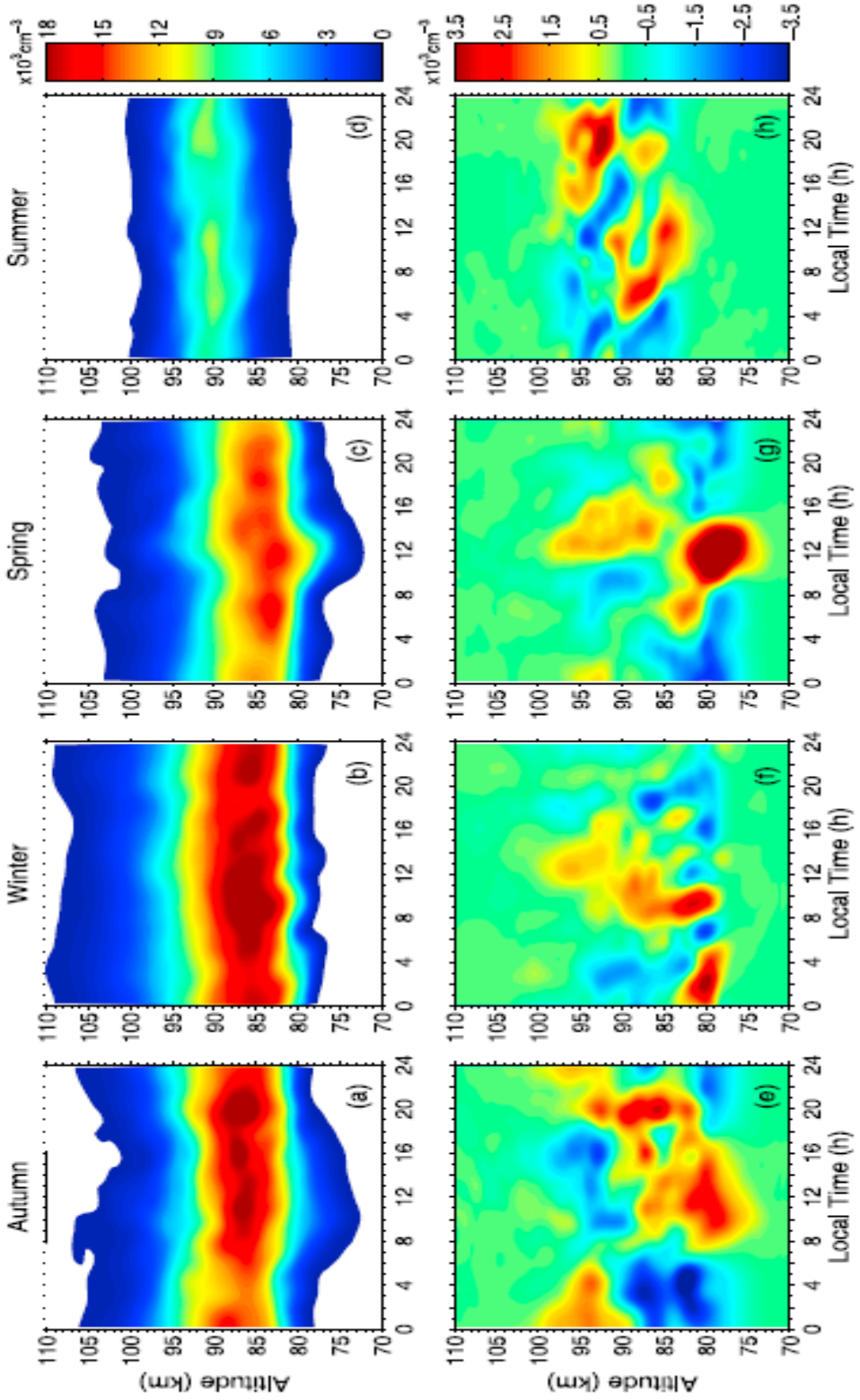

FIGURE 6.2: (a–d) Seasonal composite contours of Fe density versus local time and altitude, and (e–h) Fe density perturbations for autumn, winter, spring and summer seasons. Note that Fe densities below 300 cm^{-3} have been set to white in a–d. The density perturbations for summer in Figure 2h have been multiplied by a factor of 2 for better readability. The units for Fe densities and density perturbations are $\times 1000$ cm^{-3}.

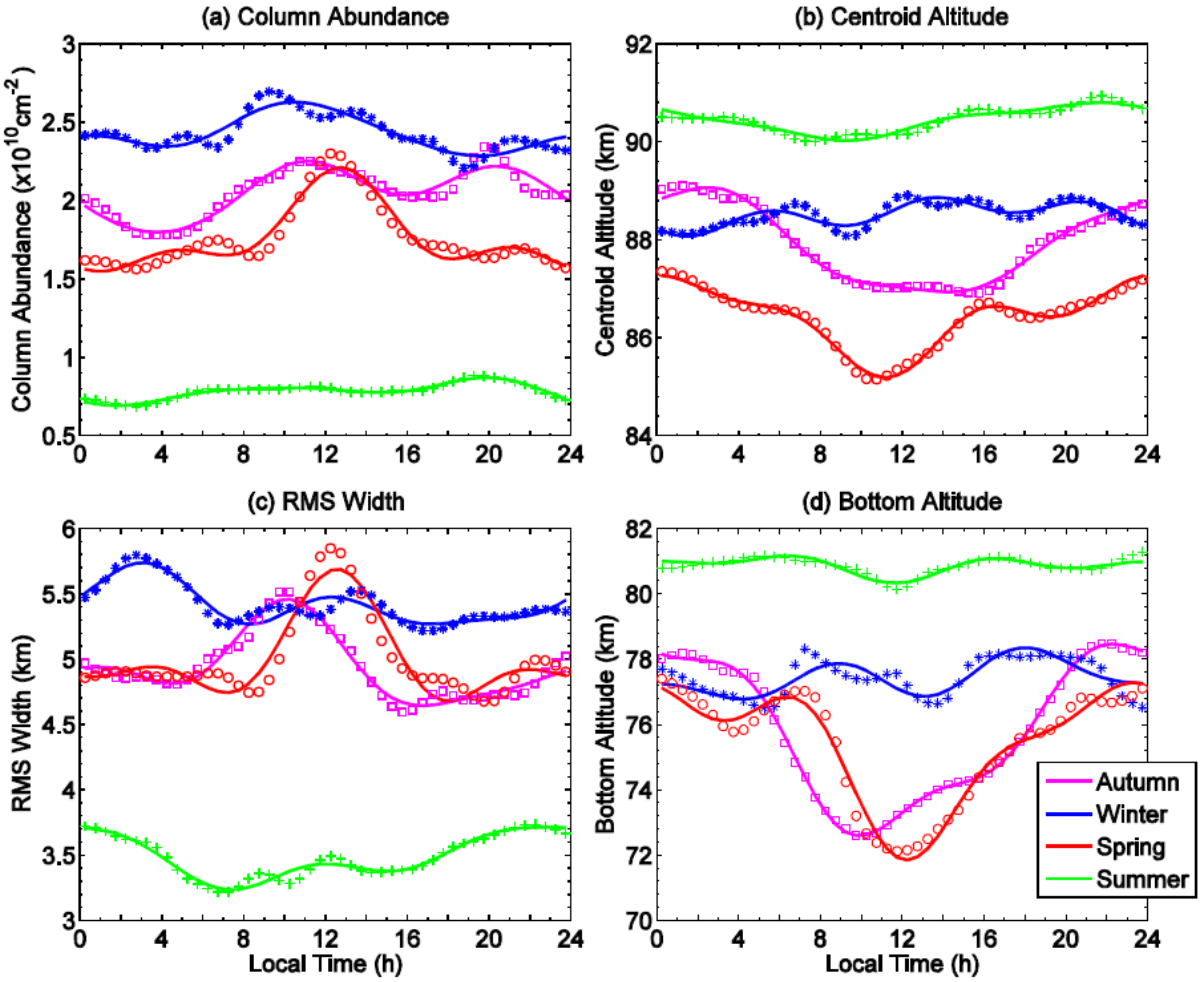

FIGURE 6.3: Diurnal variations of the Fe layer column abundance, centroid altitude, RMS width, and bottom altitude derived from the four seasonal composites (autumn: squares and pink curve; winter: stars and blue curve; spring: circles and red curve; summer: crosses and green curve). The solid curves are the harmonic fittings to the observational data points.

(i.e., 0 ± 0.5 LT and 12 ± 0.5 LT mean profiles). A distinct features is the lower altitude and higher Fe density at the underside around noon than at midnight in autumn and spring. The altitude difference between the midnight and noon 300 cm^{-3} density contours is about 5 km in both seasons, while the difference at the 3000 cm^{-3} contour is 2.8 km in autumn and 3.8 km in spring. Such bottom growth leads to the scale height of Fe density below 80 km increasing from 0.5 to 1.5 km in the night to about 2–4 km at noon in autumn and spring. The midnight and noon profiles have much smaller differences on the bottomside in summer and are essentially identical

TABLE 6.3: Parameters of Harmonic Models for Diurnal Variations in Measured Fe Layer Column Abundances, Centroid Altitudes, RMS Widths and Bottom Altitudes at McMurdo, Antarctica Through Four Seasons

	Autumn	Winter	Spring	Summer	Autumn	Winter	Spring	Summer
	Column Abundance [a]				Centroid Altitude			
A_0	2.05±0.03	2.43±0.02	1.76±0.02	0.78±0.003	87.9±0.02	88.5±0.05	86.4±0.03	90.4±0.02
A_{24}	0.15±0.02	0.12±0.02	0.23±0.02	0.043±0.005	1.07±0.03	0.22±0.05	0.75±0.03	0.34±0.03
A_{12}	0.14±0.02	0.08±0.02	0.12±0.02	0.05±0.05	0.09±0.04	0.06±0.05	0.27±0.03	0.04±0.03
A_8	0.03±0.02	0.02±0.02	0.10±0.02	0.016±0.005	0.12±0.04	0.2±0.05	0.23±0.03	0.06±0.03
P_{24}	15.4±0.5	10.2±0.7	12.7±0.4	16.0±0.4	1.2pm0.1	15.7±0.9	23.6±0.2	21.0±0.4
P_{12}	9.8±0.3	11.4±0.5	0.6±0.4	8.1±0.3	2.8pm0.8	6.4±1.6	4.0±0.3	2.5±1.9
P_8	3.6±0.9	0.8±0.8	4.8±0.3	4.5±0.4	3.9pm0.4	5.4±0.3	7.5±0.2	4.9±0.8
Correlation [b]	0.95	0.91	0.96	0.98	0.99	0.89	0.99	0.95
	RMS Width				Bottom Altitude			
A_0	4.94±0.01	5.42±0.02	5.0±0.03	3.49±0.01	75.8±0.03	77.4±0.1	75.4±0.1	80.9±0.03
A_{24}	0.25±0.02	0.13±0.02	0.26±0.04	0.20±0.02	2.83±0.05	0.36±0.14	2.1±0.1	0.17±0.05
A_{12}	0.21±0.02	0.13±0.02	0.27±0.04	0.08±0.02	0.28±0.05	0.43±0.14	0.9±0.1	0.21±0.05
A_8	0.07±0.02	0.08±0.02	0.16±0.04	0.04±0.01	0.52±0.05	0.33±0.14	0.7±0.1	0.17±0.05
P_{24}	8.8±0.3	3.6±0.2	12.2±0.6	22.2±0.3	23.7±0.1	17.5±1.5	0.8±0.2	0.9±1.0
P_{12}	10.6±0.3	14.2±0.3	12.6±0.2	11.8±0.3	3.2±0.3	7.6±0.7	6.8±0.3	5.4±0.3
P_8	2.1±0.3	3.7±0.3	4.6±0.3	3.3±0.5	5.0±0.2	1.2±0.6	7.6±0.2	7.6±0.3
Correlation	0.98	0.94	0.95	0.98	0.99	0.82	0.98	0.91

[a] A_0 is the diurnal mean, A_{24}, A_{12} and A_8 are the amplitudes and P_{24}, P_{12}, and P_8 are the phases of the diurnal, semidiurnal and terdiurnal oscillations, respectively. Means and amplitudes for column abundances, centroid altitude, RMS width and bottom altitude are given in the units of $\times 10^{10}$ cm^{-2}, km, km, and km, respectively; phase are in hours

[b] It is the correlation between hormonic fitting and observed data.

in winter. On the layer topside, the noon upper boundary is lower than the midnight profile in autumn, but nearly identical to the midnight upper boundary in spring, summer and winter.

6.5 Solar Effects on the Fe Layer Bottomside

The autumn and spring composite profiles clearly show diurnal variations of the Fe layer, and the daytime bottom extension appears to be correlated with solar illumination. Therefore, it is essential to investigate how the observed Fe diurnal variations are related to solar elevation angles. This is done most effectively by analysing individual days of observations to avoid artifacts caused by seasonal changes of solar elevation angle with local time. Here we present four case studies with continuous lidar observations spanning ~24 h at McMurdo. They represent four different solar

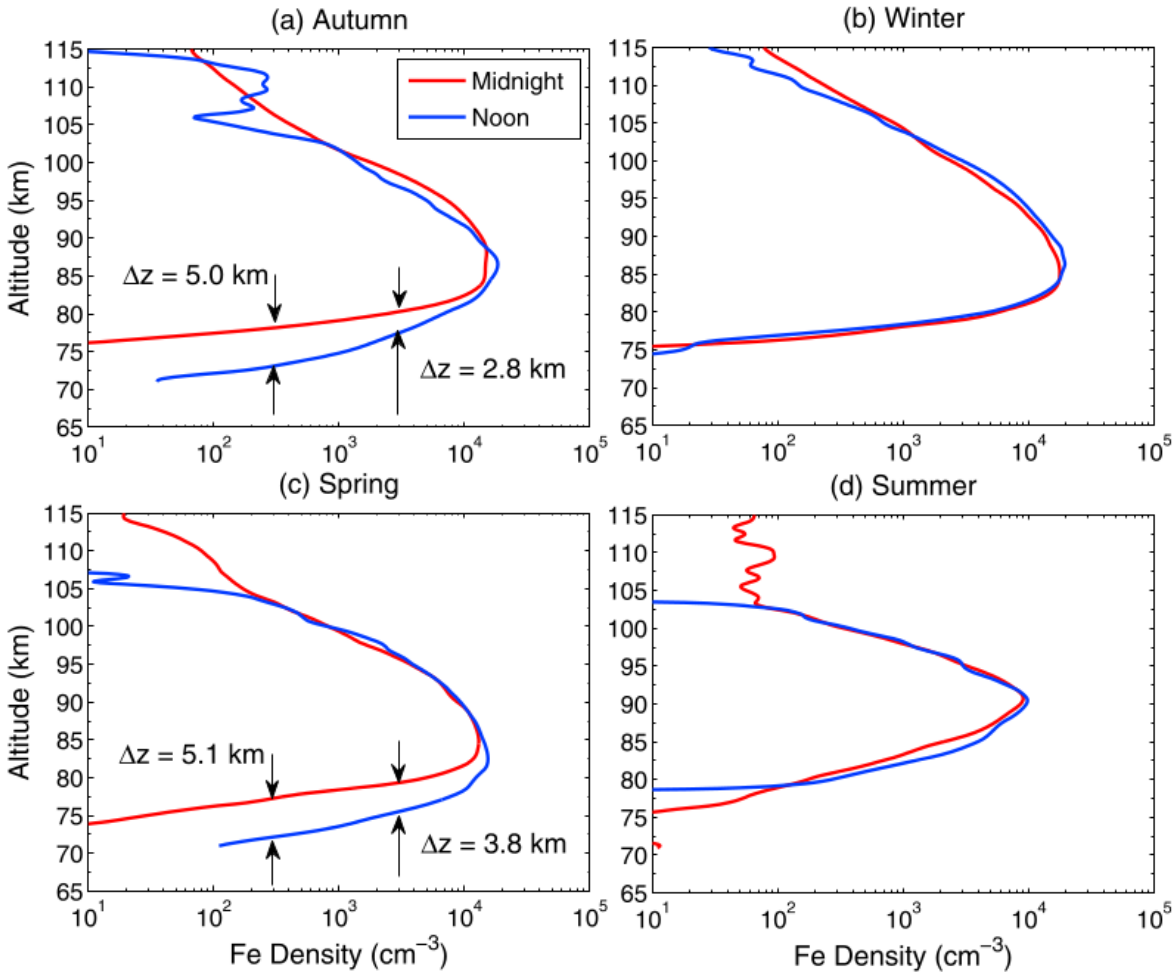

FIGURE 6.4: Comparison of Fe density profiles between noon and midnight through four seasons: (a) autumn, (b) winter, (c) spring, and (d) summer.

illumination and MLT conditions. The solar elevation is defined as the angle from the horizon at sea level up to the geometric center of the Sun's apparent disk.

Figure 6.5 shows contour plots of the Fe layer on 20-21 March 2012, 7-8 April 2011, 11-12 August 2011, and 19-20 September 2012. These four cases are 1, 17, 40 and 2 days away from the autumn equinox (21 March) or spring equinox (21 September), respectively, so they represent quite different solar illuminations. The day and night switch in the MLT is clearly shown in all four cases, with the nighttime bottom around or slightly below 80 km and the daytime bottom extended to 70–73 km. The observations on 2021 March 2012 start in the daytime under quite strong solar

radiation. By ∼19 LT the relatively wide Fe layer begins to "shrink" as the layer bottom starts to contract and reaches its nighttime high around 21 LT. After going through a relatively short night, the layer bottom begins to extend downward around 4 LT, and finishes the descent by 5 LT. Afterward, the layer bottom resides stably around 72–73 km throughout the remainder of the observations. The ascending rate at sunset appears to be slower than the descending rate at sunrise. For the 7–8 April 2011 case, growth is observed at the layer bottom during the morning hours around 6 LT when sunlight hits the MLT. The bottom altitude quickly descends to 72–73 km within an hour and then stays at this low altitude for ∼10 h before ascending back to the night altitude around 17 LT. The ascending rate at dusk appears to be slower than the descending rate at dawn. The case on 11–12 August 2011 (Figure 6.5c) experiences the Sun below the horizon at sea level through the entire 25 h of observations, but sunlight reaches the MLT region for several hours around noontime. This situation is reflected in Figure 6.5c, where the bottom extension is very obvious around noon hours. This August case indicates that after long dark nighttime, the return of sunlight to the MLT region, even for only a few hours, can cause significant enhancement of Fe densities at the underside of the Fe layers. Interestingly, in this August case, the Fe layer bottom extends to nearly 70 km at noon, to our knowledge the lowest ever reported in the literature. The above three representative cases clearly show that the bottom growth/contraction of the Fe layer is a solar effect and not tidal in nature.

To quantify the solar effects on the Fe layer bottomside, the bottom altitudes are plotted versus local time in Figures 6.6a–6.6l for the four cases. Here the definition of the bottom of Fe layer is the altitude of 300 cm^{-3} density contour. The minimum sunlit altitude and solar elevation angle are plotted versus local time, respectively, as black and red curves in Figures 6.6e–6.6h. Here the minimum sunlit altitude refers to the lowest altitude that sunlight can reach for a given solar

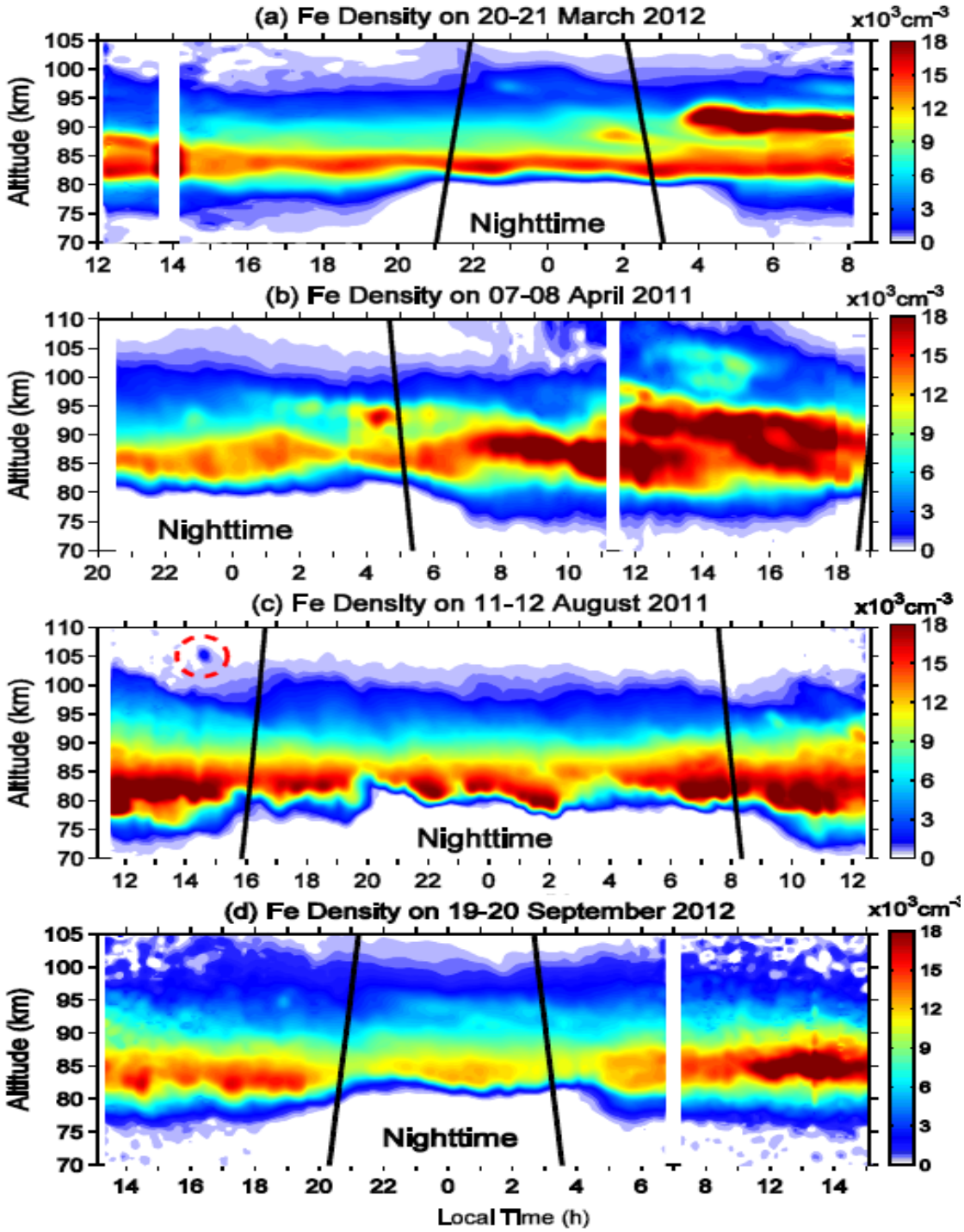

FIGURE 6.5: Contours of Fe density versus local time and altitude observed on (a) 20-21 March 2012, (b) 7-8 April 2011, (c) 11-12 August 2011, (d) 19-20 September 2012 at McMurdo, Antarctica. Black lines denote the minimum sunlit altitudes in MLT region and corresponding local time.

elevation. Note that the scales for solar elevations on the right side have different ranges for the 4 days. Figures 6.6i–6.6l plot the bottom altitudes versus their corresponding solar elevations.

A nearly flat bottoms in day and night (excluding the transition periods from night to day or from day to night) exhibit in the March, April and September cases (Figures 6.6a, 6.6b, 6.6d). The Fe layer bottom stays near 80 km in the night and around 72–73 km during the day quite stably, altough the bottom altitude can still be perturbed by waves during the day and night as shown in Figure 6.6a–6.6d. The duration of the daytime flat bottom is closely correlated with the period of solar elevation above the horizon at sea level. The flat bottom around 72-73 km on 20-21 March 2012 lasts ∼14 h from 5 to 19 LT, while it is ∼10 h from 7 to 17 LT in the case of 7–8 April 2011, and ∼13 h from 5 to 18 LT in the case of 19–20 September 2012. The period for solar elevation above the horizon is ∼ 13 h from 5.5 to 18.5 LT for the March case, ∼9 h from 7.5 to 16.5 LT for the April case, and ∼12h from 5.5 to 17.5 LT for the September case. In four cases, the daytime flat bottom duration is about 1 h longer than the sunlit period above the sunlit period above the horizon. This is illustrated by the bottom altitude completing its descent about a half hour before sunrise and beginning its ascent about a half hour after sunset at sea level. These transition periods correspond to solar elevations angles between -1° to -2° and -7° to -9° as shown in Figures 6.6i–6.6l, when sunlight intersects with the lower atmosphere before reaching the MLT. Here the lower atmosphere refers to the atmosphere below the MLT region, say below 70 km or lower. In the August case, because the sun is never above the horizon on 11–12 August 2011 but below -2° through the entire observations, the daytime is short at the MLT, leading to the continuously varying bottomside altitude around the noon hour in Figure 6.6c. It is also apparent in Figure 6.6 that the solar elevation angle at which the bottom altitude begins its descent from the nighttime high during sunrise, as well as completing its ascent to the nighttime high during

sunset, is around $-8°$.

The transition of bottom altitude occurs during dawn and dusk periods in a nearly linear fashion with local time in Figure 6.6a, 6.6b and 6.6d.Even for the August case in Figure 6.6c, the transitions can be simplified to linear variations in the first-order approximation. Linear fits to the transition periods provide the change rates of bottom altitude Z_B with time, dZ_B/dt, which are given in Table 6.4. The descent during sunrise is much faster than the ascent during sunset, confirming the asymmetry findings from Figure 6.5. For example, in the case of 20–21 March 2011, the sunrise descending rate dZ_B/dt is -5.0±0.5 km/h, compared to the sunset ascending rate of 3.6±0.2 km/h. Such asymmetry exists in all four cases. Comparing among these four cases, the ascending rate in the sunset exhibits a trend that the bottom transition takes the minimum time at the March equinox but becomes slower when the day of year moves away from the equinox. The descending rate of the April case is comparable or slightly faster than the March equinox case, while both are much faster than the descending rate on 11–12 August 2011.

The bottom transition corresponds to solar elevation angles between $-1°$ to $-2°$ and $-7°$ to $-9°$ as shown in Figures 6.6i-6.6l, when sunlight intersects with the lower atmosphere before reaching the MLT. The absorption and scattering of sunlight by the lower atmosphere apparently influences the solar flux and spectrum that reach the MLT region, producing pronounced effects on the bottom growth/contraction. This transition shape is consistent in all four cases. It appears that the transition corresponds to certain solar elevations rather than fixed local time. This explains the near 'V' shape of the bottom altitudes derived from the autumn and spring composites (Figure 6.3d). Because the bottom transition is "locked" to the solar elevation angle and the corresponding local time changes through the season, averaging the data in the same local time but with different solar elevations smears out the flat bottom feature on individual days, resulting the 'V' shape.

TABLE 6.4: Transition Rates of Fe Layer Bottom Altitude with Local Time and Solar Elevation.

	dZ_B/dt (km/h) [a]				$dZ_B/d\theta_E$ (km/deg)			
	20Mar2012	07Apr2011	11Aug2011	19Sep2012	20Mar2012	07Apr2011	11Aug2011	19Sep2012
Sunrise	-5.0±0.5	-5.4 ±1.0	-3.4±0.2	-3.9±0.5	-1.54±0.14	-1.70±0.30	-1.75±0.08	-1.3±0.2
Sunset	3.6±0.2	2.6±0.2	1.8±0.1	1.6±0.5	-1.18± 0.04	-0.94±0.10	-0.92±0.06	-0.6±0.1
Correlation[b]	0.99/0.99	0.98/0.99	0.99/0.98	0.99/0.99	0.99/0.99	0.97/0.99	0.99/0.99	0.97/0.98

[a]Notation: Z_B–bottom altitude, t–local time, and θ_E–solar elevation angle.
[b]The first and second numbers are the correlation coefficients for sunrise and sunset fittings, respectively.

The bottom altitudes are plotted versus solar elevations in different colors in Figure 6.6i–6.6l for for sunrise (0–12 LT) and sunset (12-24 LT). It is apparent that the bottom altitude change rate with solar elevation angle ($dZ_B/d\theta_E$) during sunrise is steeper than during sunset in all four cases. Although the August case exhibits an altitude shift downward as compared to the March, April and September cases, these four cases give similar sunrise rates or sunset rates, indicating that the rate with solar elevation does not change with season. To quantify the rates, linear fits are applied to the transition periods. Because the April case experienced large wave perturbations, the fit is limited to a smaller range than the other two cases in order to minimize the wave influences. The results of $dZ_B/d\theta_E$ are listed in Table 6.4. On average the rate during sunrise is about -1.58 km/deg, steeper than the average rate of about -0.9 km/deg during sunset. The rate difference is consistent with the descent-ascent asymmetry observed above.

To further characterize the bottom transition, we investigate how fast the Fe layers respond to sunrise and sunset at the MLT. The minimum sunlit altitudes plotted as blackness in Figure 6.6 denote the sunrise and sunset times for each altitude in the MLT. The refraction of sunlight by the Earth's atmosphere introduces time correction less than 10 min, and is thus negligible for the purpose of this study. When sunlight first reaches the Fe layer bottom at 78–80 km during sunrise, the corresponding solar elevation is about $-9°$ in all four cases, regardless the day of year or latitude. However, the Fe layer bottom descent does not start until the solar elevation rises to about -8°. Therefore, there are considerable time delays between sunrise at the MLT and

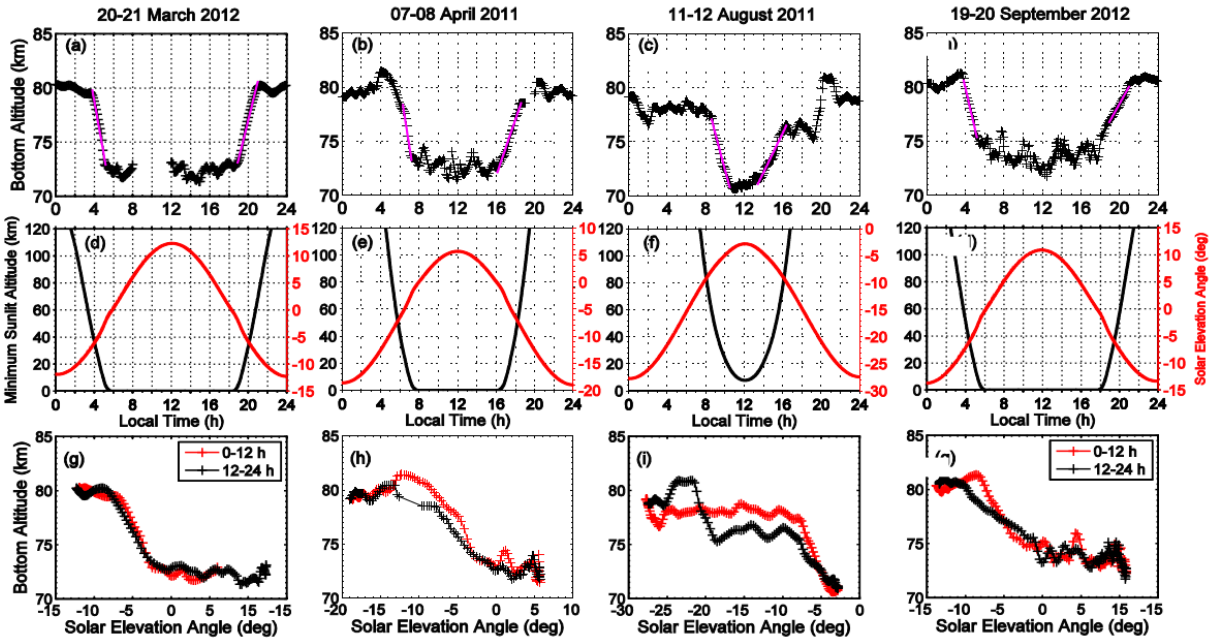

FIGURE 6.6: (top) Fe layer bottom altitudes versus local time, (middle) the corresponding minimum sunlit altitude and solar elevation angle, and (bottom) altitudes versus solar elevation angle for the lidar observations on (a, e, i) 20–21 March 2012, (b, f, j) 7–8 April 2011, (c, g, k) 11–12 August 2011, (d, h, l) 19–20 September 2012. The black and red lines in Figures 6.6e–6.6h represent the minimum sunlit altitude and solar elevation angle, respectively. The purple lines in Figures 6.6a–6.6e are linear fits to the transition periods at dawn and dusk. The red and black crosses in Figures 6.6i–6.6l are the sunrise (0–12 h) and sunset (12–24) h, respectively.

appreciable Fe density growth at the bottom. As shown in Figure 6.7, such time delays increase with decreasing altitude. Using the March equinox case as an example, the sunrise at 79 km is 2.83 LT in Figure 6.6e, but the bottom descent starts at 3.9 LT from this altitude (Figure 6.6a), giving a delay time of ∼1.07 h (Figure 6.7). The sunrise time at 75 km is 2.93 LT, and the Fe density at 75 km increases to 300 cm^{-3} at 4.85 LT, giving the time delay of 1.92 h. Such delay time also varies with the season, e.g., the time delay at 75 km changes to 1.6 h on 7–8 April 2011 and 0.97 h on 11–12 August 2011. On the other hand, the bottom density starts to decrease a few hours before sunset at MLT altitudes. The sunset time difference also varies with season, being shortest in the August case and longest in the March case. For example, the Fe density starts to decrease about 1.7, 1.4 and 0.45 h before the sunset at 75 km in the March, April and August cases, respectively.

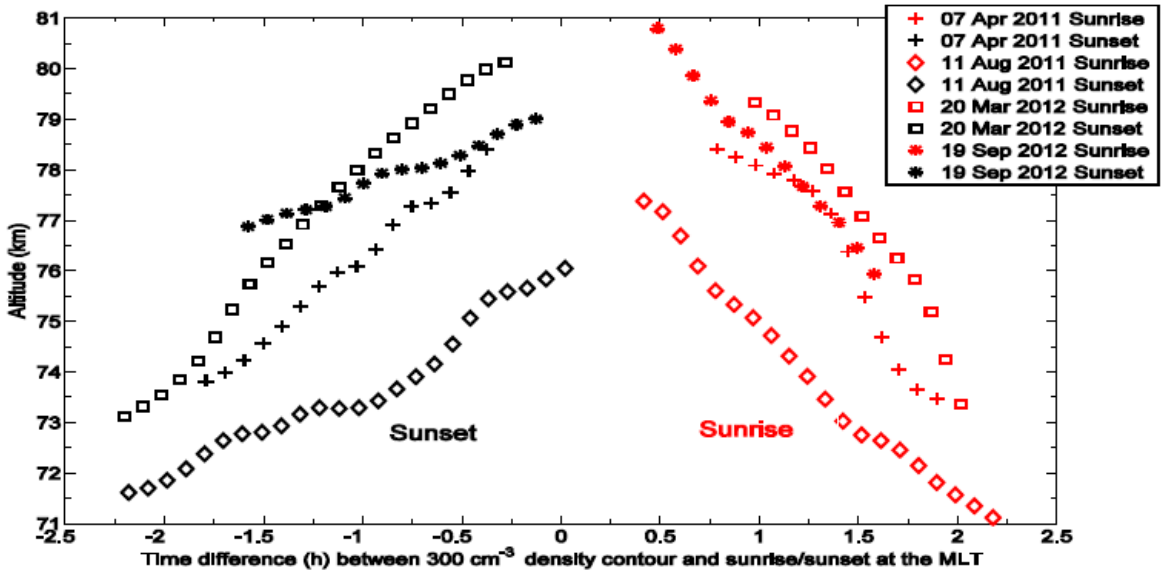

FIGURE 6.7: Time difference between the 300 cm^{-3} Fe density contour and sunrise/sunset at the corresponding MLT altitude for the three cases in March (squares), April (crosses), August (diamonds), September (stars). Positive time difference are for the bottom extension during the sunrise and negatives are for the bottom contraction during the sunset.

As with sunrise, the lower altitudes experience longer time differences at sunset in all four cases (Figure 6.7).

The noon and midnight Fe density profiles are compared for the four case studies in Figure 6.8. The noon bottom extensions are substantial in all cases, and they are very significant on 11-12 August 2011 when the altitude difference is as large as ∼8 km for the density 300 cm^{-3}. The noon profiles have consistently higher density and lower altitude at the layer peak than the midnight profiles. Both the April and August cases exhibit enhancement of the layer topside at noon as compared to midnight. Checking the topside altitude of the 300 cm^{-3} Fe density contour, all four cases show neither local time nor solar elevation dependence. The upward extension of the topside around noon on 7–8 April 2011 is likely caused by a high-altitude sporadic Fe layer event, whereas the August case lacks sporadic activity. We note that 11 August 2011 was close to the peak time of Perseids meteor shower, and in fact our lidar observed a meteor trail, shown as a dot around 14.5

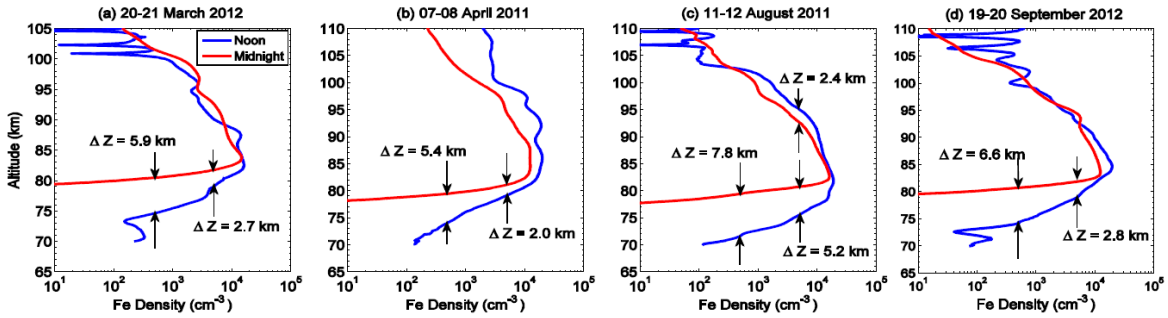

FIGURE 6.8: Comparision of Fe density profiles between noon and midnight on (a) 20–21 March 2012, (b) 7–8 April 2011, and (c) 11–12 August 2011, and 19–20 September 2012

LT and near 105 km in Figure 6.5c. Such a meteor shower may impact the layer topside through enhanced direct meteor deposition.

6.6 Observational Conclusions

The McMurdo Fe layer undergoes significant diurnal variations on the bottomside below 80 km in autumn and spring when this region experiences appreciable diurnal variations of solar illumination. The lidar observations show that the bottomside of the Fe layer extends downward by ∼5 km or more during the day, and then contracts at night. In the polar winter with 24-h darkness, the Fe layer bottom altitudes are strongly perturbed by waves, but they are not tied to local time or solar elevation. The Fe density perturbations exhibit downward phase progression in the summer main layer (84–98 km) with a vertical phase speed of about -1.25 km/h. These are most likely due to diurnal and semidiurnal tidal perturbations. The other three seasons do not show clear tidal signatures in the main layers, and the density perturbations are dominated by residual gravity wave perturbations. Around the layer peak (∼84–90 km), the Fe density undergoes substantial variations throughout the day in each season with a tendency to higher peak density around local noon and lower density near local midnight. Summer Fe layers show lower density, higher altitude, and narrower width than those of the other three seasons, principally because of heterogeneous removal

of Fe atoms below 90 km by ice particles, low temperature, and upward advective transport in the polar summer MLT.

The case studies with 24-h continuous lidar observations in March, April, August and September clearly demonstrate that the diurnal variations at the Fe layer bottomside are closely correlated with solar elevation angle. The bottomside growth/contraction of the Fe layer is not related to any obvious tidal or wave effect, whereas it is clearly revealed as a solar effect. The layer bottomside altitudes (i.e., constant density contours) are nearly flat during both day and night in the March and April cases. The duration of the daytime flat bottom is closely correlated with the period of solar elevation above the horizon. The bottom extension occurs even when the MLT is only sunlit for a few hours as in the August case, but is absent through the dark polar winter nights. The bottom transition occurs when the solar elevation angles are between $-9°$ and $-1°$ as measured from sea level. That is when sunlight illuminates the MLT region after first passing through the lower atmosphere. Once the solar elevation is above $-1°$, the layer bottomside is stable at its daytime altitude ($\sim$70–73 km) and density ($\sim$200–500 cm^{-3}). Similarly, once the solar elevation falls below $-9°$, the layer bottomside is stable at its nighttime altitude ($\sim$78-80 km).

The transition of bottom altitude occurs during dawn and dusk in a nearly linear fashion with local time. Asymmetry exists between the bottom downward extension at dawn and the upward contraction at dusk. In general the descending (formation) rate is faster than the ascending (dissipation) rate. The bottom ascent during sunset takes the minimum time at the March equinox and becomes slower when moving away from the equinox. However, the descending rates during sunrise are comparable between the March and April cases, and both are much faster than the August case when the Sun stays below the horizon at sea level. The rate of change of the bottom altitude with solar elevation angle ($dZ_B/d\theta_E$) does not vary with season, and the average rate of

about 1.6 km/deg during sunrise is steeper than the rate of 1.0 km/deg during sunset. There is a time delay between sunrise at the MLT and appreciable bottomside growth. Conversely, the contraction of the layer bottomside starts earlier than MLT sunset. Such time delays vary with altitude and season. For a given day, it takes a longer time to produce appreciable changes in Fe bottomside density at the lower altitudes than at higher altitudes. For a fixed altitude, the delay time is longest on 20–21 March, intermediate on 7–8 April and shortest on 11–12 August when the daily mean solar elevation varies from the highest to the lowest.

Finally, the bottom enhancement during the day leads to the noon profile having higher peak and bottom densities, as well as lower peak and bottom altitudes, than the midnight profile. This is true for the autumn and spring composites as well as in four individual case studies. A direct consequence is that the noon profiles possess larger scale heights of Fe density on the underside than the midnight profiles in autumn and spring (If Fe increases with height, the scale height is negative). The autumn composite profiles exhibit a small reduction in Fe density on the layer topside at noon, but such a reduction is not pronounced in the spring composite. Furthermore, the topside altitudes (constant density contours) show neither local time nor solar elevation dependence in the four individual cases.

In summary, significant solar effects in diurnal variations of the Fe layer are observed at McMurdo, and the daytime bottomside extension is clearly correlated with the solar elevation. The observed Fe diurnal variations are obviously much larger than the Na diurnal variations reported in the literature. These results provide direct evidence for the influence of solar UV radiation on the chemistry and composition of the mesopause region.

6.7 Implications for Fe Chemistry in the MLT

Although this is the first formal report of significant diurnal variations of the Fe layer to appear in the scientific literature, we are aware that J. Höffner has observed a similar daytime extension of the Fe layer bottomside at Andoya from 2008 to 2009 (J. Höffner, private communication, 2012). In addition, our group also observed this same feature at Boulder, Colorado in August and September 2010 when testing this lidar prior to its McMurdo deployment. Unfortunately, existing modeling work has not addressed the potential impact of varying solar illumination on Fe layer densities. Nevertheless, *Plane* [2004] presented a comprehensive modeling of Na Diurnal variations, which serves as guideline in the discussion.

At the underside of the Fe layer, FeOH is believed to be the major reservoir species. Partitioning among Fe, FeOH and other Fe-containing species is largely determined by the ratio of [O], [H] and $[O_3]$. Fe is converted to the relatively stable reservoir FeOH through a series of reactions beginning with oxidation of Fe by O_3. FeO and FeO_2 produced by this oxidation are short-lived according to *Self and Plane* [2003]. They can be recycled back to Fe by atomic O or further converted to reservoir species via reactions with H_2O, CO_2 and O_2. FeOH is recycled back to Fe by reaction with H. Therefore, the Fe layer density and shape on the bottomside are strongly dependent on the concentration profiles of [H], [O] and $[O_3]$. Atomic O and H are produced during the day by photolysis of O_2 and H_2O, respectively. Above 82 km there is little diurnal variation in these species, but below 80 km the atomic O and H concentrations increase by about 4–5 orders of magnitude from night to day [*Rodrigo et al.*, 1991; *Plane*, 2003]. The sharp transition between 75 and 85 km at night corresponds to atomic oxygen shelf. As a consequence, FeOH is converted back to Fe much faster during the day while the loss of Fe via reaction with O_3 is slower during

day than night. As a consequence, the balance between atomic Fe and its reservoirs is shifted to the way of net Fe being produced from FeOH by the increase of O and H. Furthermore, by analogy with Na diurnal variations, photolysis of Fe-containing molecules (e.g. FeOH) under sunlight, if any, can help enhance the daytime growth and extension on the layer bottomside.

However, the situation is not as simple as described above, which assumes a large supply of FeOH near the layer bottomside. The potential removal of FeOH and other Fe species must also be considered here. In principle, Na species have similar partitioning among Na, $NaHCO_3$ and other Na-containing molecules is a closed system, a large diurnal variation of Na should also be observed [see *Plane*, 2004, Figure 4a]. That is, the noon Na profile should be lower in height and much larger in density than the midnight profile. Because earlier Na observations did not show such large diurnal variations [*Clemesha et al.*, 1982; *States and Gardner*, 1999], *Plane* [2004] suggests that the reservoir species $NaHCO_3$ is removed via dimerization of $NaHCO_3$ and permanent attachment of the Na species on meteoric smoke particles. Such removal diminishes the concentration of $NaHCO_3$ that accumulate during the night. Therefore, when sunlight returns to the MLT, the release of Na from $NaHCO_3$ is significantly reduced in comparison to the situation when no removal mechanisms are implemented. Because Fe diurnal variations are significant in the McMurdo observations, there must be appreciable FeOH concentrations at the underside of the Fe layer when sunlight returns. One implication is that the removal of FeOH and other reservoir species may not be as extensive as the removal of $NaHCO_3$. Nevertheless, the permanent removal of Fe or Na species by meteor smoke particles is unavoidable in order to balance out the meteoric input. The permanent removal rate of Na species is unlikely much higher than that of Fe species considering the ratio of Na/Fe in the MLT. It is possible that other removal mechanisms, e.g. via dimerization, are significant in removing $NaHCO_3$ but not so for the Fe species.

The photolysis of O_2 and H_2O to produce O and H requires UV solar radiation, viz, the Lyman-α at 121.6 nm for breaking H_2O and the Schumann bands for breaking O_2. It is likely that the photolysis of FeOH and other Fe species also requires UV sunlight. It is well known that water vapor and ozone in the lower atmosphere efficiently absorb the UV sunlight over a large spectral range. For the period when solar elevation lies between -1° and -9°, sunlight passes through the lower atmosphere before reaching the MLT. Therefore, the solar flux in the UV spectrum received at the MLT is attenuated. Within this elevation range, for the transition from night to day, the higher solar elevation leads to a shorter path through the lower atmosphere and thus, larger UV solar flux $\Phi(\lambda)$ reaching the layer bottomside below 80 km. Consequently, the photolysis rate of FeOH increases with time, which is given by $R_{photolysis} = \int \sigma(\lambda)\Phi(\lambda)d\lambda$ (in the unit of s^{-1}), where $\sigma(\lambda)$ is the photolysis cross section at wavelength λ [*Self and Plane*, 2002]. The increased photolysis of H_2O results in higher [H] thus higher release rate of Fe from FeOH, which is given by $R_H = k[H]$ (in the unit of s^{-1}), where k is the rate coefficient for the reaction of $FeOH + H \rightarrow Fe + H_2O$. Overall the production rate of Fe – given by $(R_{photolysis} + R_H)[FeOH]$ in the unit of $cm^{-3}s^{-1}$ – increases as the Sun rises from solar elevation of $-9°$. On the other hand, the loss rate of Fe via reaction with O_3 is given by $k[O_3]$ in the unit of s^{-1}, but it is competed by the reaction of $FeO + O \rightarrow Fe + O_2$. As there is no appreciable [Fe] on the bottomside at night, the total loss rate of $k[O_3][Fe]$ (in the unit of $cm^{-3}s^{-1}$) at the beginning of the transition is close to zero. Once the [Fe] starts to build up, the total loss rate will increase with time during the transition, eventually matching the simultaneously increasing production rate of Fe. Fe density will continue increasing until the production rate and the loss rate reach a balance, after which the Fe density will remain at the daytime steady state. As long as sunlight propagates above the lower atmosphere before reaching the MLT, it is not strongly absorbed by water vapor ozone. Therefore, the UV solar flux

reaching the MLT remains nearly constant (to first order) once above -1° at dawn until the sun sets below -1° at dusk. Constant UV solar flux leads to the constant concentration of O, H, and O_3 and constant photolysis of FeOH or other Fe-containing species. As a consequence, the production and loss of Fe reach a balance at the underside, leading to the nearly constant bottom altitude during the daytime period of the solar elevation above -1°. Once the Sun sets below -9°, sunlight is totally blocked by the Earth from reaching the MLT. The concentrations of O and H dramatically decrease in the absence of UV light and the photolysis of Fe species stops. Thus, the production of Fe on the underside is significantly reduced and the density reaches a new balance with the loss of Fe at higher altitude ($\sim$80 km) in the night. Consequently, the nighttime bottomside resides at the higher altitude around 80 km and the daytime bottomside resides at lower altitude around 72 km. Furthermore, the bottomside altitudes are quite stable during both day and night, although they are still susceptible to wave and tidal perturbations. In the above picture, factors like meteor ablation, transport and permanent removal by smoke particles are neglected in the transition time scale of 1–3 h. However, these factors are important in determining the steady state Fe densities among different seasons.

For any given altitude at the bottomside during the transition period, appreciable Fe density increase will not be observed until after sufficient integration time to build up Fe density to detectable levels (e.g., 100–300 cm^{-3}). Therefore, there is a time delay between sunrise and the 300 cm^{-3} Fe density contour. For the same day but at different altitudes, Fe loss via oxidation with O_3 increases substantially with decreasing altitude because the concentration of O_3 increases with decreasing altitude [*Rodrigo et al.*, 1991]. A consequence is that longer build-up time is required to produce detectable Fe density at lower altitude. According to *Helmer et al.* [1998], the [FeOH] concentration increases with decreasing altitude, while the photolysis rate is quite constant through

the MLT altitudes according to *Self and Plane* [2002]. As a result, the Fe production by photolysis of FeOH increases with decreasing altitude at the underside. The Fe production via FeOH being recycled back by H and O can have either increasing or decreasing altitude dependence depending on the actual H, O and FeOH concentration profiles [*Rodrigo et al.*, 1991; *Plane*, 2003]. To first order, the production rate of Fe may be comparable in the altitude range of 70–80 km. The increasing loss is therefore likely the major factor determining the increasing time delay at lower altitude.

The transition rate from higher to lower altitudes at the bottomside is affected by $d\theta_E/dt$, the rate of change of solar elevation with local time. Since the UV solar flux at the same solar elevation but on different days of year should be the same on the first order of approximation, smaller $d\theta_E/dt$ slows down the increase of UV solar flux thus the Fe production rate at the layer bottomside. This leads to longer transition time and lower transition rate dZ_B/dt. The variation of $d\theta_E/dt$ with season may explain the different transition rates in Table 6.4. In all four cases the transition time ($\sim$1.3 h) for solar elevation to rise from -9° to -6° is similar according to Figure 6.6e–6.6h; however, from -6° to -3°, it takes $\sim$2 h on 11–12 August but only $\sim$0.9 h on 20–21 March. The $d\theta_E/dt$ slows down significantly during the later half of the sunrise transition in the August case, which is consistent with the August transition rate being the slowest.

Besides $d\theta_E/dt$ affecting the increasing rate of Fe production rate, several other factors can also influence the seasonal change of the transition rate and time delay: the history of FeOH, the temperature in the MLT, and the concentration of H_2O and O_3. The accumulation of FeOH over long dark polar nights coupled with downward transport results in higher FeOH concentration in August than in March or April, so more Fe atoms can be released even when sunlight only returns for several hours. At the same time, the rate coefficients of the reaction of FeOH with H are higher at

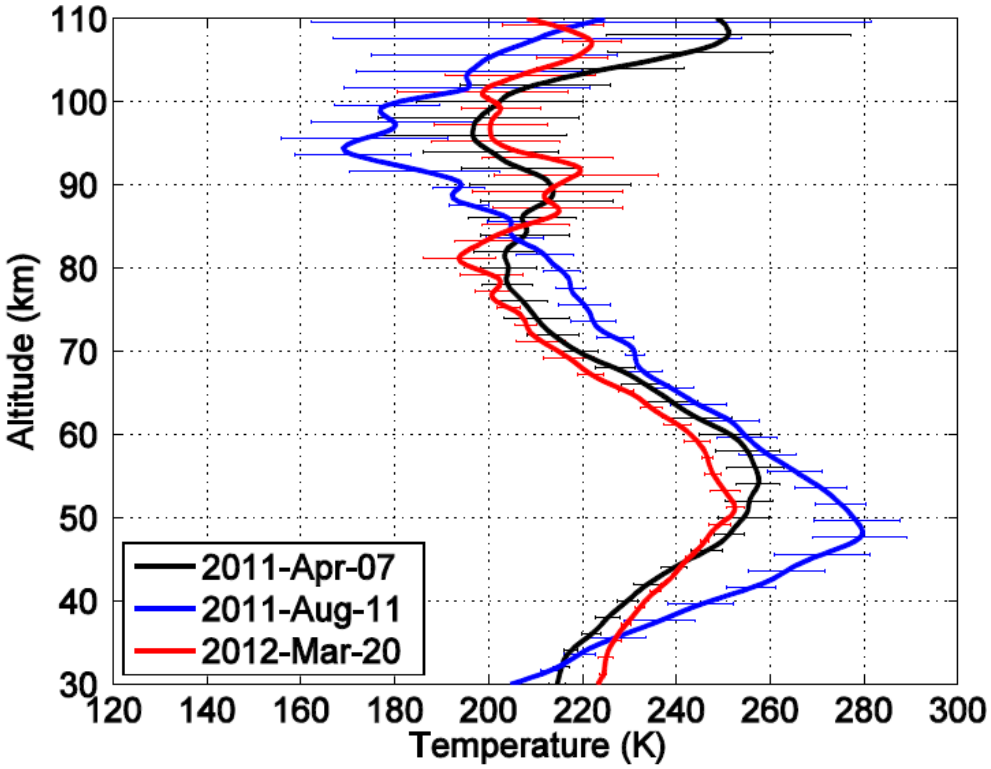

FIGURE 6.9: Comparison of SABER temperatures among 20–21 March 2012, 7–8 April 2011, and 11–12 August 2012. SABER version 1.07 data are used in this comparison. The horizontal bars on each curve represent the geophysical variability on the observational day.

higher temperatures, and the photolysis cross sections are most likely larger at warmer temperature based on the study of photolysis of Na species [*Self and Plane*, 2002]. Due to the insufficient signal-to-noise ratio, the Fe Boltzmann lidar cannot provide reliable temperatures between 70 and 80 km that are relevant to the current discussion. We can, however, use temperature profiles from the TIMED-SABER instrument, taking the mean of McMurdo overpasses within a range of ±5° in latitude and ±10° in longitude during the same period of lidar observations. Using the results of SABER v1.07 data in Figure 9, we find that the temperatures of 11–12 August 2011 are on average 10–20 K warmer than those of 7–8 April 2011 while the temperatures on 20–21 March 2012 are ∼5 K colder than those of the April case in the altitude range of 70–80 km. Thus, the release of Fe from FeOH or other Fe-containing species is expected to be fastest on 11–12 August 2011 and

slowest on 20–21 March 2012. Therefore, the 11 August case is expected to have a much shorter time delay, just as observed. Furthermore, the seasonal change of H_2O concentration below 80 km can affect the increased production of [H] via photolysis, and thus an increase of Fe production rate. If the concentration of O_3 varies with season, e.g., if $[O_3]$ in August is lower than in March or April, the Fe loss can be much smaller in August, helping the August case to build up appreciable Fe density faster as compared to March and April. Overall it is the magnitude of the net production rate of Fe (the difference between the Fe production and loss rates) and its variation during the transition period (solar elevation of $-9°$ to $-1°$) that determine how fast the bottomside Fe density increases to a detectable level, thereby determining the transition time and build-up time observed. Although the photolysis rates of FeOH, O_2, and H_2O are symmetric with respect to solar elevations, the loss rates of H, O, and Fe at dawn and dusk are not symmetric. Neither are the variations of O_3 concentration. Therefore, it is not surprising to observe the asymmetry between the bottomside descent and ascent.

Constituent vertical transport can have profound influences on the Fe layers and its diurnal variations [*Gardner and Liu*, 2010]. Advective transport certainly contributes to the stark contrast between the summer and winter layers, as the upwelling advection in summer helps lift the layer upward while the downwelling advection in winter pushes the layer downward [*Gardner et al.*, 2005]. The MLT above McMurdo experiences strong gravity wave activity throughout the year. Whether these waves introduce large dynamical, chemical and eddy transports and how they influence the Fe layers and their diurnal variations are largely unknown. Furthermore, none of the photochemical reaction rates of Fe-containing species have been reported in the literature except the photoionization rate of Fe [*Brown*, 1973; *Nahar et al.*, 1997]. The FeOH, O, H, and O_3 concentration profiles are also important to the quantitative modeling of the Fe diurnal variations, along

with the rate coefficients of many neutral and ion chemical reactions associated with Fe. Many unknowns exist as roadblocks to the comprehensive understanding of the Fe diurnal variations and Fe chemistry in the MLT. Future lidar observations, laboratory measurements, and detailed modeling work are required to resolve these uncertain terms and to explain the observed Fe diurnal variations quantitatively and unequivocally.

Chapter 7

Conclusions and Future Work

7.1 Conclusions and Merits

This dissertation builds upon years of pioneering work on resonance-fluorescence lidar research to explore the neutral properties of the polar mesosphere and thermosphere. The science motivation to explore these neutral properties is compelling. By blocking extreme hazards from space and regulating radio wave propagation, the space-atmosphere interaction region (SAIR) — our window to open space — is essential for life on Earth and modern society. However, the physical and chemical processes governing the SAIR are not sufficiently understood due to the woefully incomplete measurements of neutral properties in this region, especially between 100 and 200 km altitude. Thermospheric Fe layers extending from ~70 to 170 km discovered by the Fe Boltzmann lidar at McMurdo, Antarctica have opened a new door to observing the neutral thermosphere and mesosphere. This dissertation focuses on revealing such new discoveries and advancing our understanding of the formation of thermospheric Fe layers. The first major discovery is the thermospheric neutral Fe layers with gravity wave signatures observed for the first time in the altitude range of

100–200 km in Antarctica. The second major finding is the observations of significant solar effects on the Fe layer bottom side during local sunrise and sunset.

We have developed a new high-latitude thermospheric Fe/Fe^+ model with advanced numerical modules solving transport and chemistry, to quantitatively study the source, formation and evolution mechanisms of the lidar-observed thermospheric Fe layers (100–200 km) in Antarctica. Numerical simulations confirm the theory proposed by *Chu et al.* [2011] that the thermospheric Fe layers are produced through the neutralization of vertically converged Fe^+ layers, mainly through the direct electron-Fe^+ recombination. While the meteor injection rate of iron species is negligible above 120 km, the polar electric field is sufficient in transporting Fe^+ from their main deposition region to the thermosphere, supplying the source for neutral Fe. Wave-induced vertical shears of vertical and horizontal winds along with the electric field can converge Fe^+ layers in the polar regions. Vertical winds play a key role in transporting Fe to form the observed wave structures, but horizontal divergence can largely offset the effects of vertical convergence. This 1-D thermospheric Fe/Fe^+ model is able to simulate the major features of 28 May 2011 event, like the wave structures, layer heights, densities, etc. However, it cannot reproduce the observed high contrast while keeping comparable layer width.

The discoveries of neutral metal layers reaching near 200 km in the thermosphere have significant scientific meanings because such discoveries challenge the current understandings of the upper atmosphere composition, chemistry, dynamics and energetics, and these neutral metal layers provide tracers for direct measurements of the neutral properties in the least understood but crucially important space-atmosphere interaction region in the altitude range of 100–200 km. The observations of Fe layer diurnal variations and solar effects on the Fe layer bottomside are entirely new results that provide direct, real-time, quantitative evidence for the influence of solar UV

radiation on the chemistry and composition of the mesopause region. Combining these discoveries together, the McMurdo lidar observations have significantly expanded the meteoric metal layer range from the original 80–110 km to the new 70–170 km altitude.

The new observations of Fe, neutral temperatures and gravity waves up to 170 km have opened the door to exploring the neutral polar thermosphere with ground-based instruments. These measurements of plasma-neutral atmosphere coupling and Joule heating, in the critical region above 100 km, are an objective of highest priority for the upper atmosphere science community and for the NRC 2013-2022 Decadal Strategy for Solar and Space Physics. The newly developed thermospheric Fe/Fe^+ model has significantly helped establish a new theory of the source, formation, and evolution of thermospheric neutral metal layers. The theoretical studies with this model lay the foundation for exploring the thermosphere with resonance Doppler and Boltzmann lidars in the future.

7.2 Summary of Scientific Findings

The newfound neutral Fe atoms in the thermosphere not only enable the neutral metal layer studies to extend from the mesosphere to the thermosphere, but also allow resonance lidar to directly measure range-resolved compositions, temperatures and winds in the thermosphere. The thermospheric Fe layers discovered at McMurdo, Antarctica, which lies at the poleward edge of auroral oval, also provide new perspectives of how the ionospheric E-F region responds to geomagnetic disturbances, and the neutral-ion (Fe/Fe^+) coupling in the E-F region. The chief findings of the characteristics of thermospheric Fe layers at McMurdo in Chapter 2 include:

1. The discoveries of thermospheric Fe layers have demonstrated a new approach of studying 100-200 km region by resonance fluorescence lidar. This is a major breakthrough in the metal

layer research of the upper atmosphere

2. These thermospheric layers exhibit layered structures with wave signatures. The relative Fe density perturbations are much larger than the concomitant perturbations caused by atmospheric waves in the neutral atmosphere and the electron density. This key observational fact indicates that the thermospheric Fe layers are not the existing neutral Fe atoms perturbed by atmospheric wave in the thermosphere, but are formed via the coupling between chemical and neutral/electro dynamical processes.

3. The occurrence of thermospheric Fe layers is likely correlated to geomagnetic activities. The high-altitude thermospheric Fe layers are associated with strong geomagnetic disturbances.

4. The temperature measurement capability of this Fe Boltzmann lidar reveals an entirely new perspective of the response of neutral atmosphere temperature to geomagnetic disturbances by providing range-resolved temperature profiles. Under high geomagnetic activity conditions, Fe temperature largely deviated from the MSIS00 temperature above 100 km by increasing a few hundreds Kelvins. A local peak of Fe temperature profile lies at around 130 km and inversion layers were found between about 130 and 145 km. When geomagnetic system is quie, the measured temperatures, to a great degree, are consistent with the temperature of MSIS00.

These characteristics of thermospheric Fe layers at McMurdo suggest that the formations of the thermospheric Fe layers are different from the main layer that is formed by the direct meteor ablation, and impose several challenging questions of understanding the processes associated with the formation of thermospheric Fe layers. A new theory in Chapter 2 details the formation of thermospheric Fe layers by providing a comprehensive picture of forming processes as follows.

1. The thermospheric Fe layers are generated by the neutralization of layered Fe^+ through direct recombination of Fe^+ with electron e^-: $Fe^+ + e^- \longrightarrow Fe + h\nu$.

2. As one of the products of meteor ablation, Fe^+ ions are mainly produced at the main deposition region below 125 km. The ultimate source of thermospheric Fe^+ is the Fe^+ in main deposition region, but transported by upward lifting into thermosphere by electric field or Joule heating induced atmosphere expansion.

3. The gravity-wave structured Fe layers are produced by the wave-structured Fe^+ layers that are converged by neutral wind shears induced by atmospheric waves. The densities of converged Fe^+ layers are significantly high, leading to net production of neutral Fe through direct neutralization with electrons.

4. The formed neutral Fe layers are transported by background winds, and follow the motions of the background medium driven by atmospheric waves.

5. This theory explains the elevated temperatures that are the outcome of the enhanced Joule heating due to powerful geomagnetic activities.

The comprehensive qualitative explanations of the formation of thermospheric Fe layers need numerical support, and some of the details are still mystified by the complex and dynamic coupling between Fe chemistry and dynamics. To provide specific examinations of thermospheric Fe layers and quantify the contributions of chemical and dynamical processes, a new advection-reaction thermospheric Fe/Fe^+ model has been developed from the first principles of physics and chemistry and under the first-order approximation. Compared to other models studying layering phenomena, the primary goal of this model is to study the neutral Fe layers in the thermosphere coupled with

ions and other neutrals via chemical reactions, and it is needed to particularly designed to solve some special issues as follows:

1. The model should be numerically accurate in solving chemistry system. A particular solution is to adopt backward differential formula method to solve the Fe and related chemistry, providing accurate numerical solutions. The advantages of this method are that the solutions converge to desired accuracy, and it is suitable for stiff problems.

2. The model should be numerically accurate in computing mass transport, because we deal with layered phenomenon with large density gradients. High-order flux corrected transport algorithm eliminating numerical diffusion is utilized to compute mass advection. As a result, lower ion drift velocities are required to produce the same magnitude of converged ion layer by eliminating numerical diffusion.

3. We implement the climatology electric potential model, Weimer2005, at high latitudes into the Fe/Fe^{+} model. This is the one of the best options under the situation of lack of polar electric field measurements.

4. To quantify the impact of auroral electron precipitations, we embed the GLOW model into the Fe/Fe^{+} model to parametrize the impact of auroral electron precipitation on Fe chemistry. This includes the parametrization of the ionization of neutral Fe by the impact of energetic electrons.

5. A special issue has also been taken care of in this model for the first time. That is, the effects of the divergence of horizontal winds are taken into account, and the response of minor species like Fe to gravity waves in the diffusely separated thermosphere is explicitly calculated.

The new Fe/Fe^+ model firstly quantifies the formation processes of thermospheric Fe layers. Aimed to provide quantitative support to the theory, the chief scientific findings by the numerical simulations in Chapters 4 and 5 are as follows:

1. First and foremost, the modelling studies in Chapter 4 support the theory of thermospheric Fe formation.

2. The formation of thermospheric Fe layer via direct electron-Fe^+ recombination is confirmed by comparing its productions with dissociative recombination. More importantly, the source of thermospheric Fe^+ has been identified.

3. We demonstrate that the uplifting by polar electric fields is a significant source of thermospheric Fe^+. The large scale feature of polar electric field suggests that thermospheric Fe^+ ions could also have large scale distributions, and the thermospheric Fe layers would not be a localized phenomenon but more universally exist in the polar thermosphere.

4. We confirm that gravity-wave-induced wind shears can produce wave-structured Fe^+ layers at high latitudes, and the significance of vertical wind shears has been identified.

5. The influence of auroral electron precipitation on Fe/Fe^+ chemistry has been quantified for the first time. The roles played by auroral electrons are: the enhanced electron density speeds up the neutralization of Fe^+ inside the converged Fe^+ layers, while the enhanced NO^+ and O_2^+ densities remove neutral Fe by charge transfer when Fe and Fe^+ layers are decoupled.

6. Our model can reasonably reproduce many features of the observations of thermospheric Fe layers on 28 May 2011 with an assumption of Fe^+ abundance of $3.6 \times 10^{10}\ cm^{-2}$. We cannot reproduce the extra high contrast of observed Fe layers without put extreme conditions.

The gravity-wave wind shears, to a great extent, explain the shapes of Fe layers on May 28 2011, but it can not fully explain the 100% densities perturbations in the observed Fe layers.

The observational efforts conducted by Z. Yu during the 2011 season have provided a comprehensive data set, offering the first comprehensive report of diurnal variations of Fe layer through four seasons and the solar effects on the bottomside of Fe layer. The highlights of the scientific merits in Chapter 6 are as follows:

1. Case studies with 24-h continuous lidar observations in March, April, August and September clearly demonstrate that the bottom growth/contraction of Fe layer is a solar effect, closely correlated with the solar elevation angle.

2. The bottom transition corresponds to the solar elevation between -9° to -1° when sunlight passes through the lower atmosphere before reaching the MLT. The bottom altitudes of the Fe layer transit from ~78–80 km in the night to ~70–73 km during the day.

3. The transition of bottom altitude occurs during dawn and dusk in a nearly linear fashion with local time. An asymmetry is found between the downward extension at dawn and the upward contraction at dusk. The descending transition rate at dawn is faster than the ascending rate at dusk. The time delay between appreciable Fe density and the MLT sunrise/sunset increases with decreasing altitude and varies with season.

4. We describe qualitatively how both neutral Fe chemistry with H, O and O_3 and photolysis of Fe-containing molecular species may play important roles in the Fe diurnal variations. It is most likely that the observed bottom extension is due to Fe release from $FeOH$ and other Fe reservoir species by enhanced H and O concentrations during the day and photolysis of these Fe-containing species.

5. Summer layer bottom is uptaken up by visible and sub-visible ice particles, while the winter layers are perturbed strongly by waves.

7.3 Extra Model Simulations for Davis Observations

In this dissertation, numerical simulations have been conducted to study the formation of the thermospheric Fe layers with gravity wave signatures, which are frequently observed at McMurdo. However, the observations from other station at Antarctica are not different from those at McMurdo. Intrigued by the diurnal Fe density perturbations reported by *Lübken et al.* [2011], we investigate the tidal Fe density perturbations with the Fe/Fe^+ model. Figure 7.1 present a contour plot of daily relative Fe density perturbations from 75 to 130 km [*Lübken et al.*, 2011]. From 75 km to ~108 km, the tidal phase speed estimated from the density perturbations is about ~1.5 km/h, corresponding to the vertical wavelength of 36 km. Above 108 km, the phase speed of Fe density perturbations dramatically increased, and the corresponding vertical wavelength seems to approach a significantly larger number. Obviously, the phases of Fe density perturbations above 120 km are not consistent with the classical tidal phases. Recall the formation of thermospheric Fe layers with gravity-wave signatures, we find that the neutral Fe layers are not solely perturbed by the wave dynamics, but, the shapes of neutral Fe layers are heavily influenced by the shapes of Fe^+ layer via $Fe - Fe^+$ coupling.

Therefore, we propose the following theory: below 100 km, tides directly modulate the main Fe layer, producing perturbations following tidal winds in the daily Fe densities; above 100 km and below 110 km, neutral Fe layer perturbations are not only caused by tides, but also by the Fe^+ layer converged by tidal wind shears due to the strong ion-neutral coupling. These two channels are consistent with tidal phases; above 120 km, neutral Fe layers are mainly formed by

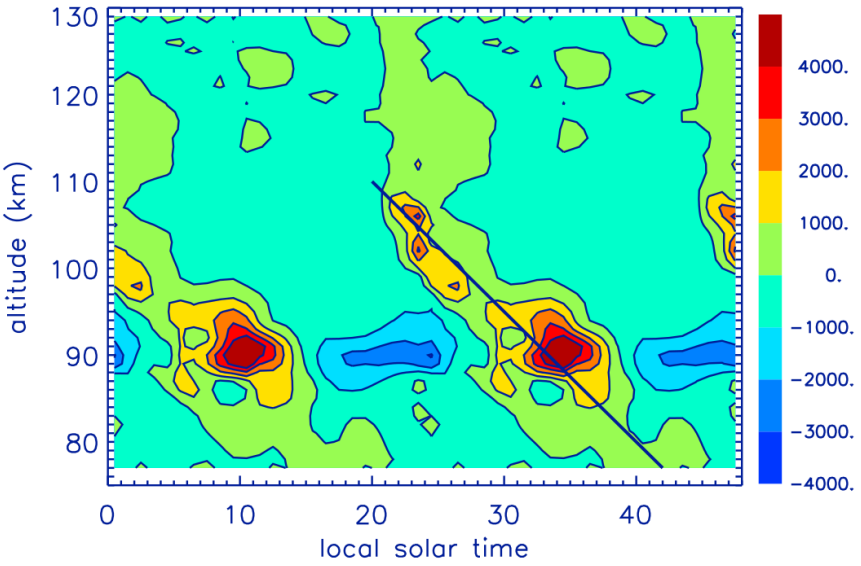

FIGURE 7.1: Relative Fe density perturbations in cm^{-3} to the seasonal mean versus local time and altitude. The black solid line indicate the phase of diurnal tides whose vertical wavelength is -36 km. The Fe densities were measured by a mobile Fe lidar installed by IAP at Davis (geographic 69^{o}S, 78^{o}E). From *Lübken et al.* [2011].

the neutralization of Fe^+ converged by electric field. Therefore, tidal-induced vertical wind is negligible, the shapes of Fe layer above 120 km rely on the shapes of Fe^+ layers.

This scenario is examined by the simulation shown in 7.2. In this simulation, we take the same set-up of initial profiles of Fe/Fe^+ in Figure 4.1. The electric field is set up by the solar wind velocity of 450 m/s, density of 3 cm^{-3}, B_y and B_z of 5 nT. The GLOW model is on, using the same parameters in Chapter 4. Tidal winds are set up by the Global Scale Wave Model (GSWM09). The preliminary results are shown in Figure 7.2. In the left panel, below 110 km, the converged Fe^+ layers mainly follow the tidal phase and above 120 km, the converged Fe^+ layers are generated by electric field. The corresponding Fe layers are shown in the right planel. The straight line of converged Fe^+ layers produces straight Fe layers above 120 km. More thorough investigation should be carried out in the future.

Furthermore, the phase relationship between the wave-driven wind shear and the convective

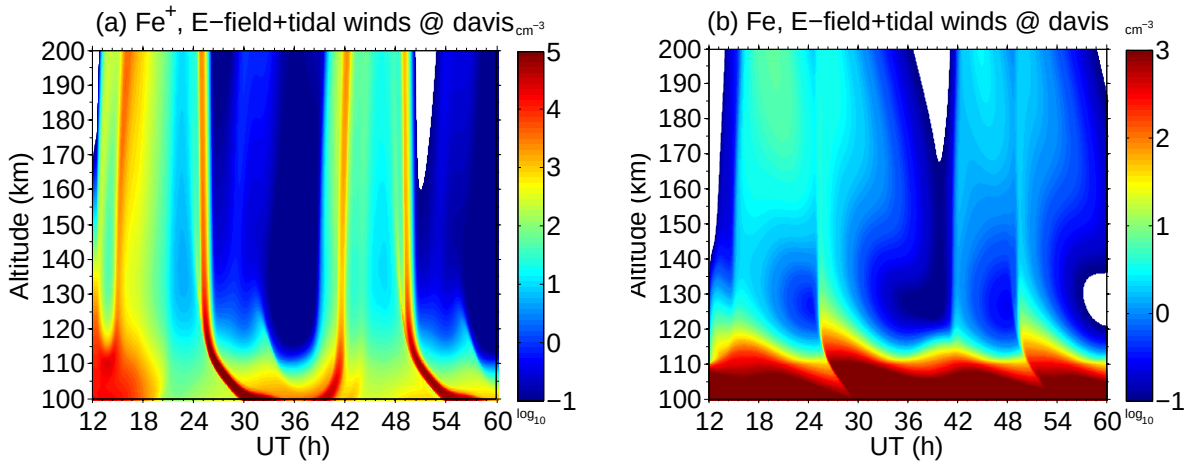

FIGURE 7.2: Experiments of Fe/Fe^+ transport by the combination of electric field and tidal winds at Davis.

electric field is very likely to be crucial to formation or disappearance of Fe/Fe^+ layers in the thermosphere. While the electric field helps transport Fe^+ ions to higher altitudes, the electric field can help converge the Fe^+ layers but also destroy wind-shear-converged Fe^+, depending on the relative phase. Therefore, the combined effects of wind shear with electric field must be studied via more realistic simulations in the future.

7.4 Implications and Suggestions for the Future

There are several implications from our simulation results:

1. No particularly special conditions are needed to form thermospheric Fe layers as long as sufficient Fe^+ can be transported into the thermosphere. Such layers can be a frequently occurring phenomenon globally, and it is a matter of lidar detection sensitivity issue.

2. Such phenomenon is not special to McMurdo but thermospheric Fe layers can exist over large scale in the polar regions. Outside the polar regions, higher chances of observing thermospheric metal layers are at fountain effect regions. Global distributions of thermospheric

metal layers highly relies on the upward transports of metallic ions.

3. Although Fe densities can be formed as long as Fe^+ densities are large enough, to form the Fe layers with very high contrast requires adequate loss mechanisms to remove Fe in order to form the minima between layer crests.

The extreme auroral electron conditions needed to model the extra high contrast of observed Fe layers suggest that some loss mechanisms of neutral Fe are not well-parametrized or missed in this model. Firstly, the model only includes the horizontal transport associated with horizontal divergence of horizontal winds, but neglects that associated with the horizontal gradients of Fe nubmer density. The significance of the impact of the horizontal gradients of Fe number density on the layer contrast is a remaining issue. Secondly, the parametrization of horizontal divergence of horizontal winds is based on a set of relatively idealized wave equations. How accuately the derived $\nabla \cdot \vec{V}_h$ represents the reality remains an issue. Thirdly, since the 1-D model cannot track the mass transport in horizontal direction, the mass of simulated Fe-containing species does not conserve anymore after implementing the horizontal divergence. Whether this introduces problems in calculating the densities of Fe-containing speceies is unclear. Fourthly, how significantly the horizontal divergence of electric field contributs to the convergence of Fe^+ is unclear. Fifthly, horizontal transport is very important. In reality, the horizontal ion drift velocities at polar region are much larger than the vertical drifts. The chemical module solves Fe chemistry grid by grid. If the 1-D mass transport module is extended to multiple dimensional transport module, this model would be potentially capable of being extended to 2-D or 3-D model. However, will 2-D or 3-D model solve or clarify these remaining issues? Finally, this 1-D thermospheric Fe/Fe^+ model includes all known physical and chemical processes, however, does the difficulty of reproducing oberseved high contrast of thermospheric Fe layers suggest any mising physics or chemistry?

Bibliography

[1] Aikin, A. C., and R. A. Goldberg, Metallic ions in the equatorial ionosphere, *Journal of Geophysical Research*, *78*(4), 734–745, doi:10.1029/JA078i004p00734, 1973.

[2] Aikin, A. C., and H. J. P. Smith, Mesospheric constituent variations during electron precipitation events, *Journal of Geophysical Research: Atmospheres*, *104*(D21), 26,457–26,471, doi:10.1029/1999JD900752, 1999.

[3] Allen, M., J. I. Lunine, and Y. L. Yung, The vertical distribution of ozone in the mesosphere and lower thermosphere, *Journal of Geophysical Research: Atmospheres*, *89*(D3), 4841–4872, doi:10.1029/JD089iD03p04841, 1984.

[4] Alpers, M., J. Höffner, and U. von Zahn, Iron atom densities in the polar mesosphere from lidar observations, *Geophysical Research Letters*, *17*(13), 2345–2348, doi:10.1029/GL017i013p02345, 1990.

[5] Alpers, M., T. Blix, S. Kirkwood, D. Krankowsky, F.-J. Lübken, S. Lutz, and U. von Zahn, First simultaneous measurements of neutral and ionized iron densities in the upper mesosphere, *Journal of Geophysical Research: Space Physics*, *98*(A1), 275–283, doi:10.1029/92JA01665, 1993.

[6] Alpers, M., J. Höffner, and U. von Zahn, Sporadic Fe and E layers at polar, middle, and low latitudes, *Journal of Geophysical Research: Space Physics*, *99*(A8), 14,971–14,985, doi: 10.1029/94JA00589, 1994.

[7] Anderson, J. G., and C. A. Barth, Rocket investigation of the Mg I and Mg II dayglow, *Journal of Geophysical Research*, *76*(16), 3723–3732, doi:10.1029/JA076i016p03723, 1971.

[8] Axford, W. I., The formation and vertical movement of dense ionized layers in the ionosphere due to neutral wind shears, *Journal of Geophysical Research*, *68*(3), 769–779, doi:10.1029/ JZ068i003p00769, 1963.

[9] Axford, W. I., and C. O. Hines, A uinfying theory of high-latitude geophysical phenomena and geomagnetic storms, *Can. J. Phys.*, *39*, 1433, 1961.

[10] Bailey, S. M., C. A. Barth, and S. C. Solomon, A model of nitric oxide in the lower thermosphere, *Journal of Geophysical Research: Space Physics*, *107*(A8), SIA 22–1–SIA 22–12, doi:10.1029/2001JA000258, 2002.

[11] Banks, P. M., and A. F. Nagy, Concerning the influence of elastic scattering upon photoelectron transport and escape, *Journal of Geophysical Research*, *75*(10), 1902–1910, doi: 10.1029/JA075i010p01902, 1970.

[12] Banks, P. M., C. R. Chappell, and A. F. Nagy, A new model for the interaction of auroral electrons with the atmosphere: Spectral degradation, backscatter, optical emission, and ionization, *Journal of Geophysical Research*, *79*(10), 1459–1470, doi:10.1029/JA079i010p01459, 1974.

[13] Bass, H. E., C. H. Hetzer, and R. Raspet, On the speed of sound in the atmosphere as a function of altitude and frequency, *Journal of Geophysical Research: Atmospheres*, *112*(D15), doi:10.1029/2006JD007806, 2007.

[14] Bates, H. F., Atmospheric expansion from joule heating, *Planetary and Space Science*, *22*(6), 925 – 937, doi:10.1016/0032-0633(74)90162-7, 1974.

[15] Batsanov, S., Van der waals radii of elements, *Inorganic Materials*, *37*(9), 871–885, doi: 10.1023/A:1011625728803, 2001.

[16] Behnke, R. A., and J. F. Vickrey, Radar evidence of Fe^+ in a sporadic-E layer, *Radio Science*, *10*(3), 325–327, doi:10.1029/RS010i003p00325, 1975.

[17] Bilitza, D., International reference ionosphere: Recent developments, *Radio Science*, *21*(3), 343–346, doi:10.1029/RS021i003p00343, 1986.

[18] Bilitza, D., International reference ionosphere 2000, *Radio Science*, *36*(2), 261–275, doi:10. 1029/2000RS002432, 2001.

[19] Bilitza, D., and B. Reinisch, International reference ionosphere 2007: Improvements and new parameters, *Advances in Space Research*, *42*(4), 599 – 609, doi:10.1016/j.asr.2007.07.048, 2008.

[20] Bilitza, D., L.-A. McKinnell, B. Reinisch, and T. Fuller-Rowell, The international reference ionosphere today and in the future, *Journal of Geodesy*, *85*(12), 909–920, doi: 10.1007/s00190-010-0427-x, 2011.

[21] Bishop, R. L., and G. D. Earle, Metallic ion transport associated with midlatitude intermediate layer development, *Journal of Geophysical Research: Space Physics*, *108*(A1), SIA 3–1–SIA 3–8, doi:10.1029/2002JA009411, 2003.

[22] Bishop, R. L., G. D. Earle, F. A. Herrero, and T. T. Bateman, Observations of an intermediate layer during the coqui ii campaign, *Journal of Geophysical Research: Space Physics*, *105*(A11), 24,963–24,971, doi:10.1029/1999JA000453, 2000.

[23] Bowman, M., A. Gibson, and M. sandford, Atmospheric sodium measured by a tuned laser radar, *Nature*, *221*(5179), 456–&, doi:{10.1038/221456a0}, 1969.

[24] Brasseur, G. P., and S. Solomon, *Aeronomy of the Middle Atmosphere 3rd*, Springer, 2005.

[25] Bristow, W., and B. Watkins, Effect of the large-scale convection electric field structure on the formation of thin ionization layers at high latitudes, *Journal of Atmospheric and Terrestrial Physics*, *56*(3), 401 – 415, doi:10.1016/0021-9169(94)90221-6, 1994.

[26] Bristow, W. A., and B. J. Watkins, Numerical simulation of the formation of thin ionization layers at high latitudes, *Geophysical Research Letters*, *18*(3), 404–407, doi:10.1029/90GL02588, 1991.

[27] Broadfoot, A., Twilight Ca^+ emission from meteor trails up to 280 km, *Planetary and Space Science*, *15*(3), 503 – 514, doi:10.1016/0032-0633(67)90159-6, 1967.

[28] Brown, P., A. Hindmarsh, and L. Petzold, Using krylov methods in the solution of large-scale differential-algebraic systems, *SIAM Journal on Scientific Computing*, *15*(6), 1467–1488, doi:10.1137/0915088, 1994.

[29] Brown, T. L., The chemistry of metallic elements in the ionosphere and mesosphere, *Chemical Reviews*, *73*(6), 645–667, doi:10.1021/cr60286a003, 1973.

[30] Burns, A. G., T. L. Killeen, and R. G. Roble, A theoretical study of thermospheric composition perturbations during an impulsive geomagnetic storm, *Journal of Geophysical Research: Space Physics*, *96*(A8), 14,153–14,167, doi:10.1029/91JA00678, 1991.

[31] Carter, L., and J. Forbes, Global transport and localized layering of metallic ions in the upper atmosphere, *Annales Geophysicae*, *17*(2), 190–209, doi:10.1007/s00585-999-0190-6, 1999.

[32] Carter, L. N. J., A comprehensive model of global transport and localized layering of metallic ions in the upper atmosphere, Ph.D. thesis, Boston Unversity, 1995.

[33] Ceplecha, Z., J. Borovika, W. Elford, D. ReVelle, R. Hawkes, V. Poruban, and M. imek, Meteor phenomena and bodies, *Space Science Reviews*, *84*(3-4), 327–471, doi:10.1023/A:1005069928850, 1998.

[34] Chen, A., R. Johnsen, and M. A. Biondi, Measurements of the $O^+ + N_2$ and $O^+ + O_2$ reaction rates from 300 to 900 k, *The Journal of Chemical Physics*, *69*(6), 2688–2691, doi:10.1063/1.436917, 1978.

[35] Chen, C., X. Chu, A. J. McDonald, S. L. Vadas, Z. Yu, W. Fong, and X. Lu, Inertia-gravity waves in Antarctica: A case study using simultaneous lidar and radar measurements at Mcmurdo/Scott Base (77.8° S, 166.7° E), *Journal of Geophysical Research: Atmospheres*, *118*(7), 2794–2808, doi:10.1002/jgrd.50318, 2013.

[36] Chimonas, G., and W. I. Axford, Vertical movement of temperate-zone sporadic E layers, *Journal of Geophysical Research*, *73*(1), 111–117, doi:10.1029/JA073i001p00111, 1968.

[37] Chu, X., W. Pan, G. C. Papen, C. S. Gardner, and J. A. Gelbwachs, Fe boltzmann temperature lidar: Design, error analysis, and initial results at the north and south poles, *Appl. Opt.*, *41*(21), 4400–4410, doi:10.1364/AO.41.004400, 2002a.

[38] Chu, X., C. S. Gardner, and S. J. Franke, Nocturnal thermal structure of the mesosphere and lower thermosphere region at Maui, Hawaii (20.7°N), and Starfire Optical Range, New Mexico (35°N), *Journal of Geophysical Research: Atmospheres*, *110*(D9), doi:10.1029/2004JD004891, 2005.

[39] Chu, X., W. Huang, W. Fong, Z. Yu, Z. Wang, J. A. Smith, and C. S. Gardner, First lidar observations of polar mesospheric clouds and Fe temperatures at McMurdo (77.8°S, 166.7°E), Antarctica, *Geophysical Research Letters*, *38*(16), doi:10.1029/2011GL048373, 2011.

[40] Chu, X., Z. Yu, C. S. Gardner, C. Chen, and W. Fong, Lidar observations of neutral Fe layers and fast gravity waves in the thermosphere (110–155 km) at McMurdo (77.8°S, 166.7°E), Antarctica, *Geophysical Research Letters*, *38*(23), doi:10.1029/2011GL050016, 2011.

[41] Chu, X., et al., Gravity waves from 30 to 155 km observed by an Fe lidar at McMurdo, Antarctica, in *AGU Fall Meeting 2012*, AGU, 2012.

[42] Clemesha, B. R., V. W. J. H. Kirchhoff, D. M. Simonich, and H. Takahashi, Evidence of an extra-terrestrial source for the mesospheric sodium layer, *Geophysical Research Letters*, *5*(10), 873–876, doi:10.1029/GL005i010p00873, 1978.

[43] Clemesha, B. R., D. M. Simonich, P. P. Batista, and V. W. J. H. Kirchhoff, The diurnal variation of atmospheric sodium, *Journal of Geophysical Research: Space Physics*, *87*(A1), 181–186, doi:10.1029/JA087iA01p00181, 1982.

[44] Collins, R. L., T. J. Hallinan, R. W. Smith, and G. Hernandez, Lidar observations of a large high-altitude sporadic Na layer during active aurora, *Geophysical Research Letters*, *23*(24), 3655–3658, doi:10.1029/96GL03337, 1996.

[45] Collins, S. C., et al., A study of the role of ionmolecule chemistry in the formation of sporadic sodium layers, *Journal of Atmospheric and Solar-Terrestrial Physics*, *64*(7), 845 – 860, doi: http://dx.doi.org/10.1016/S1364-6826(02)00129-3, 2002.

[46] Cox, R. M., and J. M. C. Plane, An ion-molecule mechanism for the formation of neutral sporadic Na layers, *Journal of Geophysical Research: Atmospheres*, *103*(D6), 6349–6359, doi:10.1029/97JD03376, 1998.

[47] Diettrich, J. C., G. J. Nott, P. J. Espy, X. Chu, and D. Riggin, Statistics of sporadic iron layers and relation to atmospheric dynamics, *Journal of Atmospheric and Solar-Terrestrial Physics*, *68*(1), 102 – 113, doi:10.1016/j.jastp.2005.08.008, 2006.

[48] Djuth, F. T., L. D. Zhang, D. J. Livneh, I. Seker, S. M. Smith, M. P. Sulzer, J. D. Mathews, and R. L. Walterscheid, Arecibo's thermospheric gravity waves and the case for an ocean source, *Journal of Geophysical Research: Space Physics*, *115*(A8), doi:10.1029/2009JA014799, 2010.

[49] Dou, X.-K., X.-H. Xue, T.-D. Chen, W.-X. Wan, X.-W. Cheng, T. Li, C. Chen, S. Qiu, and Z.-Y. Chen, A statistical study of sporadic sodium layer observed by Sodium lidar at Hefei (31.8°N, 117.3°E), *Annales Geophysicae*, *27*(6), 2247–2257, doi:10.5194/angeo-27-2247-2009, 2009.

[50] Dufay, M., l'émission des raies h and k du calcium ionisé dans le spectre du ciel crépusculaire, *Ann. Geophys.*, *14*(9), 391, 1958.

[51] Dungey, J. W., Interplanetary magnetic field and the auroral zones, *Phys. Rev. Lett.*, *6*, 47–48, doi:10.1103/PhysRevLett.6.47, 1961.

[52] Earle, G. D., R. L. Bishop, S. C. Collins, S. A. Gonzlez, and M. P. Sulzer, Descending layer variability over arecibo, *Journal of Geophysical Research: Space Physics*, *105*(A11), 24,951–24,961, doi:10.1029/2000JA000029, 2000.

[53] Eckermann, S. D., and C. J. Marks, An idealized ray model of gravity wave-tidal interactions, *Journal of Geophysical Research: Atmospheres*, *101*(D16), 21,195–21,212, doi:10.1029/96JD01660, 1996.

[54] Eymard, r., T. Gallout, R. Herbin, M. Dutnic, and D. Hilhorst, Approximation by the finite volume method of an elliptic-parabolic equation arising in environmental studies, *Mathematical Models and Methods in Applied Sciences*, *11*(09), 1505–1528, doi:10.1142/S0218202501001446, 2001.

[55] Fang, X., C. E. Randall, D. Lummerzheim, S. C. Solomon, M. J. Mills, D. R. Marsh, C. H. Jackman, W. Wang, and G. Lu, Electron impact ionization: A new parameterization for 100 eV to 1 Mev electrons, *Journal of Geophysical Research: Space Physics*, *113*(A9), doi:10.1029/2008JA013384, 2008.

[56] Farley, D. T., E. Bonelli, B. G. Fejer, and M. F. Larsen, The prereversal enhancement of the zonal electric field in the equatorial ionosphere, *Journal of Geophysical Research: Space Physics*, *91*(A12), 13,723–13,728, doi:10.1029/JA091iA12p13723, 1986.

[57] Fazio, R., and A. Jannelli, Second Order Numerical Operator Splitting for 3D Advection–Diffusion–Reaction Models, in *Numerical Mathematics and Advanced Applications 2009*,

edited by G. Kreiss, P. Ltstedt, A. Mlqvist, and M. Neytcheva, pp. 317–324, Springer Berlin Heidelberg, doi:10.1007/978-3-642-11795-4_33, 2010.

[58] Feng, W., D. R. Marsh, M. P. Chipperfield, D. Janches, J. Hffner, F. Yi, and J. M. C. Plane, A global atmospheric model of meteoric iron, *Journal of Geophysical Research: Atmospheres*, *118*(16), 9456–9474, doi:10.1002/jgrd.50708, 2013.

[59] Fesen, C. G., and P. B. Hays, Mg^+ morphology from visual airglow experiment observations, *Journal of Geophysical Research: Space Physics*, *87*(A11), 9217–9223, doi:10.1029/JA087iA11p09217, 1982.

[60] Fesen, C. G., P. B. Hays, and D. N. Anderson, Theoretical modeling of low-latitude Mg^+, *Journal of Geophysical Research: Space Physics*, *88*(A4), 3211–3223, doi:10.1029/JA088iA04p03211, 1983.

[61] Fong, W., X. Lu, X. Chu, T. J. Fuller-Rowell, Z. Yu, B. R. Roberts, C. Chen, C. S. Gardner, and A. J. McDonald, Winter temperature tides from 30 to 110km at mcmurdo (77.8^{o}S, 166.7^{o}E), antarctica: Lidar observations and comparisons with wam, *Journal of Geophysical Research: Atmospheres*, *119*(6), 2846–2863, doi:10.1002/2013JD020784, 2014.

[62] Forbes, J. M., Atmospheric tides: 1. model description and results for the solar diurnal component, *Journal of Geophysical Research: Space Physics*, *87*(A7), 5222–5240, doi:10.1029/JA087iA07p05222, 1982.

[63] Forbes, J. M., Atmospheric tide: 2. the solar and lunar semidiurnal components, *Journal of Geophysical Research: Space Physics*, *87*(A7), 5241–5252, doi:10.1029/JA087iA07p05241, 1982.

[64] Frahm, R. A., J. D. Winningham, J. R. Sharber, R. Link, G. Crowley, E. E. Gaines, D. L. Chenette, B. J. Anderson, and T. A. Potemra, The diffuse aurora: A significant source of ionization in the middle atmosphere, *Journal of Geophysical Research: Atmospheres*, *102*(D23), 28,203–28,214, doi:10.1029/97JD02430, 1997.

[65] Fricke, K., and U. von Zahn, Mesopause temperatures derived from probing the hyperfine structure of the {D2} resonance line of sodium by lidar, *Journal of Atmospheric and Terrestrial Physics*, *47*(5), 499 – 512, doi:10.1016/0021-9169(85)90116-3, 1985.

[66] Fricke-Begemann, C., J. Höffner, and U. von Zahn, The potassium density and temperature structure in the mesopause region (80–105 km) at a low latitude (28°N), *Geophysical Research Letters*, *29*(22), 24–1–24–4, doi:10.1029/2002GL015578, 2002.

[67] Friedman, J. S., C. A. Tepley, S. Raizada, Q. H. Zhou, J. Hedin, and R. Delgado, Potassium doppler-resonance lidar for the study of the mesosphere and lower thermosphere at the arecibo observatory, *Journal of Atmospheric and Solar-Terrestrial Physics*, *65*(1618), 1411 – 1424, doi:10.1016/j.jastp.2003.09.004, 2003.

[68] Friedman, J. S., X. Chu, C. G. M. Brum, and X. Lu, Observation of a thermospheric descending layer of neutral K over arecibo, *Journal of Atmospheric and Solar-Terrestrial Physics*, (0), doi:10.1016/j.jastp.2013.03.002, 2013.

[69] Gardner, C. S., Introduction to ALOHA/ANLC-93: The 1993 airborne lidar and observations of the Hawaiian Airglow/Airborne Noctilucent Cloud Campaigns, *Geophysical Research Letters*, *22*(20), 2789–2792, doi:10.1029/95GL02782, 1995.

[70] Gardner, C. S., and A. Z. Liu, Seasonal variations of the vertical fluxes of heat and horizontal momentum in the mesopause region at starfire optical range, new mexico, *Journal of Geophysical Research: Atmospheres*, *112*(D9), doi:10.1029/2005JD006179, 2007.

[71] Gardner, C. S., and A. Z. Liu, Wave-induced transport of atmospheric constituents and its effect on the mesospheric Na layer, *Journal of Geophysical Research: Atmospheres*, *115*(D20), doi:10.1029/2010JD014140, 2010.

[72] Gardner, C. S., T. J. Kane, J. H. Hecht, R. L. Walterscheid, J. H. Yee, R. J. Niciejewski, R. P. Lowe, and D. N. Turnbull, Formation characteristics of sporadic Na layers observed simultaneously by lidar and airglow instruments during ALOHA-90, *Geophysical Research Letters*, *18*(7), 1369–1372, doi:10.1029/91GL01515, 1991.

[73] Gardner, C. S., X. Tao, and G. C. Papen, Observations of strong wind shears and temperature enhancements during several sporadic Na layer events above Haleakala, *Geophysical Research Letters*, *22*(20), 2809–2812, doi:10.1029/95GL02555, 1995.

[74] Gardner, C. S., G. C. Papen, X. Chu, and W. Pan, First lidar observations of middle atmosphere temperatures, Fe densities, and polar mesospheric clouds over the north and south poles, *Geophysical Research Letters*, *28*(7), 1199–1202, doi:10.1029/2000GL012622, 2001.

[75] Gardner, C. S., Y. Zhao, and A. Z. Liu, Atmospheric stability and gravity wave dissipation in the mesopause region, *Journal of Atmospheric and Solar-Terrestrial Physics*, *64*(811), 923 – 929, doi:10.1016/S1364-6826(02)00047-0, 2002.

[76] Gardner, C. S., J. M. C. Plane, W. Pan, T. Vondrak, B. J. Murray, and X. Chu, Seasonal variations of the Na and Fe layers at the South Pole and their implications for the chemistry and

general circulation of the polar mesosphere, *Journal of Geophysical Research: Atmospheres*, *110*(D10), doi:10.1029/2004JD005670, 2005.

[77] Gardner, C. S., X. Chu, P. J. Espy, J. M. C. Plane, D. R. Marsh, and D. Janches, Seasonal variations of the mesospheric Fe layer at Rothera, Antarctica (67.5°S, 68.0°W), *Journal of Geophysical Research: Atmospheres*, *116*(D2), doi:10.1029/2010JD014655, 2011.

[78] Gardner, J. A., R. A. Viereck, E. Murad, D. J. Knecht, C. P. Pike, A. L. Broadfoot, and E. R. Anderson, Simultaneous observations of neutral and ionic magnesium in the thermosphere, *Geophysical Research Letters*, *22*(16), 2119–2122, doi:10.1029/95GL01769, 1995.

[79] Gérard, J.-C., Satellite measurements of high-altitude twilight Mg^+ emission, *Journal of Geophysical Research*, *81*(1), 83–87, doi:10.1029/JA081i001p00083, 1976.

[80] Gérard, J.-C., and A. Monfils, Satellite observations of the equatorial Mg II dayglow intensity distribution, *Journal of Geophysical Research*, *79*(16), 2544–2550, doi:10.1029/JA079i016p02544, 1974.

[81] Gerding, M., M. Alpers, U. von Zahn, R. J. Rollason, and J. M. C. Plane, Atmospheric Ca and Ca^+ layers: Midlatitude observations and modeling, *Journal of Geophysical Research: Space Physics*, *105*(A12), 27,131–27,146, doi:10.1029/2000JA900088, 2000.

[82] Gerding, M., M. Alpers, J. Höffner, and U. von Zahn, Sporadic Ca and Ca^+ layers at mid-latitudes: Simultaneous observations and implications for their formation, *Annales Geophysicae*, *19*(1), 47–58, doi:10.5194/angeo-19-47-2001, 2001.

[83] Gong, S. S., G. T. Yang, J. M. Wang, X. W. Cheng, F. Q. Li, and W. X. Wan, A double sodium layer event observed over Wuhan, China by lidar, *Geophysical Research Letters*, *30*(5), doi:10.1029/2002GL016135, 2003.

[84] Gossard, E. E., and W. H. Hooke, *Waves in the atmosphere: atmospheric infrasound and gravity waves : their generation and propagation*, Elsevier Scientific Pub. CO., 1975.

[85] Granier, C., J. P. Jegou, and G. Megie, Iron atoms and metallic species in the earth's upper atmosphere, *Geophysical Research Letters*, *16*(3), 243–246, doi:10.1029/GL016i003p00243, 1989.

[86] Granier, G., J. P. Jégou, and G. Mégie, Resonant lidar detection of Ca and Ca^+ in the upper atmosphere, *Geophysical Research Letters*, *12*(10), 655–658, doi:10.1029/GL012i010p00655, 1985.

[87] Grebowsky, J., and M. P. III, The source of midlatitude metallic ions at F-region altitudes, *Planetary and Space Science*, *33*(7), 807 – 815, doi:10.1016/0032-0633(85)90034-0, 1985.

[88] Grebowsky, J. M., and A. C. Aikin, In situ measurements of meteoric ions, in *Meteors in the Earth's Atmosphere*, edited by E. Murad and I. P. Williams, pp. 189–214, Cambridge Univ. Press, New York, 2002.

[89] Grebowsky, J. M., and H. C. Brinton, Fe^+ ions in the high latitude F-region, *Geophysical Research Letters*, *5*(9), 791–794, doi:10.1029/GL005i009p00791, 1978.

[90] Grebowsky, J. M., and N. Reese, Another look at equatorial metallic ions in the F region, *Journal of Geophysical Research: Space Physics*, *94*(A5), 5427–5440, doi:10.1029/JA094iA05p05427, 1989.

[91] Green, A., and T. Sawada, Ionization cross sections and secondary electron distributions, *Journal of Atmospheric and Terrestrial Physics*, *34*(10), 1719 – 1728, doi:http://dx.doi.org/10.1016/0021-9169(72)90031-1, 1972.

[92] Haldoupis, C., A Tutorial Review on Sporadic E Layers, in *Aeronomy of the Earth's Atmosphere and Ionosphere*, *IAGA Special Sopron Book Series*, vol. 2, edited by M. A. Abdu and D. Pancheva, pp. 381–394, Springer Netherlands, doi:10.1007/978-94-007-0326-1_29, 2011.

[93] Hanson, W. B., and R. J. Moffett, Ionization transport effects in the equatorial F region, *Journal of Geophysical Research*, *71*(23), 5559–5572, doi:10.1029/JZ071i023p05559, 1966.

[94] Hanson, W. B., and S. Sanatani, Meteoric ions above the F2 peak, *Journal of Geophysical Research*, *75*(28), 5503–5509, doi:10.1029/JA075i028p05503, 1970.

[95] Hanson, W. B., D. L. Sterling, and R. F. Woodman, Source and identification of heavy ions in the equatorial F layer, *Journal of Geophysical Research*, *77*(28), 5530–5541, doi:10.1029/JA077i028p05530, 1972.

[96] Hedin, A. E., Extension of the msis thermosphere model into the middle and lower atmosphere, *Journal of Geophysical Research: Space Physics*, *96*(A2), 1159–1172, doi:10.1029/90JA02125, 1991.

[97] Heelis, R., Ionization layers observed at middle latitudes by Atmosphere Explorer-C, *Journal of Atmospheric and Solar-Terrestrial Physics*, *61*(5), 407 – 414, doi:10.1016/S1364-6826(98)00153-9, 1999.

[98] Helmer, M., J. M. C. Plane, J. Qian, and C. S. Gardner, A model of meteoric iron in the upper atmosphere, *Journal of Geophysical Research: Atmospheres*, *103*(D9), 10,913–10,925, doi:10.1029/97JD03075, 1998.

[99] Hines, C., The upper atmosphere in motion, *Quarterly journal of the royal meteorological society*, *89*(379), 1–42, doi:{10.1002/qj.49708937902}, 1963.

[100] Hines, C. O., Internal atmospheric gravity waves at ionospheric heights, in *The Upper Atmosphere in Motion*, edited by C. O. Hines, pp. 248–328, AGU, 1974.

[101] Hoffman, R. A., and E. R. Schmerling, Dynamics Explorer program: an overview., *Space Science Instrumentation*, *5*, 345–348, 1981.

[102] Höffner, J., and J. Friedman, The mesospheric metal layer topside: Examples of simultaneous metal observations, *Journal of Atmospheric and Solar-Terrestrial Physics*, *67*(13), 1226 – 1237, doi:10.1016/j.jastp.2005.06.010, 2005.

[103] Höffner, J., and J. S. Friedman, The mesospheric metal layer topside: a possible connection to meteoroids, *Atmospheric Chemistry and Physics*, *4*(3), 801–808, doi:10.5194/acp-4-801-2004, 2004.

[104] Istomin, V., Absolute concentrations of ion components of the earth's atmosphere at altitudes between 100 and 200 km, *Planetary and Space Science*, *11*(2), 169 – 172, doi:10.1016/0032-0633(63)90139-9, 1963.

[105] Janches, D., L. P. Dyrud, S. L. Broadley, and J. M. C. Plane, First observation of micrometeoroid differential ablation in the atmosphere, *Geophysical Research Letters*, *36*(6), doi:10.1029/2009GL037389, 2009.

[106] Jensen, D. E., and G. A. Jones, Catalysis of radical recombination in flames by iron, *The Journal of Chemical Physics*, *60*(9), 3421–3425, doi:10.1063/1.1681554, 1974.

[107] Jones, A. V., Ca II emission lines in the twilight spectrum, *Nature*, *178*(4527), 276–277, doi:10.1038/178276a0, 1956.

[108] Kane, T., and C. Gardner, Lidar observations of the meteoric deposition of mesospheric metals., *Science*, *259*(5099), 1297–300, 1993.

[109] Kane, T. J., and C. S. Gardner, Structure and seasonal variability of the nighttime mesospheric Fe layer at midlatitudes, *Journal of Geophysical Research: Atmospheres*, *98*(D9), 16,875–16,886, doi:10.1029/93JD01225, 1993.

[110] Kelly, M., *The Earth's Ionosphere 2nd*, Academic Press, 2009.

[111] Kirchhoff, V. W. J. H., and B. R. Clemesha, The atmospheric neutral sodium layer: 2. diurnal variations, *Journal of Geophysical Research: Space Physics*, *88*(A1), 442–450, doi:10.1029/JA088iA01p00442, 1983.

[112] Kirchhof.VW, and B. Clemesha, Atmospheric sodium measurements at 23°, *Journal of atmospheric and terrestrial physics*, *35*(8), 1493–1498, doi:{10.1016/0021-9169(73)90150-5}, 1973.

[113] Kirkwood, S., and H. Nilsson, High-latitude sporadic-e and other thin layers the role of magnetospheric electric fields, *Space Science Reviews*, *91*(3-4), 579–613, doi:10.1023/A:1005241931650, 2000.

[114] Kirkwood, S., and U. von Zahn, On the role of auroral electric fields in the formation of low altitude sporadic-E and sudden sodium layers, *Journal of Atmospheric and Terrestrial Physics*, *53*(5), 389 – 407, doi:10.1016/0021-9169(91)90034-5, 1991.

[115] Kopp, E., On the abundance of metal ions in the lower ionosphere, *Journal of Geophysical Research: Space Physics*, *102*(A5), 9667–9674, doi:10.1029/97JA00384, 1997.

[116] Kumar, S., and W. B. Hanson, The morphology of metallic ions in the upper atmosphere, *Journal of Geophysical Research: Space Physics*, *85*(A12), 6783–6801, doi:10.1029/JA085iA12p06783, 1980.

[117] Langford, A. O., V. M. Bierbaum, and S. R. Leone, Auroral implications of recent measurements on O(1S) and O(1S) formation in the reaction of N^+ with $\{O_2\}$, *Planetary and Space Science*, *33*(10), 1225 – 1228, doi:10.1016/0032-0633(85)90078-9, 1985.

[118] Langowski, M., C. von Savigny, J. P. Burrows, W. Feng, J. M. C. Plane, D. R. Marsh, D. Janches, M. Sinnhuber, and A. C. Aikin, Global investigation of the mg atom and ion layers using sciamachy/envisat observations between 70 km and 150 km altitude and waccm-mg model results, *Atmospheric Chemistry and Physics Discussions*, *14*(2), 1971–2019, doi:10.5194/acpd-14-1971-2014, 2014.

[119] Larsen, M. F., and J. W. Meriwether, Vertical winds in the thermosphere, *Journal of Geophysical Research: Space Physics*, *117*(A9), doi:10.1029/2012JA017843, 2012.

[120] Lindinger, W., and E. Ferguson, Laboratory investigation of the ionospheric O_2^+(X2πg, v$\neq$0) reaction with {NO}, *Planetary and Space Science*, *31*(10), 1181 – 1182, doi:10.1016/0032-0633(83)90108-3, 1983.

[121] Lu, X., X. Chu, T. Fuller-Rowell, L. Chang, W. Fong, and Z. Yu, Eastward propagating planetary waves with periods of 15days in the winter antarctic stratosphere as revealed by merra and lidar, *Journal of Geophysical Research: Atmospheres*, *118*(17), 9565–9578, doi:10.1002/jgrd.50717, 2013.

[122] Lübken, F.-J., and U. von Zahn, Thermal structure of the mesopause region at polar latitudes, *Journal of Geophysical Research: Atmospheres*, *96*(D11), 20,841–20,857, doi: 10.1029/91JD02018, 1991.

[123] Lübken, F.-J., J. Höffner, T. P. Viehl, B. Kaifler, and R. J. Morris, First measurements of thermal tides in the summer mesopause region at antarctic latitudes, *Geophysical Research Letters*, *38*(24), doi:10.1029/2011GL050045, 2011.

[124] Lui, A. T. Y., P. D. Perreault, A. S. I., and C. D. Anger, The diffuse aurora, *Planet. Space Sci.*, *21*, 867, 1973.

[125] Ma, Z., and F. Yi, High-altitude sporadic metal atom layers observed with na and fe lidars at 30n, *Journal of Atmospheric and Solar-Terrestrial Physics*, *72*(56), 482 – 491, doi:10.1016/j. jastp.2010.01.005, 2010.

[126] MacDougall, J., Seasonal variation of semidiurnal winds in the dynamo region, *Planetary and Space Science*, *26*(8), 705 – 714, doi:10.1016/0032-0633(78)90001-6, 1978.

[127] MacDougall, J., P. Jayachandran, and J. Plane, Polar cap sporadic-E: Part 1, observations, *Journal of Atmospheric and Solar-Terrestrial Physics*, *62*(13), 1155 – 1167, doi:http://dx. doi.org/10.1016/S1364-6826(00)00093-6, 2000.

[128] MacDougall, J., J. Plane, and P. Jayachandran, Polar cap sporadic-E: part 2, modeling, *Journal of Atmospheric and Solar-Terrestrial Physics*, *62*(13), 1169 – 1176, doi:10.1016/ S1364-6826(00)00092-4, 2000.

[129] MacLeod, M. A., T. J. Keneshea, and R. S. Narcisi, Numerical modelling of a metallic ion sporadic-e layer, *Radio Science*, *10*(3), 371–388, doi:10.1029/RS010i003p00371, 1975.

[130] Maeda, S., S. Nozawa, Y. Ogawa, and H. Fujiwara, Comparative study of the high-latitude e region ion and neutral temperatures in the polar cap and the auroral region derived from the eiscat radar observations, *Journal of Geophysical Research: Space Physics*, *110*(A8), doi: 10.1029/2004JA010893, 2005.

[131] Marsh, D. R., D. Janches, W. Feng, and J. M. C. Plane, A global model of meteoric sodium, *Journal of Geophysical Research: Atmospheres*, *118*(19), 11,442–11,452, doi:10.1002/jgrd. 50870, 2013.

[132] Mathews, J., and F. Bekeny, Upper atmosphere tides and the vertical motion of ionospheric sporadic layers at arecibo, *Journal of Geophysical Research: Space Physics*, *84*(A6), 2743–2750, doi:10.1029/JA084iA06p02743, 1979.

[133] Mathews, J., Y. Morton, and Q. Zhou, Observations of ion layer motions during the {AIDA} campaign, *Journal of Atmospheric and Terrestrial Physics*, *55*(3), 447 – 457, doi:10.1016/ 0021-9169(93)90080-I, 1993.

[134] McDaniel, E. W., *Collision Phenomena in Ionized Gases*, John Wiley and Sons, New Yor, 1964.

[135] McFarland, M., D. L. Albritton, F. C. Fehsenfeld, E. E. Ferguson, and A. L. Schmeltekopf, Flow-drift technique for ion mobility and ion-molecule reaction rate constant measurements. II. Positive ion reactions of N^+, O^+, and H_2^+ with O_2 and O^+ with N_2 from thermal to [inverted lazy s]2 eV, *The Journal of Chemical Physics*, *59*(12), 6620–6628, doi:10.1063/1. 1680042, 1973.

[136] McFarland, M., D. L. Albritton, F. C. Fehsenfeld, E. E. Ferguson, and A. L. Schmeltekopf, Energy dependence and branching ratio of the N_2^+ + O reaction, *Journal of Geophysical Research*, *79*(19), 2925–2926, doi:10.1029/JA079i019p02925, 1974.

[137] McNeil, W. J., S. T. Lai, and E. Murad, A model for meteoric magnesium in the ionosphere, *Journal of Geophysical Research: Space Physics (19782012)*, *101*(A3), 5251–5259, doi:10.1029/95JA02888, 1996.

[138] McNicol, R. W. E., and G. d. V. Gipps, Characteristics of the es region at brisbane, *Journal of Geophysical Research*, *56*(1), 17–31, doi:10.1029/JZ056i001p00017, 1951.

[139] Meier, R. R., D. J. Strickland, J. H. Hecht, and A. B. Christensen, Deducing composition and incident electron spectra from ground-based auroral optical measurements: A study of auroral red line processes, *Journal of Geophysical Research: Space Physics*, *94*(A10), 13,541–13,552, doi:10.1029/JA094iA10p13541, 1989.

[140] Mende, S. B., G. R. Swenson, and K. L. Miller, Observations of e and f region Mg^+ from spacelab 1, *Journal of Geophysical Research: Space Physics*, *90*(A7), 6667–6673, doi:10.1029/JA090iA07p06667, 1985.

[141] Miller, N. J., J. M. Grebowsky, A. E. Hedin, and N. W. Spencer, Equatorial ion composition, 140-200 km, based on atmosphere explorer e data, *Journal of Geophysical Research: Space Physics*, *98*(A9), 15,685–15,692, doi:10.1029/93JA01147, 1993.

[142] Moore, T. E., and J. L. Horwitz, Stellar ablation of planetary atmospheres, *Reviews of Geophysics*, *45*(3), doi:10.1029/2005RG000194, 2007.

[143] Morton, Y. T., J. Mathews, and Q. Zhou, Further evidence for a 6-h tide above arecibo, *Journal of Atmospheric and Terrestrial Physics*, *55*(3), 459 – 465, doi:10.1016/0021-9169(93)90081-9, 1993.

[144] Mul, P. M., and J. W. McGowan, Merged electron-ion beam experiments. III. Temperature dependence of dissociative recombination for atmospheric ions NO^+ , O_2^+ and N_2^+, *Journal of Physics B: Atomic and Molecular Physics*, *12*(9), 1591, 1979.

[145] Nagy, A. F., and P. M. Banks, Photoelectron fluxes in the ionosphere, *Journal of Geophysical Research*, *75*(31), 6260–6270, doi:10.1029/JA075i031p06260, 1970.

[146] Nahar, S. N., M. A. Bautista, and A. K. Pradhan, Electron-ion recombination of neutral iron, *The Astrophysical Journal*, *479*(1), 497, 1997.

[147] Narcisi, R. S., Composition studies of the lower ionosphere, lecture presented at the international school of atmospheric physics, *Erice*(Italy), 1971.

[148] Narcisi, R. S., and A. D. Bailey, Mass spectrometric measurements of positive ions at altitudes from 64 to 112 kilometers, *Journal of Geophysical Research*, *70*(15), 3687–3700, doi:10.1029/JZ070i015p03687, 1965.

[149] Nygrén, T., L. Jalonen, J. Oksman, and T. Turunen, The role of electric field and neutral wind direction in the formation of sporadic e-layers, *Journal of Atmospheric and Terrestrial Physics*, *46*(4), 373 – 381, doi:10.1016/0021-9169(84)90122-3, 1984.

[150] Nygrén, T., A. T. Aikio, M. Voiculescu, and J. M. Ruohoniemi, IMF effect on sporadic-E layers at two northern polar cap sites: Part II. Electric field, *Annales Geophysicae*, *24*(3), 901–913, doi:10.5194/angeo-24-901-2006, 2006.

[151] Osterman, G. B., R. A. Heelis, and G. J. Bailey, Modeling the formation of intermediate layers at arecibo latitudes, *Journal of Geophysical Research: Space Physics*, *99*(A6), 11,357–11,365, doi:10.1029/94JA00519, 1994.

[152] Pan, W., and C. S. Gardner, Seasonal variations of the atmospheric temperature structure at south pole, *Journal of Geophysical Research: Atmospheres*, *108*(D18), doi:10.1029/2002JD003217, 2003.

[153] Parkinson, M., P. Dyson, D. Monselesan, and R. Morris, On the role of electric field direction in the formation of sporadic E-layers in the southern polar cap ionosphere, *Journal of Atmospheric and Solar-Terrestrial Physics*, *60*(4), 471 – 491, doi:10.1016/S1364-6826(97)00095-3, 1998.

[154] Picone, J. M., A. E. Hedin, D. P. Drob, and A. C. Aikin, NRLMSISE-00 empirical model of the atmosphere: Statistical comparisons and scientific issues, *Journal of Geophysical Research: Space Physics*, *107*(A12), SIA 15–1–SIA 15–16, doi:10.1029/2002JA009430, 2002.

[155] Plane, J., R. Cox, and R. Rollason, Metallic layers in the mesopause and lower thermosphere region, *Advances in Space Research*, *24*(11), 1559 – 1570, doi:10.1016/S0273-1177(99)00880-7, 1999.

[156] Plane, J., D. Self, T. Vondrak, and K. Woodcock, Laboratory studies and modelling of mesospheric iron chemistry, *Advances in Space Research*, *32*(5), 699 – 708, doi:10.1016/S0273-1177(03)00401-0, 2003.

[157] Plane, J. M. C., Atmospheric chemistry of meteoric metals, *Chemical Reviews*, *103*(12), 4963–4984, doi:10.1021/cr0205309, 2003.

[158] Plane, J. M. C., A time-resolved model of the mesospheric Na layer: constraints on the meteor input function, *Atmospheric Chemistry and Physics*, *4*(3), 627–638, doi:10.5194/acp-4-627-2004, 2004.

[159] Plane, J. M. C., B. J. Murray, X. Chu, and C. S. Gardner, Removal of meteoric iron on polar mesospheric clouds, *Science*, *304*(5669), 426–428, doi:10.1126/science.1093236, 2004.

[160] Raizada, S., and C. A. Tepley, Seasonal variation of mesospheric iron layers at arecibo: First results from low-latitudes, *Geophysical Research Letters*, *30*(2), doi:10.1029/2002GL016537, 2003.

[161] Rawer, K., D. Bilitza, and S. Ramakrishnan, Goals and status of the international reference ionosphere, *Reviews of Geophysics*, *16*(2), 177–181, doi:10.1029/RG016i002p00177, 1978.

[162] Richmond, A., Thermospheric dynamics and electrodynamics, in *Solar-Terrestrial Physics*, *Astrophysics and Space Science Library*, vol. 104, edited by R. Carovillano and J. Forbes, pp. 523–607, Springer Netherlands, doi:10.1007/978-94-009-7194-3_21, 1983.

[163] Richmond, A. D., Gravity wave generation, propagation, and dissipation in the thermosphere, *Journal of Geophysical Research: Space Physics*, *83*(A9), 4131–4145, doi:10.1029/JA083iA09p04131, 1978.

[164] Richmond, A. D., The ionospheric wind dynamo: Effects of its coupling with different atmospheric regions, in *The Upper Mesosphere and Lower Thermosphere: A Review of Experiment and Theory*, edited by R. M. Johnson and T. L. Killeen, pp. 49–65, Am. Geophys. Union, doi:10.1029/GM087p0049, 1995.

[165] Richmond, A. D., et al., An empirical model of quiet-day ionospheric electric fields at middle and low latitudes, *Journal of Geophysical Research: Space Physics*, *85*(A9), 4658–4664, doi: 10.1029/JA085iA09p04658, 1980.

[166] Robinson, R. M., and R. R. Vondrak, Characteristics and sources of ionization in the continuous aurora, *Radio Science*, *20*(3), 447–455, doi:10.1029/RS020i003p00447, 1985.

[167] Roble, R. G., and E. C. Ridley, An auroral model for the NCAR thermospheric general circulation model (TGCM), *Annales Geophysicae*, *5*, 369–382, 1987.

[168] Roddy, P. A., Spatial and temporal structuring of nighttime intermediate layers above wallops island, Ph.D. thesis, The University of Texas at Dallas, 2005.

[169] Roddy, P. A., G. D. Earle, C. M. Swenson, C. G. Carlson, and T. W. Bullett, Relative concentrations of molecular and metallic ions in midlatitude intermediate and sporadic-e layers, *Geophysical Research Letters*, *31*(19), doi:10.1029/2004GL020604, 2004.

[170] Rodrigo, R., M. Lpez-Gonzlez, and J. Lpez-Moreno, Variability of the neutral mesospheric and lower thermospheric composition in the diurnal cycle, *Planetary and Space Science*, *39*(6), 803 – 820, doi:10.1016/0032-0633(91)90086-P, 1991.

[171] Rollason, R. J., and J. M. C. Plane, A study of the reactions of Fe^+ with O_3, O_2 and N_2, *J. Chem. Soc., Faraday Trans.*, *94*, 3067–3075, doi:10.1039/A805140B, 1998.

[172] Rollason, R. J., and J. M. C. Plane, The reactions of FeO with O_3, H_2 , H_2O, O_2 and CO_2, *Phys. Chem. Chem. Phys.*, *2*, 2335–2343, doi:10.1039/B000877J, 2000.

[173] Rutherford, J. A., and D. A. Vroom, Formation of iron ions by charge transfer, *The Journal of Chemical Physics*, *57*(8), 3091–3093, doi:10.1063/1.1678724, 1972.

[174] Sandford, P., Variations of auroral emissions with time, magnetic activity and the solar cycle, *Journal of Atmospheric and Terrestrial Physics*, *30*(12), 1921 – 1942, doi:http://dx.doi.org/10.1016/0021-9169(68)90001-9, 1968.

[175] Saunders, R. W., and J. M. Plane, A laboratory study of meteor smoke analogues: Composition, optical properties and growth kinetics, *Journal of Atmospheric and Solar-Terrestrial Physics*, *68*(18), 2182 – 2202, doi:10.1016/j.jastp.2006.09.006, 2006.

[176] Self, D. E., and J. M. C. Plane, A kinetic study of the reactions of iron oxides and hydroxides relevant to the chemistry of iron in the upper mesosphere, *Phys. Chem. Chem. Phys.*, *5*, 1407–1418, doi:10.1039/B211900E, 2003.

[177] Senft, D. C., G. C. Papen, C. S. Gardner, J. R. Yu, D. A. Krueger, and C. Y. She, Seasonal variations of the thermal structure of the mesopause region at Urbana, IL (40°N, 88°W) and Ft. Collins, CO (41°N, 105°W), *Geophysical Research Letters*, *21*(9), 821–824, doi:10.1029/94GL00891, 1994.

[178] Shah, M. B., P. McCallion, K. Okuno, and H. B. Gilbody, Multiple ionization of iron by electron impact, *Journal of Physics B: Atomic, Molecular and Optical Physics*, *26*(15), 2393, 1993.

[179] She, C., and D. A. Krueger, Impact of natural variability in the 11-year mesopause region temperature observation over Fort Collins, {CO} (41°N, 105°W), *Advances in Space Research*, *34*(2), 330 – 336, doi:10.1016/j.asr.2003.02.047, 2004.

[180] She, C. Y., J. R. Yu, and H. Chen, Observed thermal structure of a midlatitude mesopause, *Geophysical Research Letters*, *20*(7), 567–570, doi:10.1029/93GL00808, 1993.

[181] She, C. Y., S. Chen, Z. Hu, J. Sherman, J. D. Vance, V. Vasoli, M. A. White, J. Yu, and D. A. Krueger, Eight-year climatology of nocturnal temperature and sodium density in the mesopause region (80 to 105 km) over Fort Collins, Co (41°N, 105°W), *Geophysical Research Letters*, *27*(20), 3289–3292, doi:10.1029/2000GL003825, 2000.

[182] She, C. Y., S. Chen, B. P. Williams, Z. Hu, D. A. Krueger, and M. E. Hagan, Tides in the mesopause region over Fort Collins, Colorado (41°N, 105°W) based on lidar temperature observations covering full diurnal cycles, *Journal of Geophysical Research: Atmospheres*, *107*(D18), ACL 4–1–ACL 4–12, doi:10.1029/2001JD001189, 2002.

[183] She, C. Y., et al., The first 80-hour continuous lidar campaign for simultaneous observation of mesopause region temperature and wind, *Geophysical Research Letters*, *30*(6), doi:10.1029/2002GL016412, 2003.

[184] Sinnhuber, M., H. Nieder, and N. Wieters, Energetic particle precipitation and the chemistry of the mesosphere/lower thermosphere, *Surveys in Geophysics*, *33*(6), 1281–1334, doi:10.1007/s10712-012-9201-3, 2012.

[185] Smith, L., A sequence of rocket observations of night-time sporadic-e, *Journal of Atmospheric and Terrestrial Physics*, *32*(7), 1247 – 1257, doi:10.1016/0021-9169(70)90055-3, 1970.

[186] Solomon, S. C., and V. J. Abreu, The 630 nm dayglow, *Journal of Geophysical Research: Space Physics*, *94*(A6), 6817–6824, doi:10.1029/JA094iA06p06817, 1989.

[187] Solomon, S. C., P. B. Hays, and V. J. Abreu, The auroral 6300 emission: Observations and modeling, *Journal of Geophysical Research: Space Physics*, *93*(A9), 9867–9882, doi:10.1029/JA093iA09p09867, 1988.

[188] Solomon, S. C., S. M. Bailey, and T. N. Woods, Effect of solar soft X-rays on the lower ionosphere, *Geophysical Research Letters*, *28*(11), 2149–2152, doi:10.1029/2001GL012866, 2001.

[189] Spiro, R. W., R. A. Heelis, and W. B. Hanson, Rapid subauroral ion drifts observed by atmosphere explorer c, *Geophysical Research Letters*, *6*(8), 657–660, doi:10.1029/GL006i008p00657, 1979.

[190] St.-Maurice, J. P., and D. G. Torr, Nonthermal rate coefficients in the ionosphere: The reactions of O^+ with N_2, O_2, and NO, *Journal of Geophysical Research: Space Physics*, *83*(A3), 969–977, doi:10.1029/JA083iA03p00969, 1978.

[191] States, R., and C. Gardner, Thermal structure of the mesopause region (80–105 km) at 40° N latitude. Part I: Seasonal variations, *Journal of the atmospheric sciences*, *57*(1), 66–77, doi:10.1175/1520-0469(2000)057⟨0066:TSOTMR⟩2.0.CO;2, 2000.

[192] States, R., and C. Gardner, Thermal structure of the mesopause region (80-105 km) at 40 degrees n latitude. part ii: Diurnal variations, *Journal of the atmospheric sciences*, *57*(1), 78–92, doi:10.1175/1520-0469(2000)057⟨0078:TSOTMR⟩2.0.CO;2, 2000.

[193] States, R. J., and C. S. Gardner, Structure of the mesospheric Na layer at 40°N latitude: Seasonal and diurnal variations, *Journal of Geophysical Research: Atmospheres*, *104*(D9), 11,783–11,798, doi:10.1029/1999JD900002, 1999.

[194] Stevens, M. H., R. R. Meier, X. Chu, M. T. DeLand, and J. M. C. Plane, Antarctic mesospheric clouds formed from space shuttle exhaust, *Geophysical Research Letters*, *32*(13), doi:10.1029/2005GL023054, 2005.

[195] Strang, G., On the construction and comparison of difference schemes, *SIAM Journal on Numerical Analysis*, *5*(3), pp. 506–517, 1968.

[196] Taylor, H. A., Parametric description of thermospheric ion composition results, *Journal of Geophysical Research*, *78*(1), 315–319, doi:10.1029/JA078i001p00315, 1973.

[197] Thayer, J. P., and J. Semeter, The convergence of magnetospheric energy flux in the polar atmosphere, *Journal of Atmospheric and Solar-Terrestrial Physics*, *66*(10), 807 – 824, doi:10.1016/j.jastp.2004.01.035, 2004.

[198] Thome, G. D., Incoherent scatter observations of traveling ionospheric disturbances, *Journal of Geophysical Research*, *69*(19), 4047–4049, doi:10.1029/JZ069i019p04047, 1964.

[199] Tong, Y., J. D. Mathews, and W. P. Ying, An upper e region quarterdiurnal tide at arecibo?, *Journal of Geophysical Research: Space Physics*, *93*(A9), 10,047–10,051, doi:10.1029/JA093iA09p10047, 1988.

[200] Torr, D. G., *The photochemistry of the upper atmosphere*, pp. 165–278, 1985.

[201] Vadas, S. L., Horizontal and vertical propagation and dissipation of gravity waves in the thermosphere from lower atmospheric and thermospheric sources, *Journal of Geophysical Research: Space Physics*, *112*(A6), doi:10.1029/2006JA011845, 2007.

[202] Vadas, S. L., and M. J. Nicolls, Temporal evolution of neutral, thermospheric winds and plasma response using {PFISR} measurements of gravity waves, *Journal of Atmospheric and Solar-Terrestrial Physics*, *71*(67), 744 – 770, doi:10.1016/j.jastp.2009.01.011, 2009.

[203] Viereck, R., E. Murad, S. Lai, D. Knecht, C. Pike, J. Gardner, A. Broadfoot, E. Anderson, and W. McNeil, Mg^+ and other metallic emissions observed in the thermosphere, in *Thermosphere-ionosphere-middle atmosphere coupling and dynamics*, *Advances in space*

research-series, vol. 18, edited by Rottger, J and Wickwar, VB, pp. 61–64, COSPAR, Pergamon press LTD, The Boulevard Langford Lane Kidlington, Oxford OX5 1GB, England, doi:{10.1016/0273-1177(95)00839-7}, 1996.

[204] von Zahn, U., P. von der Gathen, and G. Hansen, Forced release of sodium from upper atmospheric dust particles, *Geophysical Research Letters*, *14*(1), 76–79, doi:10.1029/GL014i001p00076, 1987.

[205] Vondrak, T., J. M. C. Plane, S. Broadley, and D. Janches, A chemical model of meteoric ablation, *Atmospheric Chemistry and Physics*, *8*(23), 7015–7031, doi:10.5194/acp-8-7015-2008, 2008.

[206] Wang, J., Y. Yang, X. Cheng, G. Yang, S. Song, and S. Gong, Double sodium layers observation over beijing, china, *Geophysical Research Letters*, *39*(15), doi:10.1029/2012GL052134, 2012.

[207] Weimer, D. R., Improved ionospheric electrodynamic models and application to calculating joule heating rates, *Journal of Geophysical Research: Space Physics*, *110*(A5), doi:10.1029/2004JA010884, 2005.

[208] Whalen, J. A., A quantitative description of the spatial distribution and dynamics of the energy flux in the continuous aurora, *Journal of Geophysical Research: Space Physics*, *88*(A9), 7155–7169, doi:10.1029/JA088iA09p07155, 1983.

[209] Whitehead, J., Recent work on mid-latitude and equatorial sporadic-E, *Journal of Atmospheric and Terrestrial Physics*, *51*(5), 401 – 424, doi:http://dx.doi.org/10.1016/0021-9169(89)90122-0, 1989.

[210] Whitehead, J. D., The formation of the sporadic-E layer in the temperate zones, *Journal of Atmospheric and Terrestrial Physics*, *20*(1), 49–58, doi:10.1016/0021-9169(61)90097-6, 1961.

[211] Williams, B. P., F. T. Berkey, J. Sherman, and C. Y. She, Coincident extremely large sporadic sodium and sporadic e layers observed in the lower thermosphere over colorado and utah, *Annales Geophysicae*, *25*(1), 3–8, doi:10.5194/angeo-25-3-2007, 2007.

[212] Woodcock, K. R. S., T. Vondrak, S. R. Meech, and J. M. C. Plane, A kinetic study of the reactions FeO^+ + O, $Fe^+ \cdot N_2$ +O,$Fe^+ \cdot O_2$ + O and FeO^+ + CO: implications for sporadic E layers in the upper atmosphere, *Phys. Chem. Chem. Phys.*, *8*, 1812–1821, doi:10.1039/B518155K, 2006.

[213] Worden, E. F., B. Comaskey, J. Densberger, J. Christensen, T. M. McAfee, T. A. Paisner, and J. G. Conway, The ionization potential of neutral iron, fe i, by multistep laser spectroscopy, *J. Opt. Soc. Am. B*, *1*(2), 314–316, doi:10.1364/JOSAB.1.000314, 1984.

[214] Xue, X. H., et al., Lower thermospheric enhanced sodium layers observed at low latitude and possible formation: Case studies, *Journal of Geophysical Research: Space Physics*, doi:10.1002/jgra.50200, 2013.

[215] Yi, F., C. Yu, S. Zhang, X. Yue, Y. He, C. Huang, Y. Zhang, and K. Huang, Seasonal variations of the nocturnal mesospheric Na and Fe layers at 30∘N, *Journal of Geophysical Research: Atmospheres*, *114*(D1), doi:10.1029/2008JD010344, 2009.

[216] Yu, Z., X. Chu, W. Huang, W. Fong, and B. R. Roberts, Diurnal variations of the Fe layer in the mesosphere and lower thermosphere: Four season variability and solar effects on the layer bottomside at McMurdo (77.8°S, 166.7°E), Antarctica, *Journal of Geophysical Research: Atmospheres*, *117*(D22), doi:10.1029/2012JD018079, 2012.

[217] Yuan, T., H. Schmidt, C. Y. She, D. A. Krueger, and S. Reising, Seasonal variations of semidiurnal tidal perturbations in mesopause region temperature and zonal and meridional winds above Fort Collins, Colorado (40.6°N, 105.1°W), *Journal of Geophysical Research: Atmospheres*, *113*(D20), doi:10.1029/2007JD009687, 2008.

[218] Yuan, T., C.-Y. She, D. A. Krueger, F. Sassi, R. Garcia, R. G. Roble, H.-L. Liu, and H. Schmidt, Climatology of mesopause region temperature, zonal wind, and meridional wind over Fort Collins, Colorado (41°N, 105°W), and comparison with model simulations, *Journal of Geophysical Research: Atmospheres*, *113*(D3), doi:10.1029/2007JD008697, 2008.

[219] Zbinden, P., M. Hidalgo, P. Eberhahdt, and J. Geiss, Mass spectrometer measurements of the positive ion composition in the d- and e-regions of the ionosphere, *Planetary and Space Science*, *23*(12), 1621 – 1642, doi:10.1016/0032-0633(75)90090-2, 1975.

[220] Zhao, Y., A. Z. Liu, and C. S. Gardner, Measurements of atmospheric stability in the mesopause region at starfire optical range, {NM}, *Journal of Atmospheric and Solar-Terrestrial Physics*, *65*(2), 219 – 232, doi:10.1016/S1364-6826(02)00288-2, 2003.

[221] Zhlood'ko, A., V. N. Lebedinets, and V. B. Shushkova, Meteor ions in the polar ionosphere: Rocket mass-spectrometeric measurements and theoretical calculations, *Space Res.*, *14*, 277, 1974.

[222] Zhou, Q., S. Raizada, C. A. Tepley, and J. M. Plane, Seasonal and diurnal variation of electron and iron concentrations at the meteor heights above arecibo, *Journal of Atmospheric and Solar-Terrestrial Physics*, *70*(1), 49 – 60, doi:10.1016/j.jastp.2007.09.012, 2008.

Appendix A

Fe Boltzmann Temperature Lidar

A.1 Inversion Algorithm of Fe Density

The Fe Boltzmann temperature lidar takes advantage of the Rayleigh and resonance fluorescence lidar techniques to measure densities and temperature. The details of the principles of measuring density and temperature by Fe Boltzmann lidar are given by *Chu et al.* [2002]. In this section, we particularly introduce the algorithm of calculating Fe density from photon counts detected by lidar.

The resonance of fluorescence techniques relies on the unique energy-level distribution diagram of the ground-state manifold of Fe atoms, as shown in Figure A.1 [*Chu et al.*, 2002]. The strength of Fe fluorescence is not only determined by the probing wavelength, but also the number Fe densities. The Fe photon counts detected by lidar system is given by lidar equation A.1:

$$N_{Fe}(\lambda, z) = \Big(\frac{P_L(\lambda)\Delta t}{hc/\lambda}\Big)[\sigma_{eff}(\lambda, T, \sigma_L)R_{B\lambda}n_{Fe}(z)]\Delta z\Big(\frac{A}{4\pi z^2}\Big)(T_a^2(\lambda)T_c^2(\lambda, z))\eta(\lambda)G(z) \qquad \text{(A.1)}$$

where N_{Fe} is detected Fe photon count, z is the altitude; P_L is power of the laser; Δt is the temporal

resolution; Δz is the vertical resolution; h is Plank constant, c is speed of light in vacuum; λ is probing wavelength; $\sigma_{eff}(\lambda, T, \sigma_L)$ is the effective absorption cross section of the Fe transition; $R_{B\lambda}$ is the branching ratio; n_{Fe} is the number density of Fe; A is the area of the receiving telescope; η is the overall optical efficiency of the system; G is geometry factor.

The pure Rayleigh signal in Fe region is given by equation A.2

$$N_R(\lambda, z) = \Big(\frac{P_L(\lambda)\Delta t}{hc/\lambda}\Big)[\sigma_R(\pi, \lambda)n_{air}(z)]\Delta z\Big(\frac{A}{z^2}\Big)(T_a^2(\lambda)T_c^2(\lambda))\eta(\lambda)G(z) \tag{A.2}$$

and the Rayleigh signal in molecular scattering region below Fe region is given by equation A.3

$$N_R(\lambda, z_R) = \Big(\frac{P_L(\lambda)\Delta t}{hc/\lambda}\Big)[\sigma_R(\pi, \lambda)n_{air}(z_R)]\Delta z\Big(\frac{A}{z_R^2}\Big)T_a^2(\lambda)\eta(\lambda)G(z_R) \tag{A.3}$$

where $\sigma_R(\pi, \lambda)$ is the effective atmospheric Rayleigh angular backscatter cross section, which is equal to $\frac{\sigma_R(\lambda)}{4\pi}$ and $\sigma_R(\lambda)$ is the total effective atmospheric Rayleigh backscatter cross section.

Now, we have two equations, but more than 2 unknown variables. To calculate the Fe number density, we ultilize the Rayleigh normalization method that the Fe photons counts are normalized to lower-altitude (typically 50 km) Rayleigh photon counts. Therefore, the normalized Fe photon count is defined as:

$$N_{Norm}(\lambda, z) = \frac{N_{Fe}(\lambda, z)}{N_R(\lambda, z_R)T_c^2(\lambda, z)}\frac{z^2}{z_R^2} \tag{A.4}$$

From the actual measured photon counts, the normalized Fe count is:

$$N_{Norm}(\lambda, z) = \frac{N_S(\lambda, z) - N_B - N_R(\lambda, z)}{(N_s(\lambda, z_R) - N_B)T_c^2(\lambda, z)}\frac{z^2}{z_R^2} \tag{A.5}$$

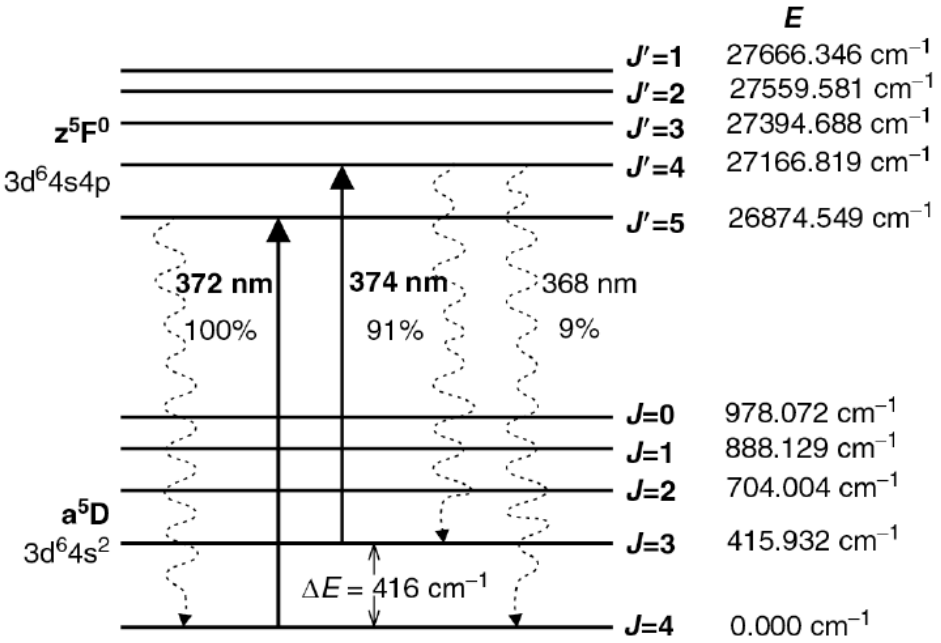

FIGURE A.1: Fe atomic energy levels. From *Chu et al.* [2002].

TABLE A.1: Isotopic Data of Fe Atoms

	^{54}Fe	^{56}Fe	^{57}Fe	^{58}Fe
Z	26	26	26	26
A	54	56	57	58
Nuclear spin	0	0	1/2	0
Natural abundance	5.845%	91.754%	2.119%	0.282%

where N_S and N_B are the measured photon counts and background photon counts. Equation A.5 becomes

$$N_{Norm}(\lambda, z) = \frac{(N_S(\lambda, z) - N_B)}{(N_S(\lambda, z_R) - N_B)} \frac{z^2}{z_R^2} \frac{1}{T_c^2(\lambda, z)} - \frac{n_{air}(z)}{n_{air}(z_R)} \tag{A.6}$$

where $n_{air}(z)$ and $n_{air}(z_R)$ are air number densities at altitude z and z_R

Substitute equations A.1 and A.2 into equation A.5, we have equation A.7

$$N_{Norm}(\lambda, z) = \frac{\sigma_{eff}(\lambda, T, \sigma_L) R_{B\lambda} n_{Fe}(\lambda, z)}{\sigma_R(\pi, \lambda) n_{air}(\lambda, z_R) T_c^2(\lambda, z)} \frac{1}{4\pi} \tag{A.7}$$

TABLE A.2: Fe Resonance Line Parameters

Transition wavelength λ	372.0993 nm	373.8194 nm
Degeneracy for ground state	$g_1 = 9$	$g_2 = 7$
Degeneracy for excited state	$g_1' = 11$	$g_2' = 9$
Radiative lifetime of excited state (ns)	61.0	63.6
Einstein coefficient A_{ki} $(10^8\ s^{-1})$	0.163	0.142
Oscillator strength f_{ik}	0.0413	0.0382
Branching ratio R_B	0.9959	0.9079
σ_0 (10^{-17}) m^2	9.4	8.7

The equations A.6 and A.7 give the Fe number density:

$$n_{Fe}(\lambda, z) = 4\pi\Big(\frac{(N_S(\lambda, z) - N_B)}{(N_S(\lambda, z_R) - N_B)}\frac{z^2}{z_R^2}\frac{1}{T_c^2(\lambda, z)} - \frac{n_{air}(z)}{n_{air}(z_R)}\Big)\Big(\frac{\sigma_R(\pi, \lambda)n_{air}(\lambda, z_R)}{\sigma_{eff}(\lambda, T, \sigma_L)R_{B\lambda}}\Big) \tag{A.8}$$

The temperature in the MLT region is measured by Boltzmann techniques. In thermal equilibrium, the population distributions of Fe atoms at energy level is constrained by Maxwell-Boltzmann distribution law, is given by equation A.9.

$$\frac{n_{Fe}(J=3)}{n_{Fe}(J=4)} = \frac{g_2}{g_1}e^{-\frac{\Delta E}{k_B T}} \tag{A.9}$$

In order to measure the temperature T by Boltzmann techniques, we need two channels to measure the population ratio of energy level (J=3) to energy level (J=4). As Figure A.1 equation A.7 suggest, the population ratio of energy level (J=3) to energy level (J=4) can be measured by the ratio of normalized photon counts of two probing wavelengths 374 nm and 372 nm.

$$\begin{aligned} R_T(z) &= \frac{N_{Norm}(\lambda_{374}, z)}{N_{Norm}(\lambda_{372}, z)} \\ &= \frac{g_2}{g_1}\frac{R_{B374}}{R_{B372}}\Big(\frac{\lambda_{374}}{\lambda_{372}}\Big)^{4.0117}\frac{\sigma_{eff}(\lambda_{374}, T, \sigma_{L374})}{\sigma_{eff}(\lambda_{372}, T, \sigma_{372})}\frac{T_c^2(\lambda_{372}, z)}{T_c^2(\lambda_{374}, z)}e^{-\Delta E/k_B T} \end{aligned} \tag{A.10}$$

From equation A.10, we can derive the temperature:

$$T = \frac{\Delta E/k_B}{\ln\left[\frac{g_2}{g_1}\frac{R_{B374}}{R_{B372}}\left(\frac{\lambda_{374}}{\lambda_{372}}\right)^{4.0117}\frac{\sigma_{eff}(\lambda_{374},T,\sigma_{374})}{\sigma_{eff}(\lambda_{372},T,\sigma_{372})}\frac{T_c^2(\lambda_{372},z)}{T_c^2(\lambda_{374},z)}\right]} \tag{A.11}$$

A.2 Instrumentation of Fe Boltzmann Lidar System

The lidar system was upgraded in 2009–2010 at University of Colorado Boulder, including seed laser upgrade, data acquisition program (DAQ) software upgrade [*Wang, et al.*, 2012]. The upgraded Fe Boltzmann lidar system is shown in Figure 1.12. The system consists two independent channels, including two independent transmitters and two independent receivers. The two channels are coordinated by a timing controller called prohibited box that prohibit the signal in one receiver from being contaminated by the other channel. The system parameters of the Fe Boltzmann lidar is given by Table A.3.

The core component of each transmitter is one frequency-doubled pulsed solid-state Alexandrite laser [*Walling et al.*, 1980; *Samelson et al.*, 1988] made by Light Age Inc.. Alexandrite is the common name for chromium-doped chrysoberyl ($Cr^{3+} : BeAl_2O_4$) crystal. It is a four-level, low-gain, and broadly tunable laser (nominal range 700–820 nm). The Alexandrite crystal is mechanically strong, and relatively good thermal conductor, allowing Alexandrite laser can be Q-switched with higher repetition rates and emit a high average output power. Alexandrite works better under higher temperature. The Alexandrite lasers made by Light Age Inc. stabilize Alexandrite crystal at 80° C.

The output of Q-switched alexandrite laser is spectrally narrow with pulse length in the range of 20–300 nsec. In order to make the alexandrite laser lase at desired wavelength, the alexandrite laser is controlled by seeding the laser with narrow-band and frequency stabilized CW diode laser.

TABLE A.3: System Parameters for Fe Boltzmann Temperature Lidar. *Chu et al.* [2002], *Wang et al.* [2012]

Lidar Transmitter		
Characteristics	Channel I (374 nm)	Channel II (372 nm)
Laser	Light Age, Inc., Model PAL 101 Frequency-Doubled Pulsed Alexandrite Laser	
Linewidth (FWHM) (MHz)	864	876
Pulse energy (mJ)	100	100
Pulse length (ns)	55–65	55–65
Repetition reate (Hz)	33.2	34.1
Average power (W)	3	3
Beam divergence (mrad)	0.35	0.35
Injection Seeder Laser	ECDL Diode Lasers	
Wavelength (nm)	747.6390	744.1990
Output power (mW)	14	14
Linewidth (MHz) (50 ms)	$< 100\ kHz$	$< 100\ kHz$
Lidar Receiver		
Characteristics	Nighttime	Daytime
Telescope	Meade, Model LX200 (f/10) Schmidt-Cassegrain Design	
Diameter (m)	0.4064	0.4064
Aperture area (m^2)	0.130	0.130
Telescope focal length (mm)	4064	4064
Field of view (mrad)	1	0.5
Interference filter bandwidth (nm)	4.2	03
Etalon bandwidth (GHz)	–	30
Photomultiplier tube quantum efficiency	28%	28%
Receiver optical efficiency	58.7%	18.0%
Total receiver efficiecy	16.4%	5.0%

The seeder lasers used in McMurdo project are ECDLs (External Cavity Diode Laser) from Toptica Photonics. The injected photons by diode laser are concentrated and dominate in the cavity before the Q-switch opens. When the Q-switch opens, the gain of alexandrite laser at the injected frequency suppresses the other frequencies and make the laser lase at the injected frequency. Therefore, the output of the Alexandrite laser spectrally well constrained by the frequencies of injection laser ECDLs itself. In the application of Fe Boltzmann system, the desired frequencies (372 and 374 nm) are way off the gain spectrum of alexandrite crystal (700–820 nm). Therefore,

the seeding lasers are chosen at frequencies of 744 and 748 nm, and double the output frequency from alexandrite cavity through a non-linear optics crystal, lithium triborate (LiB_3O_5) "LBO".

In the receiver chain, we have three techniques to suppress background noise. First we utilize pinhole to constrain the field of view the telescope. At daytime, we use 4 mm pinhole and change to 2 mm at nighttime, and the field of view decreases from 1 mrad to 0.5 mrad. Second, we utilize interference filters passing bandwidth of 5 nm at nighttime and 0.3 m at daytime to suppress the out band photon noise. For nighttime operation, the first two steps are sufficient enough to obtain high signal to noise ratio. At daytime, another step is needed to suppress the solar background. An air-spaced pressure-tuning Fabry-Perot etalon is utilized before the interference filter. These etalons are pressure and temperature stabilized. The free spectral range of the etalon we used is 650 GHz, and the finesse and FWHM of the etalon are approximately 21 and 30.9 GHz.

Appendix B

Solution of Ion's Motion

B.1 Vector Solution of Ion's Motion

Under the first-order assumption, the ion's motion is steady state, balanced by Coulomb force, Lorentz force and the collision between neutral and ions, gravity and ion's pressure, which is given by equation B.1,

$$q\vec{E} + q\vec{V_i} \times \vec{B} + m_i\nu_{in}(\vec{V_n} - \vec{V_i}) + \vec{F} = 0 \tag{B.1}$$

where $\vec{F} = m_i\vec{g}$ - $\frac{\nabla P_i}{N_i}$, $P_i = N_i k_B T_i$, ν_{in} is ion-neutral collision frequency.

The gradient of the pressure P_i is given by $\nabla P_i = k_B T_i \ \nabla N_i + k_B N_i \ \nabla T_i = m_i\nu_{in} D_i \ \nabla N_i + m_i\nu_{in} D_i N_i \frac{\nabla T_i}{T_i}$. The D_i is the diffusion coefficient, which is $D_i = \frac{k_B T_i}{m_i\nu_{in}}$. Therefore the term $\frac{\nabla P_i}{N_i}$ can also be written as $\frac{\nabla P_i}{N_i} = m_i\nu_{in} D_i \ \frac{\nabla N_i}{N_i} + m_i\nu_{in} D_i \ \frac{\nabla T_i}{T_i}$.

The cross product of the equation B.1 and $\vec{B}$ gives the equation B.2

$$(q\vec{E} + q\vec{V_i} \times \vec{B} + m_i\nu_{in}(\vec{V_n} - \vec{V_i}) + \vec{F}) \times \vec{B} = 0 \tag{B.2}$$

The dot product of the equation B.1 and $\vec{B}$ gives the equation B.3

$$(q\vec{E} + q\vec{V}_i \times \vec{B} + m_i\nu_{in}(\vec{V}_n - \vec{V}_i) + \vec{F}) \cdot \vec{B} = 0 \tag{B.3}$$

Equation B.2 becomes

$$q\vec{E} \times \vec{B} + q(\vec{V}_i \times \vec{B}) \times \vec{B} + m_i\nu_{in}(\vec{V}_n \times \vec{B} - \vec{V}_i \times \vec{B}) + \vec{F} \times \vec{B} = 0 \tag{B.4}$$

Since $(\vec{a} \times \vec{b}) \times \vec{c}$ = -$(\vec{b} \cdot \vec{c})\vec{a}$ + $(\vec{a} \cdot \vec{c})\vec{b}$, then equation B.4 becomes equation B.5

$$q\vec{E} \times \vec{B} - qB^2\vec{V}_i + q(\vec{V}_i \cdot \vec{B})\vec{B} + m_i\nu_{in}(\vec{V}_n \times \vec{B} - \vec{V}_i \times \vec{B}) + \vec{F} \times \vec{B} = 0 \tag{B.5}$$

From equation B.1, we get equation B.6

$$\vec{V}_i \times \vec{B} = -\vec{E} - \frac{m_i\nu_{in}}{q}(\vec{V}_n - \vec{V}_i) - \frac{\vec{F}}{q} \tag{B.6}$$

Due to $(\vec{V}_i \times \vec{B}) \cdot \vec{B} = 0$, equation B.3 gives equation B.7

$$\vec{V}_i \cdot \vec{B} = \frac{q\vec{E} \cdot \vec{B}}{m_i\nu_{in}} + \vec{V}_n \cdot \vec{B} + \frac{\vec{F} \cdot \vec{B}}{m_i\nu_{in}} \tag{B.7}$$

Substitute equation B.6 and B.7 into equation B.5, we get

$$\begin{aligned} q\vec{E} \times \vec{B} - qB^2\vec{V}_i + q(\frac{q\vec{E} \cdot \vec{B}}{m_i\nu_{in}} + \vec{V}_n \cdot \vec{B} + \frac{\vec{F} \cdot \vec{B}}{m_i\nu_{in}})\vec{B} + m_i\nu_{in}\vec{V}_n \\ \times \vec{B} + m_i\nu_{in}\vec{E} + \frac{(m_i\nu_{in})^2}{q}(\vec{V}_n - \vec{V}_i) + \frac{m_i\nu_{in}}{q}\vec{F} + \vec{F} \times \vec{B} = 0 \end{aligned} \tag{B.8}$$

From equation B.8, we get equation B.9

$$\begin{aligned}\Big(qB^2+\frac{(m_i\nu_{in})^2}{q}\Big)\vec{V_i} = q\vec{E}\times\vec{B}+\frac{q^2(\vec{E}\cdot\vec{B})}{m_i\nu_{in}}\vec{B}+q(\vec{V_n}\cdot\vec{B})\vec{B}+m_i\nu_{in}\vec{V_n}\times\vec{B}\\ +m_i\nu_{in}\vec{E}+\frac{(m_i\nu_{in})^2}{q}\vec{V_n}+\Big(\frac{q\vec{F}\cdot\vec{B}}{m_i\nu_{in}}\vec{B}+\frac{m_i\nu_{in}}{q}\vec{F}+\vec{F}\times\vec{B}\Big)\end{aligned} \tag{B.9}$$

Let's define ion gyrofrequency, which is $\omega_i=\frac{qB}{m_i}$, and the ratio of ion-neutral collision frequency ν_{in} to ion gyrofrequency ω_i, which is $\xi=\frac{\nu_{in}}{\omega_i}$. Divide equation B.9 with qB^2, we get equation B.10,

$$\begin{aligned}(1+\xi^2)\vec{V_i} = \frac{1}{B^2}\vec{E}\times\vec{B}+\frac{q(\vec{E}\cdot\vec{B})}{m_i\nu_{in}}\frac{\vec{B}}{B^2}+\frac{(\vec{V_n}\cdot\vec{B})}{B^2}\vec{B}+\frac{\xi}{B}\vec{V_n}\times\vec{B}\\ +\frac{\xi}{B}\vec{E}+\xi^2\vec{V_n}+\Big(\frac{\vec{F}\cdot\vec{B}}{m_i\nu_{in}B^2}\vec{B}+\frac{\xi}{qB}\vec{F}+\frac{\vec{F}\times\vec{B}}{qB^2}\Big)\end{aligned} \tag{B.10}$$

Equation B.10 gives the solution of ion's motion equation B.11,

$$\begin{aligned}\vec{V_i} = \frac{1}{1+\xi^2}\frac{\vec{E}\times\vec{B}}{B^2}+\frac{q(\vec{E}\cdot\vec{B})}{m_i\nu_{in}(1+\xi^2)}\frac{\vec{B}}{B^2}+\frac{\xi}{1+\xi^2}\frac{\vec{E}}{B}+\frac{\xi}{1+\xi^2}\frac{\vec{V_n}\times\vec{B}}{B}+\frac{1}{1+\xi^2}\frac{(\vec{V_n}\cdot\vec{B})\vec{B}}{B^2}\\ +\frac{\xi^2}{1+\xi^2}\vec{V_n}+\Big(\frac{\vec{F}\times\vec{B}}{qB^2(1+\xi^2)}+\frac{\vec{F}\cdot\vec{B}}{m_i\nu_{in}B^2(1+\xi^2)}\vec{B}+\frac{\xi}{Bq(1+\xi^2)}\vec{F}\Big)\end{aligned} \tag{B.11}$$

B.2 Without Ambipolar Diffusion

Without ambipolar diffusion, we can assume that the electric field is approximately perpendicular to magnetic field, $\vec{E}\cdot\vec{B}\approx 0$. Because of the definition of the coordinate system, $\vec{B}$ is in the y-z plane, and can be decomposed into (0, B_y, B_z). $\vec{E}=(E_x, E_y, E_z)$, $\vec{V_n}=(V_{n,x}, V_{n,y}, V_{n,z})$. Θ_D is the dip angle, so $B_y=\cos\Theta_D B$, $B_z=-\sin\Theta_D B$,

$$\vec{E}\times\vec{B}=(E_yB_z-E_zB_y)\vec{e_x}-E_xB_z\vec{e_y}+E_xB_y\vec{e_z} \tag{B.12}$$

$$\vec{V_n}\cdot\vec{B}=V_{n,y}B_y+V_{n,z}B_z \tag{B.13}$$

$$\vec{V_n} \times \vec{B} = (V_{n,y}B_z - V_{n,z}B_y)\vec{e_x} - V_{n,x}B_z\vec{e_y} + V_{n,x}B_y\vec{e_z} \tag{B.14}$$

$$\frac{\vec{F}\cdot\vec{B}}{(1+\xi^2)m_i\nu_{in}B^2}\vec{B} + \frac{\xi}{(1+\xi^2)qB}\vec{F} = \frac{(\sin\Theta_D)^2}{1+\xi^2}\frac{F_z}{m_i\nu_{in}} + \frac{\xi^2}{1+\xi^2}\frac{F_z}{m_i\nu in} \tag{B.15}$$

The vertical ion drift is given by dot product of equation B.11 and unit vector $\vec{e_z}$ of z axis, giving equation B.16

$$\begin{aligned}\vec{V_i}\cdot\vec{e_z} = {} & \frac{1}{1+\xi^2}\frac{E_xB_y}{B^2}\vec{e_z} + \frac{\vec{V_n}\cdot\vec{B}}{(1+\xi^2)B^2}B_z\vec{e_z} + \frac{\xi V_{n,x}B_y}{1+\xi^2}\vec{e_z} + \frac{\xi}{1+\xi^2}E_z \\ & + \frac{\xi^2}{1+\xi^2}V_{n,z} + \Big(\frac{(\sin\Theta_D)^2}{1+\xi^2} + \frac{\xi^2}{1+\xi^2}\Big)\frac{F_z}{m_i\nu in} + \frac{(\vec{F}\times\vec{B})\cdot\vec{e_z}}{qB^2}\end{aligned} \tag{B.16}$$

Where $(\vec{F}\times\vec{B})$ generates the horizontal ion drift, so $(\vec{F}\times\vec{B})\cdot\vec{e_z} = 0$, Therefore, $V_{i,z} = V_{iz1} + V_{iz2}$ + V_{iz3}, where V_{iz1}, V_{iz2} and V_{iz3} are given by B.18, B.19, B.21:

$$V_{iz1} = -\frac{sin\Theta_D\cos\Theta_D}{1+\xi^2}V_{n,y} + \frac{\xi\cos\Theta_D}{1+\xi^2}V_{n,x} + \frac{\xi^2}{1+\xi^2}V_{n,z} + \frac{(\sin\Theta_D)^2}{1+\xi^2}V_{n,z} \tag{B.17}$$

$$= -\frac{\sin(2\Theta_D)}{2(1+\xi^2)}V_{n,y} + \frac{\xi\cos\Theta_D}{1+\xi^2}V_{n,x} + \Big(1 - \frac{\cos^2\Theta_D}{1+\xi^2}\Big)V_{n,z} \tag{B.18}$$

$$V_{iz2} = \frac{\cos\Theta_D}{1+\xi^2}\frac{E_x}{B} + \frac{\xi}{1+\xi^2}\frac{E_z}{B} \tag{B.19}$$

$$V_{iz3} = \Big(\frac{(\sin\Theta_D)^2}{1+\xi^2} + \frac{\xi^2}{1+\xi^2}\Big)\frac{F_z}{m_i\nu_{in}} \tag{B.20}$$

$$= \Big(1 - \frac{\cos^2\Theta_D}{1+\xi^2}\Big)\Big(-\frac{g}{\nu_{in}} - \frac{D_i}{N_i}\frac{\partial N_i}{\partial z} - \frac{D_i}{T_i}\frac{\partial T_i}{\partial z}\Big) \tag{B.21}$$

where $F = m_ig$ - $\frac{m_i\nu_{in}D_i}{N_i}\nabla N_i$ - $m_i\nu_{in}D_i\frac{\nabla T_i}{T_i}$

B.3 With Ambipolar Diffusion

In the gravitational field, the charge separation due to the large diffusivity of the electrons can establish an electric field, whose function is to increase the diffusivity of ions. The gyro motions around geomagnetic field line make electrons and ions can easily move along with geomagnetic field line. So the separation electric field along with the geomagnetic field is not negligible, $\vec{E} \cdot \vec{B} \neq 0$. In order to obtain the term $\vec{E} \cdot \vec{B}$, we need to take the motions of electrons into consideration. Under the first approximation, the motions of electrons is given by equation B.22

$$q_e\vec{E} + q_e\vec{V_e} \times \vec{B} + m_e\vec{g} - \frac{\nabla P_e}{N_e} + m_e\nu_{en}(\vec{V_n} - \vec{V_e}) + m_e\nu_{ei}(\vec{V_i} - V_e) = 0 \tag{B.22}$$

where q_e is the charge of electron, $\vec{V_e}$ is the velocity of electron, m_e is the mass of electron, P_e is the pressure of electron gas, ν_{en} is the electron-neutral collision frequency, ν_{ei} is the electron-ion collision frequency. Due to the high mobility of electrons, we neglect the last two terms of equation B.22, therefore it can be approximated by equation B.23

$$q_e\vec{E} + q_e\vec{V_e} \times \vec{B} + m_e\vec{g} - \frac{\nabla P_e}{N_e} \approx 0 \tag{B.23}$$

The dot production of equation B.23 and $\vec{B}$ give rise to equation B.24

$$q_e\vec{E} \cdot \vec{B} + (m_e\vec{g} - \frac{\nabla P_e}{N_e}) \cdot \vec{B} \approx 0 \tag{B.24}$$

or

$$q_e\vec{E} \cdot \vec{B} + \vec{F_e} \cdot \vec{B} \approx 0 \tag{B.25}$$

where $F_e = m_e\vec{g}$ - $\frac{\nabla P_e}{N_e}$. Therefore we have,

$$\vec{E}\cdot\vec{B} \approx -\frac{1}{q_e}\vec{F}_e\cdot\vec{B} \tag{B.26}$$

Substitute equation B.26 into equation B.11, we have a new version of solution of ion's motion, given by equation B.27, ($q_e = -q$)

$$\begin{aligned}\vec{V}_i = &\frac{1}{1+\xi^2}\frac{\vec{E}\times\vec{B}}{B^2} + \frac{(\vec{F}_e\cdot\vec{B})}{m_i\nu_{in}(1+\xi^2)}\frac{\vec{B}}{B^2} + \frac{\xi}{1+\xi^2}\frac{\vec{E}}{B} + \frac{\xi}{1+\xi^2}\frac{\vec{V_n}\times\vec{B}}{B} + \frac{1}{1+\xi^2}\frac{(\vec{V}_n\cdot\vec{B})\vec{B}}{B^2}\\ &+ \frac{\xi^2}{1+\xi^2}\vec{V}_n + \Big(\frac{\vec{F}\times\vec{B}}{qB^2(1+\xi^2)} + \frac{\vec{F}\cdot\vec{B}}{m_i\nu_{in}B^2(1+\xi^2)}\vec{B} + \frac{\xi}{Bq(1+\xi^2)}\vec{F}\Big)\end{aligned} \tag{B.27}$$

By taking the similar steps in Section B.2,

$$\frac{\vec{F}\cdot\vec{B}+\vec{F_e}\cdot B}{(1+\xi^2)m_i\nu_{in}B^2}\vec{B} + \frac{\xi}{(1+\xi^2)qB}\vec{F} = \frac{(\sin\Theta_D)^2}{1+\xi^2}\frac{F_z+F_{e,z}}{m_i\nu_{in}} + \frac{\xi^2}{1+\xi^2}\frac{F_z}{m_i\nu in} \tag{B.28}$$

where $F_z + F_{e,z}$ is equal to, assuming $n_i = n_e$:

$$\begin{aligned}F_z + F_{e,z} &= -m_i g - \frac{1}{N_i}kT_i\frac{\partial N_i}{\partial z} - k\frac{\partial T_i}{\partial z} - m_e g - \frac{1}{N_e}kT_e\frac{\partial N_e}{\partial z} - k\frac{\partial T_e}{\partial z}\\ &= -(m_i+m_e)g - k(T_i+T_e)\Big(\frac{1}{N_i}\frac{\partial N_i}{\partial z} + \frac{1}{T_i+T_e}\frac{\partial(T_i+T_e)}{\partial z}\Big)\end{aligned} \tag{B.29}$$

The mass of electron is much less than that of proton, $m_i + m_e \approx m_i$, so

$$\frac{F_z+F_{e,z}}{m_i\nu_{in}} = -\frac{g}{\nu_{in}} - D_i(1+\frac{T_e}{T_i})\Big(\frac{1}{N_i}\frac{\partial N_i}{\partial z} + \frac{1}{T_i+T_e}\frac{\partial(T_i+T_e)}{\partial z}\Big) \tag{B.30}$$

Therefore the V_{iz3} can be rewritten as:

$$\begin{aligned}V_{iz3} = -\Big(1-\frac{\cos^2\Theta_D}{1+\xi^2}\Big)\frac{g}{\nu_{in}} - \frac{\cos^2\Theta_D}{1+\xi^2}D_i(1+\frac{T_e}{T_i})\Big(\frac{1}{N_i}\frac{\partial N_i}{\partial z}\\ + \frac{1}{T_i+T_e}\frac{\partial(T_i+T_e)}{\partial z}\Big) - \frac{\xi^2}{1+\xi^2}D_i\Big(\frac{1}{N_i}\frac{\partial N_i}{\partial z} + \frac{1}{T_i}\frac{\partial T_i}{\partial z}\Big)\end{aligned} \tag{B.31}$$

Below 200 km, $T_i \approx T_e$ the vertical component of the solution of ion's motion can be simplified as equations B.32 – B.34,

$$V_{iz1} = -\frac{\sin(2\Theta_D)}{2(1+\xi^2)}V_{n,y} + \frac{\xi\cos\Theta_D}{1+\xi^2}V_{n,x} + \Big(1 - \frac{\cos^2\Theta_D}{1+\xi^2}\Big)V_{n,z} \tag{B.32}$$

$$V_{iz2} = \frac{\cos\Theta_D}{1+\xi^2}\frac{E_x}{B} + \frac{\xi}{1+\xi^2}\frac{E_z}{B} \tag{B.33}$$

$$V_{iz3} = -\Big(1 - \frac{\cos^2\Theta_D}{1+\xi^2}\Big)\frac{g}{\nu_{in}} - \Big(1 - \frac{\cos 2\Theta_D}{1+\xi^2}\Big)D_i\Big(\frac{1}{N_i}\frac{\partial N_i}{\partial z} + \frac{1}{T_i}\frac{\partial T_i}{\partial z}\Big) \tag{B.34}$$

Appendix C

Numerical Solution of Chemistry

Let's start with a single reaction,

$$A + B \xrightarrow{k} C + D \tag{C.1}$$

The change of concentration of reactant A and product C can be described by an ordinary differential equations (ODEs):

$$\begin{cases} \frac{dA}{dt} = -k \cdot A \cdot B \\ \frac{dC}{dt} = k \cdot A \cdot B \end{cases}$$

Given the initial values of A and B, the ODEs provide exact solutions of A and C as function of time, t. This methodology can also be applied to a complicated system. In our model, we will solve the atmospheric metallic Fe chemistry, and molecular ions chemistry in E-F region. The chemical reactions and respective rate coefficients are shown in Table **??** and **??**. The photoionization and electron ionization reactions are not listed in the table. Define, $\mathbf{C} = (Fe,\ Fe^+,\ FeO,\ FeO^+,\ FeO_2,\ FeO_2^+,\ FeO_3,\ FeN_2^+,\ Fe(OH)_2,\ Fe(OH),\ NO^+,\ O_2^+,\ N_2^+,\ O^+,\ N^+,\ N\ )^T$. The change of $\mathbf{C}$, caused by chemical reactions are governed by the system (equations C.2 $\sim$ C.17).

The right-hand side (RHS) of the ODEs, equations C.2 $\sim$ C.17, represents the net rate, which is the sum of production and loss rate of the species. The RHS is the function of reaction rate coefficients and the number density of reactants as shown in equation C.18. In general, there is no rigorous solution for the ODEs, equations C.2 $\sim$ C.17, but numerical method can be applied for approaching the true solution.

$$\frac{dFe}{dt} = R_1(\mathbf{C}) \tag{C.2}$$
$$\frac{dFe^+}{dt} = R_2(\mathbf{C}) \tag{C.3}$$
$$\frac{dFeO}{dt} = R_3(\mathbf{C}) \tag{C.4}$$
$$\frac{dFeO^+}{dt} = R_4(\mathbf{C}) \tag{C.5}$$
$$\frac{dFeO_2}{dt} = R_5(\mathbf{C}) \tag{C.6}$$
$$\frac{dFeO_2^+}{dt} = R_6(\mathbf{C}) \tag{C.7}$$
$$\frac{dFeN_2^+}{dt} = R_7(\mathbf{C}) \tag{C.8}$$
$$\frac{dFeO_3}{dt} = R_8(\mathbf{C}) \tag{C.9}$$
$$\frac{dFe(OH)_2}{dt} = R_9(\mathbf{C}) \tag{C.10}$$
$$\frac{dFeOH}{dt} = R_{10}(\mathbf{C}) \tag{C.11}$$
$$\frac{dNO^+}{dt} = R_{11}(\mathbf{C}) \tag{C.12}$$
$$\frac{dN_2^+}{dt} = R_{12}(\mathbf{C}) \tag{C.13}$$
$$\frac{dN^+}{dt} = R_{13}(\mathbf{C}) \tag{C.14}$$
$$\frac{dN}{dt} = R_{14}(\mathbf{C}) \tag{C.15}$$
$$\frac{dO_2^+}{dt} = R_{15}(\mathbf{C}) \tag{C.16}$$
$$\frac{dO^+}{dt} = R_{16}(\mathbf{C}) \tag{C.17}$$

where $R_1 \sim R_{16}$ are given by:

$$R_1(\mathbf{C}) = k_1[Fe^+][e^-] + k_2[FeO^+][e^-] + k_9[FeO_2^+][e^-] + k_{10}[FeN_2^+][e^-] + k_{15}[FeO][O] + k_{25}[FeOH][H] - k_3[Fe][NO^+] - k_4[Fe][O_2^+] - k_{14}[Fe][O_3] \tag{C.18}$$

$$R_2(\mathbf{C}) = -k_1[Fe^+][e^-] + k_3[Fe][NO^+] + k_4[Fe][O_2^+] + k_6[FeO^+][O] - k_8[Fe^+][O_3] - k_{11}[Fe^+][O_2][M] - k_{12}[Fe^+][N_2][M] - k_{13}[Fe^+][O][M] \tag{C.19}$$

$$R_3(\mathbf{C}) = k_{14}[Fe][O_3] - k_{15}[FeO][O] - k_{16}[FeO][O_3] - k_{17}[FeO][O_2][M] + k_{18}[FeO_2][O] - k_{22}[FeO][H_2O][M] \tag{C.20}$$

$$R_4(\mathbf{C}) = -k_2[FeO^+][e^-] + k_5[FeO_2^+][O] - k_6[FeO^+][O] + k_7[FeN_2^+][O] + k_8[Fe^+][O_3] + k_{13}[Fe^+][O][M] \tag{C.21}$$

$$R_5(\mathbf{C}) = k_{16}[FeO][O_3] - k_{18}[FeO_2][O] - k_{19}[FeO_2][O_3] + k_{20}[FeO_3][O] \tag{C.22}$$

$$R_6(\mathbf{C}) = -k_5[FeO_2^+][O] - k_9[FeO_2^+][e^-] + k_{11}[Fe^+][O_2][M] \tag{C.23}$$

$$R_7(\mathbf{C}) = k_{17}[FeO][O_2][M] + k_{19}[FeO_2][O_3] - k_{20}[FeO_3][O] - k_{21}[FeO_3][H_2O] - k_{24}[FeO_3][H] \tag{C.24}$$

$$R_8(\mathbf{C}) = -k_7[FeN_2^+][O] - k_{10}[FeN_2^+][e^-] + k_{12}[Fe^+][N_2][M] \tag{C.25}$$

$$R_9(\mathbf{C}) = k_{21}[FeO_3][H_2O] + k_{22}[FeO][H_2O][M] - k_{23}[Fe(OH)_2][H] \tag{C.26}$$

$$R_{10}(\mathbf{C}) = k_{23}[Fe(OH)_2][H] + k_{24}[FeO_3][H] - k_{25}[FeOH][H] - k_{26}[FeOH][FeOH] \tag{C.27}$$

$$R_{11}(\mathbf{C}) = -k_3[Fe][NO^+] - k_{27}[NO^+][e^-] + k_{30}[O^+][N_2] + k_{32}[O_2^+][NO] + k_{33}[O_2^+][N_2] + k_{34}[N_2^+][O] + k_{38}[O_2^+][N] + k_{40}[N^+][O_2] + k_{42}[O^+][NO] \tag{C.28}$$

$$R_{12}(\mathbf{C}) = -k_4[Fe][O_2^+] - k_{28}[O_2^+][e^-] + k_{31}[O^+][O_2] - k_{32}[O_2^+][NO] - k_{33}[O_2^+][N_2] + k_{36}[N_2^+][O_2] + k_{37}[O^+][CO_2] - k_{38}[O_2^+][N] + k_{39}[N^+][O_2] \tag{C.29}$$

$$R_{13}(\mathbf{C}) = -k_{34}[N_2^+][O] - k_{35}[N_2^+][O] - k_{36}[N_2^+][O_2] + k_{N_2}[N_2] \tag{C.30}$$

$$R_{14}(\mathbf{C}) = -k_{30}[O^+][N_2] - k_{31}[O^+][O_2] + k_{35}[N_2^+][O] - k_{37}[O^+][CO_2] + k_{41}[N^+][O] - k_{42}[O^+][NO] \tag{C.31}$$

$$R_{15}(\mathbf{C}) = -k_{39}[N^+][O_2] - k_{40}[N^+][O_2] - k_{41}[N^+][O] \tag{C.32}$$

$$\begin{aligned} R_{16}(\mathbf{C}) = {} & k_{27}[NO^+][e^-] + 2k_{29}[N_2^+][e^-] + k_{30}[O^+][N_2] \\ & + k_{34}[N_2^+][O] - k_{38}[O_2^+][N] + k_{39}[N^+][O_2] + k_{41}[N^+][O] \end{aligned} \tag{C.33}$$

where k_i is the reaction rate coefficients, $[M]$ the number density of species 'M'.

Equation C.2 $\sim$ C.17 can be written as a matrix form,

$$\frac{d}{dt}\begin{pmatrix} Fe \\ Fe^+ \\ \vdots \\ N \end{pmatrix} = \begin{pmatrix} a_{1,1} & a_{1,2} & \cdots & a_{1,16} \\ a_{2,1} & a_{2,2} & \cdots & a_{2,16} \\ \vdots & \vdots & \ddots & \vdots \\ a_{16,1} & a_{16,2} & \cdots & a_{16,16} \end{pmatrix} \begin{pmatrix} Fe \\ Fe^+ \\ \vdots \\ N \end{pmatrix} \tag{C.34}$$

where the first row of the coefficient matrix is

$$\begin{cases} a_{1,1} = -k_3[NO^+] - k_4[O_2^+] - k_{14}[O_3] \\ a_{1,2} = k_1[e^-] \\ a_{1,3} = k_{15}[O] \\ a_{1,4} = k_2[e^-] \\ a_{1,6} = k_9[e^-] \\ a_{1,8} = k_{10}[e^-] \\ a_{1,10} = k_{25}[H] \\ a_{1,*} = 0 \quad (* \ represents \ the \ left \ elements \ in \ the \ first \ row) \end{cases}$$

Equation C.34 can be simplified as,

$$\frac{d\mathbf{C}}{dt} = \mathbf{A} \cdot \mathbf{C} \tag{C.35}$$

where $\mathbf{A}$ is the coefficient matrix and $\mathbf{C}$ is the vector.

The idea for solving the differential algebraic equations (DAEs) is to replace the derivative in equation C.35 by difference approximation, and solve the resulting equation for the solution at time step t_n using Newton iteration method. By applying backward-Euler approximation to equation C.35, we obtain the first-order formula:

$$\frac{\mathbf{C^n} - \mathbf{C^{n-1}}}{\Delta t} = \mathbf{A} \cdot \mathbf{C^n} \tag{C.36}$$

or equation C.36 can be written as:

$$\mathbf{C^n} - \mathbf{C^{n-1}} - \Delta t \mathbf{A} \cdot \mathbf{C^n} = 0 \tag{C.37}$$

We use Newton iteration method to solve equation C.37 through seeking a root of equation C.37

Define $\mathbf{f}$

$$\mathbf{f}(\mathbf{C^n}) = \mathbf{C^n} - \mathbf{C^{n-1}} - \Delta t \mathbf{G}(\mathbf{C^n}) \tag{C.38}$$

where $\mathbf{G}(\mathbf{C^n})$ is defined as $\mathbf{A} \cdot \mathbf{C^n}$. Define $\mathbf{J}$ to be the Jacobian matrix, whose ijth element is $\partial G_i / \partial C_j$. Differentiating C.38 with respect to C_j, we obtain equation C.39

$$\mathbf{F}(\mathbf{C^n}) = I - \Delta t \mathbf{J}(\mathbf{C^n}) \tag{C.39}$$

where $\mathbf{F}$ is the matrix whose ijth element is equal to $\partial f_i/\partial C_j$, and I is the identity matrix.

Starting with the solution of the previous time step, $(\mathbf{C^n})^1 = \mathbf{C^{n-1}}$, the kth Newton iterate by solving the linear system equation C.40

$$\mathbf{F}[(\mathbf{C^n})^k](\mathbf{C^n})^{k+1} = \mathbf{F}[(\mathbf{C^n})^k](\mathbf{C^n})^k - \mathbf{f}[(\mathbf{C^n})^k] \tag{C.40}$$

for $(\mathbf{C^n})^{k+1}$. The solution of $\mathbf{C^n}$ is the $(\mathbf{C^n})^{k+1}$ when the iteration is converged. If the convergence is not found, the time step Δt can be reduced in order to obtain convergence.

Appendix D

Algorithm of Flux Corrected Transport

The conservation equations of Eulerian hydrodynamics take the general form

$$\frac{\partial \rho}{\partial t} + \nabla \cdot (\rho \vec{V}) = S \tag{D.1}$$

where ρ is a fluid variable (mass, momentum, or energy density), $\vec{V}$ is the fluid velocity, and S is a source term. In a finite-volume, the change of ρ in each computational cell evolves due to sources and due to the convective fluxes through the faces of that cell. If the external source S is equal to zero, this would leave the total mass of the system unchanged.

D.1 Numerical Diffusion

The equation D.1 can be numerically solved through discretization. Because of the finite approximation, any discrete representation of equation D.1 introduces numerical errors into the solution for ρ. A typical numerical error is false numerical diffusion when the low-order finite difference scheme is used to approximate the spatial gradient term $\nabla \cdot (\rho \vec{V})$ in equation D.1. Take the low-order Lax-Friedrichs scheme as an example. Assume the velocity is constant, the Lax-Friedrichs scheme

(LFS) can be written as equation D.2

$$\rho_i^{n+1} = \frac{1}{2}(\rho_{i+1}^n + \rho_{i-1}^n) - V\frac{\Delta t}{\Delta x}(\rho_{i+1}^n - \rho_{i-1}^n) \tag{D.2}$$

To illustrate the numerical diffusion of the LFS, I utilize an initial profile with square wave shape under a normalized velocity 1 to test the equation D.2. The results are shown in the left figure of Figure D.1. Under the constant convection velocity, we expect that ρ profile would only change its location but keep the exact shape. However, a severe distortion can be seen at time step 150 and 300. Firstly, the sharp edges of the square wave are smoothed out as it should be still square. Secondly, the maxima of the square wave are gradually decrease. On the one side of the coin, the first order LFS introduces severe numerical diffusion. On the other side of the coin, the LFS guarantee the positivity of the solution, and smooth profile of ρ. Therefore it does not provide any non-physical solution of ρ.

Theoretically, if step size Δx approaches to zero, the LFS would give accurate solutions. However, with finite Δx, one way to compensate the numerical diffusion is to adopt higher order scheme, for instance Lax-Wendroff scheme (LWS), which can be approximated to the convection term. The LWS is given by equation D.3.

$$\rho_i^{n+1} = \rho_i^n - V\frac{\Delta t}{2\Delta x}(\rho_{i+1}^n - \rho_{i-1}^n) + V^2\frac{(\Delta t)^2}{2(\Delta x)^2}(\rho_{i+1}^n - 2\rho_i^n + \rho_{j-1}^n) \tag{D.3}$$

The results with the LWS are given in the right plot of Figure D.1. The advantage of the LWS is maxima of the square wave are maintained and so do the shape, to a better degree. However, this scheme generates Gibson phenomenon at the steepest gradient of density profile in the solution, leading to instability eventually. In addition, the oscillations generate non-physical negative ρ.

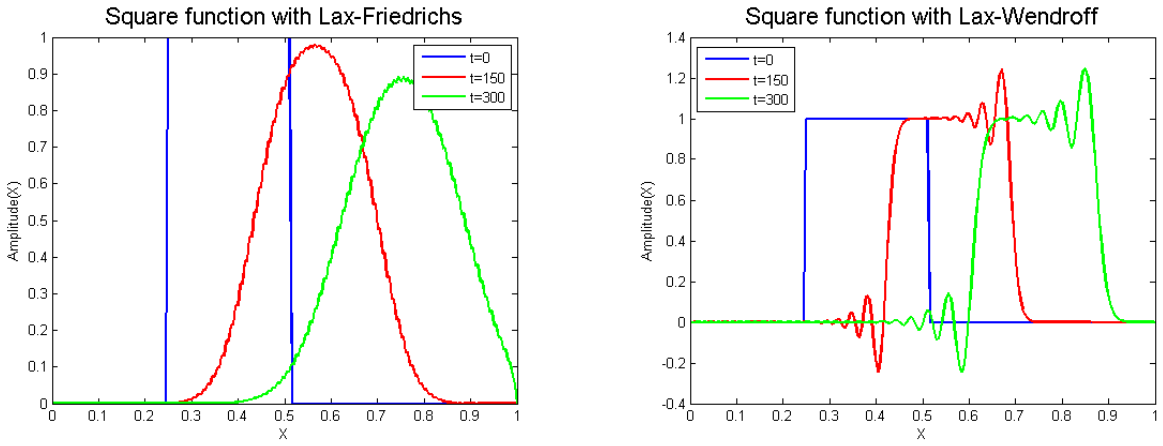

FIGURE D.1: Numerical solution of square wave obtained by LFS (left) and LWS (right).

D.2 Flux Corrected Method

By taking the advantage of the numerical diffusion of low order scheme to maintain positivity and higher accuracy of the high-order scheme to obtain anti-diffusive fluxes, flux corrected transport (FCT) method can achieve non-diffusive solution and maintain positivity at the same time. The idea of FCT is originated from *Boris and book* [1973]. Written in conservation (or "flux") form with a finite difference approximation, equation D.1 is given by

$$\rho_i^{n+1} = \rho_i^n - \Delta x_i^{-1}[F_{i+1/2} - F_{i-1/2}] + S_i^n \tag{D.4}$$

where $F_{i+1/2}$ are called transportive fluxes, which is defined by the product of ρ and $\vec{V}$ at time levels t^n. Assuming the external source term is zero, the procedures of the algorithm to solve euqation D.4 are given by

1. Utilize a low-order scheme to compute $F_{i+1/2}^L$, sufficiently ensure the positivity and monotonic (ripple-free) of the solution everywhere;

2. Utilize a order-order scheme to compute $F^H_{i+1/2}$;

3. Compute numerical anti-diffusive fluxes with the difference between $F^H_{i+1/2}$ and $F^L_{i+1/2}$, which is $A_{i+1/2} \equiv F^H_{i+1/2} - F^L_{i+1/2}$;

4. Advect ρ with lower-order scheme, $\rho^{td}_i = \rho^n_i$ - $\Delta x_i^{-1}[F^L_{i+1/2}$ - $F^L_{i-1/2}]$;

5. Limit these anti-diffusive fluxes so that no new extrema will be created and no existing extrema will be enhanced, $A^c_{i+1/2} = C_{i+1/2}\ A_{i+1/2}$, where $0 \leqslant C_{i+1/2} \leqslant 1$;

6. Apply the corrected fluxes to ρ^l to obtain the desired solution, $\rho^{n+1}_i = \rho^{td}_i$ - $\Delta x_i^{-1}[A^c_{i+1/2}$ - $A^c_{i-1/2}]$.

The heart of the FCT algorithm is how to obtain the flux limiter, $C_{i+1/2}$. The original corrected flux in *Boris and Book* [1973] is given by equation D.5,

$$A^c_{i+1/2} = S_{i+1/2} max\Big\{0, min[|A_{i+1/2}|, S_{i+1/2}(\rho^{td}_{i+2} - \rho^{td}_{i+1})\Delta x_{i+1}, S_{i+1/2}(\rho^{td}_i - \rho^{td}_{i-1}\Delta x_i)]\Big\} \quad \text{(D.5)}$$

Zalesak [1979] developed a better algorithm by considering the action of the anti-diffusive fluxes at neighbouring grid points. The procedures of determining flux limiter in *Zalesak* [1979] are shown the following steps:

1. Set certain down-gradient anti-diffusive fluxes to zero,

$$\begin{aligned} A_{i+1/2} = 0, \quad & if \quad && A_{i+1/2}(\rho^{td}_{i+1} - \rho^{td}_j) < 0 \\ and \quad & either \quad && A_{i+1/2}(\rho^{td}_{i+2} - \rho^{td}_{j+1}) < 0 \\ & or \quad && A_{i+1/2}(\rho^{td}_j - \rho^{td}_{j-1}) < 0 \end{aligned} \quad \text{(D.6)}$$

2. Evaluate the range of permissible value for ρ_i^{n+1},

$$\rho_i^{max} = max(\rho_{i-1}^n, \rho_i^n, \rho_{i+1}^n, \rho_{i-1}^{td}, \rho_i^{td}, \rho_{i+1}^{td}) \tag{D.7}$$

$$\rho_i^{min} = min(\rho_{i-1}^n, \rho_i^n, \rho_{i+1}^n, \rho_{i-1}^{td}, \rho_i^{td}, \rho_{i+1}^{td}) \tag{D.8}$$

3. Compute the sum of all anti-diffusive fluxes into grid cell i,

$$P_i^+ = max(0, A_{i-1/2}) - min(0, A_{i+1/2}) \tag{D.9}$$

4. Compute the maximum net anti-diffusive flux divergence that will preserve $\rho_i^{n+1} \leqslant \rho_i^{max}$,

$$Q_i^+ = (\rho_i^{max} - \rho_i^{td})\frac{\Delta x_i}{\Delta t_i} \tag{D.10}$$

5. Compute the required limitation on the net anti-diffusive flux into grid cell i,

$$R_i^+ = \begin{cases} min(1, Q_i^+/P_i^+) & if \quad P_i^+ > 0 \\ 0 & if \quad P_i^+ = 0 \end{cases} \tag{D.11}$$

6. Compute the corresponding quantities involving the net anti-diffusive flux out of grid cell i,

$$P_i^- = max(0, A_{i+1/2}) - min(0, A_{j-1/2}) \tag{D.12}$$

$$Q_i^- = (\rho_i^{td} - \rho_i^{min})\frac{\Delta x_i}{\Delta t_i} \tag{D.13}$$

$$R_i^- = \begin{cases} min(1, Q_i^-/P_i^-) & if \quad P_i^- > 0 \\ 0 & if \quad P_i^- = 0 \end{cases} \tag{D.14}$$

7. Limit the anti-diffusive flux so that it neither produces an overshoot in the grid cell into which it is directed nor generates an undershoot in the grid cell out of which is flows,

$$C_{i+1/2} = \begin{cases} min(R^+_{i+1}, R^-_i), & if \quad A_{i+1/2} \geqslant 0 \\ min(R^+_i, R^-_{i+1}), & if \quad A_{i+1/2} < 0 \end{cases} \tag{D.15}$$

Figure D.4 is a example of illustrating the performance of the Zalesak FCT algorithm. In this example, the upstream method (equation D.16) is utilized to compute monotone flux,

$$F^L_{i+1/2} = \frac{V}{2}(\rho_i + \rho_{i+1}) - \frac{|V|}{2}(\rho_{i+1} - \rho_i) \tag{D.16}$$

and the high-order flux is computed using the fourth order scheme, equation D.17

$$F^H_{i+1/2} = \frac{7}{12}(V_{i+1}\rho_{i+1} + V_i\rho_i) - \frac{1}{12}(V_{i+2}\rho_{i+2} + V_{i-1}\rho_{i-1}) \tag{D.17}$$

Figure D.4 shows that the FCT scheme significantly reduces numerical dispersion by capturing the steepness of the jump much better than the upstream method, also completely eliminates the dispersive ripples in the uncorrected LWS. A "clipping" phenomenon is observed from the right plot of Figure D.4. The peak of the Gaussian wave gradually declines. As discussed by *Zalesak* [1979], the diffusion term causes the peak in ρ^{td} to be smaller than the peak in ρ^n_i, leaving the flux limiter D.15 with no way of resurrecting the original peak. *Zalesak* [1979] provided a new limiter to eliminate the "clipping" phenomenon. The procedures of the algorithm of new limiter is similar to the original procedures from equation D.6 to D.15. The only difference is replace equation D.7

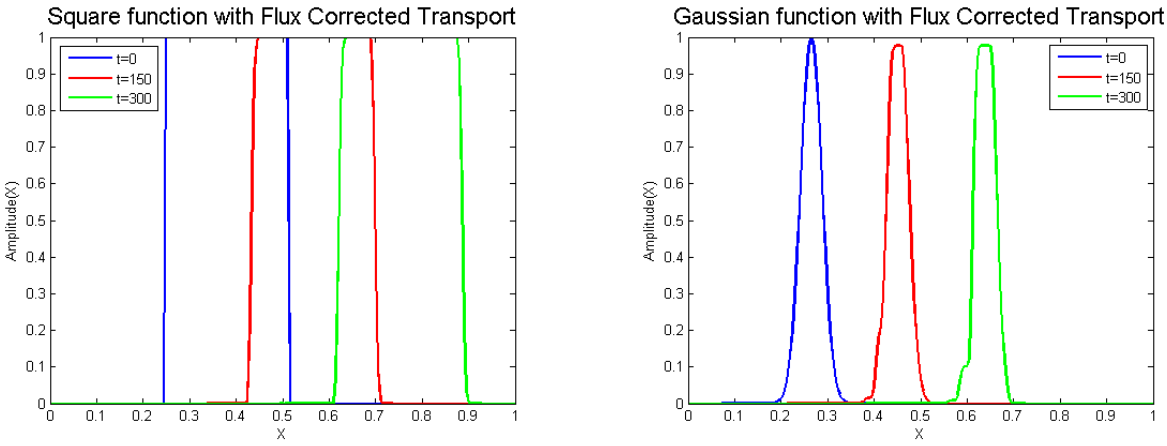

FIGURE D.2: Results from constant-wind-speed advection tests: (left) numerical solution of square wave obtained by Zalesak FCT; (right) numerical solution of Gaussian function obtained by by Zalesak FCT.

and D.8 with the new equation D.19 and D.21

$$\rho_i^a = max(\rho_i^n, \rho_i^{td}) \tag{D.18}$$

$$\rho_i^{max} = max(\rho_{i-1}^a, \rho_i^a, \rho_{i+1}^a, \rho_{i+1/2}^{peak}, \rho_{i-1/2}^{peak}) \tag{D.19}$$

$$\rho_i^b = max(\rho_i^n, \rho_i^{td}) \tag{D.20}$$

$$\rho_i^{min} = max(\rho_{i-1}^b, \rho_i^b, \rho_{i+1}^b, \rho_{i+1/2}^{peak}, \rho_{i-1/2}^{peak}) \tag{D.21}$$

The $\rho_{i+1/2}^{peak}$ is defined by the ρ^{td} value at the intersection of the line segments formed by connecting the point $(x_{i-1}, \rho_{i-1}^{td})$ with (x_i, ρ_i^{td}) and the point $(x_{i+1}, \rho_{i+1}^{td})$ with $(x_{i+2}, \rho_{i+2}^{td})$. If the x coordinate of this intersection lies between x_i and x_{i+1}, then we consider this $\rho_{i+1/2}^{peak}$ to be an allowable ρ^{max} or ρ^{min} for either ρ_i^{n+1} or ρ_{i+1}^{n+1}, as shown in Figure D.3. With the new limiter, we can eliminate the clipping, as shown in Figure D.4.

Some of the choices of F^L and F^H are summarized here:

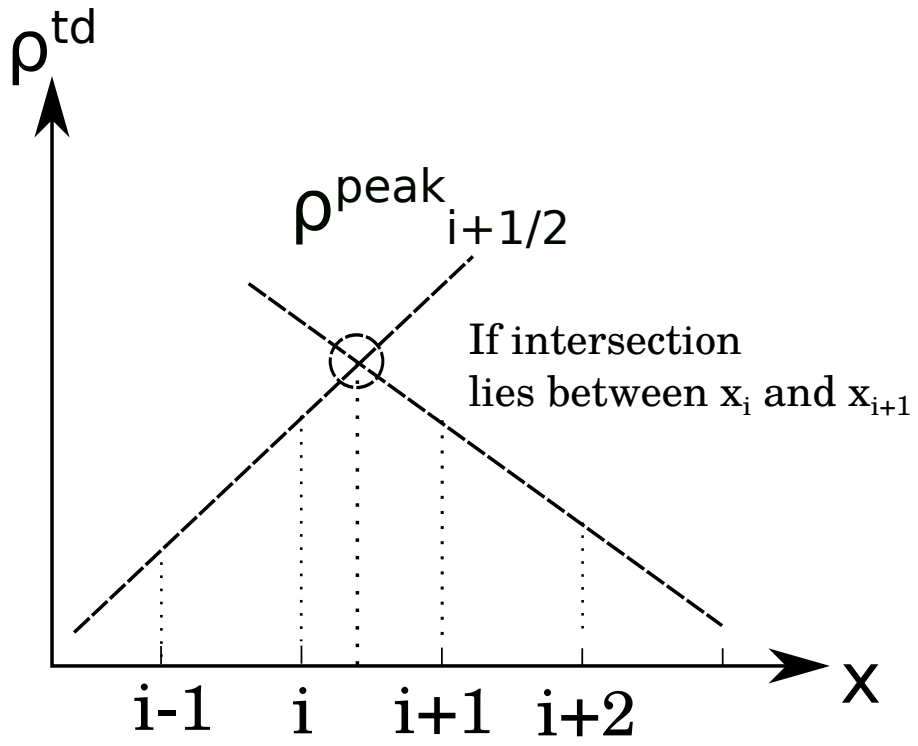

FIGURE D.3: If an extrema lies between grid points i and i+1, the ρ^{td} coordinate of the intersection is then used in the computation of ρ^{max} and ρ^{min} [*Zalesak*, 1979].

1. The low order flux of the leapfrog-trapezoidal FCT schemes is donor cell plus a zero order diffusive flux with coefficient $\frac{1}{8}$.

$$F^L_{i+1/2} = V_{i+1/2}\rho^{DC}_{i+1/2} - \frac{1}{8}\frac{(x_{i+1} - x_i)}{\Delta t}(\rho^0_{i_1} - \rho^0_i) \tag{D.22}$$

where $V_{i+1/2} = \frac{1}{2}\ (V_{i+1} + V_i)$; $\rho^{DC}_{i+1/2} = \rho^0_i$ if $V_{i+1/2}$ *geqslant* 0 or $\rho^{DC}_{i+1/2} = \rho^0_{i+1}$ if $V_{i+1/2}$ *le* 0; $\rho^0_{i+1/2} = \rho^{n-1}_i$ for leapfrog step or $\rho^0_{i+1/2} = \rho^n_i$ for trapezoidal step.

2. First order upstream scheme [*Durran*, 2010]:

$$F^L_{i+1/2} = \frac{V}{2}(\rho_i + \rho_{i+1}) - \frac{|V|}{2}(\rho_{i+1} - \rho_i) \tag{D.23}$$

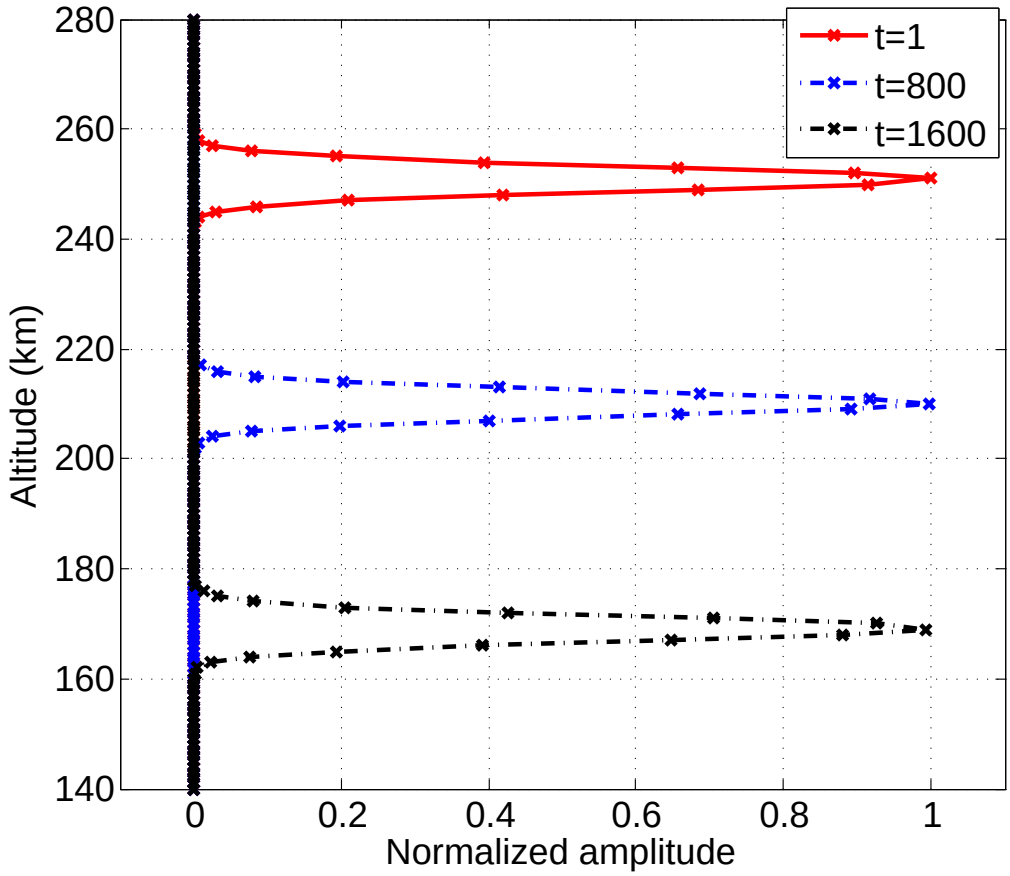

FIGURE D.4: No clipping FCT, we utilize the ρ^{peak} to compute ρ^{max} and ρ^{min} in the new flux limiter. Note that the clipping has been virtually eliminated.

3. Second order leapfrog-trapezoidal finite difference scheme [*Zalesak*, 1979]:

$$F^H_{i+1/2} = \frac{1}{2}(V_{i+1}\rho_{i+1} + V_i\rho_i) \tag{D.24}$$

4. Second order Lax-Wendroff scheme [*Durran*, 2010]:

$$F^H_{i+1/2} = \frac{V_{i+1/2}}{2}(\rho_i + \rho_{i+1}) - \frac{V^2_{i+1/2}\Delta t}{2\Delta x}(\rho_{i+1} - \rho_i) \tag{D.25}$$

5. Forth order scheme [*Zalesak*, 1979]:

$$F^H_{i+1/2} = \frac{7}{12}(V_{i+1}\rho_{i+1} + V_i\rho_i) - \frac{1}{12}(V_{i+2}\rho_{i+2} + V_{i-1}\rho_{i-1}) \tag{D.26}$$

6. Sixth order scheme [*Zalesak*, 1979]:

$$F^H_{i+1/2} = \frac{37}{60}(V_{i+1}\rho_{i+1} + V_i\rho_i) - \frac{2}{15}(V_{i+2}\rho_{i+2} + V_{i-1}\rho_{i-1}) + \frac{1}{60}(V_{i+3}\rho_{i+3} + V_{i-2}\rho_{i-2}) \tag{D.27}$$

7. Eigth order scheme [*Zalesak*, 1979]:

$$\begin{aligned} F^H_{i+1/2} = &\frac{533}{840}(V_{i+1}\rho_{i+1} + V_i\rho_i) - \frac{139}{840}(V_{i+2}\rho_{i+2} + V_{i-1}\rho_{i-1}) \\ &+ \frac{29}{840}(V_{i+3}\rho_{i+3} + V_{i-2}\rho_{i-2}) - \frac{1}{280}(V_{i+4}\rho_{i+4} + V_{i-3}\rho_{i-3}) \end{aligned} \tag{D.28}$$

In order to reduce numerical diffusion as much as possible, higher-order scheme is necessary. However, the disadvantage of higher-order scheme is the weaker stability, leading to algorithm crash eventually. *Gottlieb et al.* [2001], "Strong Stability-Preserving High-order Time Discretization Methods", reviewed a class of strong stablity-preserving (SSP) high-order time discretizations for semi-discrete method of lines approximations of partial differential equations. In this paper, they provided comprehensive studies of SSP linear Runge-Kutta methods, including the construction of optimal explicit SSP linear Runge-Kutta methods. In the high-latitude Fe/Fe^+ model, I used third-order Runge-Kutta methods for nonlinear spatial discretizations, which are the equations from D.29 to D.31.

An optimal third-order SSP Runge-Kutta method [*Gottlieb et al.*, 2001]:

$$\rho^{(1)} = \rho^n + \Delta t L(\rho^n), \tag{D.29}$$

$$\rho^{(2)} = \frac{3}{4}\rho^n + \frac{1}{4}\rho^{(1)} + \frac{1}{4}\Delta t L(\rho^{(1)}), \tag{D.30}$$

$$\rho^{(n+1)} = \frac{1}{3}\rho^n + \frac{2}{3}\rho^{(2)} + \frac{2}{3}\Delta t L(\rho^{(2)}), \tag{D.31}$$

with a CFL coefficient C=1. The $L(\rho^n)$ is the spatial operator, which is the spatial discretization

$$\rho^{n+1} = \rho^n + \Delta t L(\rho^n) \tag{D.32}$$

Appendix E

Divergence of Gravity-wave Horizontal Wind and Relative Phase and Amplitude Response to Gravity Waves of Minor Species

E.1 Wave-Induced Density Perturbations

E.1.1 The results of $\nabla_h \cdot \vec{u}_h$

One example of computing the $\nabla_h \cdot \vec{u}_h$ is provided in the section. In this test, the vertical wave number and wave amplitude were set up the same values as 4.2. One example of vertical wind profile is given by Figure 4.6a. Here the horizontal wavelength and wave period are set up to 800 km and 1.57h, but there is another way of computing the phase speed.

First, we utilize the following formula to calculate buoyancy frequency,

$$N^2 = \frac{g}{T_n}\left(\frac{\partial T_n}{\partial z} + \frac{g}{C_p}\right) \tag{E.1}$$

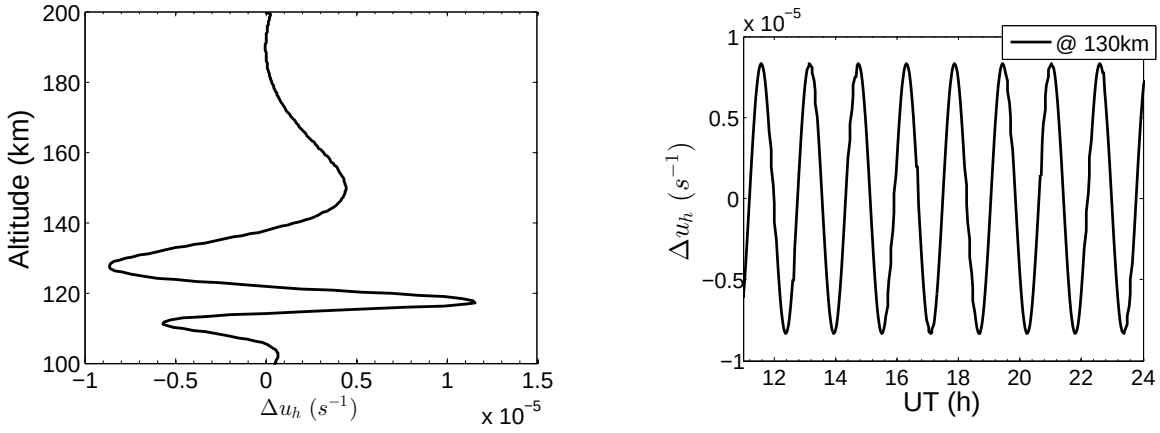

FIGURE E.1: Both $\nabla_h u_h$ are calculated by Hines's formula. The left figure is $\nabla_h u_h$ chaging with altitude; the right plot is $\nabla_h u_h$ temporal variations at 130 km.

where C_p is the heat capacity at constant pressure. C_p is a function of temperature, and the nominal value of C_p used for air at 300 K is 1005 $JKg^{-1}K^{-1}$, and at 550 K is 1040 $JKg^{-1}K^{-1}$, T_n is the neutral temperature.

If the vertical wavenumber is known, the horizontal wavenumber can be calculated by the equation E.2 [*Richmond*, 1983]:

$$m^2 = \frac{N^2}{C_s^2}\Big(1 - \frac{\omega_i^2}{N^2}\Big)\Big(\frac{C_s^2}{(\omega_i/k_h)^2} - 1\Big) - \Big(\frac{2-\gamma}{2\gamma H}\Big)^2 \tag{E.2}$$

The value of $(\frac{\omega_i}{k_h})^2$ can be obtained from equation E.2. Substituting the intrinsic phase speed to equation 5.16, the divergence of gravity-wave horizontal wind $\nabla_h u_h$ can be obtained. To simplify the calculation, the phase speed is just set up by $\frac{800}{1.57}$ km/h in the example as follows.

To illustrate the effects of equation 5.16, Figure E.1 present the spatial and temporal variations of $\nabla_h u_h$. The peak value of $\nabla_h u_h$ is at the altitude of 116 km where the vertical gradient of vertical wind is largest. For a fixed altitude, for example 130 km, the temporal variations of $\nabla_h u_h$ is function of sinusoidal wave, which is consistent with the set-up gravity wave. The second test

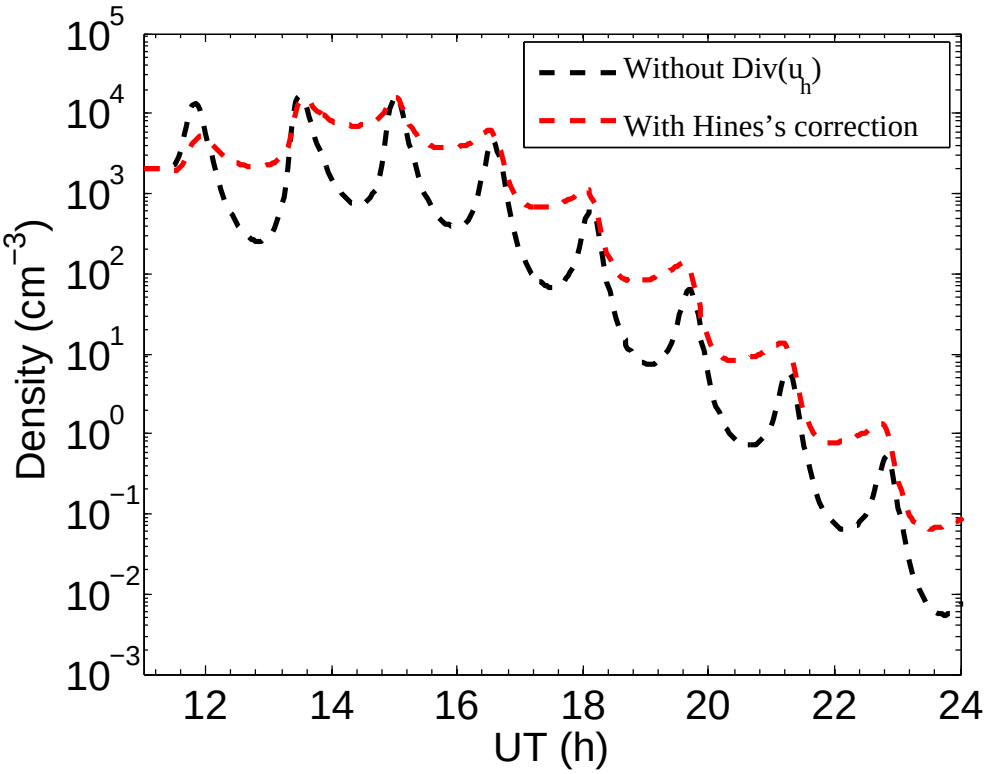

FIGURE E.2: Density perturbations at 130 km. In this test, the initial Fe densities were set to 2000 cm^3, and chemistry module is turned off. The black dashed line is calculated without horizontal divergence, and the red dashed line is corrected by equation 5.16 (Hines).

is to utilize this $\nabla_h u_h$ to correct the Fe density perturbations. In this numerical experiment, the chemistry module is turned off, and the initial Fe densities are 2000 cm^{-3} through all altitudes. Two simulations have been run: one is without the correction of the divergence of horizontal winds; the other on is corrected with $\nabla_h u_h$. The results are compared in Figure E.2. The black dashed line is the Fe density perturbations without correction and the corrected density perturbations is red dashed line. The wave ripples in the density profiles are caused by gravity wave perturbations, and the averaged density decreases w.r.t time because of the downward transport induced by gravity. The local relative density perturbations of the black line is almost 100%. After we offset the density perturbations via equation 5.16, the relative perturbations reduce to around 20%.

E.2 Motions of Fe in Diffusely Separated Atmosphere

In the well mixed region below 100 km, the velocity of minor species $\vec{V}_{s,n}$ is exactly same as the velocity of major gas species, $\vec{V}_{t,n}$. Since molecular diffusion dominates the region above 100 km, $\vec{V}_{s,n}$ maybe differ from $\vec{V}_{t,n}$ because of their different inertial and particle characteristics like collision cross section. Assuming the background atmosphere consists of two motionless, inviscid, neutral ideal gases, the continuity and momentum equations are given by E.3 and E.4:

$$\frac{\partial n_s}{\partial t} + n_s \nabla \cdot \vec{v_s} + v_{(s,z)} \frac{\partial n_s}{\partial z} = 0 \tag{E.3}$$

$$m_s n_s \frac{\partial \vec{v}_s}{\partial t} + \nabla p_s - m_s n_s \vec{g} = K_{st}(\vec{v}_t - \vec{v}_s) \tag{E.4}$$

where s and t refer to minor and major atmospheric constituents, respectively. n_s is the number density of s, and m_s is the atomic mass, K_{st} is the collision parameter describing the efficiency of momentum and heat exchange between the major and minor species, p and v is temperature, pressure and velocity, respectively. If the minor species has no influcence on the motions of major fluid, the major species are still governed by equations 5.1 – 5.3.

By adopting hard elastic sphere model, the collision parameter can be parameterized as equation E.5

$$K_{st} = \frac{8}{3}\sigma^2 n_s n_t \left(\frac{2\pi m_s m_t k_b T}{m_s + m_t}\right)^{1/2} \tag{E.5}$$

where σ is the sum of the radii of the spheres. An example of $K_{st}/(n_s m_s)$ is shown in Figure E.3

If the number density of minor species is extreme low, for instance, 50 cm^{-3} Fe atoms in 10^{10} cm^{-3} air gases, the chance of two Fe atoms colliding is negligible. Therefore, we simplify the equation of momentum converservation E.4 by neglecting the term of partial pressure $\nabla p'_s$,

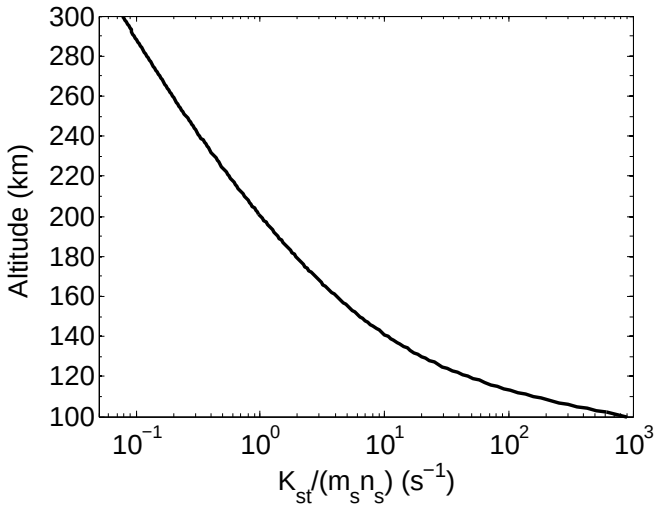

FIGURE E.3: The minor species is set to Fe, and K_{st} is normalized to n_{Fe} and m_{Fe} and the major species are N_2, O_2 and O.

therefore we have equation E.6

$$m_s n_s \frac{\partial \vec{v}_s}{\partial t} - m_s n_s \vec{g} = K_{st}(\vec{v}_t - \vec{v}_s) \tag{E.6}$$

The horizontal component of equation E.6 is given by equation E.7

$$\frac{\partial v_{(s,h)}}{\partial z} + \frac{K_{st}}{m_s \bar{n_s}} v_{(s,h)} = \frac{K_{st}}{m_s \bar{n_s}} v_{(t,h)} \tag{E.7}$$

Assume $v_{(t,h)}$ is a wave form forcing, $v_{(t,h)} = \tilde{v}_{(t,h)} e^{i\omega t}$, the equation E.7 has an analytical solution, as given in equation E.8

$$v_{(s,h)} = C_0 + C_1 e^{-\frac{K_{st}}{m_s \bar{n_s}} t} + C_2 (\frac{K_{st}}{m_s \bar{n_s}} - i\omega) e^{i\omega t} \tag{E.8}$$

where C_0, C_1 and C_2 are determined by the intial condition of $v_{(s,h)}$. The C_1 term is the decay

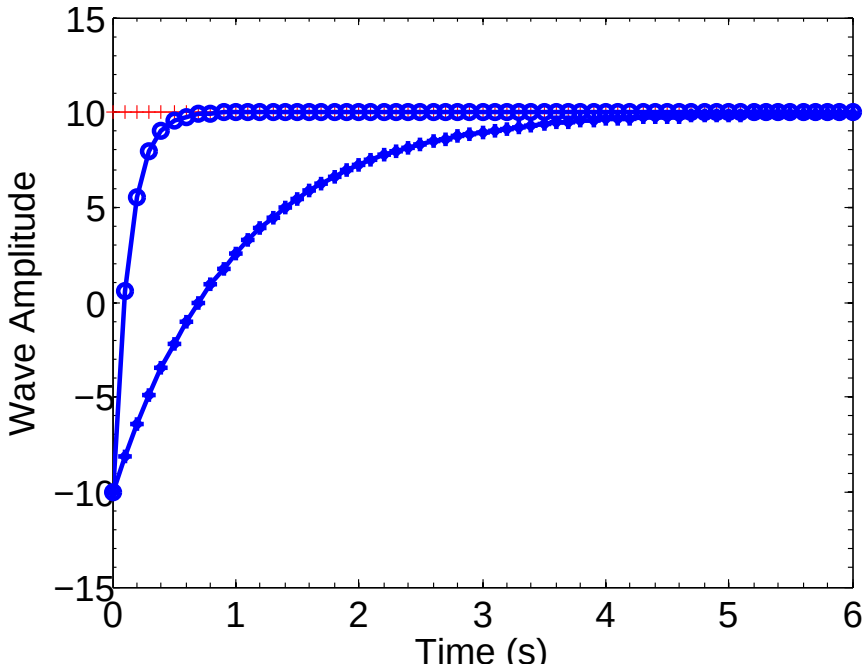

FIGURE E.4: The red lines with plus signs represent the temporal variation of $v_{(t,h)}$, and the blue lines are the solution of $v_{(s,h)}$ at the first 6 seconds. The blue line with circles is at 140 km and the altitude of the blue solid line is 200 km.

term, exponentially approaching zero. The period term in Equation E.8 indicates that $v_{(s,h)}$ has exact the same period as ω.

For example, we set $v_{(t,h)} = 10e^{-i2\pi t/5400}$, the initial condition $v_{(Fe,h)}|_{t=0} = -10$, which is opposite to the intial value of $v_{(t,h)}$. Due to the altitude dependence of K_{st}, we test two altitudes, 140 km and 200 km, respectively. The solutions of $v_{(Fe,h)}$ in the first 6 seconds is given in Figure E.4. By the forcing of the red line, both lines essentially approach the red line within 12 seconds. At 140 km, $v_{(Fe,h)}$ (the blue circled line) is forced to follow $v_{(t,h)}$ (the red plussed line) within 0.5 s, and at altitude of 200 km, it needs to take about 3.5 s for the major species to force minor speices Fe to follow their motions. The less time it takes at lower altitude, and the longer time at higher altitude, because the momentum transfer efficiency factor K_{st} decrease with respect to altitude. Compared to the time scale of thermospheric Fe layer events, which are in hours usually, the time

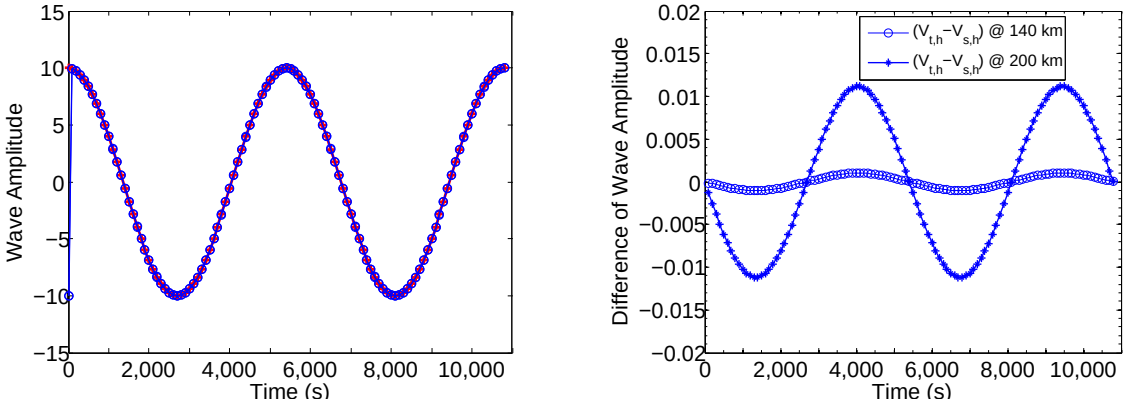

FIGURE E.5: Same as Figure E.4, but with different time scale. 3 periods are showed in this figure. The left panel shows the comparison of $v_{(t,h)}$ and $v_{(s,h)}$, and right panel provides the difference of the $v_{(t,h)}$ and $v_{(s,h)}$.

for thermospheric Fe to be totally governed by major species is significant short. It implies a good approximation that the neutral Fe would immediately follow the motion of background air, when neutral Fe atoms are formed by neutralization of Fe^+, whose velocities may differ from the neutral velocity by a great extent.

Once the motion of Fe atoms couple with the motion of major species, they would follow the motion of the major species. As show in Figure E.5, the blue lines that are the solutions of $v_{(Fe,h)}$ basically overlap the red line $v_{(t,h)}$ at two altitudes with slight differences. To make clear a plot, only the first 3 periods are showed. The differences between $v_{(t,h)}$ and $v_{Fe,h}$ are presented in the left plot of Figure E.5. At 140 km, the difference is constrained within 0.01%, it increase to 0.1% at altitude of 200 km. The periodic variations of the differences suggests the period of Fe motion is the same as that of major species, and the phase of Fe motion is slightly lagging behind the phase of the motion of major species, due to the heavier weight of Fe atom.

Appendix F

Impact of Gravity-wave Propagation Direction on the Formation of Thermospheric Fe/Fe^+ Layers

In the set of experiments, I test the impact of gravity-wave propagation direction on the shapes of thermospheric Fe/Fe^+. All the experiments are set up with the same conditions and parameters as the simulation of Figure 17 in the paper draft except the gravity wave propagation direction.

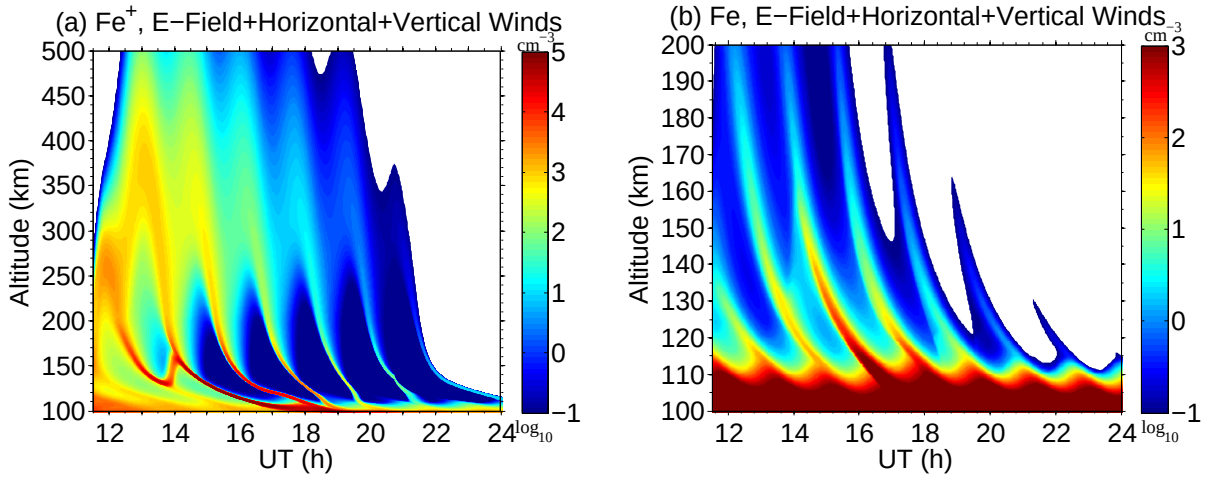

FIGURE F.1: Experiment I: gravity-wave propagation direction is north-east.

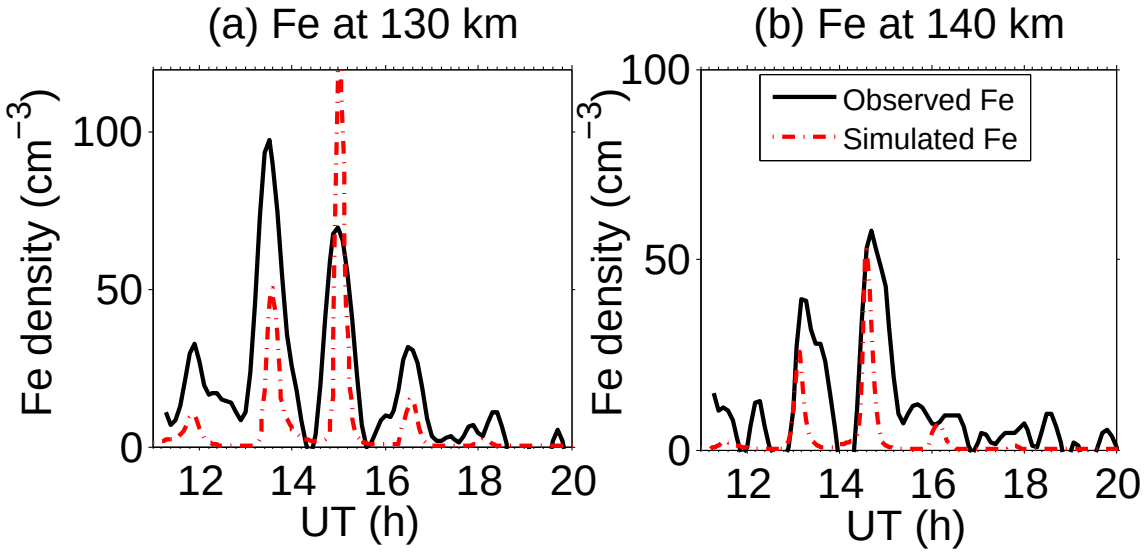

FIGURE F.2: Experiment I: gravity-wave propagation direction is north-east.

Experiment I The direction of gravity-wave propagation is north-east. Figure F.1 and F.2 are identical with the Figures 17 and 18 in the paper draft.

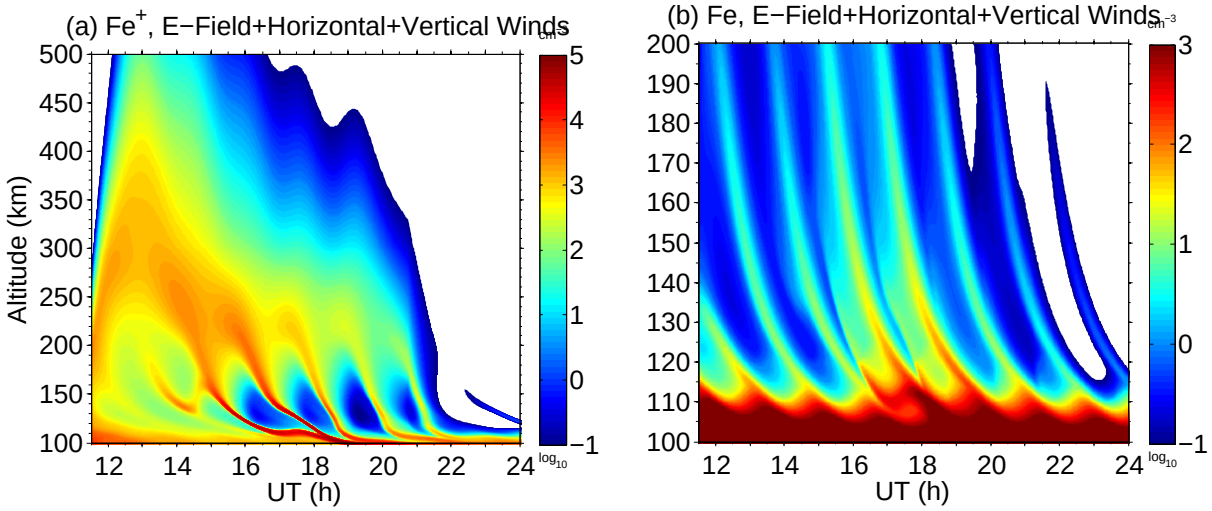

FIGURE F.3: Experiment II, gravity-wave propagation direction is south-west.

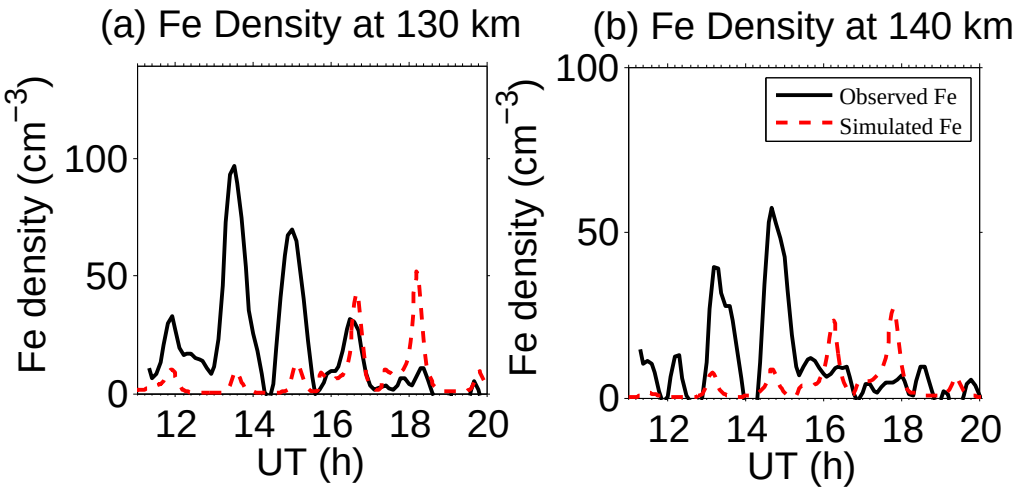

FIGURE F.4: Experiment II, gravity-wave propagation direction is south-west.

Experiment II The direction of gravity-wave propagation is south-west.

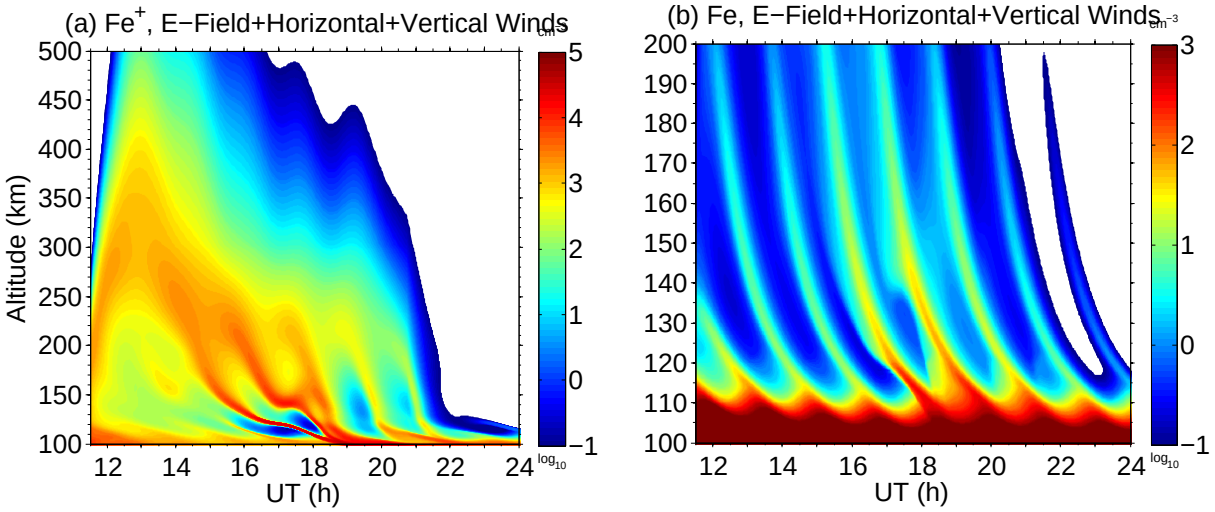

FIGURE F.5: Experiment III, gravity-wave propagation direction is south-east.

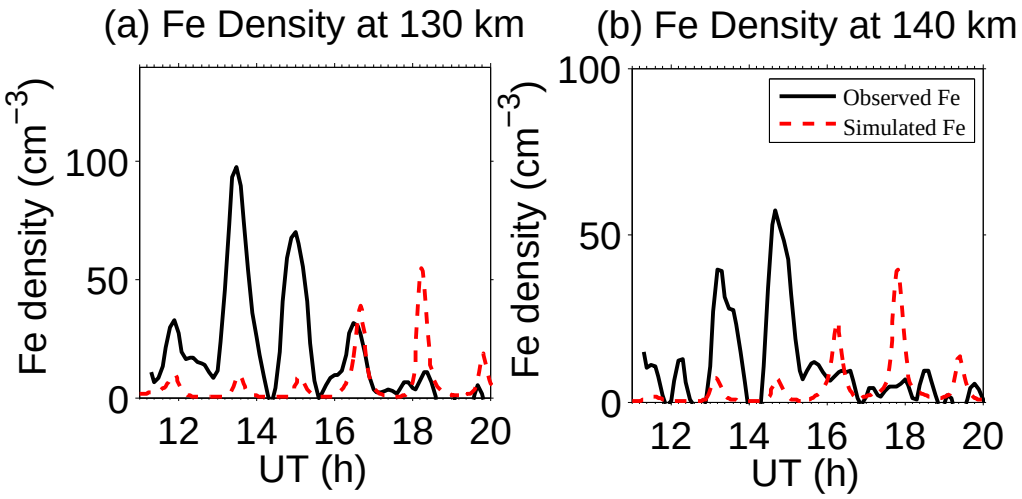

FIGURE F.6: Experiment III, gravity-wave propagation direction is south-east.

Experiment III The direction of gravity-wave propagation is south-east.

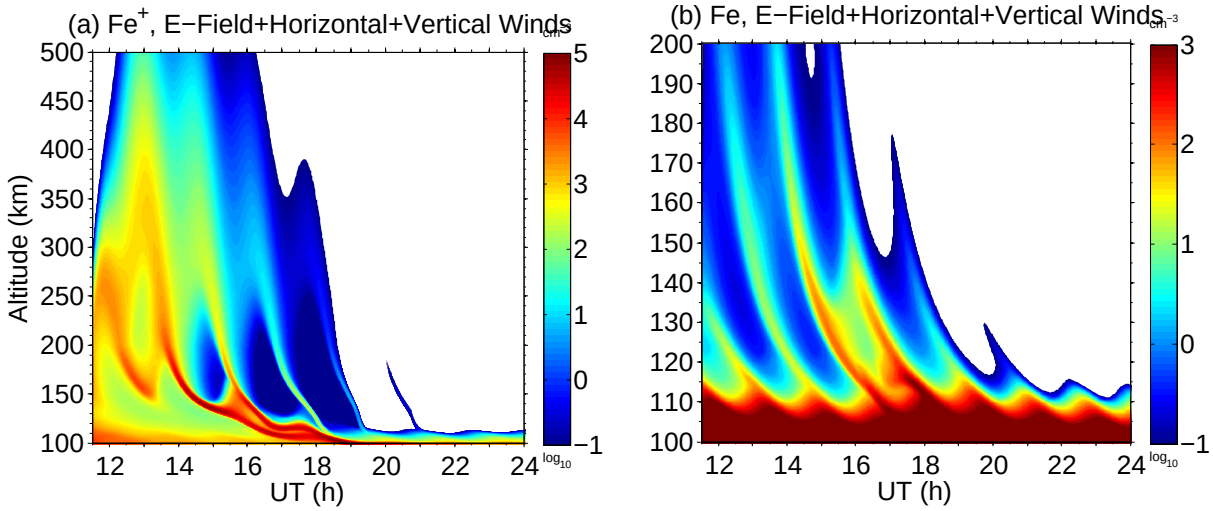

FIGURE F.7: Experiment IV, gravity-wave propagation direction is north-west

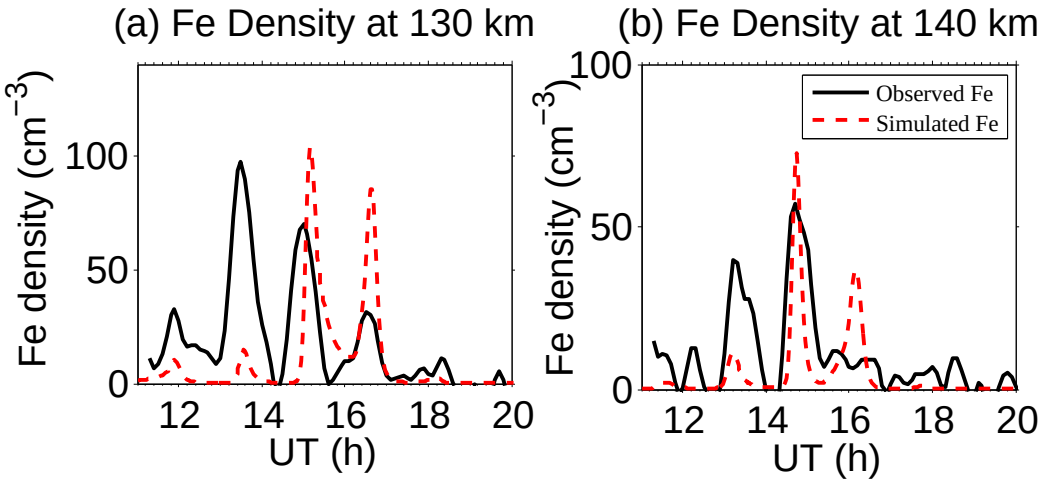

FIGURE F.8: Experiment IV, gravity-wave propagation direction is north-west.

Experiment IV The direction of gravity-wave propagation is north-west.

Appendix G

Identifying Outliers by Box Plot

G.1 Box plot

In statistics, an outlier is an data point that is distant from the most populated observations. Identifying outliers, it depends on the statistical distribution. For instance, if the data set is large enough and can be approximated by a normal distribution, the outlier can be identified according to the standard deviation. When the data set is small and its statistical distribution is unknown, Tukey's [1977] method, identifying outliers graphically by constructing a box plot, is suitable for this situation.

The central tendency of the box plot is the median, and the "box" represents the third quartile (75 percent) Q_3 and first quartile Q_1 (25 percent) of the data, which is known as the interquartile range (IQR): $IQR = Q_3$-Q_1. *Tukey* [1977] suggests that the outliers are determined by a lower interquartile limit (LIQL):

$$LIQL = Q_1 - (factor \times IQR) \tag{G.1}$$

and an upper interquartile limit (UIQL):

$$UIQL = Q_3 + (factor \times IQR) \tag{G.2}$$

The *factor* varying from 1.5 to 3 is determined by the sensitivity is detecting an outlier. The procedure of making box plot is:

1. Given the univariate distribution data set $X_n = \{x_1, x_2, \cdots, x_n\}$, sorted from lowest value to highest;
2. Find the median of the data set;
3. Find the first and third quartiles, and calculate the IQR;
4. Calculate the LIQL and UIQL;
5. Draw and label the axes of the graph;
6. Draw the box plots;
7. The outliers are inside or outside the box.

The original factor by *Tukey* [1977] is chose to be 1.5. In particular, why is it 1.5 not 2? Paul Velleman's interview of John Tukey reveals this "secret" that is the official answer given by John Tukey – "Because 1 is too small and 2 is too large".

G.2 Adjusted box plot

The box plot [*Tukey*, 1977] is based on robust measures of LIQL, UIQL and IQR without considering the skewness of the data. *Vandervier and Huber* [2004] developed an adjusted box plot taking into

account the mecouple (MC), a robust measure of skewness for a skewed distribution. The MC is defined as

$$MC(X) = \underset{x_1<M_X<X_2}{med} h(x_1, x_2) \tag{G.3}$$

with x_1 and x_2 sampled independently from X, m_X is the median of X and h is given by

$$h(x_i, x_j) = \frac{(x_j - m_F) - (m_F - x_i)}{x_j - x_i} \tag{G.4}$$

The LIQL:

$$LIQL = Q_1 - h_l(MC)IQR \tag{G.5}$$

The UIQL:

$$UIQL = Q_3 - h_r(MC)IQR \tag{G.6}$$

Vandervier and Huber [2004] gave three models to calculate h_l and h_r

1. Linear model: $h_l(\text{MC}) = 1.5 + \text{a}\cdot$ MC, $h_r(\text{MC}) = 1.5 + \text{b}\cdot$ MC.
2. Quadratic model: $h_l(\text{MC}) = 1.5 + a_1 \cdot MC + a_2 \cdot MC^2$, $h_r(\text{MC}) = 1.5 + b_1 \cdot MC + b_2 \cdot MC^2$.
3. Exponential model: $h_l(\text{MC}) = 1.5e^{aMC}$, $h_r(\text{MC}) = 1.5e^{bMC}$.

G.3 Example

We use box-plot to identify the outlier in the values of X_n = {39, 13, 0, 1, 5, 4, 7, 10, 5, 2, 10, 17, 12}.

1. The first step, sort X_n from lowest value to highest value, X'_n = {0, 1, 2, 4, 5, 5, 7, 10, 10, 12, 13, 17, 39};

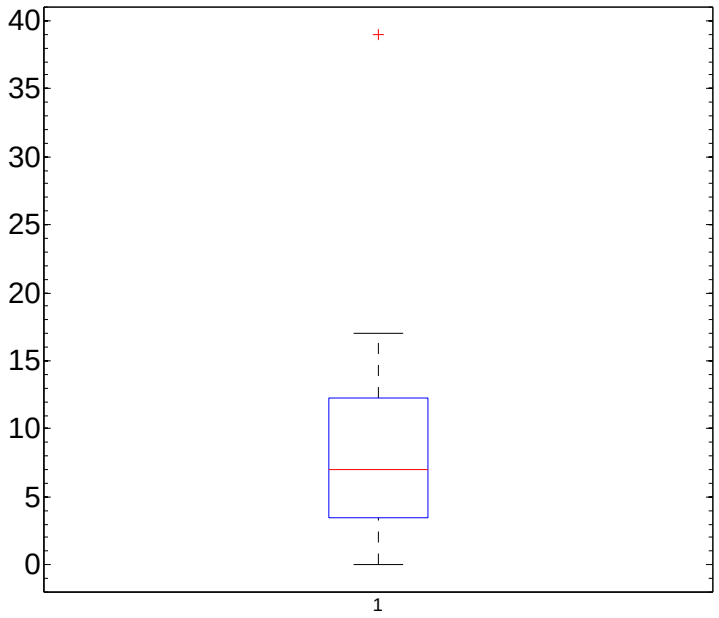

FIGURE G.1: The lower boundary goes to 0, and the upper boundary goes to 17 because it is the largest number before the upper limit of 26.75 is hit.

2. The second step, identify the lower quartile (Q_1), Median (Q_2), and upper quartile (Q_3), which are $Q_1 = 3$ (which is the mean of [2,4]), $Q_2 = 7$, and $Q_3 = 12.5$ (which is the mean of [12, 13]), respectively;

3. The third step, the IQR = Q_3 - Q_1 = 9.5;

4. The forth step, LIQL = Q_1 - 1.5×IQR = 3 - 1.5×9.5 = -11.25; UIQL = Q_3 + 1.5× IQR = 12.5 + 1.5×9.5 = 26.75;

5. The fifth step, the box plot is drawn in Figure G.1;

6. Therefore, any value less than -11.25, or more than 26.75 is an outlier. In this case, number 39 is identified as an outlier

Appendix H

Calculation of Solar Elevation Angle

Assume the Earth to an ideal sphere, its orbit around sun to be an ideal circle, and the Sun to be an ideal point light source, solar elevation angle can be approximated by the equation H.1

$$\theta_{el} = \cos^{-1}\left(\frac{\sqrt{(\Delta x)^2 + (\Delta y)^2}}{R_e}\right) \tag{H.1}$$

where Δx and $Deltay$ are given by equations H.2 and H.3

$$\Delta x = R_e \sin(\phi)\cos(\delta) - R_e \cos(\phi)\sin(\delta)\cos\left(2\pi\frac{lt}{24}\right) \tag{H.2}$$

$$\Delta y = R_e \cos(\phi)\sin\left(2\pi\frac{lt}{24}\right) \tag{H.3}$$

where ϕ is the latitude, lt is local time in hours, δ is the declination angle of the Sun, which is equal to

$$\delta = 23.45 \sin\left(2\pi\frac{284 + DoY}{365.25}\right)$$

where DoY is day of year. Figure H.1 provides the variation of solar elevation angle through a day and a year at McMurdo, Antarctica ($-77.8°$, $166.7°$).

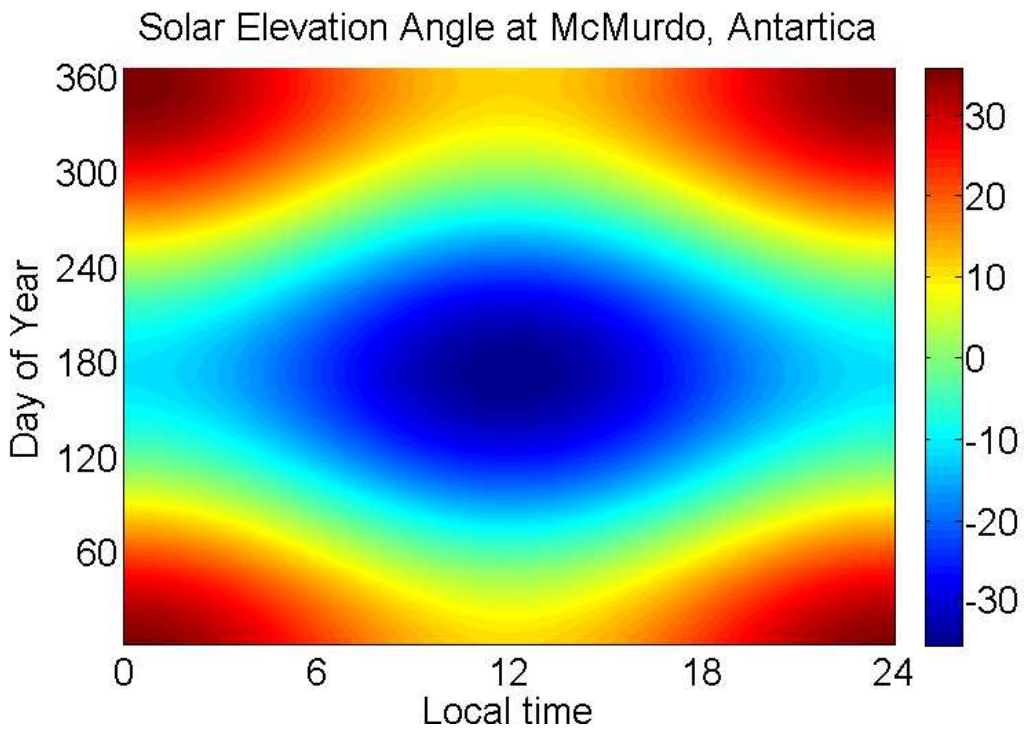

FIGURE H.1: Computed by equation H.1, the elevation of the Sun changes with local time and day of year at McMurdo, Antartica

The more accurate algorithm of calculating the Sun's position is provided by *Reda and Andreas* [2003] in the report of "Solar Position Algorithm for Solar Radiation Application". This document is avalaible at *http://rredc.nrel.gov/solar/codesandalgorithms/spa/*. A MATLAB code is avalaible at *http://www.mathworks.com/matlabcentral/fileexchange/4605-sun-position-m* provided by *Vincent Roy*. In the paper of *Yu et al.*, [2012], we used *Reda and Andreas*'s algorithm to calculate the solar elevation angle. The equation H.1 is suitable for the situation with low-accuracy solar elevation angle calculation. An online tool for calculating the solar elevation angle provided by *NOAA ESRL* is at *http://www.esrl.noaa.gov/gmd/grad/solcalc/azel.html*.

The definition of minimum sunlit altitude is the lowest altitude that sunlight can reach for a given solar elevation, which is computed using a simple geometry model wherein sunlight is treated as parallel light and the Earth is treated as an ideal sphere, as shown in Figure H.2. The formula

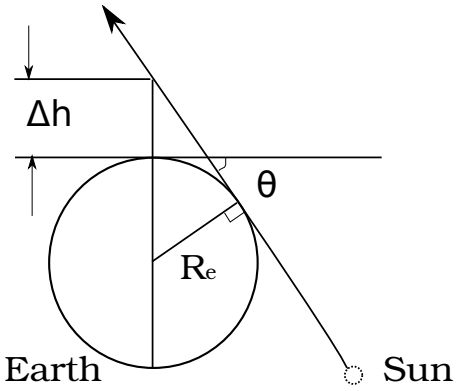

FIGURE H.2: The geometry model of minimum sunlit altitude

of calculating the minimum sunlit altitude is given by the equation H.4,

$$\Delta h = R_e \frac{1 - \cos\theta}{\cos\theta} \tag{H.4}$$